



TOWARDS MOBILE QUANTUM SENSORS FOR GRAVITY SURVEYS.

by

Alexander Niggebaum

A thesis submitted to
The University of Birmingham
for the degree of
DOCTOR OF PHILOSOPHY

Quantum Matter Research Group
School of Physics and Astronomy
College of Engineering and Physical Sciences
The University of Birmingham

October 2015

UNIVERSITY OF
BIRMINGHAM

University of Birmingham Research Archive

e-theses repository

This unpublished thesis/dissertation is copyright of the author and/or third parties. The intellectual property rights of the author or third parties in respect of this work are as defined by The Copyright Designs and Patents Act 1988 or as modified by any successor legislation.

Any use made of information contained in this thesis/dissertation must be in accordance with that legislation and must be properly acknowledged. Further distribution or reproduction in any format is prohibited without the permission of the copyright holder.

Unsere Kenntnisse über die räumliche Variation der Schwere sind wegen Unzulänglichkeit der sie messenden gebräuchlichen Instrumenten bisher sehr lückenhaft.

So far, knowledge of the local variation of heaviness are fragmentary due to the inadequacy of the customary measuring instruments.

Loránd Eötvös, 1896[139]

Abstract

Design and first characterisations of the mobile sensor head in the **Gravity Gradient Technologies and Opportunities Programme (GG^{top})** are presented. The aim of the project is the development of a mobile gravity gradiometer and faces the challenge of condensing a normally lab filling experiment in a portable and robust package. A fibre network replaced free space optics light distribution and fibre based components free space equivalents. Although stable against misalignment, the systems performance is limited by polarisation changes of the guided light which arise from birefringence fluctuations along the length of the network due to external temperature fluctuations and mechanical disturbances. These instabilities limit the achievable temperature of the trapped rubidium 87 cloud to $\approx 18\mu\text{K}$. In preparation for gravity measurements, Rabi oscillations and Ramsey fringes with a $\pi/2$ time of $7.4\mu\text{s}$ were successfully demonstrated in a co-propagating Raman beam configuration. The atom cloud was launched vertically as a first step towards gravity gradiometry. As the system was designed to be portable, the complete system fits into a 1.5m x 2m x 0.5m package plus a 14u rack of support electronics.

Contents

1	Introduction	1
2	A Cold Atom Source	7
2.1	Forces on Atoms	8
2.1.1	Atom Light Interaction	9
2.1.2	The Optical Bloch Equations	11
2.2	Magneto Optical Trapping	14
2.2.1	Light Force	15
2.2.2	Atom Confinement	18
2.2.3	Pre-cooling Atoms	21
2.2.4	Loading Rate and Lifetime	23
2.2.5	Cooling Rubidium 87	23
2.3	Sub Doppler Cooling	26
2.3.1	Atoms in a Standing Wave	26
2.3.2	Sub-Doppler Cooling in a real MOT	35
3	Atom Interferometry	39
3.1	Raman Transitions	41
3.2	Interferometer Geometries and Phase Shifts	46
3.2.1	Classical Action	47
3.2.2	Phase Shift in a Gravitational Field	49
3.2.3	Light Contributions	50

3.2.4	Phase Shifts in an Atom Interferometer	51
3.2.5	Gravity Gradients	52
3.2.6	Raman Beam Configurations	54
3.2.7	Rotation Contributions	58
3.2.8	Sensitivity to Noise	59
4	Polarisation Control	67
4.1	Control Electronics	68
4.2	Polarisation Analysis	69
4.3	Accessible Polarisation	71
4.4	Performance	73
4.5	Misalignment Effects	74
4.6	Possible Improvements	75
5	Experiment	79
5.1	Vacuum System	80
5.1.1	Vacuum Techniques	82
5.1.2	System Mounting	82
5.2	Laser System	83
5.2.1	2D MOT Geometry	87
5.2.2	Laser Frequency Stabilisation	87
5.3	Magnetic Fields	97
5.4	Compensation Fields	99
5.5	Experimental Control	101
5.5.1	Molasses Timing Sequence	102
5.6	Raman Laser	103
6	Results	105
6.1	MOT Loading	105
6.1.1	Fluorescence Imaging	105
6.1.2	Pressure Estimation	107
6.2	Lifetime	108
6.3	Cloud Temperature	109

6.3.1	Absorption Imaging	110
6.3.2	MOT Temperature	112
6.3.3	Molasses Temperature	112
6.4	Atom Launch	116
6.5	Rabi Oscillations	119
6.5.1	Experimental Sequence	122
6.5.2	Extracted Oscillation	122
6.6	Ramsey Fringes	125
6.7	Stability	130
6.7.1	Experimental Reproducibility	131
7	Conclusion	135
A	Raman transitions in Rb87	I
B	Arduino firmware	III
C	Laser Locking	V
C.1	Offset lock components	V
C.2	Laser stability	VII
D	AOM characteristics	VIII
E	Apparatus images	IX
F	Atom Launch	X

List of Figures

1.1	Eötvös pendula	3
1.2	Modern gravimeters	4
2.1	Two level energy scheme	9
2.2	Rabi oscillations	11
2.3	Absorption and emission of resonant light by an atom.	14
2.4	Velocity dependent damping force (Doppler cooling)	17
2.5	level scheme responsible for cooling in a MOT	19
2.6	3D MOT geometry	20
2.7	Rb ⁸⁷ level scheme	24
2.8	Energy level manifolds of an atom in an external field.	28
2.9	De-excitation ladder in the Sisyphus cooling process	29
2.10	Resulting polarisation change in a lin \perp lin configuration	30
2.11	Cooling mechanism of the lin. \perp lin. configuration	31
2.12	Comparison of Doppler and Sisyphus cooling	32
2.13	σ^+ - σ^- 'corkscrew' configuration	33
2.14	σ^+ - σ^- configuration cooling mechanism	34
3.1	Basic light interferometer	39
3.2	Energy Scheme of a <i>Raman transitiostn.</i>	42
3.3	Different interferometer geometries	46
3.4	Gravity influence of the atom trajectory in a Mach-Zehnder interferometer	48

3.5	Interferometer geometries under constant gravity and gravity gradient	53
3.6	Population transfer in Raman pulses	58
3.7	Sensitivity function $g(t)$	61
3.8	Weighting function	62
3.9	Transfer function for mirror vibrations	63
4.1	LCR driver circuit schematic	68
4.2	Polarisation state analyser	70
4.3	Effect of $\frac{\lambda}{2}$ and $\frac{\lambda}{4}$ wave plates and spherical coordinate system	71
4.4	Polarisation control with liquid crystal retarders	72
4.5	LCR Switching performance $\frac{\lambda}{2} \leftrightarrow \frac{\lambda}{4}$	73
4.6	Polarisation with misaligned LCR	75
4.7	Phase shift due to non-perpendicular beams	76
5.1	System layout; mechanical components	81
5.2	Indium sealing	82
5.3	Fibre and laser network	83
5.4	MOT Telescopes	85
5.5	Schematic of the 2D MOT	86
5.6	Modulation transfer spectroscopy	89
5.7	Modulation transfer and DAVL spectroscopy error signals	90
5.8	Schematic of the offset lock circuitry	91
5.9	Offset lock electronics response	92
5.10	Offset lock error signals	93
5.11	Follow speed of the offset lock	94
5.12	Allan deviation of cooler and master lock	95
5.13	Main chamber and attached coils	96
5.14	3D MOT fields	97
5.15	IGBT switching speed	99
5.16	Expected compensation fields	100
5.17	Experiment control scheme	101
5.18	Molasses timing example	102

5.19	Raman laser system	103
6.1	Loading rates for different 2D MOT powers	106
6.2	Fluorescence imaging geometry	106
6.3	Loading curve of the main trap	108
6.4	Lifetime of the MOT	109
6.5	Example optical density extraction	111
6.6	Magneto-optical trap temperature	113
6.7	Molasses temperature	114
6.8	Efficient multi step molasses	115
6.9	Scattering forces in launch configuration	117
6.10	Launching speed vs. relative detuning	118
6.11	Theoretical Rabi oscillation for experiment parameters	120
6.12	Differential light shift	121
6.13	Differential light shift compensated by detuning δ	121
6.14	Rabi sequence	123
6.15	Rabi oscilloscope trace	124
6.16	Rabi oscillation	125
6.17	Expected Ramsey fringes	127
6.18	Measured Ramsey fringes	128
6.19	Analysed Ramsey fringes	128
6.20	PANDA fibre structure	131
6.21	Power fluctuations in MOT telescopes	132
6.22	Position drift of trapped Rb cloud	133
6.23	Loading instabilities	134
7.1	Gravity and gravity gradient signal of a unit size cube	137
A.1	Possible Raman transitions in Rb ⁸⁷	II
C.1	Image of the offset circuit box	VI
C.2	Trace of recorded master frequency	VII
D.1	AOM transmission vs. frequency	VIII

E.1	Open fibre network box	IX
F.1	Launched cloud positions in time	X
F.2	Images of launched clouds	XI

List of Tables

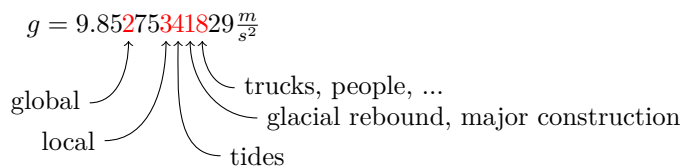
1.1 Gravity signal contributions	2
3.1 Raman transition phase contributions	50
3.2 Raman beam configurations and their momentum transfer	54
C.1 Repumper beat microwave circuit	V
C.2 Cooler beat microwave circuit	VI

1 Introduction

Gravity, the acceleration of masses towards each other, is experienced as a constant and uniform force in everyday life. It gives rise to *Newton's law* which connects two masses m_1 and m_2 via the gravitational constant G^1 and their distance r to the mutual attraction force:

$$|F| = G \frac{m_1 m_2}{r^2}$$

It is this potential which dominates on astronomical scales and forms structures from galaxy clusters down to solar systems. Found by empirical observations the relation is accurate enough to plot the course of spacecraft. This pull, which attracts objects to the Earth's surface, is experienced as constant. It does however change ever so slightly depending on the surrounding masses. The largest influence, in the permille region, is the earth's shape which is, due to rotation, not a perfect sphere but has a larger radius on the equator ($\approx 9.864 \frac{m}{s^2}$) than close to the poles ($\approx 9.864 \frac{m}{s^2}$). On the smaller scales effects by mountains and buildings contribute:



The sixth digit is formed, mountains, hills and variations from localised geological features, such as karst² with a high content of voids, enter. The next order is occupied by the movement of the moon around the earth which displaces the water masses and causes tides. Glacial rebound, the up- and down-shift of tectonic plates which were depressed by glaciers during the ice age and are now relaxing. Major man made constructions and buildings the size of skyscrapers or stadiums occupy the 8th digit. Variations at the next lower order of

¹ $G = 6.673 \cdot 10^{-11} \frac{Nm^2}{kg^2}$

²barren and rocky ground with caves, sinkholes and underground rivers typically limestone. The previously overground rivers and lakes excavated new beds in the soluble material.

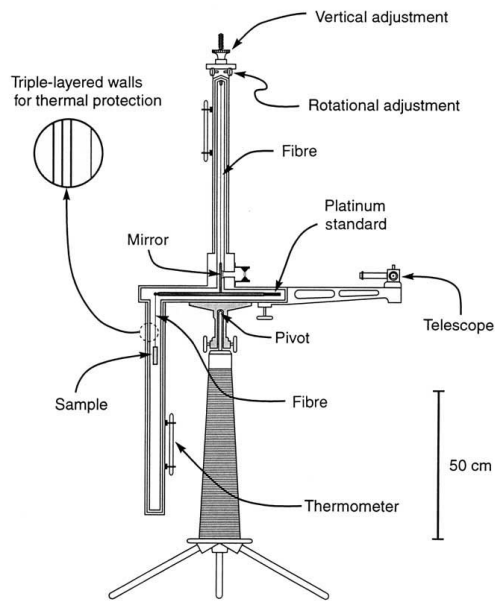
magnitude, one part per billion, are caused by smaller man made objects. They range from lorries, cars and people to infrastructure such as sewer and pipeline systems. Table 1.1, taken from [105] summarizes various influences and their magnitude.

Geographical	
global	$\approx 10^{-3}g$
local	$\approx 10^{-6}g$
natural gradient	$\approx 10^{-7} \frac{g}{m}$
Tidal effects	
base contribution	$\approx 10^{-7}g$
elastic response	$\approx 10^{-8}g$
ocean loading	$\approx 10^{-8}g$
polar motion	$\approx 10^{-8}g$
atmospheric pressure and water table	$\approx 10^{-10}g/mbar$
Human sources	$\approx 10^{-8}g$ to $\approx 10^{-9}g$
Geophysical sources	
postglacial rebound, tectonic movement...	$\approx 10^{-9}g/year$

Table 1.1: Different sources for changes in local gravity and their order of magnitude. List and values are taken from [105]

The first apparatus to quantify gravitational acceleration was developed by Loránd Eötvös in 1885. He developed a pendulum that allowed the comparison of the local attraction of a platinum reference to a sample (see figure 1.1a taken from [54]). This allows studying of the question if all masses are attracted equally, now referred to as the *equivalence principle*. But also the relative gravitational force at different places is observable. Measurements are taken from the rotation of a small mirror attached to the suspension string which is observed through a telescope. The method is precise enough that Eötvös was able to estimate the mass of a hill close to the University of Budapest. Due to its reliability and compactness, the device remained the standard for gravitational surveys and led to the discovery of oil deposits in the United States of America[57, 127] in the middle of the 20th century.

The reason gravity is used to search for oil and gas is the decay and shielding characteristic. Although falling off with $1/r^2$, where r is the distance to the source, it is not shielded by other objects between origin and observer. Other survey methods, such as ground penetrating radar, magnetometry and resistance measurements yield high detail but rely on the electromagnetic conductivity of the local ground or the absorption of radar waves. They are therefore highly susceptible to environmental influences. For example the range of ground penetrating radar can decrease to half a metre from previously up to four, if the soil is saturated in water. Gravity surveys on the other hand benefit from the size of the object that is searched for. An oil deposit is large and therefore casts a detectable signal with the previously mentioned pendulum but



(a) Eötvös pendulum taken from [54]. The gravitational pull of a sample compared to a platinum reference is observed through a pendulum suspended on a fibre. Smallest rotations of the pendulum are observed via a mirror attached to the fibre.



(b) Eötvös pendulum showcased in the *Deutsches Museum* (German Museum) in Munich. The device features two tubes in which both, the sample and the reference mass are suspended.

Figure 1.1: The Eötvös pendulum in schematic and as a museum exhibit



(a) Scintrex CG5 spring based gravimeter

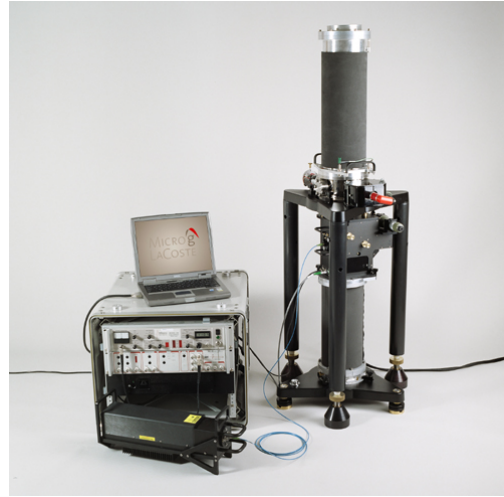
(b) Micro-g LaCoste FG5 falling corner cube gravimeter^a^a<http://www.microglacoste.com/fg5.php>

Figure 1.2: Modern gravimeters using sensor technology based on classical physics.

also modern gravimeters. Figure 1.2 shows two currently available commercially gravimeters: The Scintrex CG5 (figure 1.2a) spring-based gravimeter and the Micro-g LaCoste FG5 (figure 1.2b) falling corner cube gravimeter. The first produces a relative gravity signal by observing the elongation of a well-characterised spring while the latter measures the acceleration of a freely falling reflecting corner cube by way of a laser interferometer. This gives absolute measurements but reduces the sampling rate. The Scintrex device is small and portable and hence widely used in field surveys while the Micro-g requires longer set up times and is used for base reference measurements due to high its precision.

Both gravimeters rely on classical effects to measure local gravity and are limited by the drift and wear of the mechanical parts and the resulting systematics. This work presents efforts to move atom interferometry based gravity measurements out of the laboratory environment into a package which is fit for field surveys. Instead of a macroscopic test mass connected by mechanical parts to the frame, the interference pattern of a freely expanding rubidium cloud is observed. Cooled to low temperatures (μK region) the coherence length of the atoms is long enough to show self interference. This can be achieved by creating a Mach-Zehnder interferometer through a well defined sequence of laser pulses and it will be shown that the phase of such an interferometer depends on the local gravitational acceleration. Because the atoms can be seen as quantum particles and because quantum particles of the same type cannot be distinguished, the measurement

is absolute. It will also be shown that the achievable sensitivity of this technique is high enough to reach precisions which approach the 10^{-9} g region and can therefore be seen as the next generation of survey devices.

The first experiments based on this technology have been demonstrated outside the lab[123, 125] and characterised outside the laboratory[51]. Space based missions[100, 2] based on atom interferometry have been proposed and technologies such as compact laser systems[121] and complete sources of Bose-Einstein-Condensates[118] presented. These projects seek to improve the accuracy of previous gravity mapping missions such as GOCE[119] and tests of general relativity by comparing the acceleration of two atomic species[124]. While the step to space poses an even higher challenge, the seemingly easy step out of a laboratory has its own difficulties. While research groups have been performing laboratory atom interferometer experiments for several decades, there is a significant difference between a noisy outside environment and a controlled and stabilised laboratory. Problems start with external magnetic and electrical fields, and range from vibrations and thermal changes to size, weight and power constraints. Furthermore, there is the issue that a more precise but passive sensor, such as for gravity, involuntarily includes noise from unwanted sources. While a radar detects objects by varying the emission frequency and investigating the returned parts, a gravity signal does contain all contributions and it is not possible to actively make a differentiation. The process of finding the source from a passive signal is called *inversion*. Its quality, mainly how close it is to the 'real' source, depends on resolution and sample density. But even under optimal conditions an infinite number of solutions and therefore density arrangements are possible and assumptions about the expected shape need to be made. This is only a complication if one seeks to create a density map of the underground without any previous knowledge and does not look for oil, gas or pipes, which have well known shape and density characteristics. If, for example, the recorded signal is used for navigation through comparison with a pre-recorded map, a simple filter is sufficient. Thus, the data precision and sampling structure must be tailored to the application in mind.

The general loss of contrast due to the fast signal fall-of in atomic gravimetry can be reduced by using a gradiometric measurement[116]. Instead of observing the gravity signal directly, the difference at two spatially separated positions is measured. For atom interferometry, this approach has the advantage of high common mode and hence noise rejection because the two necessary atom interferometers are driven by the same laser pulses which share the same noise but is cancelled by using the signal's difference. This is the reason why the GGtop apparatus was designed around a gradiometer which could record as many components of the full three dimensional gravity tensor as possible. A second, identical device could be used to complement the vertical measurement direction with horizontal components. Besides the increased robustness against noise,

this approach also yields better localisation possibilities in the aforementioned inversion process.

Scope of this Work

The presented work will summarize the development and first test results of the gravity gradiometer developed in the GGtop (Gravity Gradient Technologies and Opportunities Programme) at the University of Birmingham. The apparatus is part of the sensor work-package which develops the mobile atom interferometer platform. Other parts of the research team are investigating methods of efficient and fast signal interpretation, the problem of moving and aligning the device in the field and the modelling of different sources of interest.

I was the first postgraduate researcher on the sensor part of the project and therefore responsible for the basic design of the apparatus, which includes vacuum system, laser system and light distribution system. Sub-systems such as support electronics for stabilising the laser frequencies and amplification of rf signals to drive acousto-optical modulators were also built. The goal was to lay the foundations for a portable cold atoms experiment for gravity surveys. The primary challenge is to reduce weight and size. While the vacuum system has limited potential, especially in the gradiometer configuration, the heaviest part is the light delivery system with its lenses, mirrors and mounts. Free space optics also have the complication of misalignment when the device is moved. For this reason the decision was made to replace all optical elements with fibre based devices. This bears the risk of an extremely static system which, once it has been connected, is hard to alter if components need to be added or removed. Debugging is hindered by the same reason as it is not possible to investigate the light quality at points in the network. On the other side the advantage of highly reduced size and excellent portability outweighed the anticipated complications at the time of decision.

The choice of a gradiometer scheme over a gravimeter was born from the improved sensitivity to gravity signatures and hence the suitability to detect smaller objects. To implement this double interferometer scheme, the cloud should be launched vertically into a vacuum tube and while in transit, a second one loaded and launched shortly after. The vertical acceleration requires very precise control of the beam balance in the atom trap because any shift does also change the trajectory. The combination with the decision to use all fibre based optics made this approach a high risk one because the performance of a network of the used size was unknown at the time of design. As this work will explain, it is the polarisation stability in the fibre network which limits the performance and reduces contrast. This work is therefore intended as a summary of technologies and findings accumulated during the development of the prototype and will hopefully serve as a resource to improve next generation devices.

2 A Cold Atom Source

Every measurement is only as precise as the references used. Commercial gravimeters use a free falling test mass tracked with a light interferometer¹ or suspended on a sensitive and well characterised spring². Both approaches need to overcome the problem that mechanical parts experience wear over time and therefore the measured values shift and require frequent re-calibration. Elimination of all masses seems not possible because one needs an observable which is influenced by gravitation. One solution to reduce error sources due to degradation is the use of a single particle as a reference, be it an atom or any of its constituents. The complexity comes with isolation and control but since the beginning of the twentieth century, a full catalogue of tools has been developed ranging from single and multi electron and ion traps[28], neutral atom fountains[74] of a single or multiple species to eventually full molecules[147].

Using such an isolated particle in free fall to measure its local acceleration has unfortunately no advantage over a falling corner cube because one would need to track individual particles, which is challenging. However the difference between a trapped and freely moving particle is its kinetic energy which, in order for the particle to stay in confinement, needs to be limited. Expressed in units of energy, a trap can only hold elements which have a lower kinetic energy than the height of its walls. The energy scales are typically low enough that the quantum nature of the trapped matter becomes more apparent and superposition states and interference can be observed. Precisely these effects are used to measure gravity with slow, and therefore cold, atoms. Instead of tracking their trajectory, the phase of an atom interferometer (see chapter 3) reveals the smallest changes of local acceleration. The measurement is absolute, very precise and has no drift in absolute value. Trapped atoms are therefore *the* key prerequisite and the technique to confine them is presented in this chapter. First the general formalism of atom-light interaction is developed to also give the foundation for later chapters which investigate light-based mirrors and beam-splitters for cold atoms.

Methods to describe and understand light as a particle and the interaction of *photons*, the particles of quantized light, with atoms was developed around the 1920s. Einstein presumed in a theoretical discussion[45]

¹Micro-g LaCoste - FG5

²Scintrex FG-5

that atoms could be interpreted as oscillators which react to external resonant stimulus, in this case photons, by change of momentum and internal energy. Following this argument it can be derived that atoms in a resonant light field are expected to undergo directed momentum transfer and in 1933 Frisch[56] demonstrated that an atomic beam is in fact deflected by resonant light. After a short introduction to the basic formalism to describe the interaction, it will become clear that careful engineering of light fields can be used to manipulate the momentum distribution of an atomic cloud and therefore cool and trap them.

2.1 Forces on Atoms

The discovery of the particle nature of light sparked the development of the particle-wave dualism. It describes light as an electro-magnetic wave consisting of photons which are momentum carrying light particles. This raises the question of how the interaction between atoms and light should be treated; as an interaction of the atom with a single photon or interaction with the light field as a whole. Generally, there are three approaches to this. Firstly the classical approach, which uses mechanics to describe the light field and the atom as classical entities and their interaction by conservation of momentum and energy. While capturing all motion effects, quantum mechanical additions such as state superpositions of the atom are not discussed. The second method is the quantum approach which describes the atom and light field as wave functions. Although complete from a quantum mechanical point of view, this quickly leads to a high degree of complexity which is not necessary to develop a sufficient understanding of interaction mechanics. The third and commonly used way is the *semi-classical approach*[131]. While fully considering the quantum properties of the atoms state, external forces and especially momentum transfer to and from photons are treated classically. This is allowed under the assumption that the light field does not vary significantly over the size of the atom (see beginning of section 2.2).

The following sections will derive the *optical Bloch equations*, which describe the evolution of an atom in an external field. It is noteworthy that the same approach is valid for any two level system interacting with an external potential[53]. It might seem over-simplistic at first to apply this formalism to something as complex as an atom, which has multiple core constituents and electrons. Section 2.2.5 however will clarify how it applies specifically to rubidium 87 (87 Rb), which is used in the presented experiment, and potentially other atom species by highlighting the effective two level structure of certain transitions. Depending on the available laser frequencies more complex atoms, such as strontium[34], are treatable in the same way.

2.1.1 Atom Light Interaction

A two level system consists of a ground ($|g\rangle$) and excited ($|e\rangle$) state with the energies ω_g and ω_e separated by $\hbar\omega_0 = \hbar(\omega_e - \omega_g)$ (see figure 2.1). Therefore the general state of the system, being an arbitrary superposition, reads

$$|\Psi\rangle = a(t)e^{-i\omega_g t} |g\rangle + b(t)e^{-i\omega_e t} |e\rangle \quad (2.1)$$

where $|a(t)|^2 + |b(t)|^2 = 1$ needs to be satisfied. The interacting field is represented by

$$\mathbf{E}(\mathbf{r}) = \frac{1}{2}\epsilon(\mathbf{r})E_0(\mathbf{r})e^{i\omega t} + c.c. \quad (2.2)$$

with the polarisation vector ϵ and field amplitude E_0 , which are generally position dependent, but for simplicity this will be omitted in the following. The *Schrödinger equation* describes the temporal evolution of the system:

$$(\mathcal{H} - \mathbf{E} \cdot \mathbf{d}) |\Psi\rangle = i\hbar \frac{d}{dt} |\Psi\rangle \quad (2.3)$$

Interaction of the atom with the field \mathbf{E} is consolidated in the *dipole operator* \mathbf{d} . Exploiting the orthogonality

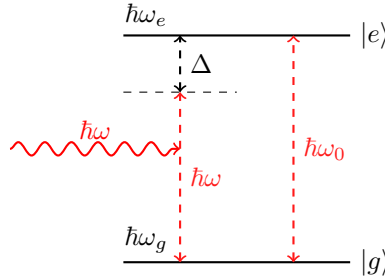


Figure 2.1: Energy diagram of a generic two level system. The levels are separated by $\hbar\omega_0$ and commonly denoted as excited ($|e\rangle$) and ground state ($|g\rangle$). An external light field of photons with energy $\hbar\omega$ might promote the state from $|g\rangle$ to $|e\rangle$ if $\omega = \omega_0$ and therefore the detuning $\Delta = 0$

of the states $|e\rangle$ and $|g\rangle$, that $\langle e|g\rangle = 0$ and $\langle e|e\rangle = \langle g|g\rangle = 1$, as well as the eigenvalue of the *Hamiltonian* $\mathcal{H} |g\rangle = \hbar\omega_g |g\rangle$, leads to the evolution of $a(t)$ and $b(t)$:

$$\frac{d}{dt}a(t) = ib(t)e^{-i\omega_g t} \frac{\langle g|\mathbf{d} \cdot \mathbf{E}|e\rangle}{\hbar} \quad (2.4)$$

$$\frac{d}{dt}b(t) = ia(t)e^{-i\omega_e t} \frac{\langle e|\mathbf{d} \cdot \mathbf{E}|g\rangle}{\hbar} \quad (2.5)$$

Inserting the time dependence of the field from equation 2.2 gives

$$\frac{d}{dt}a(t) = \frac{i\Omega_0 e^{-i\Theta}}{2} b e^{i\Delta t} \quad (2.6)$$

$$\frac{d}{dt}b(t) = \frac{i\Omega_0 e^{i\Theta}}{2} a e^{i\Delta t} \quad (2.7)$$

where fast oscillating terms were dropped using the *rotating wave approximation*. If the time scale of interest is much larger than the oscillation frequency of individual terms, their contributions are assumed to average to zero and can therefore be omitted without significant loss of precision. Equations 2.6 and 2.7 introduced the detuning $\Delta = \omega_g - \omega_e$ and the complex *Rabi frequency*:

$$\Omega_0 e^{i\Theta} = \frac{E_0 \langle e | \mathbf{d} \cdot \boldsymbol{\epsilon} | g \rangle}{\hbar} \quad (2.8)$$

The term frequency will become clear after solving for an atom that is initially in the ground state $|g\rangle$ ($a(0) = 1$ and $b(0) = 0$). The time dependent solutions for $a(t)$ and $b(t)$ become

$$a(t) = e^{\frac{i\Delta t}{2}} \left[\cos\left(\frac{\Omega t}{2} - \frac{i\Delta}{\Omega}\right) \sin\left(\frac{\Omega t}{2}\right) \right] \quad (2.9)$$

$$b(t) = e^{-\frac{i\Delta t}{2}} \frac{i\Omega_0 e^{i\Theta}}{\Omega} \sin\left(\frac{\Omega t}{2}\right) \quad (2.10)$$

which shows that population oscillates between $|g\rangle$ and $|e\rangle$ proportionally to Ω , the *generalized Rabi frequency* ($\Omega = \sqrt{\Omega_0^2 + \Delta^2}$). The probability of finding the system in the excited state after an interaction time t with the field is

$$\begin{aligned} |b(t)|^2 &= \frac{\Omega_0^2}{\Omega^2} \sin^2\left(\frac{\Omega t}{2}\right) \\ &= \frac{\Omega_0^2}{2\Omega^2} (1 - \cos(\Omega t)) \end{aligned} \quad (2.11)$$

which shows periodic excitation and de-excitation of the frequency 2Ω . Such an evolution for varying detunings Δ is shown in figure 2.2. If Δ is zero, the population cycles between the ground and excited state. An increasing Δ however reduces the maximum transition probability while increasing the oscillation's frequency.

Any superposition of $|g\rangle$ and $|e\rangle$ can therefore be reached with a light pulse of matching frequency and duration. For example a pulse of length $\Omega t \frac{\pi}{2} = \frac{\pi}{2}$ results in the state $|\Psi\rangle = \frac{1}{\sqrt{2}} (|g\rangle + |e\rangle)$ if the system starts

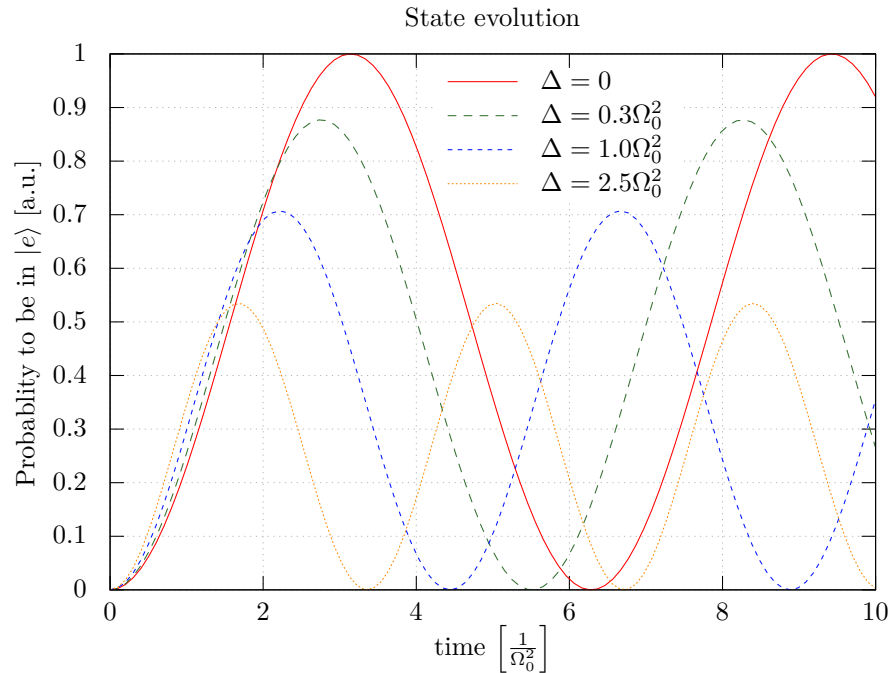


Figure 2.2: State oscillation between a ground state $|g\rangle$ and the excited state $|e\rangle$ of a two level system for different detuning. For higher detuning, the population transfer becomes incomplete, but faster. The latter can directly be seen by an increased *Rabi frequency* for larger detuning.

in $|g\rangle$. The initial discussion argued that photons, as the quasi-particles of light, do carry momentum and naturally light interaction as described above is connected with momentum transfer. To reach the excited state through absorption of a photon, the atom will have also absorbed the momentum so the full state reads $|g, p\rangle \rightarrow |e, p + \hbar k\rangle$, where the wave vector of the photon $k = \frac{2\pi}{\lambda}$ was introduced. It can be pre-empted that this allows the creation of the optical equivalent of beam splitters for atoms (see chapter 3 for the discussion) which enables the construction of a matter interferometer where photons in a conventional interferometer are replaced by atoms and mirrors and polarising beam splitters by laser pulses.

2.1.2 The Optical Bloch Equations

Such population manipulation pulses are generally short enough (μs region) that spontaneous emission is negligible. If this effect is considered, the traces in figure 2.2 would undergo damping and equilibrate to a probability greater than zero. This averaging effect is observed in larger ensembles of atoms. If the population in the excited state $|e\rangle$ is measured over time, the oscillation is damped (see section 6.5) and for long time scales expected to thrive towards 50% (for $\Delta = 0$). While the time scales in an interferometer sequence are too short for spontaneous effects to contribute, they do influence on the loading speed and possible size of an

atom trap. To include these processes in the discussion, it is instructive to describe the system via a *density matrix* $\rho = |\Psi\rangle\langle\Psi|$ and derive the *optical Bloch equations*. For a state $|\Psi\rangle$ ρ has the form

$$\rho = |\Psi\rangle\langle\Psi| = \begin{bmatrix} \rho_{gg} & \rho_{ge} \\ \rho_{eg} & \rho_{ee} \end{bmatrix} \quad (2.12)$$

where the diagonal elements ρ_{ee} and ρ_{gg} represent energies of the ground and excited states and the off-diagonal elements ρ_{ge} and ρ_{eg} the coupling of the two. The time evolution is given by the *Von Neumann equation*

$$i\hbar\frac{\partial\rho}{\partial t} = [\mathcal{H}, \rho]. \quad (2.13)$$

Using the same ansatz as in equation 2.1, the density matrix of a two level system becomes

$$\rho = \begin{bmatrix} a^\dagger(t)a(t) & b^\dagger(t)ae^{i\omega_0 t} \\ a^\dagger(t)b(t)e^{i\omega_0 t} & b^\dagger(t)b(t) \end{bmatrix} \quad (2.14)$$

which needs to satisfy the normalisation condition $\text{Tr}(\rho) = 1$. Using this relation and the above solutions for $a(t)$ and $b(t)$, equation 2.14 reduces to a system of three coupled variables

$$\begin{aligned} u &= e^{-i\Theta}e^{i\Delta t}a^\dagger(t)b(t) + c.c. \\ v &= ie^{-i\Theta}e^{i\Delta t}a^\dagger(t)b(t) + c.c. \\ w &= |b|^2 - |a|^2 \end{aligned} \quad (2.15)$$

with their time dependent forms

$$\begin{aligned} \frac{\partial u}{\partial t} &= \Delta u \\ \frac{\partial v}{\partial t} &= -\Delta u + \Omega_0 w \\ \frac{\partial w}{\partial t} &= -\Omega v \end{aligned} \quad (2.16)$$

This set is known as the *optical Bloch equations* and has a compact vector form[53]

$$\frac{d\mathbf{B}}{dt} = \mathbf{W} \times \mathbf{B} \quad \mathbf{B} = \begin{bmatrix} u \\ v \\ w \end{bmatrix} \quad \mathbf{W} = \begin{bmatrix} -\Omega_0 \\ 0 \\ -\Delta \end{bmatrix} \quad (2.17)$$

The state of the system is easily visualised through a vector that points from the centre of a sphere to its surface. The poles are pure states, such as $|e\rangle$ and $|g\rangle$, any other point is a superposition of the two with an eventual complex phase. This concept is also used to represent quantum bits (qubits) in quantum computation experiments or the polarisation of light[89] (see section 4.2).

Spontaneous Processes

Spontaneous relaxation is introduced by making the elements of ρ time dependent:

$$\frac{\partial \rho_{ee}}{\partial t} = -\Gamma \rho_{ee} \quad \frac{\partial \rho_{gg}}{\partial t} = +\Gamma \rho_{ee} \quad (2.18)$$

where Γ is the linewidth or inverse lifetime of $|e\rangle$. Iterating this to the later vector form yields the components for \mathbf{B} of

$$\frac{\partial u}{\partial t} = \Delta v - \frac{\Gamma}{2}u \quad \frac{\partial v}{\partial t} = -\Delta u + \Omega_0 w - \frac{\Gamma}{2}v \quad \frac{\partial w}{\partial t} = -\Omega_0 v - (1+w)\Gamma \quad (2.19)$$

In a steady state $\frac{\partial u}{\partial t} = \frac{\partial v}{\partial t} = \frac{\partial w}{\partial t} = 0$ the vector relation 2.17 becomes

$$\begin{bmatrix} u \\ v \\ w \end{bmatrix} = \frac{-1}{\Omega_0(1+s)} \begin{bmatrix} 2\Delta s \\ \Gamma s \\ \Omega_0 \end{bmatrix} \quad (2.20)$$

with the newly introduced *saturation parameter*

$$s = \frac{2\Omega_0^2}{\Gamma^2 + 4\Delta^2} \quad (2.21)$$

The third component $w = |b|^2 - |a|^2$ (see equation (2.15)) is the difference in population between $|e\rangle$ and $|g\rangle$. For a small saturation parameter ($s \ll 1$) the population is mainly in the ground state and therefore $w = 1$. Likewise all the population in the excited state is described by $w = 1$. By construction $w = \rho_{gg} - \rho_{ee}$ and $\rho_{ee} + \rho_{gg} = 1$ which allows to calculate the population in the excited state:

$$\rho_{ee} = \frac{1}{2}(1-w) = \frac{s}{2(s+1)} = \frac{s_0/2}{1+s_0 + \left(\frac{2\Delta}{\Gamma}\right)^2} \quad (2.22)$$

Where s_0 is defined as in equation (2.25). For a large saturation parameter ($s \gg 1$) ρ_{ee} is limited to 1/2. Consequently, the equilibrium in saturation is half the available atoms in each of the two states. An increase

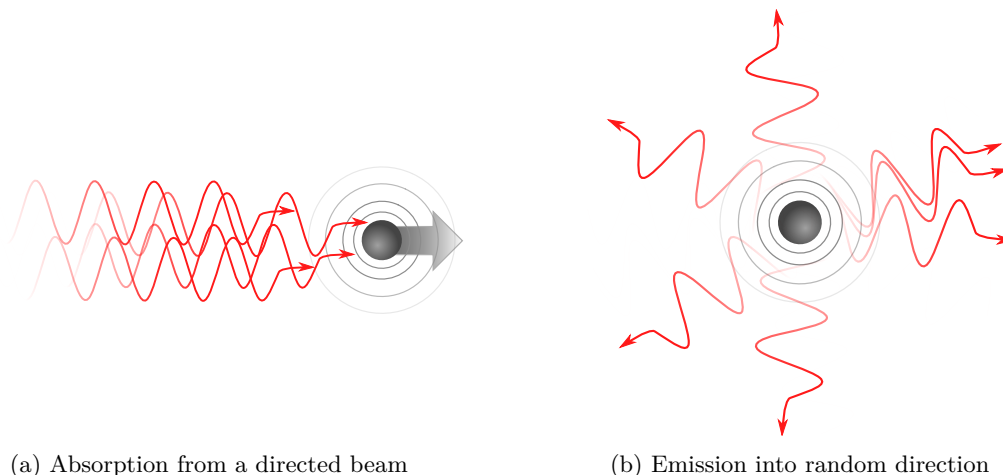


Figure 2.3: Absorption and spontaneous emission of light by an atom. In a) photons from a directed beam, such that their momentum vectors are aligned, are absorbed leading to a momentum build up of the atom in the same direction as the wave vectors. b) Photons are emitted in a random direction because the atoms orientation is random; the net momentum transfer is therefore zero.

in light intensity does therefore not produce a higher interaction rate and limits the sensible beam size and power when designing an atom trap.

2.2 Magneto Optical Trapping

The above discussion established a cycling excitation and de-excitation of an atom in a light field and a saturation behaviour for high light intensities. Both processes describe fluorescence of elements in resonant light but not the beam *deflection* observed by Frisch[56]. Since this process manipulates the atom's momentum, it is the key component in building an atom trap and can be understood from simple arguments: Every absorption and emission of a photon by the atom transfers energy and momentum ($\hbar k = 2\pi/\lambda$). All wave vectors \vec{k} in a collimated light beam are aligned as the photons share a common propagation direction. An atoms absorbing from such a field therefore gathers a momentum impulse in the same direction. Now that the atom was promoted to an excited state, it will spontaneously decay to its ground state on the time scale of its lifetime ($\tau = 1/\Gamma$, where Γ is the linewidth of the state). The emission of the photon has a defined direction with respect to the atom's magnetic axis however if the atom is moving freely and no external field constraints its orientation, photon emission in the full solid angle is equally probable. Hence the momentum of all emitted photons eventually adds up to zero. These two situations are sketched in figure 2.3.

A fluorescing atom undergoes cycling absorption and emission that the overall transferred momentum becomes the sum of the two processes above and shares the direction with the collimated light beam. This

explains the deflection of an atomic beam through resonant light. The previous section also suggests that non-resonant light at a certain detuning creates a lower force and that there is a limit to the force associated with the saturation intensity. In 1975 Hänsch and Schawlow published their famous proposal[63] to use these effects to decelerate and thus cool atom gases¹. Initially thought of as a tool to increase interaction time with, for example, microwave fields in a otherwise limited area, it soon became clear that slow, and therefore cool, atoms require quantum mechanical rather than classical description. The engineering of atomic superposition states came into reach and the study of the same was proposed in the 1980s[6, 7]. The first experimental realisation of a cooled sodium cloud was presented in 1982 by Phillips and Metcalf[107].

Before proceeding to the working principles of atomic traps, the term ‘cold atom cloud‘ or ‘cold atoms‘ shall be clarified. The goal is to remove kinetic energy from the atoms and thus reduce their velocity, while at the same time confining them to a restricted volume. Because not a single atom but rather a dilute gas is captured, the characterising parameter is the velocity distribution of the cloud. It is related to temperature in the theory of kinetic gases

$$E = \frac{3}{2}k_B T = \frac{1}{2}m\bar{v}^2 \quad (2.23)$$

via the *Boltzmann constant* k_B . This assumes that the gas in question is in thermal equilibrium with itself, the surrounding and undergoes *Brownian motion*[44], a random movement induced by collisions. Cooled atom clouds are very dilute (large traps reach $\approx 8 \cdot 10^{16} \frac{\text{atoms}}{\text{m}^3}$ while air at room temperature has $\approx 2.5 \cdot 10^{25} \frac{\text{molecules}}{\text{m}^3}$). The equilibrium assumption is difficult to hold because a trap isolates its contents from the surrounding. Still the term *temperature* is kept but merely reflects the average speed, hence energy the atoms carry.

2.2.1 Light Force

Photons transfer momentum to atoms through absorption and emission, the minimal time between the two processes is set by the state’s lifetime which is the inverse of the linewidth Γ ($\Gamma = \frac{1}{\tau}$). The force transmitted onto the atoms is therefore proportional to the photon’s momentum $\hbar k$, the linewidth Γ and the population in the excited state ρ_{ee} (see equation (2.22)):

$$F_{\text{scat}} = \hbar k \Gamma \rho_{ee} = \frac{\hbar k s_0 \Gamma / 2}{1 + s_0 + (2\Delta/\Gamma)^2} \quad (2.24)$$

which is the *scattering force* on an atom in a light field. The second form also includes the detuning Δ and the saturation parameter s_0 . It is defined as the ratio of light field intensity I to *saturation intensity* I_s :

¹The main technological hurdle was absence of narrow line-width, high power light sources, which was solved by the development of lasers at this time.

$s_0 = \frac{I}{I_s}$, where I_s is defined as[130]

$$I_s = \frac{2\pi\hbar c}{3\lambda^3\tau} \quad (2.25)$$

for $I \geq I_s \frac{\rho_{ee}}{\rho_{gg}} \rightarrow \text{const.}$. To generate a scattering and therefore stopping force, one seeks to increase the scattering rate to the point by which it is limited by the saturation intensity. In an intuitive picture, one can imagine every atom to undergo excitation and relaxation at the maximal possible rates, limited by the lifetime of the states. An increase in light intensity does therefore not result in a higher F_{scatt} . For the rubidium 87 isotope $I_s = 1.58 \frac{\text{mW}}{\text{cm}^2}$. The expected maximal force is therefore $\max(F_{\text{sp}}) = \hbar k\Gamma/2$ and an atom would feel an acceleration or deceleration of $1.08 \cdot 10^5 \frac{\text{m}}{\text{s}^2}$ or roughly 11,000 times the earth pull.

An atom at rest in a collimated, resonant beam gains velocity until the *Doppler shift* $\Delta \Rightarrow \Delta + \vec{k} \cdot \vec{v}$ reduces the force to a minimum¹. For resonant light, the maximal force will be felt by atoms at rest which will accelerate and therefore heat already ‘cold’ atoms. To prevent this, the light is *red detuned* with respect to a stationary atom. This configuration creates an increasing stopping force for an atom moving towards the light’s source. In a one dimensional system, a pair of *counter-propagating* beams are used to account for motion in both directions. Inserting the Doppler shift into equation (2.24) and summing over both beams yields[87]

$$\mathbf{F}_{\text{OM}} \approx \frac{8\hbar k^2 \Delta s_0 \mathbf{v}}{\Gamma \left(1 + s_0 + \left(2\frac{\Delta}{\Gamma}\right)^2\right)^2} \equiv -\beta \mathbf{v} \quad (2.26)$$

where terms $\mathcal{O}(kv/\Gamma)^4$ have been neglected. Scattering is maximal for $\Delta = 0$ and equal from both beam directions, leading to equal forces. If the light is red detuned ($\Delta < 0$), forces are maximal for $v > 0$ in one and $v < 0$ for the other beam. Atoms at rest do not feel any force when the effects of both beams cancel out (see figure 2.4). An atom initially at rest and gaining negative velocity in figure 2.4 sees the beam from the right even further red shifted, the facing beam however appears blue detuned. This leads to more scattering events from the facing beam and results in a velocity dependent damping force (see equation (2.26)). The light therefore creates a thick medium for the atoms with a force proportional to $|v|$. Due to its viscous nature, this state is called *optical molasses* (hence the subscript in equation (2.4)). Although discussed here in only a single dimension, the model extends easily to three[27].

Inside counter-propagating red detuned light beams, atoms are slowed and therefore cooled. This technique is called *Doppler Cooling*, because the driving effect is the *Doppler shift*. It is limited by the *Doppler*

¹An atom at room temperature ($T=300\text{K}$, $v=297 \frac{\text{m}}{\text{s}}$) experiences a shift of $\approx 2.4\text{GHz}$ for 780nm light when it comes to a rest.

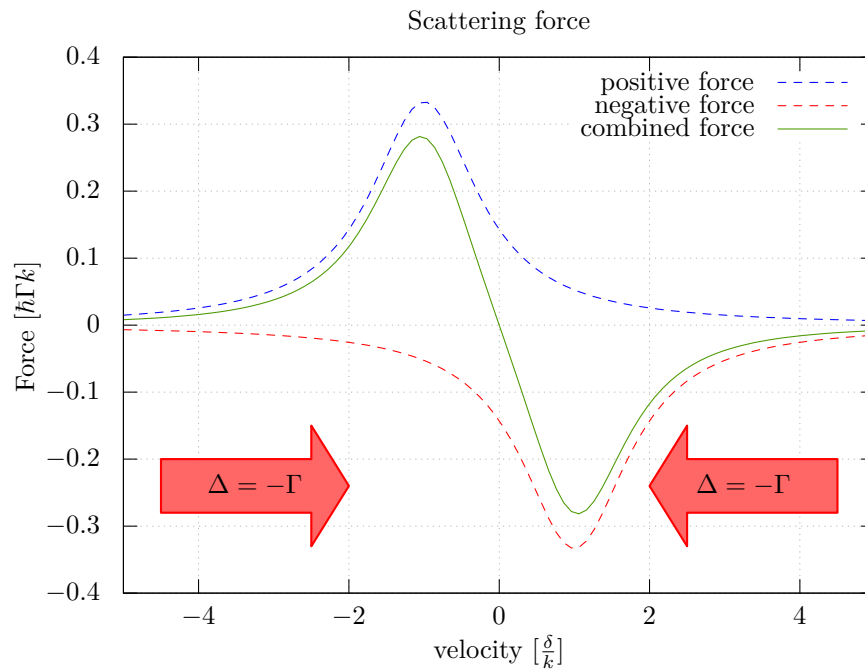


Figure 2.4: Doppler cooling force on an atom in an optical molasses for different velocities, as defined in equation (2.24). The saturation parameters was set to $s_0 = 2$ and both beams are red detuned by the linewidth $\Delta = -\Gamma$.

limit[79, 88]

$$k_B T_d = \hbar \frac{\Gamma}{2} \quad (2.27)$$

The absence of the atom's mass and used laser frequency is understandable through the nature of the energy dissipation process. Although not in thermal equilibrium with surrounding gasses, the cooled atoms exchange momentum with the light field which gives rise to *Brownian motion* and limits the minimal energy[44]. The averaging to a zero momentum transfer is only true over long time-scales but the random walk behaviour at short scales gives rise to the above limit[146].

One conclusion from the above discussion could be that operating an atom trap at much higher intensities than I_s is not beneficial but is also not counter-productive because it does not lead to higher damping forces. However for $I \gg I_s$ stimulated emission becomes more and more probable and directed momentum transfer on emission occurs. This leads to the creation of *Doppleron resonances*[136] where n photons are absorbed from the standing wave and $n - 1$ emitted in the counter-propagating beams. Higher orders of this process start to appear with increased power and lead to a more jagged curve than shown in figure 2.4 because the summation of momenta changes. Even a local reversal of the scattering force is possible[91, 31]. This local heating is generally avoided by keeping the laser intensity around 1.5 to 2 times I_s .

All of the above discussed does lead to slow atoms, but not to a trap. Chu used the term 'viscous confinement'[27] to describe the observed atomic molasses but, he also pointed out that atoms will slowly drift out of the laser fields and are lost from the experiment. A restoring force towards the centre of the crossing beams is necessary to build a true trap.

2.2.2 Atom Confinement

To build an atom trap, one seeks to find a beam configuration such that the atoms are localised in a well defined area within which their motion is confined. One complication of this setup is that a static configuration of scattering forces does not allow trapping. One argument is the Brownian motion which, independent of the beam arrangement, induces an unconfined random walk in the atoms. Another one to put forward is the *optical Earnshaw theorem* which is deduced from the *Earnshaw theorem*¹, stating that a dissipative force does not produce a stable trapping configuration[8]. The non-light equivalent is a magnetic field used to confine electrically charged particles such as ions. In this example the problem can be circumvented by constantly changing the direction of the force.

It should be pointed out that static magnetic traps for neutral atoms exist and are successfully used for

¹ $\nabla \mathbf{F} = 0$

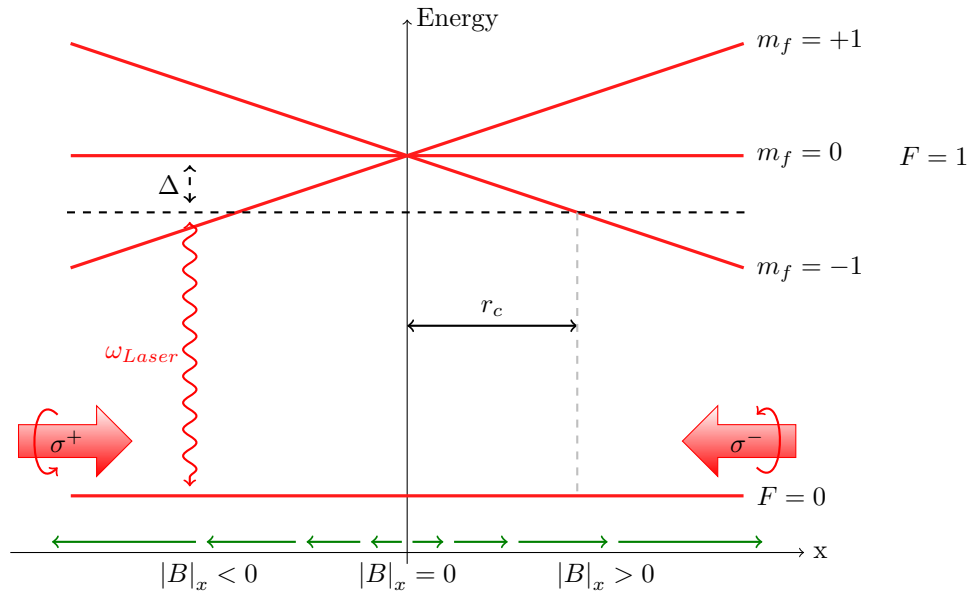


Figure 2.5: Laser and magnetic fields in a standard MOT configuration. The red detuned laser creates a velocity dependent damping force while the Zeeman shift of the m_f sub-levels due to the external fields will cause more absorption from the oncoming beam. In combination, the force on the atoms is velocity *and* position dependent. r_c is the capture range of the MOT. The labelling σ^+ and σ^- in the arrows indicating the light propagation directions refers to the correct polarisation such that σ^+ drives $\Delta m_f = +1$ and σ^- drives $\Delta m_f = -1$ while the small arrows around the indicators show the rotation of the electric field vector.

e.g. transport[60]. The working principle in this case is different because the restoring force is created by a shift of the energy levels due to the high magnitude of the field which causes the atoms to seek areas of low fields. Such a force is not dissipative and therefore a static configuration can be used as a trap.

In order to trap neutral atoms which have been Doppler cooled, spatially dependent scattering can be created through an overlaid magnetic field gradient. Rubidium is a neutral atom and while it is not moved by low fields, its internal separation of energy levels changes. Any atomic angular momentum state F has $m_f \in [-F, -F + 1, \dots, F]$ magnetic sub-levels. Without external fields, they are degenerate and energetically not distinguishable. They can however be separated through the *Zeeman effect* which splits the levels proportional to the magnetic field strength. Transitions such that $m'_f = m_f$ are driven by π -polarised (linear), $m'_f = m_f + 1$ by σ^+ -polarised (right circular) and $m'_f = m_f - 1$ by σ^- -polarised (left circular) light. Figure 2.5 sketches the splitting of these sub-levels under a linear magnetic field with zero strength in the centre.

Assuming an atom starts at $B = 0$ and drifts off to the right, the increasing magnetic field moves the $m_f = +1$ level further away from the unaffected $m_f = 0$ level by Δ . At the same time the $m_f = -1$ level moves closer to resonance with the detuned light. If the beam from right to left is σ^- polarised, light is

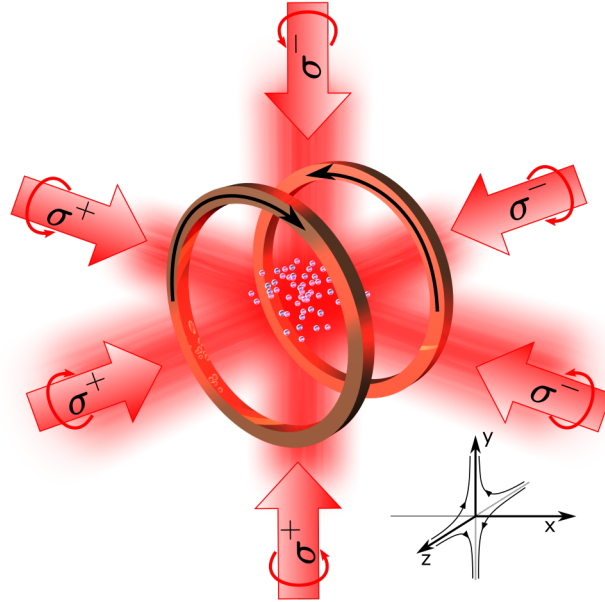


Figure 2.6: Geometry of a 3D MOT. Indicated are the polarizations of the three pairs of laser beams and the coils in *Anti-Helmholtz configuration* creating a quadrupole field with zero magnetic field in the centre and a gradient along all principal directions. Again the labels σ^+ and σ^- indicate that light from this beam should drive the $\Delta m_f = +1$ and $\Delta m_f = -1$ transition. Arrows around the direction indicators represent the rotation of the electromagnetic field vector. Polarizations along one axis have the same handedness and the x-y plane differs from the z direction. Additional lines close to the coordinate system indicator sketch magnetic field lines for one axis.

primarily scattered from this direction because it is closer to resonance and the polarisation matches the transition selection rules. The labels σ^+ and σ^- indicate that the light of this polarisation can drive a transition where $\Delta m_f = +1$ or -1 respectively. The rotation of the electric field vector is shown as circling arrow around the direction indicator in figure 2.5. The atom is hence pushed back towards the centre. The inverse happens for $x < 0$ and a restoring force towards $B = 0$ is created. Such traps are realised with geometries as shown in figure 2.6. A pair of *Anti-Helmholtz* coils creates the field gradient and six beams arranged in counter-propagating pairs provide Doppler cooling. Based on the processes involved, such a trap is called a *Magneto-Optical Trap* or short MOT. It was first demonstrated in 1987 by Raab[110] for sodium.

The *Anti-Helmholtz* configuration creates a uniform gradient in all directions, but has different slopes.

The change along the symmetry axis is double that in the other directions:

$$\begin{aligned}\nabla\mathbf{B} &= \frac{\partial B_x}{\partial x} + \frac{\partial B_y}{\partial y} + \frac{\partial B_z}{\partial z} \\ &= \frac{\partial B_z}{\partial z} + 2\frac{\partial B_r}{\partial r} \\ &= 0\end{aligned}\tag{2.28}$$

where the sub-index r indicates any direction in the x-y plane (radial symmetry plane) as defined in figure 2.6. Figure 2.6 suggests that the size of the trap depends on the change in field gradients and therefore the trapped cloud is expected to form a disk, rather than a sphere.

2.2.3 Pre-cooling Atoms

The lower temperature limit of a magneto-optical trap is estimated as the Doppler limit (equation (2.27)) but this does not yield any information about an upper boundary. If the restoring and damping forces are not strong enough to sufficiently decelerate an atom within the beam diameter, it will, even though it loses energy while traversing, exit on the other side. It is therefore helpful to define a *capture range* to estimate the trappable velocity class. One easy estimation is [128] $v_c = \sqrt{2ar}$ which assumes a deceleration of a and a trapping region of radius r . The trap which is presented later (see section 5.2) uses 2.54cm diameter beams and produces a deceleration of $a = 1.08 \cdot 10^5 \frac{m}{s^2}$. The critical velocity is therefore $v_c = 74 \frac{m}{s}$ which corresponds to $\approx 2\%$ of all atoms if a Maxwell-Boltzmann distribution and rubidium at 300K ($\bar{v} = 294 \frac{m}{s}$) is assumed. Atoms too fast for direct trapping are losing energy through collisions with other atoms or the walls. Before their velocity is decreased sufficiently for trapping, they contribute as a background gas, which reduces the lifetime and size of the trap when the pressure is too high and loss starts to dominate over loading.

The actual distribution of the background gas depends on the technique used to introduce the element into the vacuum chamber. Rubidium has a vapour pressure low enough that atoms are released from a pure block of the element¹. Such a reservoir is typically held behind a valve to interrupt the flow and does not require any external power source. It is therefore an ideal candidate for portable systems which have only limited power resources and hence used in the presented experiment. An alternative are dispensers, a small ferrule which holds the element in a buffer material and when heated expels the content through a slit. This system is more compact than a reservoir and has deterministic control of the emission rate but requires a current source capable of providing several amperes. The third option, necessary for elements with low vapour

¹ $1.67 \cdot 10^{-7}$ mbar at 20 degrees celsius

pressure, are ovens which heat a block of the pure material to temperatures where individual atoms detach. The downside is that some elements, such as sodium, require temperatures around 600K and therefore create a hot background gas. The coldest source is a reservoir but even then only the aforementioned 2% of atoms are within capture range.

Reduction of unwanted background pressure through conditioning of the velocity distribution is achieved with pre-traps, which separate the source from the main trap. Their purpose is to narrow the velocity distribution and shift it closer to $v = 0$. Ideally the pre-trap should have a wider acceptance range than the main trap. One way to increase the trapping range of a MOT is to increase the detuning which shifts the two peaks in figure 2.4 further away but leads to a plateau in the centre. To cool more atoms, the frequency could be changed with the expected deceleration of atoms. Such a *chirped* trap[14, 27, 48, 142] would need to span $\approx 2.4\text{GHz}$ for rubidium and does produce temporally separated clusters of cold atoms. This reduces the atom number in the main trap and is therefore not helpful for our purpose. Another way to change the resonance in an atom is the aforementioned *Zeeman effect* ($\Delta E \propto \mu \cdot \mathbf{B}$). Atoms from the hot source travel through a tube with a changing magnetic field towards the main chamber. The gradient is designed such that decelerating atoms are in resonance along the whole length[107, 108] and a slow beam exits at the other end. Such *Zeeman slowers* are used for heavy elements which require a hot oven and are efficient enough to load weaker magnetic[86] or dipole[26, 6, 59] traps. Such systems have high demands in space and energy but recently more compact versions, based on permanent magnets, were developed[67].

This experiment uses a third path that employs a two dimensional version of the previously discussed trap(see section 6.1) in conjunction with a rubidium reservoir at room temperature. By removal of the trapping constraint in one dimension and an extension of the general geometry along the same axis, an elongated ‘trap’ is created which ejects slow atoms on both ends[1, 103, 112, 76] (see figure 5.5). An angle in the telescopes ensures that the majority of atoms exits to the side connected to the main chamber. Removing either the light or the magnetic field disables the source completely and no disruptive atom beam can enter the area of the atom interferometer. The main advantage of this approach is that a small connection tube between the pre- and main trap can be used which makes it very unlikely for a background atom in the two-dimensional trap chamber to find its way through. A high pressure difference can be maintained allowing the main chamber to operate at $\approx 10^{-10}\text{mBar}$ while the source can have $\approx 10^{-8}\text{mBar}$. The high background pressure guarantees an intense but cooled atom beam while the experiment chamber benefits from a fast loading rate and better vacuum. Because a faster loading rate allows a higher repetition rate of the complete sequence and hence gravity measurement, the decision to use a 2D and 3D MOT was made.

2.2.4 Loading Rate and Lifetime

An empty magneto-optical trap begins to attract atoms, grows and eventually reaches a steady state where repulsive forces prevent further increase when the loss equals the filling rate. These two values describe the general loading of a magneto-optical trap

$$\frac{\partial N}{\partial t} = R_f - \gamma N(t) \quad (2.29)$$

with R_f the filling rate and γ the pressure dependent loss coefficient¹. If necessary, γ could be expanded to include two body losses, which are relevant for high density traps[5] but can be neglected for MOTs. Equation (2.29) has a solution of the form

$$N(t) = \frac{R_f}{\gamma} (1 - \exp(-\gamma t)) \quad (2.30)$$

and R_f is estimated as[5]

$$R_f = \frac{n_v V^{\frac{3}{2}} v_c^4}{2u^3} \quad (2.31)$$

where n_v is the density of the background gas, v_c is the critical capture velocity and $u = \sqrt{2k_b T_v / m}$ the most probable velocity. Values for R_f and γ are found by fitting equation (2.30) to a recorded curve and allow, for example the estimation of the local pressure (see section 6.1.2). The above model shows that a bigger trap volume generally increases the filling rate but repulsion and interaction between trapped atoms is limiting for higher atom numbers. A typical MOT behaves as an ideal gas for $N < 10^4$ and the cloud diameter as well as density increase[1]. For larger N , the density distribution changes from a Gaussian to a top hat² distribution caused by a shadowing effect of the centre. The decreased light intensity at the core creates a temperature imbalance and finally a repulsion that causes the trap to become unstable.

Loss channels in the trap are consolidated in the *lifetime*, which is measured by cutting the source and recording the draining of the trap. Because it is quick to record it is commonly used as a quick check on vacuum integrity and background pressure. Setting R_f to zero in equation (2.30) gives an expected exponential decay dominated by γ . Section 6.2 shows measurements of these parameters.

2.2.5 Cooling Rubidium 87

A key requirement for the combination of light shifts and scattering forces to create a trap is the need for a *cycling* transition. This is always achieved if there are only two levels in the system but atom structures are

¹Reference [5] estimates γ as $\approx 4.4 \cdot 10^7 \frac{1}{\text{Torr s}}$

²While a Gaussian distribution has a smooth increase and decrease, an ideal top hat distribution is a step function.

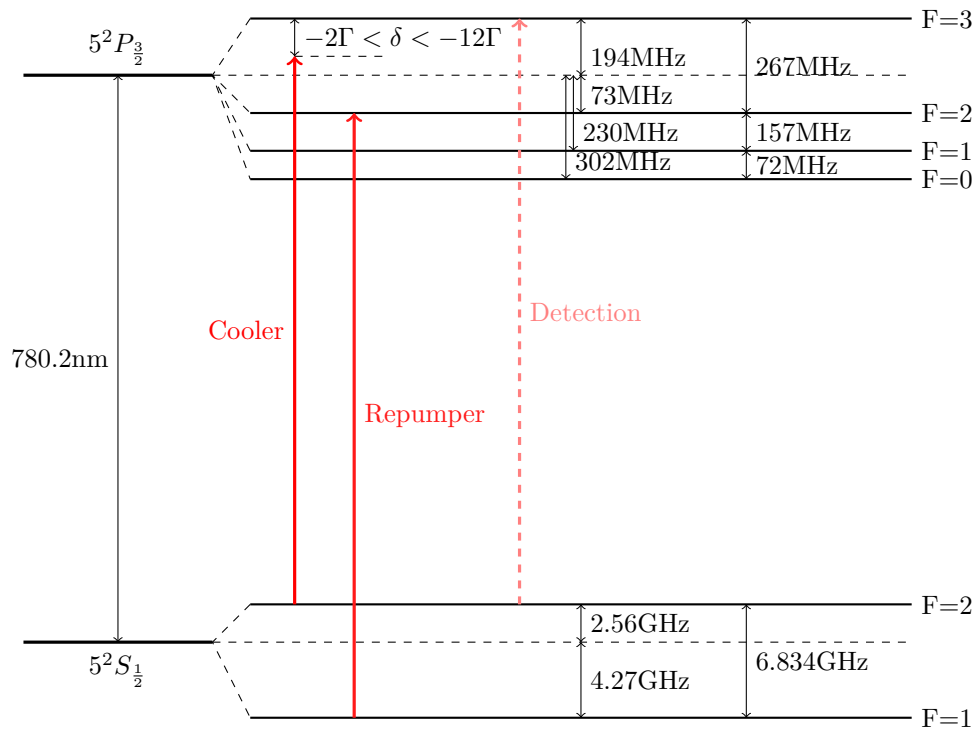


Figure 2.7: Level Scheme of Rubidium 87. Additionally to the main cooling transition line, a repumper frequency is necessary that will remove atoms from the F=1 state which is not addressable by the main cooling transition and can be populated through the detuned cooling laser.

generally more complex. Elements of the first column in the periodic table come closest to the ideal system because the lower shells are filled and a single electron leads to an almost two-level like system. Rubidium 87, one of the two stable isotopes of rubidium has a single electron in the 5s shell and all lower levels are filled. Two transitions are accessible, the D1 line with a central wavelength of $\approx 794nm$ and the D2 line with $\approx 780nm$. Due to better availability of laser frequencies, the D2 line is used. Figure 2.7 shows the level structure of the D2 line, including all relevant levels and laser frequencies. The targeted transitions connect $5^2S_{\frac{1}{2}} F = 2$ to $5^2P_{\frac{3}{2}} F = 3$, because it allows a cycling transition with reasonable short lifetime of the excited state¹. De-excitation is only possible to the $F = 2$ state, as $\Delta F = \pm 1, 0$ needs to be fulfilled. For its purpose, it is referred to as the *cooling transition* and the producing laser the *cooling laser* or *cooler*. The cooling light is red detuned to produce the Doppler force but this offset also leads to a non zero probability to excite $F = 2 \rightarrow F' = 2$ rather than $F = 2 \rightarrow F' = 3$. From this level the atom can relax to $F = 1$ and would be inaccessible for the cooling laser. To counteract this effect, a second and weaker light field is used to promote any trapped population in the $5^2S_{\frac{1}{2}} F = 1$ state back to $5^2P_{\frac{3}{2}} F = 2$ from where it can de-excite into $F = 2$ and join the cooling cycle again. This frequency is labelled as *repumper*. To image the atom cloud, resonant light is used, indicated as *detection*, for this we use the same laser source as for cooling with the detuning light removed. Using cooling light directly does produce fluorescence but with reduced intensity compared to resonant light.

All it takes for rubidium to behave like a two level system is a second and weaker laser frequency to feed atoms back into the cycling transition. The same principle applies to other elements. Early experiments were using sodium (Na)[56, 27, 110], which has a single electron in the 3s shell and the wavelength of this transition is accessible with laser systems available at this time. Later experiments with lithium[82] (Li), potassium[22] (K), rubidium[141] (Rb) and cesium[94] (Cs) have been performed. They all differ in the complexity of the repumping configuration, which might require more than a single frequency but cooling is possible if a cycling transition can be created.

¹the linewidth is $2\pi 6.06MHz$, therefore the lifetime is $26ns$ [130]

2.3 Sub Doppler Cooling

Doppler cooling is bound by the *Doppler limit* (equation (2.27), $\approx 140\mu K$ for rubidium) because it takes numerous scattering events to reduce the atom's average momentum. To the surprise of Paul Lett and his colleagues, the observed temperature of their sodium cloud was colder by a factor of five[80] when they reached $43\mu K \pm 20\mu K$ instead of the expected $240\mu K$. This observation is not a peculiarity of sodium or their experiment but a general effect of laser cooled atoms in the standard 3D magneto-optical trap configuration.

One would expect that the confining force created by the Zeeman shift of the energy levels adds heating through the acceleration towards the trap centre. The lowest temperature is therefore higher than the theoretical Doppler limit. To minimize this effect, a so called *molasses phase* (see section 6.5.1) is added, after enough atoms have been trapped in the MOT, which uses only the light field without a magnetic field. This step resembles the early experiments[6, 107] and requires a larger detuning than in the MOT phase (for Rubidium typically in the order of 60MHz to 80MHz). Because the process is still based on Doppler cooling and the inherent light scattering, the same limit should hold.

The lowest limit of any emission based cooling technique using photon absorption and emission is the *recoil limit*, the energy transferred by a single photon:

$$k_B T_R = \frac{\hbar^2 k^2}{2m} \quad (2.32)$$

k is the wave vector of the laser field and m the mass of the atom. For rubidium, this value is 361.98nK[130]. Cooling techniques not based on photon recoil, such as evaporative cooling where the hottest atoms are methodically removed from a dipole trap[61], can reach even below this limit and create macroscopically quantum degenerate gasses: *Bose-Einstein Condensates*[37]. They require high field intensities and precise control of the potential at the same time. These conditions need to be specifically created and do not occur spontaneously in a MOT.

2.3.1 Atoms in a Standing Wave

The next sections follow closely the arguments in the summary paper of Jean Dalibard and Claude Cohen-Tannoudji[35] from 1985, which shows an accessible approach to effects which bring atoms below the Doppler limit. Discussion of sub-Doppler effects is done in the *dressed atom picture*, which combines the state of the atom and the photon number of the surrounding field. The Hamiltonian of such a system has three main

contributions

$$\mathcal{H} = \mathcal{H}_A + \mathcal{H}_R + V \quad (2.33)$$

where \mathcal{H}_A describes the atom, \mathcal{H}_R the field and V the interaction of the two. Written in terms of *ladder operators*, the terms read

$$\mathcal{H}_A = \frac{\mathbf{p}^2}{2m} + \hbar\omega_0 b^\dagger b \quad \mathcal{H}_R = \sum_{\lambda} \hbar\omega_{\lambda} a^{\dagger} a \quad V = -\mathbf{d} [b^\dagger \mathbf{E}^+(\mathbf{r}) + b \mathbf{E}^-(\mathbf{r})] \quad (2.34)$$

where $b = |g\rangle \langle e|$ and $b^\dagger = |e\rangle \langle g|$ denotes the step down and up the ladder of excited atomic states. Equally a and a^\dagger stand for the emission and absorption of a photon from and into the background field with the index λ running over all possible light modes. An explicit form of the dipole operator \mathbf{d} and $\mathbf{E}^+(\mathbf{r})$ and $\mathbf{E}^-(\mathbf{r})$ can be found in [35] and is not essential for the further discussion.

Eigenstates of such a system form manifolds \mathcal{E} grouped by energies. The left part of figure 2.8 shows this structure in the absence of atom-light interaction ($V = 0$, solid lines). The state $|g, n\rangle$ signifies an atom in $|g\rangle$ and n photons in the background field. Spontaneous emission, the de-excitation of the atom and emission of a photon into the field, changes $|e, n\rangle$ to $|g\rangle$.

The right part of figure 2.8 sketches the shift of the energy levels if atom-light interaction ($V \neq 0$) is included. The separation of the levels is proportional to the light intensity and, because the counter-propagating beams in a MOT create a standing wave, position dependent¹. Eigenstates of \mathcal{H} are manifolds labelled $|1, n; \mathbf{r}\rangle$ and $|2, n; \mathbf{r}\rangle$ which are superpositions of the states for $V = 0$ with a smooth transition between the two extremes. The new states read:

$$|1, n; \mathbf{r}\rangle = \exp\left(\frac{i\varphi(\mathbf{r})}{2}\right) \cos(\theta(\mathbf{r})) |e, n\rangle + \exp\left(\frac{-i\varphi(\mathbf{r})}{2}\right) \sin(\theta(\mathbf{r})) |g, n+1\rangle \quad (2.35)$$

$$|2, n; \mathbf{r}\rangle = \exp\left(\frac{i\varphi(\mathbf{r})}{2}\right) \sin(\theta(\mathbf{r})) |e, n\rangle - \exp\left(\frac{-i\varphi(\mathbf{r})}{2}\right) \cos(\theta(\mathbf{r})) |g, n+1\rangle \quad (2.36)$$

with the added angles $\cos(2\theta(\mathbf{r})) = -\frac{\delta}{\Omega(\mathbf{r})}$ and $\sin(2\theta(\mathbf{r})) = \frac{\omega(\mathbf{r})}{\Omega(\mathbf{r})}$. The separation and the mix of $|e, n\rangle$ and $|g, n+1\rangle$ changes with position (or field intensity). This alteration of composition is *the* important result drawn from the above expression. Because any physical system tries to reach a point of lowest energy, the emission of a photon to go from \mathcal{E}_n to \mathcal{E}_{n-1} will happen if possible. This is however not very likely for $V = 0$ because there is no admixture of other states and therefore no supporting mechanism. But if the composition is changed by the external field intensity, e.g. a previously pure $|e, n\rangle$ state gains more and more contributions

¹For the case of a travelling wave, we can transform in the frame of a standing wave and adjust the velocity of the atom.

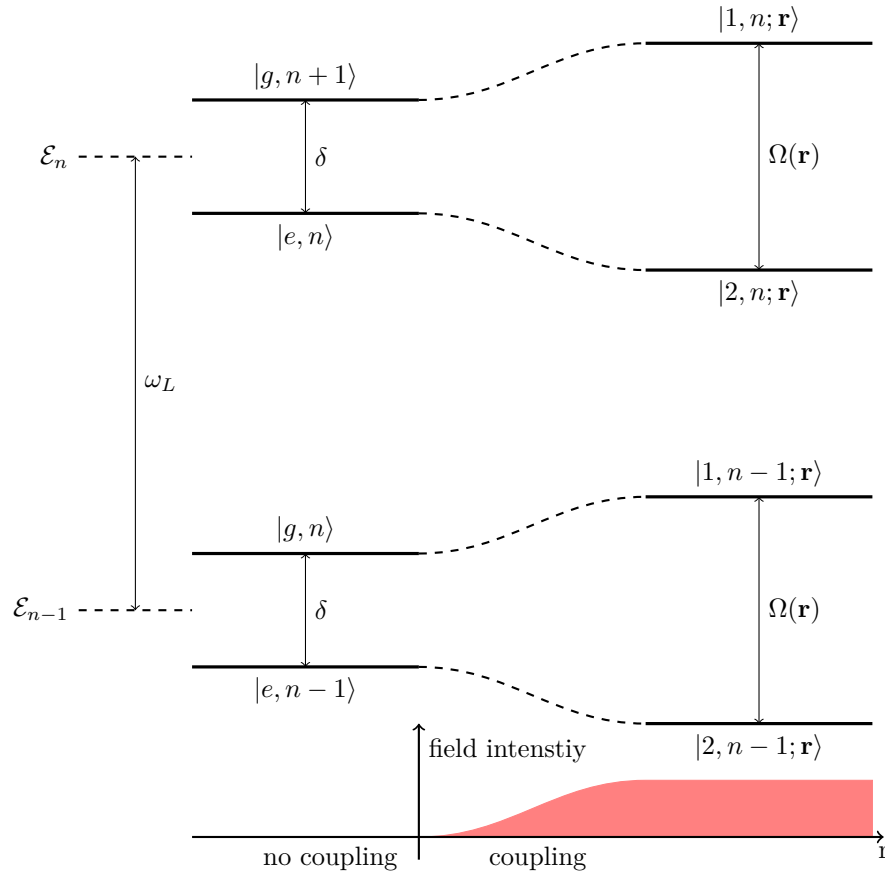


Figure 2.8: Energy level manifolds of an atom in an external field. The left half shows the energies of the eigenvectors if interaction between atom and field is neglected ($V = 0$ in equation (2.33)). This is equivalent to an external field intensity of zero. The right part shows the shift of the levels for an increase in field strength if the interaction is considered ($V \neq 0$). The transition is smooth and the levels change to superpositions of both manifold levels without interaction. e.g. $|1, n; \mathbf{r}\rangle = a|g, n-1\rangle + b|e, n\rangle$ where $a^2 + b^2 = 1$. The superposition enhances relaxation at points of maximal mix because of the inherent instability of the state.

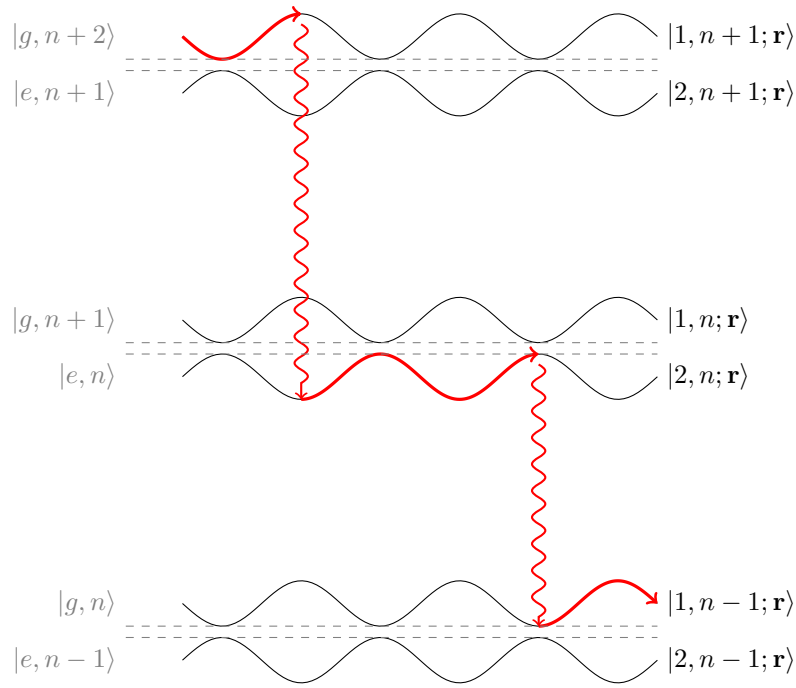


Figure 2.9: De-excitation ladder for an atom in a standing wave for $\delta > 0$. The periodic intensity fluctuations cause the energy levels of the dressed states to shift. At the maximal amplitude, the states $|1, n\rangle$ and $|2, n\rangle$ are superpositions of the non-interacting states $|g, n\rangle$ and $|e, n\rangle$ and are unstable. Therefore relaxation in a lower state is enhanced at the antinodes. Although there can be a large number of "valleys" and "hills" between consecutive emissions, the atom will on average move more potentials wells up than down. The gathered potential energy is dissipated into the light field and therefore removed from the kinetic energy of the atom.

from $|g, n\rangle$, spontaneous and stimulated emission are enhanced.

If an atom travels through areas of high and low field intensity which cause the energy levels to shift, its kinetic energy is transformed into potential energy and back. An atom moving along a standing wave therefore decelerates and accelerates as it passes through nodes and anti-nodes. Equation (2.36) shows that these changes in speed are accompanied by changes in state mixture, specifically the contribution of the energetically lower state is larger at higher field intensity. Figure 2.9 illustrates the periodic modulation of multiple bands in a standing wave for a detuning greater zero ($\delta > 0$). In the nodes, the changed mixture of states supports relaxation and is therefore more likely to occur. Parts of the atom's kinetic energy were transferred to potential energy and are radiated off by photon emission, gradually reducing the overall kinetic energy as the atom 'climbs' more hills than it 'rolls down'. The enhanced emission probability at positions where the atom's speed is lowest also leads to a repulsive force from these regions. The process resembles the Greek myth of *Sisyphus*, a king who was punished for deceitfulness and had to roll a boulder up a hill only to find that it would roll down again that he has to repeat his duty eternally, and is therefore called

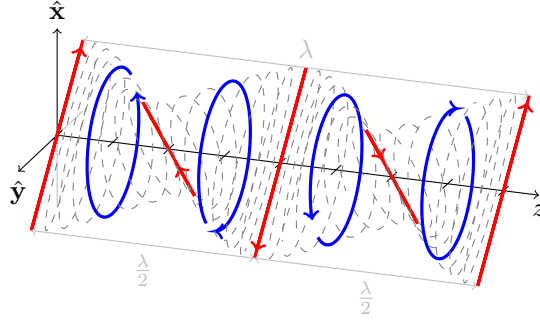


Figure 2.10: Polarisation change along the axis of two overlapped beams with perpendicular linear polarisations. The resulting light field has constant amplitude but changing polarisation. Linear polarisations are indicated in red, circular in blue. The traces indicate the path of the field vector in dependence of position z along the axis.

Sisyphus cooling.

Apart from intensity, light also has a polarisation state and the one of the overall field depends on the fields it contains. Two counter-propagating beams with parallel linear polarisation create an intensity modulated standing wave as used in the above example. Unfortunately, this is not used in MOTs, which operate with σ^+ and σ^- . The following sections will discuss two perpendicular linear polarisations to bridge to the more complex σ^+ - σ^- case used in MOTs.

Linear \perp Linear Standing Wave

The electric field of two perpendicular, but linear, polarised beams is

$$\mathbf{E} = E_0 \mathbf{x} \cos(kz + \omega t) + E_0 \mathbf{y} \cos(kz - \omega t) \quad (2.37)$$

$$= E_0 [(\mathbf{x} + \mathbf{y}) \cos(kz) \cos(\omega t) - (\mathbf{x} - \mathbf{y}) \sin(kz) \sin(\omega t)] \quad (2.38)$$

this results in a polarisation gradient along the beams axis: from linear to circular to perpendicular linear to counter rotating circular and back to linear again over the distance of a wavelength. Such an evolution is depicted in figure 2.10. The field vector is drawn for different positions and special cases of polarisation such as linear and circular are highlighted. Although light intensity is constant along the beam, an energy level shift is created because different polarisations couple to different m_f sub-levels (see discussion of atom confinement in section 2.2.2). Figure 2.11 a) shows an example of a simple system with an $J = \frac{1}{2}$ level as the ground state $|g\rangle$ and $J = \frac{3}{2}$ as the excited state $|e\rangle$. Linear polarisations drive transitions where the m_f quantum number stays constant ($\Delta m_f = 0$) whereas circular polarisations drive transitions with changing

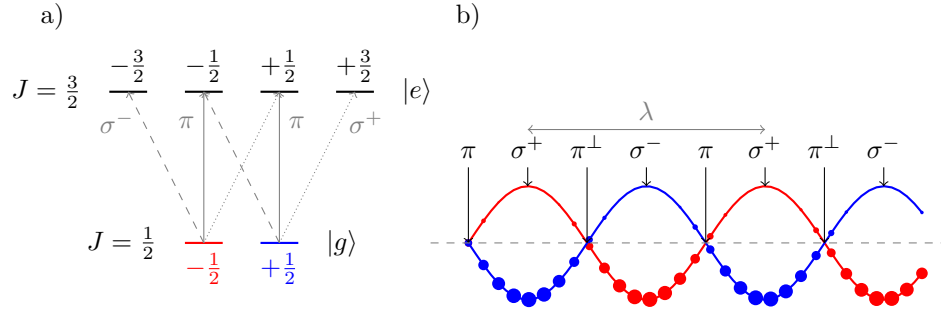


Figure 2.11: Cooling mechanism for lin \perp lin configuration on the example of an $J = \frac{3}{2} = |e\rangle$ and $J = \frac{1}{2} = |g\rangle$ system. a) shows the level scheme and possible transitions. Generally for linear light (π or π^\perp) $m'_f = m_f$ and for circular polarisations σ^\pm $m'_f = \pm m - f$. b) oscillating ground level. The changing polarisation causes the population to constantly be pumped into the lower state (circles). The movement of the atom into a region of different polarisation causes the levels to shift, lifting the highly populated one. More ‘hills’ are climbed than valleys entered, so the energy difference is dissipated, causing a friction force.

m_f ($\Delta m_f = \pm 1$). Figure 2.11 b) sketches the change of the state $|g\rangle$ as the atom travels through areas of different polarisation. In regions of σ^+ polarised light, the $m_f = -\frac{1}{2}$ level is lifted while the $m_f = \frac{1}{2}$ level is lowered. The opposite is true for σ^- light. At local linear polarisation, the energy levels are equal and therefore degenerate.

Assuming the atom starts at the left side of the sketch in 2.11 b) and moves to the right, it enters a region of σ^+ polarisation and population from the now energetically higher $m_f = -\frac{1}{2}$ state is transferred into the lower $m_f = \frac{1}{2}$ state. When moving into the next region of σ^- light the splitting of the m_f levels and the pumping direction invert. Again, population is transferred to the energetically lower level. Travelling through this configuration, the atom will not regain kinetic energy by ‘rolling down’ a slope because it is *pumped* to the energetically lower level before the peak is reached. It therefore loses speed as the energy is dissipated via the photons and a frictional force is created. The emission processes do not happen infinitely fast leading to a critical velocity that can be derived by averaging the force over the distance of a wavelength[1]

$$kv_c \approx \frac{\Gamma}{9} \frac{\frac{I}{I_{\text{sat}}}}{4 \left(\frac{\Delta}{\Gamma}\right)^2 + 1} \quad (2.39)$$

as well as an equilibrium condition

$$k_B T \approx \frac{\hbar \Gamma^2}{4|\Delta|} \frac{I}{I_{\text{sat}}} \quad (2.40)$$

which is proportional to the laser intensity, inversely to the detuning and independent of the laser’s wavelength. Figure 2.12 shows the averaged force dependent on velocity of the atom for different saturation parameters ($s = I/I_{\text{sat}}$) in figure 2.4 a) and a comparison to the Doppler Force in sub-figure b). Sisyphus

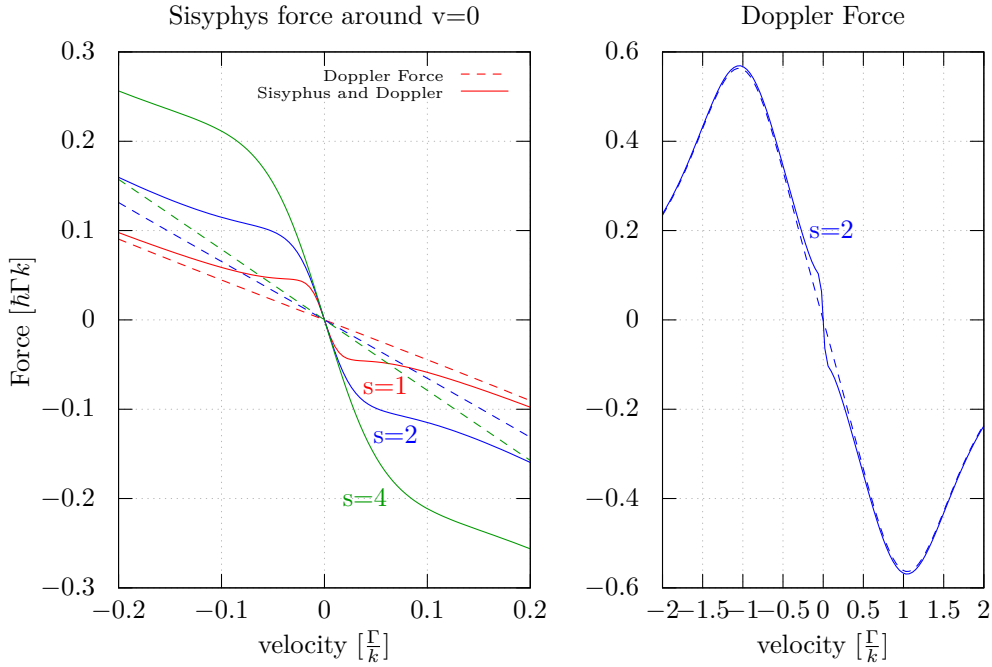


Figure 2.12: a) friction force resulting from lin. \perp lin. light configuration. The range changes stronger for different ratios of saturation intensity ($s = \frac{I}{I_s}$) than the Doppler force. b) comparison to the Doppler force as shown in figure 2.4. The effect from Sisyphus cooling produces a much steeper slope around $v = 0$ but has a limited range of influence. All plots are for a detuning equal to the linewidth ($\Gamma = \Delta$)

cooling produces a much steeper slope around $v = 0$ but has limited range. This process benefits from higher laser intensities, opposite to Doppler cooling, up to the point where heating effects dominate.

Because of the close resemblance to the previously, purely intensity based, shift, the lin. \perp lin. mechanism is referred to as *Sisyphus cooling*. Although the example was chosen to have only a few sub-levels, it also works for more complex atoms[1] and experiments have shown that the model is valid as well in 3 dimensions. This is surprising, because the formation of polarisations is not as trivial as in the 1 dimensional case and a clear polarisation gradient is not created. Experiments however have confirmed the above relation in three dimension[79, 120, 95] and a quantum mechanical analysis suggests a lower limit of six photon recoils[21].

$\sigma^+ - \sigma^-$ Corkscrew Cooling

The first experiments to use optical molasses worked with only linear polarised light. Experiments that include a MOT require circular polarised light to create the position dependent force. Such a $\sigma^+ - \sigma^-$ configuration

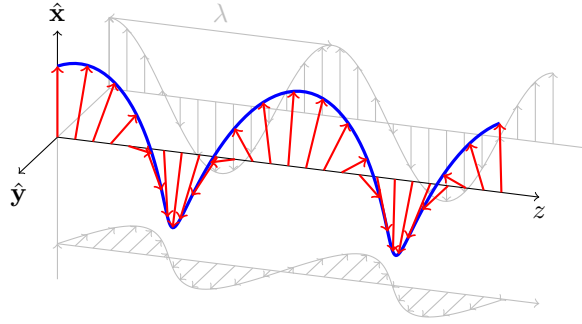


Figure 2.13: $\sigma^+ - \sigma^-$ configuration. The light is linear and of constant intensity along the axis of overlap but will rotate around the axis of propagation.

results in the field

$$\begin{aligned} E &= \frac{E_0}{\sqrt{2}} [\mathbf{x} \cos(kz - \omega t) - \mathbf{y} \cos(kz - \omega t)] + \frac{E_0}{\sqrt{2}} [\mathbf{x} \cos(kz - \omega t) - \mathbf{y} \cos(kz - \omega t)] \\ &= \sqrt{2} E_0 \cos(\omega t) [\mathbf{x} \cos(kz) - \mathbf{y} \sin(kz)] \end{aligned} \quad (2.41)$$

which creates linear polarisation everywhere along the axis of the beams but the electric field vector rotates by 2π over the distance of a wavelength (see figure 2.13). The following section presents the theory developed by Dalibard and Cohen-Tannoudji[36, 31] which names a dipole type force as the origin of additional cooling.

While the Sisyphus cooling effect requires at least a system with $J = \frac{1}{2}$, $\sigma^+ - \sigma^-$ or *corkscrew cooling* needs a system that has values of $J \geq 1$ for the ground level and $J \geq 2$ for the excited level. To emphasise this system, the states in $J = 1$ in figure 2.14 a) are labelled $|g_i\rangle$ and the excited states $|e_i\rangle$. The possible transition lines show the *Clebsch Gordon Coefficients* and the selection rules obey $\Delta m_f = 0$ for linear polarised and $\Delta m_f = \pm 1$ for circular polarised light, as before. An atom at rest at any point along the beam in figure 2.13 aligns its magnetic moment with the current polarisation orientation O_y and transitions between $|g_{-1}\rangle \rightarrow |e_{-1}\rangle$, $|g_0\rangle \rightarrow |e_0\rangle$ and $|g_{+1}\rangle \rightarrow |e_{+1}\rangle$ are driven, which are now eigenstates of J_y for the same axis. The atom can relax by emitting circular polarised light and changing the internal m_f state. The steady state population arrives at $\frac{4}{17}$ for $|g_{\pm 1}\rangle$ and $\frac{9}{17}$ for $|g_0\rangle$. To be precise, the transition $|g_{-1}\rangle \rightarrow |g_0\rangle$ has a relative strength of $\frac{1}{4}$, $\left(\frac{1}{\sqrt{2}}\right)^2 \left(\frac{1}{\sqrt{2}}\right)^2 = \frac{1}{4}$, and $|g_0\rangle \rightarrow |g_{-1}\rangle$ of $\frac{1}{9}$, $\left(\sqrt{\frac{2}{3}}\right)^2 \left(\frac{1}{\sqrt{6}}\right)^2 = \frac{1}{9}$ (see figure 2.14 a)). Therefore $|g_0\rangle$ is $\frac{4}{3}$ more populated and the transition stronger by the same factor. This is sketched in figure 2.14 a).

It is important to note that the transition from $|g_0\rangle$ is stronger and so is the light shift $\hbar\Delta'_0$. Figure 2.14

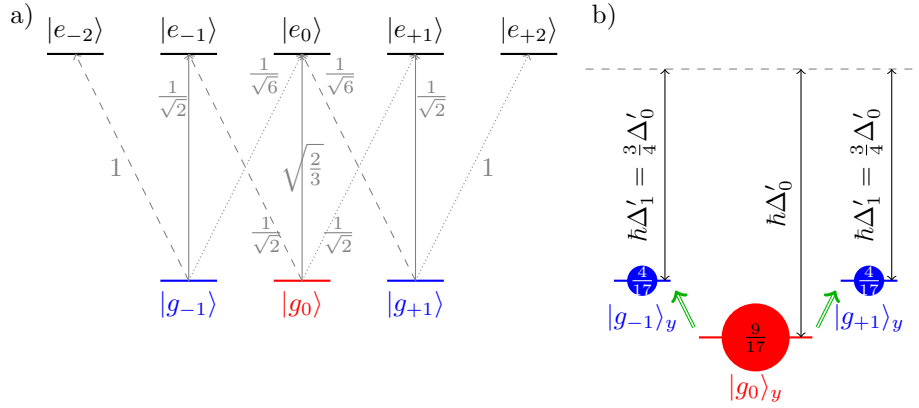


Figure 2.14: Mechanism of the $\sigma^+ - \sigma^-$ force imbalance. a) the sub-levels of a $J = 1$ and $J = 2$ system including the transition *Clebsch Gordon Coefficients*. b) shifted levels of the ground state ($J = 1$) under the influence strong transitions. The circles indicate the population ratios once the system has reached equilibrium. Green arrows indicate motion induced coupling. The system will try to push back into the state without this coupling which causes more photons to be absorbed from the facing beam, leading to a friction force.

b) shows that the dashed line is the unperturbed energy of the $J = 1$ state while the three levels below this illustrate the shifted condition in an external field. The steady state population is indicated by the circles on the levels and the sub-index y specifies that the atom has aligned with the external polarisation along the axis y . Because the levels are completely symmetric, an equal amount of photons are emitted into the $\omega_l - \frac{\Delta'_0}{4}$ and $\omega_l + \frac{\Delta'_0}{4}$ field. This is true for all positions of the atom along the axis of the beams because the choice of O_y , its current magnetic axis orientation, is arbitrary.

When the atom moves along the axis of the beams, the polarisation vector rotates away from O_y which creates new states that are superpositions the ground states, for example

$$\overline{|g_{\pm 1}\rangle}_y = |g_{\pm 1}\rangle + \frac{kv}{\sqrt{2}(\Delta'_1 - \Delta'_0)} |g_0\rangle_y \quad (2.42)$$

which in turn creates a coupling between $|g_0\rangle$ and $|g_{\pm 1}\rangle$. This coupling is indicated by the green arrows in figure 2.14 b) and leads to a population imbalance. The population imbalance is proportional to $\frac{40}{17} \frac{kv}{\Delta'_0}$, or in other terms, for $v > 0$ and $\Delta > 0$, $\Pi_{-1} > \Pi_{+1}$ where Π is the population of the state. At the new position, the magnetic axis of the atom aligns again with the current polarisation orientation O_y but the population in the m_f states is left in the shifted state. The system strives to align back toward equilibrium but to do so, more photons are absorbed from the facing, circular polarised beam to satisfy the selection rules. This creates an asymmetric force and hence dampens the atom's movement.

Similar to previously, we are interested in a friction force proportional to the speed v of the shape $F = -\alpha v$.

Summing over transferred momenta yields

$$\alpha = \frac{120}{17} \frac{-\Delta\Gamma}{5\Gamma^2 + 4\Delta^2} \hbar k^2 \quad (2.43)$$

and an equilibrium temperature of

$$k_B T = \frac{\hbar\Gamma^2}{2|\Delta|} \frac{I}{I_{\text{sat}}} \left[\frac{29}{300} + \frac{254}{75} \frac{1}{4 \left(\frac{\Delta}{\Gamma}\right)^2 + 1} \right] \quad (2.44)$$

The resulting velocity dependence is the same as in figure 2.12 but with a slightly different central slope. While forces based on the Sisyphus mechanism are only active in a small region around $v = 0$, the above polarisation gradient effect creates a profile similar the Doppler Force, with the addition of a small area around $v = 0$ with a steeper slope. However, even for optimal parameters, $\Delta = -\Gamma\sqrt{\frac{5}{4}}$, the slope is four times smaller than Sisyphus cooling.

Other Polarisation Configurations

There are cooling mechanisms associated with the omitted $\sigma^+ - \sigma^+$ configuration but an external magnetic field is required. The technical term is *Magnetically Assisted Sisyphus Effect* or MASE[70, 31]. the contributions can be assumed to be negligible, because of the low external field in the centre of a MOT.

2.3.2 Sub-Doppler Cooling in a real MOT

The above discussions investigated one dimensional systems, two counter-propagating beams, or were limited to a special atom level scheme. One might argue now, that a real MOT with six beams and atoms with different J will not allow sub-Doppler cooling. This argument would be mainly focused on the non-trivial polarisation formation. A full analysis of possible polarisations created by six beams of different polarisation states can be found in[71, 70]. The polarisation distribution in the beams' overlapping area depends on the relative phase of the involved beams and the publications show the results of a computer search algorithm based scan for areas that allow both, Sisyphus and $\sigma^+ - \sigma^-$ cooling. It was found that for any phase setting, there is always an area somewhere that creates a pattern as the two presented above, so depending on the movement direction of the atom and the phase, both effects are possible in different ratios. The strong phase dependence has also been discussed earlier for a two dimensional system[93].

The above restriction to $\Delta J = \pm 1$ can be relaxed to $\Delta J = \pm 1, 0$ for any J [129], which explains cooling of species such as rubidium. It is however surprising that with such a complex system, the above formulas

hold to a very good degree. The linear intensity dependence in equation (2.39) was confirmed for cesium experimentally[120].

Another feature of a real system is that all of the previously discussed mechanisms act at the same time. This leads to density limits, local trapping of atoms and shifts of the centre of the trap with respect to the magnetic field zero[128]. A MOT system is surprisingly stable and efficient despite the amount of different parameters involved. The intrinsic movement of the atoms, combined with the random polarisation distribution, seems to be enough to create an average over the discussed mechanisms and add substantial cooling contributions from Sisyphus-type mechanisms in a σ^+ and σ^- MOT configuration.

MOT Geometries and Types

Section 2.2.2 presented a cross of three pairs of beams as the trap configuration for a MOT. It produces a stable trap and allows for the detuning of beam pairs, a requirement for atom launching, a method used in this experiment (see section 6.4). It requires precise alignment of six beams relative to each other to prevent morphing of the trap or even instabilities such as racetrack conditions that lead to orbital shaped MOTs[10].

The inherently balanced arrangement of three retro-reflected beams is inherently power stable but does not allow the launching of atoms. A simple solution is the use of 3 retro-reflected beams, which are inherently balanced in pairs but do not allow to launch atoms. Both configurations require the coils to be far away from the trap centre and therefore need a high current to generate a sufficient field. This is solved through is the use of atom chips, as used in the iSense project[39], where etched conductors in a chip surface generate MOT and compensation fields while the gold coated surface is used as the retro-reflecting mirror. Because the atoms are close to the conductor, less current is necessary. There have been also reports of small traps in a $\text{lin} \perp \text{lin}$ configuration [69, 46] but the depth is low compared to a MOT and generally a strong pre-cooling phase necessary.

Recently, more integrated arrangements have been developed to minimize the amount of optics and reduce the degrees of freedom open for misalignment. The approaches include micromirror arrays[138], to gratings [78], pyramidal structures made from glass [16] and their etched counterparts in silicon[109]. They all share the idea that a single beam is enough to create the required trapping directions and polarisations, while optics made from a single piece eliminate possible misalignment and associated error sources. Even though such configurations do not allow an atomic fountain launch by detuning parts of the trap, the cold cloud can be dropped or launched by using a moving optical lattice[122].

Such different approaches are chosen for extremely stable and small experiments, however they lose on the

cloud size, pre-cooling and loading mechanisms. Taking the example a pyramidal geometry, it blocks access for a 2D MOT cooling beam and needs to be loaded from background gas. In turn, this limits the atom number and also the final temperature due to background gas collisions. They also require the development of specialised manufacturing processes. This is precisely the reason why the experiment presented in this work was built with a six beam configuration. The benefit of independent beam control was chosen over a more compact design. Especially in hindsight, for moving towards gravity gradiometry, a fast loading rate with low background pressure is desirable. To achieve this a two dimensional MOT is required as an atom source and a laser cross MOT as the main trap.

Summary

This chapter described the mechanisms and techniques for laser cooling. The key ingredient is a frictional force, proportional to the speed of the atom, which creates a viscous medium for the atoms. Because slow atoms do not come to a full rest due to the absence of a restoring force, a molasses is formed, which eventually will disperse. To create a trapping potential, circular polarisation and a Zeeman shift through external magnetic fields. The combination of both effects form the basis of a magneto optical trap. While this model is good enough to describe the basic mechanics, additional effects were identified, which cause the expected cloud temperature to be lower than the theoretical models based on Doppler force.

3 Atom Interferometry

The core of a cold atom based gravity sensor is the atom interferometer. Like in any interferometer (see figure 3.1 for a generic Mach-Zehnder type interferometer) the incoming wave packet is split, reflected and recombined. The signal is formed by destructive and constructive interference depending on the current phase relation of the waves in the two arms at the combining element. The signal moves from one extrema to the opposite in a phase change of π which for light is in the order of nanometre. A minuscule input change is therefore mapped onto a measurable signal. Building an interferometer with light is straight forward as the individual elements such as beam splitters and mirrors are readily available and light can be easily guided. Using the same principles with atoms, requires a different set of tools because atoms are not efficiently manipulated by other matter at the precision necessary. The interference of matter was first observed in

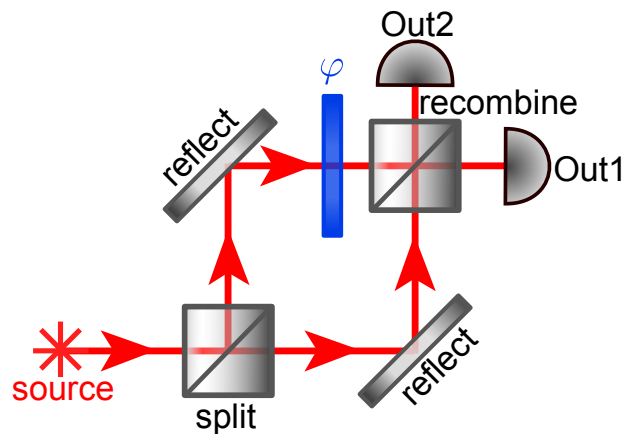


Figure 3.1: Scheme of a very basic light interferometer. Light from a coherent source is split, redirected and recombined. The phase difference between the two arms (φ) is mapped to the 2 outputs.

1927 when electrons diffracted off the surface of a nickel crystal[38]. The lattice structure of the crystal induced *Bragg scattering* and it was observed that the electrons behave the same way as electro-magnetic waves would on a grating. Their wavelength is found via the deBroglie relation ($p = h/\lambda$). Experiments with heavier particles such as neutrons[18] and eventually helium atoms[49] followed and it was in 1957 that the

first observation of the influence of gravity on the interference pattern was reported using a neutron beam[32]. In the experiment the particle ray of a narrow velocity class was guided through three layers of silicon, using the lattice structure of the crystal as a grating. The thin plates shared the same base and were produced by removing rectangular blocks from a large mono-crystal. This was done to minimize deformation of the piece. It is also important to note that the common crystal base was half the size of the original cylinder and therefore considerably thicker than the grating layers left standing. Two things were observed: Firstly, the interference pattern changed when the crystal was rotated, or the orientation of the interferometer changed with respect to \vec{g} . Secondly, the observed shift was larger than expected, though not by much. This additional contribution was explained by the bending of the crystal under gravity thus effectively changing the spacing between the gratings. Measurements of the gravitational acceleration are therefore possible with interfering matter waves and they yield high sensitivity. The important observation of the above experiment is that the bending of a several centimetre strong silicon base by distances of angstroms could be observed through means of matter interference. It also illustrates that the grating needs to be extremely stable, otherwise it is impossible to distinguish between gravitational phase shifts and systematic errors introduced by the grating.

To separate a change in lattice distance from an actual gravity signal, a stable frame needs to be found, which surpasses for example the mono crystal of silicon mentioned above. The one medium which is not significantly influenced by gravity on the surface of the Earth is light¹. As mentioned at the end of section 2.1.2, depending on the detuning, atoms are attracted or repelled from areas of high light intensity through means of the dipole force. In turn, this means that a standing wave will act like a grating for neutral atoms[96, 97, 99, 3]. Experiments of this kind follow the same idea as the previously mentioned massive gratings, they rely on *Bragg diffraction*. A series of four *Young's double slits* split, redirect and overlap a beam of single atoms or even big molecules like fullerenes[102] (C60 molecules or 'bucky-balls'). These experiments all rely on the grating's stability and the phase of the interferometer is imprinted in the output channel's momentum state. This is a reasonable approach for an experiment that uses for example a neutron beam and can have a fixed detector at a distance where the separation is reliably measurable. However atoms originating from a cold atom source, such as a magneto-optical trap, require considerable time of free expansion before the two momentum classes have sufficiently separated and can be discriminated. This poses higher demands on the initial temperature, size and expansion rate as well as efficiency of the gratings.

In 1989 Bordé[19] proposed a type of atom interferometer, based on the internal state transfer process discovered by *Rabi*[111]. A *stimulated Raman transition* is used to change the state of the atom in one

¹Gravitational lensing has no measurable contribution on the distances used in an atom interferometer

arm with respect to the other and separate them spatially. The same technique is then used to inverse the population of the two states and redirect the two clouds towards each other. Finally a third pulse overlaps both arms and maps the phase difference accumulated between the two paths to the atomic population. The two states are read out by driving resonant transitions and recording fluorescence. The signal is therefore proportional to the number of atoms in the addressed state. If the number of initial atoms is well controlled, only one state needs to be detected. In the case of rubidium 87, the $F = 1$ and $F = 2$ states of the $5^2S_{\frac{1}{2}}$ level are used because they are stable. An atom interferometer based on *Raman transitions* can therefore be built more compact than one using *Bragg diffraction* because no distance is required to separate the two arms after the merge. As a side effect, the transition is driven in a narrow velocity class only, reducing the atom cloud's spread and increasing the signal contrast[75]. However, depending on the application, atom species and apparatus design, combinations of both approaches are possible. This includes Raman transitions[23] or Bragg diffraction[98] for the beam splitter and Bloch oscillations to accelerate the atoms inside a lattice, but not spatially, in the vacuum chamber.

In the following sections atom interferometers based on *Raman transitions* are discussed. Such transitions can act as both beam splitters and mirrors depending, on frequency and intensity, and are therefore an excellent tool for atom control.

3.1 Raman Transitions

A *Raman transition* is the stimulated transfer of population between two internal states via a virtual state. *Two* fields are used to drive a transition between two levels which are energetically separated by the energy *difference* of the two involved photons and the resulting behaviour is similar to the previously discussed *Rabi Oscillations*. Starting from $|1\rangle$ a photon of frequency ω_1 is absorbed from the corresponding light field and a photon of frequency ω_2 emitted into the matching field. A schematic of the process is shown in figure 3.2. The detuning Δ from an existing level $|i\rangle$ needs to be small enough for the process to be possible but large enough to suppress spontaneous emission. Emission is stimulated which requires energy and momentum of the emitted photon to match the one of an existing light field. Although no direct transition is accessible in the optical regime, the atom is promoted from a stable internal state $|1\rangle$ to an equally stable state $|2\rangle$. A total momentum of $\mathbf{k}_1 + \mathbf{k}_2$ is transferred where \mathbf{k}_1 and \mathbf{k}_2 are the wave vectors of the two laser fields.

The following sections discuss *Raman transitions* first in general and then applied to atom interferometers which leads to the influence of gravity on the interferometer signal. The presented structure follows closely[92, 73, 11] and also uses some ideas from the thesis of Charriere[23].

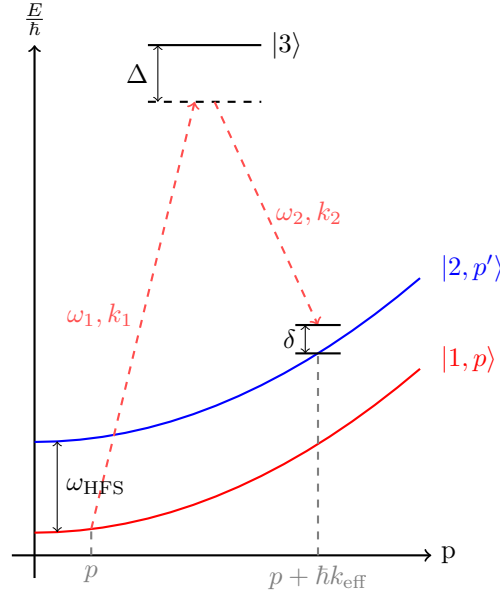


Figure 3.2: Energy scheme of a *Raman Transition*. A photon from the laser field of frequency ω_1 is absorbed and simultaneously one is emitted into the field of ω_2 via stimulated emission. Δ needs to be small enough that the transfer can happen but large enough that spontaneous processes from the intermediate level $|3\rangle$ are negligible.

Figure 3.2 shows the laser and atom levels considered for Raman transitions. The discussion here will only consider interaction with the shown transitions. A more complete discussion could include cross couplings such that ω_1 is influenced by the transition $|3\rangle \rightarrow |2\rangle$. The resulting system's behaviour is the same as in the used approach but with only minor corrections to the *Rabi frequencies*. The inclusion of more levels and cross terms can be found in [23, 104].

The state of the system as shown in figure 3.2 reads

$$|\Psi(t)\rangle = C_1(\mathbf{p}, t) |1, \mathbf{t}\rangle + C_2(\mathbf{p}, t) |2, \mathbf{p} + \hbar\mathbf{k}_{\text{eff}}\rangle + C_3(\mathbf{p}, t) |3, \mathbf{p} + \hbar\mathbf{k}_1\rangle \quad (3.1)$$

where the effective wave vector $\mathbf{k}_{\text{eff}} = \mathbf{k}_1 + \mathbf{k}_2$ has been introduced. The detuning δ is composed of the terms

$$\begin{aligned} \delta &= \omega_1 - \omega_2 - \omega_{\text{HFS}} \\ &= \frac{\mathbf{p}\mathbf{k}_{\text{eff}}}{m} + \frac{\hbar\mathbf{k}_{\text{eff}}^2}{2m} \end{aligned} \quad (3.2)$$

where the last expression accounts for Doppler and recoil shifts. This leads to a system Hamiltonian

$$\begin{aligned}\mathcal{H} &= \mathcal{H}_{\text{atom}} + \mathcal{H}_{\text{internal}} \\ &= \frac{\mathbf{p}^2}{2m} + \hbar \underbrace{(\omega_3 - \omega_1)}_{\omega_{31}} |3\rangle \langle 3| + \hbar \underbrace{(\omega_2 - \omega_1)}_{\omega_{21}} |2\rangle \langle 2| - \mathbf{d} \cdot \mathbf{E}(\mathbf{x}, t)\end{aligned}$$

with the energy of $|1\rangle$ normalized to zero. The last term ($\mathcal{H}_{\text{internal}} = -\mathbf{d} \cdot \mathbf{E}(\mathbf{x}, t)$) describes the interaction of the atom with an external field $\mathbf{E}(\mathbf{x}, t)$ through the dipole operator \mathbf{d} . This approach is referred to as the *dipole approximation* because it treats the complete atom, regardless of its structure, as a single dipole. The field of the two lasers with frequencies ω_1 and ω_2 , wave vectors k_1 and k_2 , polarisations ϵ_1 and ϵ_2 and intensities I_1 and I_2 reads in a general form:

$$\mathbf{E}(\mathbf{x}, t) = \frac{1}{2} \left(I_1 \epsilon_1 e^{i(\mathbf{k}_1 \mathbf{x} - \omega_1 t + \phi_1)} + I_2 \epsilon_2 e^{i(\mathbf{k}_2 \mathbf{x} - \omega_2 t + \phi_2)} \right) + c.c. \quad (3.3)$$

ϕ_1 and ϕ_2 are the lasers' phases relative to a fixed reference. Recalling the assumption that ω_1 only couples $|1, p\rangle \leftrightarrow |3\rangle$ and ω_2 only $|2, p'\rangle \leftrightarrow |3\rangle$ yields the interaction Hamiltonian

$$\mathcal{H}_{\text{interaction}} = \hbar \Omega_1^* e^{i(\mathbf{k}_1 \mathbf{x} - \omega_1 t + \phi_1)} |3\rangle \langle 1| + \hbar \Omega_2^* e^{i(-\mathbf{k}_2 \mathbf{x} - \omega_2 t + \phi_2)} |3\rangle \langle 2| + c.c. \quad (3.4)$$

where the *Rabi frequencies* were defined as

$$\Omega_n = -\frac{\langle n | E_n \mathbf{d} \epsilon_n | 3 \rangle}{2\hbar} \quad (3.5)$$

The notation in the numerator indicates the coupling of state $|n\rangle$ via the light field n to $|3\rangle$. This compact notation with a single index is a result of the simplifying assumptions made earlier. The expression $\langle n | E_n \mathbf{d} \epsilon_n | 3 \rangle$ depends on the polarisation of the light field and its value is connected to the *Wigner 6j* symbol and the *Clebsch Gordan coefficients* (see section 3.2.6 for the derivation and appendix A for possible transitions).

The full Hamiltonian of the considered system reads¹

$$\mathcal{H} = \begin{array}{ccc|c} & |1, \mathbf{p}\rangle & |2, \mathbf{p} + \hbar\mathbf{k}_{\text{eff}}\rangle & |3, \mathbf{p} + \hbar\mathbf{k}_1\rangle \\ \left[\begin{array}{ccc} \frac{\mathbf{p}^2}{2m} & 0 & \hbar\Omega_1 e^{i(\omega_1 t + \phi_1)} \\ 0 & \frac{(\mathbf{p} + \hbar\mathbf{k}_{\text{eff}})^2}{2m\hbar} + \hbar\omega_{21} & \hbar\Omega_2 e^{i(\omega_2 t + \phi_2)} \\ \hbar\Omega_1^* e^{-i(\omega_1 t + \phi_1)} & \hbar\Omega_2^* e^{-i(\omega_2 t + \phi_2)} & \frac{(\mathbf{p} + \hbar\mathbf{k}_1)^2}{2m} + \hbar\omega_{31} \end{array} \right] & \begin{array}{l} |1, \mathbf{p}\rangle \\ |2, \mathbf{p} + \hbar\mathbf{k}_{\text{eff}}\rangle \\ |3, \mathbf{p} + \hbar\mathbf{k}_1\rangle \end{array} & (3.6) \end{array}$$

For clarity, the spanning vectors of \mathcal{H} are noted on the sides in gray. From this point we proceed to find a solution via the Schrödinger equation $i\hbar\frac{\partial}{\partial t}|\Psi\rangle = \mathcal{H}|\Psi\rangle$. The system simplifies by introducing the variables

$$\begin{aligned} B_1(\mathbf{p}, t) &= C_1(\mathbf{p}, t) \exp\left[i\frac{\mathbf{p}^2}{2m\hbar}t\right] \\ B_2(\mathbf{p}, t) &= C_2(\mathbf{p}, t) \exp\left[i\left(\frac{(\mathbf{p} + \hbar\mathbf{k}_{\text{eff}})^2}{2m\hbar} + \omega_{21}\right)t\right] \\ B_3(\mathbf{p}, t) &= C_3(\mathbf{p}, t) \exp\left[i\left(\frac{(\mathbf{p} + \hbar\mathbf{k}_1)^2}{2m\hbar} + \omega_{31}\right)t\right] \end{aligned}$$

This choice eliminates exponential terms in the time-derivative parts, once inserted back into the Schrödinger equation and yields the coupled equations

$$\frac{\partial}{\partial t}B_1(\mathbf{p}, t) = -i\Omega_1 e^{-i(\Delta t + \phi_1)} B_3(\mathbf{p}, t) \quad (3.7)$$

$$\frac{\partial}{\partial t}B_2(\mathbf{p}, t) = -i\Omega_2 e^{-i((\Delta + \delta)t + \phi_2)} B_3(\mathbf{p}, t) \quad (3.8)$$

$$\frac{\partial}{\partial t}B_3(\mathbf{p}, t) = -i\Omega_1^* e^{-i(\Delta t + \phi_1)} B_1(\mathbf{p}, t) - i\Omega_2^* e^{i((\Delta + \delta)t + \phi_2)} B_2(\mathbf{p}, t) \quad (3.9)$$

where the detunings Δ and δ have been inserted, as defined in figure 3.2. For the special case of $\delta = 0$, the system has an exact solution. However this simplification would neglect the influence of Doppler or light shift related effects (see equation (3.2)). Nonetheless it is safe to assume that $\Delta \gg \delta$, which also includes $\Delta \gg |\Omega_1|, |\Omega_2|$. This means that the coefficients $B_1(\mathbf{p}, t)$ and $B_2(\mathbf{p}, t)$ in equation (3.9) vary much slower than their preceding factors. They can therefore be treated as constant, when carrying out the integration over t .

$$B_3(\mathbf{p}, t) \approx -\frac{\Omega_1^*}{\Delta} e^{i(\Delta t + \phi_1)} B_1(\mathbf{p}, t) - \frac{\Omega_2^*}{\Delta} e^{i((\Delta + \delta)t + \phi_2)} B_2(\mathbf{p}, t) \quad (3.10)$$

Doing so introduces errors of $\mathcal{O}\left(\frac{T\Omega^2}{\Delta^2}\right)$ and $\mathcal{O}\left(\frac{t\Omega^2\delta}{\Delta^2}\right)$ [92] which are acceptable as $\Omega \ll \Delta$ from the assumptions that lead to this result. This step is referred to as *adiabatic elimination* which generally treats parts that

¹The relation $e^{\pm i\mathbf{k}\mathbf{x}} = \int |\mathbf{p} \pm \hbar\mathbf{k}\rangle \langle \mathbf{p} d\mathbf{p}|$ was used to extract the spanning space.

oscillate slower as constant. The previously mentioned, but omitted, inclusion of more coupling terms between levels and light fields leads to a larger system similar to equation 3.6. The additional terms would be systematically eliminated, eventually resulting in a two-level system with small correction to the expressions found for Ω_1 and Ω_2 .

Inserting equation (3.10) into equations (3.7) and (3.8) results in the coupled system

$$\begin{aligned}\frac{\partial}{\partial t} B_1(\mathbf{p}, t) &= i \frac{|\Omega_1|^2}{\Delta} B_1(\mathbf{p}, t) + i \frac{\Omega_1 \Omega_2^*}{\Delta} B_2(\mathbf{p}, t) e^{i\delta t} \\ \frac{\partial}{\partial t} B_2(\mathbf{p}, t) &= i \frac{\Omega_1^* \Omega_2}{\Delta} B_1(\mathbf{p}, t) e^{-i\delta t} + i \frac{|\Omega_2|^2}{\Delta} B_2(\mathbf{p}, t)\end{aligned}$$

Introducing the variables

$$\Omega_{\text{eff}} = \frac{2\Omega_1^* \Omega_2}{\Delta} \quad (3.11)$$

$$\Omega^{\text{AC}} = \frac{|\Omega_1|^2}{\Delta} + \frac{|\Omega_2|^2}{\Delta} \quad (3.12)$$

$$\delta^{\text{AC}} = \frac{|\Omega_1|^2}{\Delta} - \frac{|\Omega_2|^2}{\Delta} \quad (3.13)$$

$$\Omega_R = \sqrt{(\delta^{\text{AC}} - \delta)^2 + \Omega_{\text{eff}}^2} \quad (3.14)$$

gives the solution as [114, 92]:

$$\begin{aligned}B_1(\mathbf{p}, t_0 + \tau) &= \exp \left[i (\Omega^{\text{AC}} + \delta) \frac{\tau}{2} \right] \left[\left\{ \cos \left(\frac{\Omega_R \tau}{2} \right) + i \frac{(\delta^{\text{AC}} - \delta)}{\Omega_R} \sin \left(\frac{\Omega_R \tau}{2} \right) \right\} B_1(\mathbf{p}, t_0) \right. \\ &\quad \left. + \left\{ i \frac{\Omega_{\text{eff}}}{\Omega_R} \sin \left(\frac{\Omega_R \tau}{2} \right) e^{i\delta t_0} \right\} B_2(\mathbf{p}, t_0) \right] \quad (3.15)\end{aligned}$$

$$\begin{aligned}B_2(\mathbf{p}, t_0 + \tau) &= \exp \left[i (\Omega^{\text{AC}} - \delta) \frac{\tau}{2} \right] \left[\left\{ i \frac{\Omega_{\text{eff}}}{\Omega_R} \sin \left(\frac{\Omega_R \tau}{2} \right) e^{-i\delta t_0} \right\} B_1(\mathbf{p}, t_0) \right. \\ &\quad \left. + \left\{ \cos \left(\frac{\Omega_R \tau}{2} \right) - i \frac{(\delta^{\text{AC}} - \delta)}{\Omega_R} \sin \left(\frac{\Omega_R \tau}{2} \right) \right\} B_2(\mathbf{p}, t_0) \right] \quad (3.16)\end{aligned}$$

These expressions describe the evolution of the two coupled states under the influence of an external laser field of duration τ . With the initial conditions $B_1(\mathbf{p}, t_0) = 1$ and $B_2(\mathbf{p}, t_0) = 0$, the probability of finding the atom in the other state is

$$P_2(\mathbf{p}, t_0 + \tau) = |B_2(\mathbf{p}, t_0 + \tau)|^2 = \frac{\Omega_{\text{eff}}^2}{\Omega_R^2} \sin^2 \left(\Omega_R \frac{\tau}{2} \right) \quad (3.17)$$

which recovers a *Rabi oscillation* type behaviour as previously discussed for a pure two-level atom (see

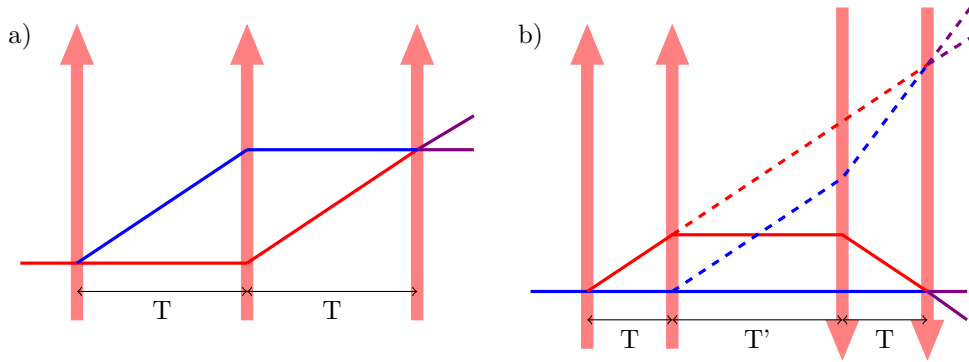


Figure 3.3: a) symmetric Mach-Zehnder type interferometry geometry. Both arms (red and blue) have exactly the same length. Such a geometry yields zero phase difference between the two arms in absence of external fields. b) asymmetric Ramsey-Bordé type interferometer in the 2 possible geometries (solid and dashed). Both arms have intrinsically different lengths, therefore the phase difference is not zero.

equation (2.11)). A pulse of the length

$$\Omega_R \tau_\pi = \pi \quad (3.18)$$

will therefore invert the original population. Likewise, a pulse of length $\Omega_R \tau_{\pi/2} = \frac{\pi}{2}$ creates an equal superposition of ground and excited states. Pulses of these lengths are referred to as π - and $\frac{\pi}{2}$ -pulses. The difference to *Rabi oscillations* is that the two coupled states are *stable* and no radiative decay into a lower state is possible. This is the first building block of an atom interferometer. The control over population and momentum transfer creates the aforementioned beam splitter and mirror equivalents for atom clouds.

3.2 Interferometer Geometries and Phase Shifts

The introductory sketch in figure 3.1 used a Mach-Zehnder type geometry which is symmetric in its arm length. Figure 3.3 a) shows trajectories of atoms in a standard $\frac{\pi}{2}$ - π - $\frac{\pi}{2}$ pulse interferometer. The two arms are coded in red and blue, laser beams are indicated as red arrows. Figure 3.3 b) shows a *Ramsey-Bordé*[20, 19] interferometer geometry using a $\frac{\pi}{2}$ - $\frac{\pi}{2}$ - $\frac{\pi}{2}$ - $\frac{\pi}{2}$ pulse sequence and asymmetric arms. Compared to the geometry in a) it requires one additional pulse and a change in the direction of momentum transfer. Both geometries are equally sensitive to gravitational acceleration as the trajectory of the atoms along the arms bends under the influence of the gravitational field. However, the Mach-Zehnder interferometer has the advantage of one less pulse and an inversion of the beam direction is not required. This is therefore the geometry that will be implemented in the future extension of this experiment.

The following sections derive the formalism to calculate phase contributions in atom interferometry. The

arguments and derivations are largely taken from Storey and Cohen-Tannoudji[133] and discuss the concept of classical action for paths in interferometers and then apply the findings to a Mach-Zehnder interferometer as sketched in figure 3.3 a). It is understood from the previous sections that this geometry is created by three Raman pulses and that the phase is encoded in the ratio of the internal states after the last element.

3.2.1 Classical Action

Interference of matter is a non-classical process and therefore needs to respect the wave nature of the atoms. Strictly speaking the interferometer's phase needs to be calculated for one atom at a time which is, similar to photons, subject to the 'which-way' problem[43, 47]. If the trajectory of a single object in the interferometer is known at any point, the interference pattern vanishes. The atom is therefore assumed to be in a superposition of both arms while traversing through the interferometer, emphasising its quantum particle nature. This means that for the phase outcome, all possible paths through the interferometer geometry contribute. The *Feynman path integral approach*[52] includes this concept by assuming that all ways are possible and interfere. The next sections will show that constructive interference occurs only close to the classical path, leaving it as the most probable one.

We start with the evolution of a quantum mechanical state $|\Psi(t)\rangle$, described by the evolution operator U which advances from t_1 to t_2 .

$$|\Psi(t_2)\rangle = U(t_2, t_1) |\Psi(t_1)\rangle$$

The projected state is consequently

$$\begin{aligned} \Psi(z_2, t_2) &= \langle z_2 | U(t_2, z_2) | \Psi(t_1) \rangle \\ &= \int_{-\infty}^{\infty} dz_1 K(z_2, t_2; z_1, t_1) \Psi(z_1, t_1) \end{aligned} \quad (3.19)$$

In which the quantum propagator $K(z_2, t_2; z_1, t_1)$ has been introduced

$$K(z_2, t_2; z_1, t_1) = \mathcal{N} \sum_{\Gamma} e^{i \frac{S_{\Gamma}}{\hbar}} \quad (3.20)$$

$$= \int_1^2 e^{i \frac{S_{\Gamma}}{\hbar}} \mathcal{D}z(t) \quad (3.21)$$

with S_{Γ} being the action along the path Γ and \mathcal{N} a normalisation factor. The integral extends between the

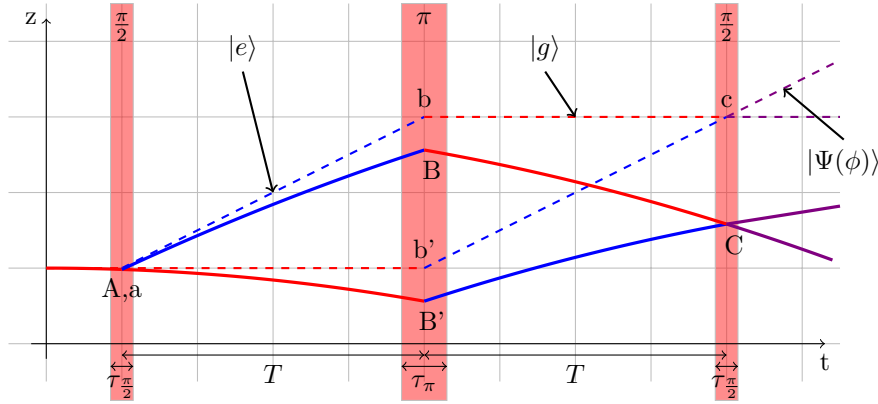


Figure 3.4: Path of an atom in an interferometer sequence without (dashed line) and with (solid line) constant gravitational field pointing in the direction of $-z$

points 1 and 2.

$$S_{\Gamma} = \int_{t_1}^{t_2} dt \mathcal{L}[z(t), \dot{z}(t)] \quad (3.22)$$

\mathcal{L} is the Lagrangian $\mathcal{L}[z(t), \dot{z}(t)] = \frac{m\dot{z}^2}{2} - V(z)$ for a particle in a potential V . In their tutorial paper Storey and Cohen-Tannoudji[133] showed that the integral in (3.19) reduces to an integral over classical paths, meaning a single trajectory determined by classical mechanics, if the Lagrangian is at most quadratic in \dot{z} . This is true for a freely moving particle in a gravitational field (see equation (3.25)), and therefore

$$K(z_2, t_2; z_1, t_1) = F(t_2, t_1) e^{i \frac{S_{\text{cl}}(z_2, t_2; z_1, t_1)}{\hbar}} \quad (3.23)$$

holds, where $F(t_2, t_1)$ is the integral over the previously introduced variables \mathcal{D} and $z(t)$ in equation (3.21). In addition, if the incoming state is a plane wave of the form $\Psi(z_1, t_1) = e^{i \frac{p_0 z_1}{\hbar}}$, the integral reduces further to a *single contribution*: that of the classical path from the space-time coordinates (z_1, t_1) to (z_2, t_2) . Since we are only interested in the phase changes of an initial state, which enters in an exponential form as a factor through K , it is sufficient to calculate the difference in action[106]

$$\Delta\phi_{\text{prop}} = \frac{(S_{\text{cl}}^B - S_{\text{cl}}^A)}{\hbar} \quad (3.24)$$

along the two arms A and B of the interferometer to extract the phase change.

3.2.2 Phase Shift in a Gravitational Field

Under the influence of gravity, the atom's trajectory in the interferometer changes as they are accelerated. Figure 3.4 shows the sketched path of an unperturbed sequence (dashed lines) and another with a constant gravitational field (solid lines). The two colours red and blue indicate now the *internal states* $F = 1$ and $F = 2$. Because atoms have mass, they are accelerated by gravity and drop, leading to bent trajectories (solid lines). Although they have changed, the trajectories still meet in the centre of the second $\frac{\pi}{2}$ Raman pulse at time $2T$ (see figure 3.4). To calculate the phase shift, we need the Lagrangian of a particle in a gravitational field of strength g :

$$\mathcal{L}(z, \dot{z}) = \frac{1}{2}m\dot{z}^2 - mgz \quad (3.25)$$

Assuming the particle starts at (z_1, t_1) and finishes at (z_2, t_2) , its speed and position along the classical path are [133]

$$\begin{aligned} v(t) &= v_1 - g(t - t_1) \\ z(t) &= z_1 + v_1(t - t_1) - \frac{1}{2}g(t - t_1)^2 \end{aligned}$$

This Lagrangian is at most quadratic in $z(t)$ and hence the argument from the previous section holds. Expressing the speed at the start and the final position in terms of the space-time coordinates of the start and end points

$$\begin{aligned} v_1 &= \frac{z_2 - z_1}{t_2 - t_1} + \frac{1}{2}g(t_2 - t_1) \\ v_2 &= v_1 - g(t_2 - t_1) \\ z_2 &= z_1 + v_1(t_2 - t_1) - \frac{1}{2}g(t_2 - t_1)^2 \end{aligned}$$

yields to the action along the classical path

$$\begin{aligned} S_{\text{cl}}(z_2, t_2; z_1, t_1) &= \int_{t_1}^{t_2} \left[\frac{1}{2}mv(t)^2 - mgz(t) \right] dt \\ &= \frac{m}{2} \frac{(z_2 - z_1)^2}{t_2 - t_1} - \frac{mg}{2}(z_2 + z_1)(t_2 - t_1) - \frac{mg^2}{24}(t_2 - t_1)^2. \end{aligned} \quad (3.26)$$

This covers phase contributions from free evolution but the laser fields of the Raman beams also need to be considered.

3.2.3 Light Contributions

The typical lengths τ of used Raman pulses are negligible compared to the pulse separation T (μs vs. ms), therefore any phase accumulating while the atom propagates inside the laser field is ignored. A momentum transfer of $\hbar k_{\text{eff}}$ associated with a transition which promotes the atom from $|1\rangle$ to $|2\rangle$, changes the wavefunction by a factor [133, 11]

$$U_{21} e^{i(k_L z - \omega t - \phi)} \quad (3.27)$$

where the atom passes the light field of frequency ω_L and phase ϕ at coordinates (z, t) . U_{21} is the transition probability for $|1\rangle \rightarrow |2\rangle$ for a coordinate origin at (z, t) and $\phi = 0$. The $k_L z$ contribution originates from the transferred momentum. Although the Raman light field has two frequencies and an intermediate level is involved, it behaves as a two level system (see section 3.1), so that k_L and ω_L can be replaced by k_{eff} and ω_{eff} . This leads to the phase contributions listed in table 3.1 [106, 11], where the AC-stark shift has been omitted [143].

State change	Momentum	phase shift
1 \rightarrow 2	$p \rightarrow p + \hbar k_{\text{eff}}$	$+(k_{\text{eff}} z(t) - \omega_{\text{eff}} t - \phi)$
2 \rightarrow 1	$p + \hbar k_{\text{eff}} \rightarrow p$	$-(k_{\text{eff}} z(t) - \omega_{\text{eff}} t - \phi)$
1 \rightarrow 1	$p \rightarrow p$	0
2 \rightarrow 2	$p + \hbar k_{\text{eff}} \rightarrow p + \hbar k_{\text{eff}}$	0

Table 3.1: phase contributions for different Raman Transitions. The phase term ϕ denotes the phase of the corresponding Raman beam

$$\Psi_2(z_2, t_2) = \underbrace{e^{i[S_{\text{cl}}(z_2, t_2; z_1, t_1)/\hbar]t}}_{2^{\text{nd}} \text{ propagation}} \underbrace{U_{21} e^{i(k_L z_1 - \omega_L t_1 - \phi)}}_{\text{Raman transition}} \underbrace{e^{i[S_{\text{cl}}(z_1, t_1; z_0, t_0)/\hbar]t}}_{1^{\text{st}} \text{ propagation}} \underbrace{\Psi_1(z_0, t_0)}_{\text{initial state}}. \quad (3.28)$$

Therefore the total phase contains a part gathered during free evolution and one of the interaction with the Raman beams

$$\Phi_{\text{total}} = \Phi_{\text{prop}} + \Phi_{\text{las}}. \quad (3.29)$$

This result does assume perfectly overlapping paths and non varying phase fronts of the beams.

3.2.4 Phase Shifts in an Atom Interferometer

Using equation (3.26) and the notation in figure 3.4, the difference between the classical actions (or phases multiplied by \hbar) of the lower and upper arm is

$$\Delta S_{\text{cl}} = \frac{m}{T} (z_{B'} - z_B) (z_B + z_{B'} - z_A - z_C - gT^2) \quad (3.30)$$

These positions along the arms are related to the uninfluenced ones via

$$z_A = z_a \quad z_B = z_b - \frac{1}{2}gT^2 \quad z_{B'} = z_{b'} - \frac{1}{2}gT^2 \quad z_C = z_c - 2gT^2 \quad (3.31)$$

which when inserted back into the previous equation, yield

$$\Delta S_{\text{cl}} = \frac{m}{T} (z_{b'} - z_b) (z_b + z_{b'} - z_a - z_c). \quad (3.32)$$

The two arms form a parallelogram and therefore $z_b = z_a$ and $z_{b'} = z_c$ and the second term vanishes. The total change in phase accumulated through progression along the two arms is

$$\Delta S_{\text{cl}} = 0.$$

Which means that the phase contribution in free propagation is zero in a symmetric Mach-Zehnder type atom interferometer.

Phase imprints from the Raman lasers are calculated using table 1.1. We will follow the upper arm through the states $|1\rangle \rightarrow |2\rangle \rightarrow |1\rangle \rightarrow 2$ and the lower arm through $|1\rangle \rightarrow |1\rangle \rightarrow |2\rangle \rightarrow |2\rangle$. Their individual phases are

$$\begin{aligned} \Phi_{\text{upper}} &= k_{\text{eff}}z_A - \omega_{\text{eff}}0 - \phi_1 - (k_{\text{eff}}z_B - \omega_{\text{eff}}T - \phi_2) + k_{\text{eff}}z_C - \omega_{\text{eff}}2T - \phi_3 \\ &= k_{\text{eff}}z_a - \omega_{\text{eff}}0 - \phi_1 - \left(k_{\text{eff}} \left(z_b - \frac{1}{2}gT^2 \right) - \omega_{\text{eff}}T - \phi_2 \right) + k_{\text{eff}}(z_c - 2gT^2) - \omega_{\text{eff}}2T - \phi_3 \\ &= k_{\text{eff}} \left(z_a - z_b + z_c - \frac{3}{2}gT^2 \right) - \omega_{\text{eff}}T - \phi_1 + \phi_2 - \phi_3 \end{aligned}$$

$$\Phi_{\text{lower}} = k_{\text{eff}}z_{B'} - \omega_{\text{eff}}T - \phi_2$$

The total contribution is the difference of these two and results in

$$\begin{aligned}\Phi_{\text{total}} &= \Phi_{\text{laser}} = \Phi_{\text{upper}} - \Phi_{\text{lower}} \\ &= k_{\text{eff}}gT^2 + (\phi_1 - 2\phi_2 + \phi_3)\end{aligned}\quad (3.33)$$

Again, the spatial coordinates z cancel out. The zero phase contribution of the free propagation arises from the symmetry of the interferometer geometry. An asymmetric interferometer such as in figure 3.3 b) would have a non-zero base term. The primary phase contribution via light interaction stems from equation (3.27). In experiments, the phase of both Raman lasers (Φ_i) is stabilised to eliminate random fluctuations but this means that the final phase shift originates from the bend trajectory entering the laser beam at a different vertical positions. The light therefore acts as a ruler. Although only gravitational acceleration was considered here, the method is easily expanded to other influences, such as rotation. Changing the Lagrangian to the appropriate form does yield the corresponding phase contributions.

3.2.5 Gravity Gradients

Gravity gradients are one example where equation (3.29) needs modification. So far uniformity of the gravitational field was assumed. However, the strength of gravitational acceleration falls off with $\frac{1}{r^2}$ where r is the distance from the source. Typical arm separations in atom interferometers are on the order of mm so one could argue that such effects do not contribute. Given the target precision for this experiment of $\mathcal{O}(10^{-9}g)$ [105], these effects need to be considered. Figure 3.5 shows the arms of an interferometer under a constant gravitational potential (solid semi-transparent) and with an added gradient (solid line). The different curvature of the trajectories in the two arms causes the interferometer to close at a later time than the third pulse, if the pulses are equally spaced. Distances in the picture are exaggerated to emphasise the effects. The dashed line indicates a closing interferometer with the same parameters; however, for the paths to overlap in the final pulse, the original position needs to be different. This separated starting position causes a significant change in the phase and can be accounted for by another term:

$$\Delta\Phi = \Phi_{\text{prop}} + \Phi_{\text{las}} + \Phi_{\text{sep}} \quad (3.34)$$

where

$$\Phi_{\text{sep}} = p_0 \frac{z_0^B - z_0^A}{\hbar}. \quad (3.35)$$

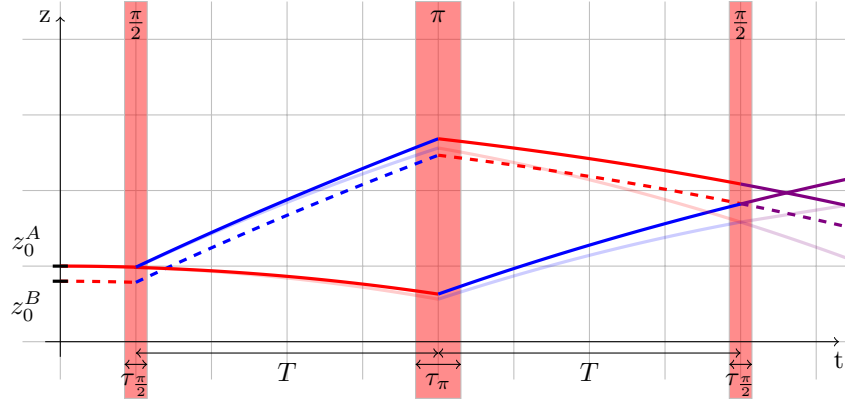


Figure 3.5: Path of an atom in an interferometer sequence under a constant gravitational field (solid faint, same as in figure 3.4) and with a gravity gradient (solid line) and same starting position. A gravity gradient causes the upper arm to bend less which leads to a later closing point. The dashed trajectory indicates the necessary starting position to close the solid interferometer at the position of the second pulse. With equal spacing, different parts of the atom cloud will interfere, unless corrected for by an asymmetric pulse spacing.

The Lagrangian in equation (3.25) now changes to

$$\mathcal{L}(z, \dot{z}) = \frac{1}{2}m\dot{z}^2 - mgz + \frac{1}{2}\gamma z^2 \quad (3.36)$$

with the linear gravity gradient γ [105, 106]. The position and velocity over time become[106]

$$\begin{aligned} z(t) &= \frac{g_0}{\gamma} + \left(z_0 - \frac{g_0}{\gamma}\right) \cosh(t\sqrt{\gamma}) + \frac{v_0}{\sqrt{\gamma}} \sinh(t\sqrt{\gamma}) \\ \dot{z}(t) &= \sqrt{\gamma} \left(z_0 - \frac{g_0}{\gamma}\right) \sinh(t\sqrt{\gamma}) + v_0 \cosh(t\sqrt{\gamma}). \end{aligned}$$

Using the same method as before with the adapted Lagrangian, the total phase change is now found to be

$$\begin{aligned} \Delta\Phi &= g_0 \left(\frac{mv_{\text{rec}}T^2}{\hbar}\right) + \gamma \left(\frac{mv_{\text{rec}}T^2}{\hbar}\right) \left(\frac{7}{12}g_0T^2 - \bar{v}_0T - z_0\right) + \mathcal{O}(\gamma^2) \\ &= g_0k_{\text{eff}}T^2 \left(1 + \gamma \left(\frac{7}{12}g_0T^2 - \bar{v}_0T - z_0\right) + \mathcal{O}(\gamma^2)\right). \end{aligned} \quad (3.37)$$

For typical operation parameters of an experiment ($z_0 = 0$, $g_0 = 9.8 \frac{m}{s^2}$, $v_{\text{rec}} = 5.98 \cdot 10^{-3} \frac{m}{s}$, $\gamma \approx 2.9 \cdot 10^{-6} \frac{1}{s^2}$ and $\bar{v}_0 \approx 0.0697 \frac{m}{s}$ for $T \approx 25 \mu K$), the first order correction is $g^1 \approx 3.92 \cdot 10^{-7} \frac{m}{s^2}$ and therefore measurable. Second order corrections are $\mathcal{O}(10^{-14} \frac{m}{s^2})$ and not expected to be significant if a sensitivity if $10^{-9}g$ or better is required. This emphasises that seemingly small effects like shifted starting positions and imperfections in the closing of the interferometer have significant effects on the precision of the sensor.

3.2.6 Raman Beam Configurations

The last two sections explained how a Raman transition drives deterministic state transfer and the application to atom interferometers. However, no comment was made on the orientation of the light beams. This is important because the states in equation (3.1) not only contain the internal excitation of the atom, but also the momentum. While the energy transfer to the internal states is independent of the direction of the light field, the transferred momentum is not. Two configurations are commonly used for different purposes (see table 3.2), noted as co- and counter-propagating. **Co-propagating Raman beams** are overlapping and advance in the same direction. When a photon of frequency ω_1 is absorbed, its momentum $\hbar\mathbf{k}_1$ is added to the momentum of the atom. In the stimulated emission process of the second photon of frequency ω_2 the momentum of $\hbar\mathbf{k}_2$ is *subtracted* from the atom's momentum because the field is oriented in the opposite direction. Therefore, the overall transfer is $\hbar\mathbf{k}_{\text{eff}} = \hbar(\mathbf{k}_1 - \mathbf{k}_2)$. In the case of **counter-propagating Raman beams** the second photon is emitted in the opposite direction, resulting in an additional momentum in the atom of $\hbar\mathbf{k}_{\text{eff}} = \hbar(\mathbf{k}_1 + \mathbf{k}_2)$.


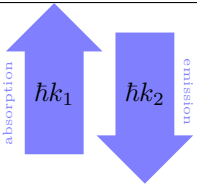
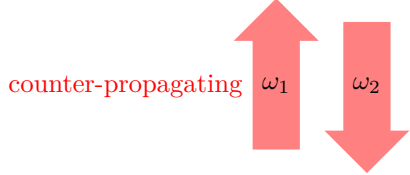
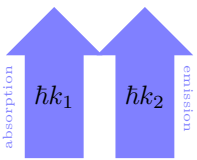
Beam configuration	momentum transfer	momentum sum
 <p>co-propagating ω_1 ω_2</p>	 <p>absorption $\hbar k_1$ $\hbar k_2$ emission</p>	$\hbar(k_1 - k_2)$
 <p>counter-propagating ω_1 ω_2</p>	 <p>absorption $\hbar k_1$ $\hbar k_2$ emission</p>	$\hbar(k_1 + k_2)$

Table 3.2: Raman beam configuration and the resulting momentum transfer from absorbing a photon from one beam and emitting into the second

The sensitivity of an atom interferometer scales, the same as light based interferometers, with the enclosed area. But separation of the two arms depends on the transferred momentum \mathbf{k}_{eff} which is quite different for the two configurations. Co-propagating beams are commonly used for initial testing of the system because both frequencies are equally Doppler shifted for fast atoms and therefore the effect cancels out. In counter-propagating configuration on the other hand, only a narrow velocity class of atoms is in resonance, where the Doppler shift of both beams cancel. This is equivalent to the difference between Doppler free and non-Doppler free spectroscopy geometries. In the first type, only atoms which are at rest, and therefore do not see any

frequency shift of the light, contribute to the signal. For Raman beams, the momentum transfer and the sensitivity of the interferometer is important. For some applications $\mathbf{k}_1 + \mathbf{k}_2$ might not give a large enough momentum transfer and experiments have been performed using different methods of momentum transfer. One such scheme is the use of *Bragg diffraction*. Originally presented as the diffraction of atoms on a standing laser wave through the dipole force in the high power nodes, it can also be realised with two laser fields and a Raman configuration. If the detuning δ in figure 3.2 is too large, no transition is driven. However because of the exponential energy dependence of the states $|1, p\rangle$ and $|2, p'\rangle$, it can be tuned in a way that the coupling of four photons (two ω_1 and two ω_2) acts as a ladder to promote the atom to $|2, p + 2\hbar k_{\text{eff}}\rangle$ [58]. Precise control over the interaction strength allows the stacking of such processes and transfers of up to $102\hbar k$ have been implemented[25]. Another method is the use of optical lattices[30] and the *Bloch oscillations* that atoms undergo in the resulting band structure. While they accelerate inside the lattice, they do not physically move outside the Brillouin zones. The interferometer can then be stretched in time, leading to a larger enclosed area with minimal spatial requirements. This is especially helpful if the size of the experiment is limited.

In its final state, the presented experiment should be deployed for a field application and could benefit from either of these approaches. At the moment, the experiment is in a basic test mode and the first scheme to be implemented is using co-propagating beams to generate atom interference. For the following discussion of phase shifts in an atom interferometer, the orientation of Raman lasers is not important as long as there is momentum transfer. For the later presented results a co-propagating configuration was used. The implementation of counter-propagating beams is left for the next steps when gravitational acceleration is measured. The larger momentum transfer gained by counter-propagating beams is necessary for a sensitive gravimeter.

Raman Transitions in Rubidium

To calculate state evolution with equations (2.6) and (2.7) one needs to find the *Rabi frequencies* defined in equation (3.5). Equations (3.11) and (3.14) also include the detuning, which depends on the involved laser frequencies. For *Raman pulses* with rubidium, typically $\mathcal{O}(\Delta) \approx \text{GHz}$ are used, which is large compared to the separation of the F sub-levels in the $5^2P_{\frac{3}{2}}$ multiplet (496MHz between the $F=0$ and $F=3$ level). Each F level is further split in $2F + 1$ m_f sub-levels that have polarisation dependent transition rules. The *Rabi*

frequency from equation (3.5) now needs to include the polarisation vector ϵ_n of the light field:

$$\Omega_n = -\frac{\langle n | E_n \epsilon_n \cdot \mathbf{d} | 3 \rangle}{2\hbar} = -\frac{E_n \langle n | \epsilon_n \cdot \mathbf{d} | 3 \rangle}{2\hbar} \quad (3.38)$$

$$= -\frac{\sqrt{\frac{2I_n}{c\epsilon_0}} \langle n | \epsilon_n \cdot \mathbf{d} | 3 \rangle}{2\hbar} \quad (3.39)$$

This equation represents the transition between the states $|n\rangle$ and $|3\rangle$ by the field n with intensity I_n . The polarisation ϵ_n can be absorbed into the start and end states $\langle Fm_f | \mathbf{e} \cdot \mathbf{d} | F'm'_f \rangle$. The selection rules $\Delta F = [-1, 0, 1]$ and $\Delta m_f = [-1, 0, 1]$, with the special case of $\Delta m_f \neq 0$ if the transition starts at $m_f = 0$, need to be fulfilled.

Further reduction factors out the *Clebsch Gordan coefficients*[130]

$$\langle Fm_f | \mathbf{e} \cdot \mathbf{d} | F'm'_f \rangle = \langle F | \mathbf{e} \cdot \mathbf{d} | F' \rangle \langle Fm_f | F'm'_f \rangle \quad (3.40)$$

$$= \langle F | \mathbf{e} \cdot \mathbf{d} | F' \rangle (-1)^{F'-2+m_f} \sqrt{2F+1} \begin{pmatrix} F' & 1 & F \\ m'_f & q & -m_f \end{pmatrix} \quad (3.41)$$

which is valid for $m_f = m'_f + q$, otherwise the coefficient is zero. For linearly polarised light $m_f = m'_f$ holds, for σ^+ $m'_f = m_f + 1$ and for σ^- follows $m'_f = m_f - 1$. The remaining element is represented in terms of the total electron angular momentum $J = L + S$ and the total nuclear momentum $F = J + I^1$ as well as the Wigner 6j symbol

$$\langle F | \mathbf{e} \cdot \mathbf{d} | F' \rangle = \langle JIF | \mathbf{e} \cdot \mathbf{d} | J'I'F' \rangle \quad (3.42)$$

$$= \langle J | \mathbf{e} \cdot \mathbf{d} | J' \rangle (-1)^{F'+J+I+1} \sqrt{(2F'+1)(2J+1)} \begin{Bmatrix} J & J' & 1 \\ F' & F & I \end{Bmatrix}. \quad (3.43)$$

The first term is a constant $\langle J | \mathbf{e} \cdot \mathbf{d} | J' \rangle$ which is estimated through the lifetime of the state² and is for the D2 transition in Rubidium:

$$\left\langle J = \frac{1}{2} \middle| \mathbf{e} \cdot \mathbf{d} \middle| J' = \frac{3}{2} \right\rangle = 3.58 \cdot 10^{-29} Cm \quad (3.44)$$

Contributing to *Raman transitions* are any two elements that connect the two states $F=1$ and $F=2$ and together with their respective detuning, the effective *Rabi frequencies* Ω_1 and Ω_2 can be calculated. Without

¹The rubidium D2 line used has $J = \frac{1}{2}$, $J' = \frac{3}{2}$ and $L = 0, L' = 1$

² $\frac{1}{\tau} = \frac{\omega_0^3}{3\pi\epsilon_0\hbar c^3} \frac{2J+1}{2J'+1} |\langle J | \mathbf{e} \cdot \mathbf{d} | J' \rangle|^2$ from [130]

an external magnetic field, the m_f levels are degenerate, and multiple parts possible. Figure A.1 gives an overview of the contributing (coloured and thick) and allowed (thin and gray) transitions. Typically for testing purposes no bias field is applied, but in the final interferometer sequence such a field ensures that only the desired transitions contribute to the result.

Light Shifts

The above discussion included shifts of the energy levels due to light intensity, the *AC stark shifts*. Because a Raman pulse uses two fields that aim to couple different levels and the Stark shift is dependent on the Rabi frequencies, both fields displace the levels differently. This *differential Stark shift* (see equation (3.13)) can be compensated if the Rabi frequencies of the two fields are matched. To do so, the intensity of the beams with the two light fields is adjusted relative to each other[24][104]. The same effect can be achieved by tuning δ . Section 6.5 presents calculations and expected values for δ and $\frac{I_2}{I_1}$ as used in the experiment to compensate the shifts.

Velocity Selection

Section 3.2.6 mentioned the velocity selection feature of counter-propagating Raman beams. Contrary to light shifts, Doppler shifts depend on the speed of the atoms, so only a small amount of atoms is transferred from a wide kinetic energy distribution. Assuming the light shifts are cancelled, the Rabi frequency reads $\Omega_R = \sqrt{\Omega_{\text{eff}}^2 + (\mathbf{v} \cdot \mathbf{k}_{\text{eff}})^2}$. For a π -pulse ($|\Omega_{\text{eff}}|\tau = \pi$), equation (3.17) becomes:

$$P_\pi(\mathbf{v}) = \left(\frac{\pi}{2} \text{sinc} \left(\frac{\pi}{2} \sqrt{1 + \left(\frac{\mathbf{v} \cdot \mathbf{k}_{\text{eff}}}{\Omega_{\text{eff}}} \right)^2} \right) \right)^2 \quad (3.45)$$

The actual transferred population is small in comparison to the thermal distribution in the cloud. Figure 3.6 sketches the transfer of population induced by a Raman π pulse for an assumed cloud temperature of $5\mu K$. While the majority of the thermal cloud is not promoted, a small centre fraction undergoes the momentum change. Raman transitions are therefore highly velocity selective (see e.g. [92]) and hot clouds produce low contrast signals because the interacting number of atoms is limited. The advantage is that atoms which do contribute to the interferometer share the same narrow distribution and hence coherence is increased. Additionally in a fountain configuration, where atoms are launched vertically and the interferometer sequence is driven at the peak of the trajectory, the frequency of the Raman lasers need to follow the current Doppler shift of the atoms. A *chirp* of the Raman frequencies ensures maximal compensation for the Doppler shift along

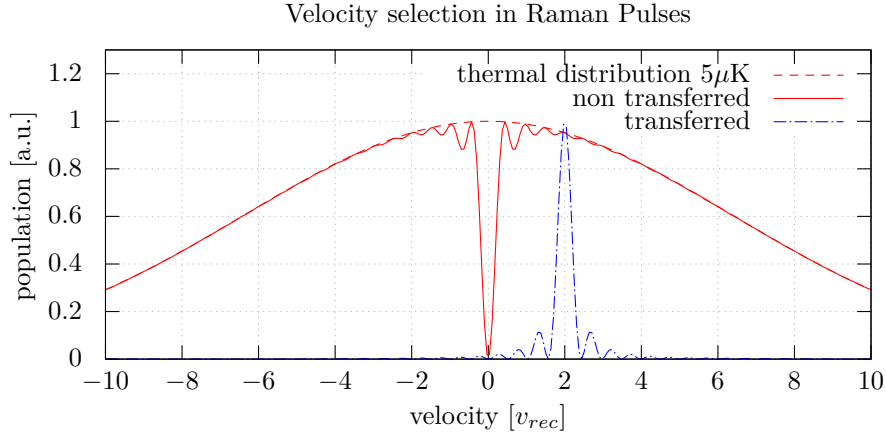


Figure 3.6: Population transfer in a Raman π pulse. the dashed line sketches the velocity distribution of a thermal cloud at $5\mu\text{K}$ in dependence of photon recoil velocity. The red solid line shows the same population after a π pulse has been applied. A narrow centre population has been transferred. The blue line indicates the promoted population to $2 v_{\text{rec}}$ as expected from 2 Raman fields.

the trajectory. Although welcome for high precision measurements, this effect requires careful calibration of the parameters and therefore co-propagating beams were chosen for first measurements.

3.2.7 Rotation Contributions

Typical interferometer times are on the order of 200ms and the achieved sensitivity is high enough to record signals from the Earth's rotation. Apparatus, vacuum system and laser system in the laboratory frame, rotate under the atom cloud during the interferometer time and add a phase shift. The classical analogue is the *Foucault pendulum*, which visualizes the *Coriolis force* through a pendulum on a long arm whose rotation axis does shift over a full day with respect to a fixed axis in the laboratory. Contributions from this effect are [17, 104]

$$\Delta\Phi_{\text{rotation}} = \underbrace{2\mathbf{k}_{\text{eff}}(\mathbf{v} \times \boldsymbol{\Omega}) T^2}_{\text{Coriolis}} + \underbrace{\mathbf{k}_{\text{eff}}(\boldsymbol{\Omega}(\times\boldsymbol{\Omega} \times \mathbf{r})) T^2 R}_{\text{Centrifugal}} \quad (3.46)$$

where \mathbf{v} is the speed of the atoms, R the earth radius and $\boldsymbol{\Omega}$ the earth rotation rate in the laboratory frame. In experiments, this extra shift is compensated for by adjusting the orientation of the Raman beams such that $\Delta\Phi_{\text{rotation}} = 0$ by for example tilting the retro-reflecting mirror. Not doing so would cause the interferometer not to close in the third dimension, perpendicular to the plane of figure 3.4, causing additional phase terms to enter because the interferometer is now partly operated as a gyroscope. This centrifugal term contributes a factor of around $1.9 \cdot 10^{-3}$ (for cesium atoms) to the signal [17].

3.2.8 Sensitivity to Noise

In a theoretical analysis as above, all values are controlled with absolute precision. An experiment however is subject to random noise. For example the phase relation ϕ_1 , ϕ_2 and ϕ_3 between the Raman beams has a finite precision because the stabilising electronics have limits. If these shortcomings are known, they can be filtered out, if they are random they would need to be monitored and then corrected for. The best approach is to build the experiment in such a way that intrinsic noise has no or minimal influence on the signal. To do so, it is important to know how and when the noise enters. Weighting and sensitivity functions are used to judge the influence of different types of disturbances. The formalism was originally developed for clock systems but is easily expanded to atom interferometer. The following sections outline the core formalism borrowed from [11]. The same discussion in various levels of details can be found in [104] and [24].

We assume a symmetric Mach-Zehnder interferometer composed of a $\frac{\pi}{2}$ - π - $\frac{\pi}{2}$ sequence in the absence of gravity. This geometry produces a signal of the shape $P(\phi) = \frac{1}{2}(1 - \cos(\phi))$ where $\phi = \phi_1 - 2\phi_2 + \phi_3$ is composed of the Raman laser phases. One defines the *sensitivity function* $g(t)$ as

$$g(t) = 2 \lim_{\delta\phi \rightarrow 0} \frac{\delta P(\delta\phi(t))}{\delta\phi} \quad (3.47)$$

for a phase distortion $\delta\phi(t)$. The phase change during the complete interferometer sequence is calculated via

$$\delta\phi = \int g(t) \frac{d\phi(t)}{dt} dt. \quad (3.48)$$

$g(t)$ acts as a weighting function for phase influences during the interferometer time. Knowledge of its shape allows an estimate of the noise impact. The change in transition probability, and hence signal, calculates via

$$\delta P = \frac{\partial P}{\partial(\delta\phi)} \delta\phi. \quad (3.49)$$

The transition probability P at any point during the interferometer is given through equations (2.6) and (2.7). The equation system can be simplified if one assumes $\Omega_1 = \Omega_2 = \Omega$ and $|\delta| \ll |\Omega|$ and terms of the order $\mathcal{O}(\frac{\delta}{\Omega})$ can be neglected. Evolution of the arm states' population, described by B_1 and B_2 , is now described by a single operator

$$\begin{pmatrix} B_1(t_0 + t) \\ B_2(t_0 + t) \end{pmatrix} = U(\Omega_{\text{eff}}^*, \phi, t, t_0) \begin{pmatrix} B_1(t_0) \\ B_2(t_0) \end{pmatrix} \quad (3.50)$$

which propagates the system from $t_0 \rightarrow t$. ϕ is the phase of the laser beam and $\Omega_{\text{eff}}^* = \Omega_{\text{eff}}/2$ (see equation (3.11)). The full form reads

$$U(\Omega_{\text{eff}}^*, \phi, t, t_0) = e^{i\Omega_{\text{eff}}^*(t-t_0)} \begin{pmatrix} \cos(\Omega_{\text{eff}}^*(t-t_0)) & ie^{i(\delta t_0 + \phi)} \sin(\Omega_{\text{eff}}^*(t-t_0)) \\ ie^{-i(\delta t_0 + \phi)} \sin(\Omega_{\text{eff}}^*(t-t_0)) & \cos(\Omega_{\text{eff}}^*(t-t_0)) \end{pmatrix}. \quad (3.51)$$

For the standard Mach-Zehnder atom interferometer with two $\frac{\pi}{2}$ -pulses of length τ , a single π pulse of length 2τ and a pulse separation of T and the starting conditions of $B_1(0) = 1$ and $B_2(0) = 0$ we get

$$\begin{pmatrix} B_1(2T + 4\tau) \\ B_2(2T + 4\tau) \end{pmatrix} = U(\Omega_{\text{eff}}^*, \phi_3, 2T + 4\tau, 2T + 3\tau) U(0, \phi_2, 2T + 3\tau, T + 3\tau) \\ U(\Omega_{\text{eff}}^*, \phi_2, T + 3\tau, T + \tau) U(0, \phi_1, T + \tau, \tau) U(\Omega_{\text{eff}}^*, \phi_1, \tau, 0) \begin{pmatrix} 1 \\ 0 \end{pmatrix}. \quad (3.52)$$

In order to use this formalism to describe errors of the phase, the operator of the corresponding section is split to accommodate for the shift. For example, if the shift occurs during the centre pulse the corresponding operator changes to

$$U(\Omega_{\text{eff}}^*, \phi_2, T + 3\tau, T + \tau) \rightarrow U(\Omega_{\text{eff}}^*, \phi_2 + \delta\phi, T + 3\tau, T + \tau + t) U(\Omega_{\text{eff}}^*, \phi_2, T + \tau + t, T + \tau) \quad (3.53)$$

where $t \in [0, 2\tau]$. Equation (3.53) assumes that the phase jump of $\delta\phi$ occurs at a time t in the third pulse. Now that the transition probability is known via $P = |c_2|^2$, it can be used to calculate the sensitivity function via equations (3.49) and (3.47). The sensitivity function $g(t)$ equates to [11]

$$g(t) = \begin{cases} -\sin(\Omega_{\text{eff}} t) & 0 < t \leq \tau \\ -1 & \tau < t \leq T + \tau \\ -\sin(\Omega_{\text{eff}}(t - T)) & T + \tau < t \leq T + 3\tau \\ 1 & T + 3\tau < t \leq 2T + 3\tau \\ -\sin(\Omega_{\text{eff}}(t - 2T)) & 2T + 3\tau < t \leq 2T + 4\tau \\ 0 & \text{otherwise} \end{cases} \quad (3.54)$$

Figure 3.7 shows a plot of $g(t)$ with the relevant time scales included where the sequence is sensitive to phase noise throughout its duration. However, this does not yield any information regarding the impact

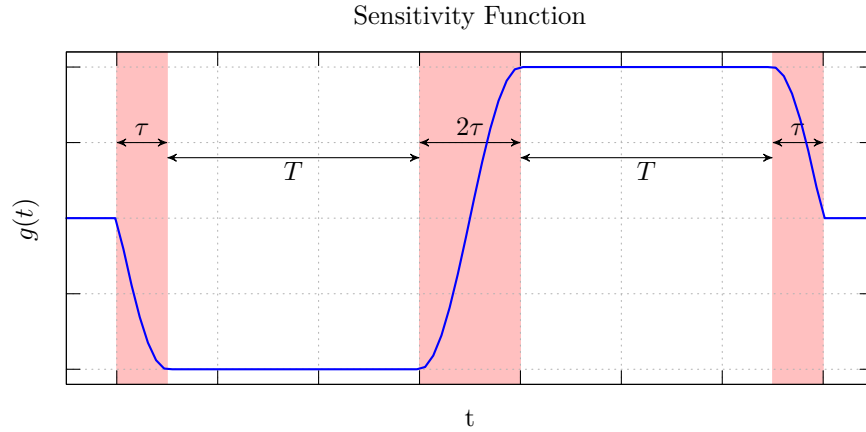


Figure 3.7: Sensitivity function $g(t)$ (equation (3.47)) for a Mach-Zehnder interferometer of two $\frac{\pi}{2}$ pulses of length τ and a π -pulse of length 2τ .

of various noise types. As an example, one can assume a modulated phase change of the form $\phi(t) = A \cos(\omega_\phi t + \theta)$. Using equation (3.48) yields $\delta\phi = A\omega_\phi \text{Im}(G(\omega_p h i)) \cos(\theta)$ where $G(\omega)$ is the Fourier transform of the sensitivity function

$$G(\omega) = \int e^{-i\omega t} g(t) dt. \quad (3.55)$$

Performance of the interferometer depends on the average noise on time scales relevant for the experiment. In a measurement, the spread of phase fluctuation determines the accuracy and a good indicator is the rms (root-mean-squared) of the phase change. For the above phase modulation, it can be shown to be $\delta\phi_{\text{rms}} = |A\omega_\phi G(\omega_\phi)|$ [11]. Therefore the spread of phase is proportional to $|\omega_\phi G(\omega_p h i)|$ and we can define the *transfer function* as

$$H(\omega) = \omega G(\omega) \quad (3.56)$$

If the noise has an arbitrary shape, but the power spectral density $S_\phi(\omega)$ is known, the standard deviation of the rms noise is calculated via

$$(\sigma_\phi^{\text{rms}})^2 = \int_0^\infty |H(\omega)|^2 S_\phi(\omega) d\omega.$$

Taking the example of the periodic noise and using equations (3.55), (3.56) and (3.54) the transfer function yields

$$H(\omega) = \frac{2i\omega\Omega_{\text{eff}}}{\omega^2 - \Omega_{\text{eff}}^2} \left(\sin(\omega(T + 2\tau)) + 2\frac{\Omega_{\text{eff}}}{\omega} \sin\left(\frac{\omega T}{2}\right) \sin\left(\frac{\omega(T + 2\tau)}{2}\right) \right) \quad (3.57)$$

Figure 3.8 shows a plot of $|H(\omega)|^2$ for parameters of the experiment (see section 3.1) with $T = 50\text{ms}$, $\tau = 7.4\mu\text{s}$ and $\Omega_{\text{eff}} = \pi/2\tau = 2\pi 33.78\text{kHz}$. The trace features regular oscillation and a drop off at higher

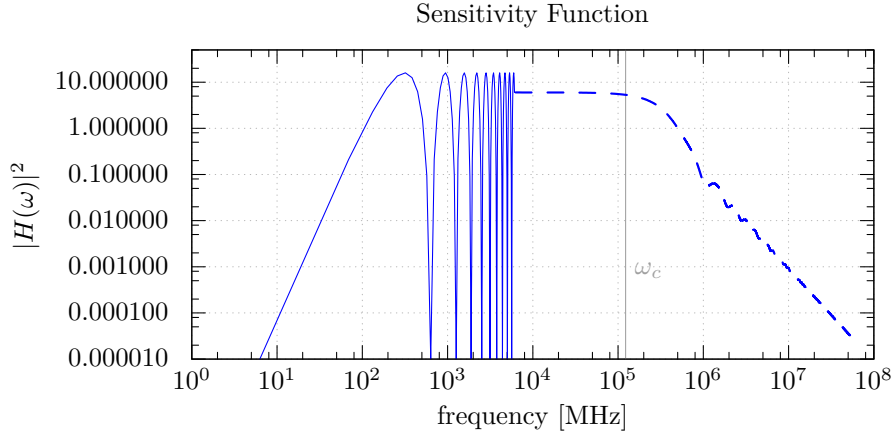


Figure 3.8: Weighting function for the same sequence as in figure 3.7. The function oscillates with a period of $(T + \tau)^{-1}$. The plot shows data for $\tau = 7.4\mu s$ and $T = 10ms$, the time scales of the experiment. Frequencies greater than 8kHz are averaged over one oscillation to eliminate sampling problems. $\omega_c = \frac{\Omega_{\text{eff}}}{\sqrt{3}}$ indicates the cutoff frequency; higher frequencies contribute less.

frequencies. Above 1kHz the signal was averaged over one oscillation period $(T + \tau)^{-1}$ to eliminate sampling errors. The function has a constant amplitude until a ‘cut-off’ frequency $\omega_c = \frac{\Omega_{\text{eff}}}{\sqrt{3}}$ is reached. Higher frequencies are attenuated, the system acts as a natural low pass filter, implying that a longer Raman pulse time τ is therefore beneficial.

Mirror Movement

Random phase changes in the Raman beams can be suppressed by active stabilisation of the mirror and the use of stable laser sources. This experiment uses a 1560nm fibre laser (see section 5.6) with added sidebands and a fibre coupled frequency doubling module to generate 780nm light for the Raman pulses. Relative phase changes and their imprint in the atom interferometer are therefore removed, because of the common laser source of both Raman frequencies. Besides these intrinsic phase noises, mechanical components introduce shifts through vibration or deformation. This can happen on windows, lenses or mirrors. The most critical component is the retro-reflecting mirror for the Raman lasers because it changes the phase relation between the counter-propagating Raman beams. Assuming a movement described by $\mathbf{r}(t)$, the corresponding phase change reads $\phi(t) = \mathbf{k}_{\text{eff}} \cdot \mathbf{v}(t)$. The change over a complete sequence (using equation (3.48)) is therefore

$$\delta\phi = \int_{-\infty}^{\infty} g(t) \mathbf{k}_{\text{eff}} \cdot \mathbf{v}(t) dt \quad (3.58)$$

$$= -\mathbf{k}_{\text{eff}} \cdot [f(t) \mathbf{v}(t)]_{-\infty}^{\infty} + \mathbf{k}_{\text{eff}} \cdot \int_{-\infty}^{\infty} f(t) \mathbf{a}(t) dt \quad (3.59)$$

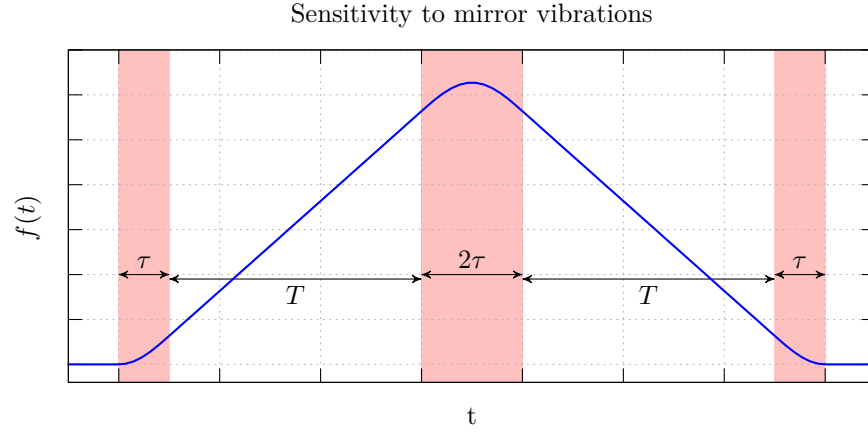


Figure 3.9: Transfer function for mirror vibrations (equation (3.61)).

Where $\mathbf{a}(t) = \dot{\mathbf{v}}(t) = \ddot{\mathbf{r}}(t)$ are the acceleration, velocity and position. The response function for this case relates to the sensitivity function via

$$f(t) = - \int_0^t g(t') dt' \quad (3.60)$$

Using the previous result from equation (3.47) gives

$$f(t) = \begin{cases} \frac{1}{\Omega_{\text{eff}}} (1 - \cos(\Omega_{\text{eff}} t)) & 0 < t \leq \tau \\ t + \frac{1}{\Omega_{\text{eff}}} - \tau & \tau < t \leq T + \tau \\ T + \frac{1}{\Omega_{\text{eff}}} (1 - \cos(\Omega_{\text{eff}}(t - T))) & T + \tau < t \leq T + 3\tau \\ 2T - t + \frac{1}{\Omega_{\text{eff}}} + 3\tau & T + 3\tau < t \leq 2T + 3\tau \\ \frac{1}{\Omega_{\text{eff}}} (1 - \cos(\Omega_{\text{eff}}(t - 2T))) & 2T + 3\tau < t \leq 2T + 4\tau \\ 0 & \text{otherwise} \end{cases} \quad (3.61)$$

The shape of $f(t)$ is plotted in figure 3.9 for the same $\frac{\pi}{2}$ - π - $\frac{\pi}{2}$ sequence as before. It shows that the influence is proportional to the cloud separation and minimal if the clouds are close together. Equation (3.54) vanishes outside the interferometer times, and so reduces to

$$\delta\phi = \mathbf{k}_{\text{eff}} \cdot \int_{-\infty}^{\infty} f(t) \mathbf{a}(t) dt \quad (3.62)$$

which is the total phase contribution due to mirror vibrations. Knowledge of $\mathbf{a}(t)$ therefore allows the calculation parasitic phase effects and that can be used to correct the output signal. This could be realised with an interferometer along the Raman beam path, using a laser frequency which does not influence the

beam splitter pulses. This will ensure that movement of the mirror is measured with respect to the Raman telescope. Such a system should be particularly helpful for a mobile system, which is the goal of this experiment. Figure 3.8 suggests that high frequency noise is automatically suppressed but low frequencies contribute. Vibrations caused by passing cars, lorries or other man made machinery however are typically in the low frequency region and therefore need to be accounted for. Similar errors can enter if the phase front of the Raman beam is distorted by the windows and if the atom cloud moves within the field, it picks up these changes.

Improved Interferometer Sequences

The main result in equation (3.33) shows that the phase shift is proportional to the local acceleration g , the effective momentum transfer k_{eff} and the separation of the Raman pulses T in quadrature. The latter two parameters define the enclosed area by the interferometer. A larger area produces a higher phase sensitivity for the same local acceleration and therefore a more sensitive measurement. The maximal momentum transfer with Raman pulses is limited to \mathbf{k}_{eff} and a larger beam separation that requires colder atom clouds. Multi-photon Bragg diffractions[25, 58, 81, 83], as mentioned before, as well as accelerated optical lattices[29, 98] are straightforward methods used to increase the enclosed interferometer area.

A different approach can be borrowed from quantum computation where quantum mechanical states are engineered for maximal robustness against external influences. This can be through either choosing the actual state or how the state is prepared. The superposition state, for example, can be reached by a single $\frac{\pi}{2}$ pulse or a sequence of pulses which together have the same effect[12, 42] but use spin-echos[62] to reduce decoherence. Although encoded in the internal state it is not beneficial to keep the atoms in two separate states over the course of the interferometer. External fields couple differently to interferometer arms and therefore create an asymmetric influence. Effectively the sensitivity function discussed above changes and instead of leading to large contributions throughout the complete sequence (compare figure 3.7), they can be reduced to certain areas only. Recently ideas have been brought forward to use squeezing techniques in atom interferometers[50].

Summary

This chapter laid out the basics of atom interferometry. With a well defined Raman pulse, momentum and state transfer are generated, creating the two arms of an interferometer. A second pulse redirects the arms back to overlap and a final pulse closes the arms and maps the phase to internal states of the atom. The

underlying principle is analogous to a light interferometer, any phase difference between the two arms is mapped onto the output signal. Under a constant gravitational field the free propagation contributions in both arms cancel out to exactly zero and only the shifts induced by atom-light interaction remain. The degree of noise and external influence cancellation directly sets the achievable precision. Tuning pulse sequences and monitoring external noises and their influence on the apparatus stretches restrictions on quietness and allows operation in the field.

4 Polarisation Control

The different circular polarisations necessary in a MOT are commonly from linearly polarised beams created with a quarter wave plate ($\lambda/4$). Once aligned, the orientation is hard to change during experimental sequences. This is not a problem for lab-based experiments which can afford one set of telescopes for trapping and separate sets for detection or state manipulation. However, different geometries of magneto optical traps require a different number of beams and for example in pyramidal¹ MOTs the number of components can be reduced if the main telescope is also used for detection, ideally with linearly polarised light. This is particularly advantageous in portable experiments where space, not only for the telescopes but also the additional optical elements necessary to create the extra output, is scarce. Polarisation control during the running experimental sequence not only reduces the number of ports but also allows for compensation of drifts of the polarisation due to external influences. Mechanical rotation of the wave plate could be one solution but the necessary motor is slow, a source of vibration and can lose precision over time. One alternative is the use of *liquid crystal retarders* (LCR); this is a liquid crystal whose birefringence changes dependent on an applied voltage. Such elements require similar or less control electronics than mechanical actuators but the element is not physically moving during adjustment.

Before describing the mechanism of LCRs, polarisation changing processes in wave plates are revised. Section 2.3 gave examples of standing waves produced by overlying different polarised beams (equations (2.38) and (2.41)). Two linear polarisations with perpendicular oscillation directions and fixed phase relation were found to create another linear polarised beam, oscillating at 45 degrees with respect to the constituent beams. If the phase relation of the two perpendicular components changes, the resulting field starts to rotate, leading to elliptically and for the special case of a phase difference of $\frac{\pi}{2}$ to circularly polarised light. In order to engineer the oscillation direction of a beam, one therefore needs to change the phase relation between two perpendicular components. Wave plates are birefringent crystals which have different refractive indices along perpendicular directions. Linear polarised light that is aligned aligned with one of these directions

¹Pyramidal MOTs use a set of four prisms and a mirror to create a beam cross from the collimated beam of a single telescope. The name comes from the shape these components form.

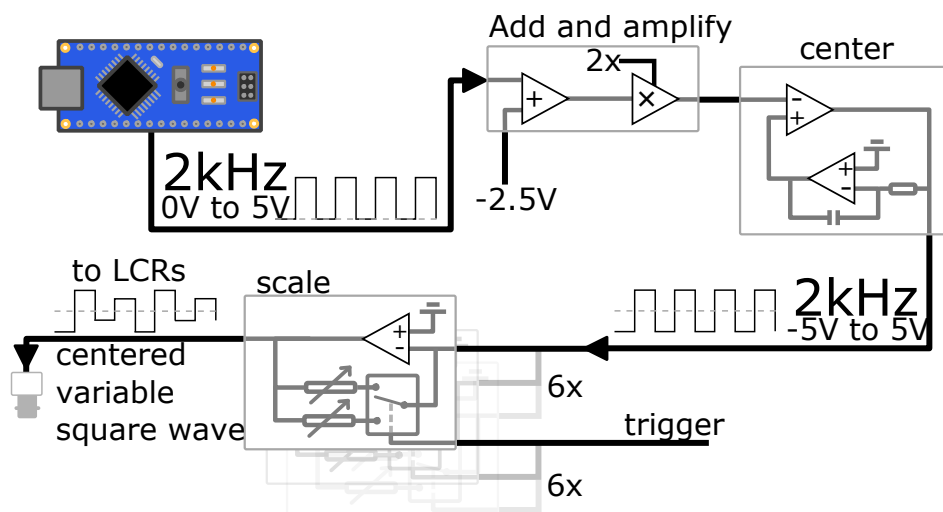


Figure 4.1: Schematic of the driving circuit used to generate a centred square wave of switchable amplitude. An arduino nano with an Atmega 328 micro-controller is used to generate a 2kHz, 50% duty cycle signal, which is then centred with a feedback loop and split to 6 individual amplification circuits for the 6 LCRs. An external trigger changes the amplification of the last stage.

would therefore see no effect. If the field is decomposed in two perpendicular directions and mapped on the two different refractive indices, the length of the crystals sets the retardation of one component relative to the other. A quarter wave plate differs from a half wave plate, if made from the same material, only in the thickness. In contrast a liquid crystal retarder has a base retardance but the relation of refractive indices along the two axes can change by applying a voltage across the capacitance it is stored in. The anode and cathode are coated with ITO (indium tin oxide) which is transparent, but electrically conducting.

4.1 Control Electronics

The crystals used are in a nematic¹ phase. It consists of linear molecules which, depending on their orientation with respect to the incoming light, change the refractive index along said orthogonal axes. Because it is a liquid and the molecules are polar, they will align to the field in the capacitance allowing for control. In the absence of a field, the molecules relax to a random distribution and the refractive index is now set by the thickness. A DC voltage forces the molecules to align along the field lines, however a continuous tuning of the birefringence is desired. To keep the molecules at a defined angle, the electrodes are driven with an AC square shaped voltage, typically at 2kHz. The amplitude sets the orientation relative to the field lines in the capacitance formed and is therefore the control parameter of the crystal.

¹the molecules form strands which build the crystal-like super structure

A standard MOT layout requires up to six retarders which should be independently adjustable. A driving circuit should be able to switch between the MOT configuration and another setting such as one for improved molasses. Figure 4.1 shows a schematic of the developed circuitry. To ensure a precise duty cycle of 50%, an Arduino nano with an Atmega328 micro-controller is used to generate a 2kHz square wave, down-sampled from the 16MHz clock¹, on one of the digital outputs. The required amplitude is $\pm 10V$, so the signal is added to a 2.5V reference and amplified by a factor of two. A feedback loop with an integrator circuit ensures that the output is centred around zero. The signal is split and fed to multiple sub-boards. The sub-boards feature a negative amplification loop with a gain which is changed between two settings through an external trigger. The output of each of the sub-boards is a centred square wave with variable amplitude which can quickly change between two settings. Reaction time is faster than one duty cycle, which is good enough for all applications as the following analysis shows. This design was intended to switch between two pre-defined settings, however it can be easily extended to a more versatile scheme by replacing the switch and two fixed potentiometers with a single digitally controlled potentiometer. This not only allows arbitrary settings, but also active correction during operation. Measurement of the polarisation and a PID loop programmed on the Arduino micro controller could be used to correct for slow polarisation drifts in the optical fibre.

4.2 Polarisation Analysis

Polarisation measurements are based on an idea of Sir George Gabriel Stokes[132] from 1852. He reasoned that it takes four parameters to completely characterise the polarisation of any light beam. These parameters are: components along two orthogonal directions, components along two directions at 45 degrees with respect to the previous ones, circular components and the total light intensity, used for normalisation. For light, this corresponds to linear, horizontal, $\pm 45^\circ$ and σ^+ and σ^- circular polarisations. To measure these parts, one needs to project onto said states and record the relative contributions. A polarising beam splitter does precisely this for linear horizontal and vertical polarisation. The 45 degree states are measured by placing a half wave plate before the cube ($\frac{\lambda}{2}$ -wave plate at 22.5 degrees) that will map +45 on horizontal and -45 on vertical. Circular polarisations are mapped with a quarter wave plate ($\frac{\lambda}{4}$ at 45 degrees). Figure 4.3 a) illustrates these effects on an originally vertically polarised beam.

The complete analysis scheme is shown in figure 4.2. The rotation of the wave plates is manually adjusted

¹The program can be found in the Appendix B

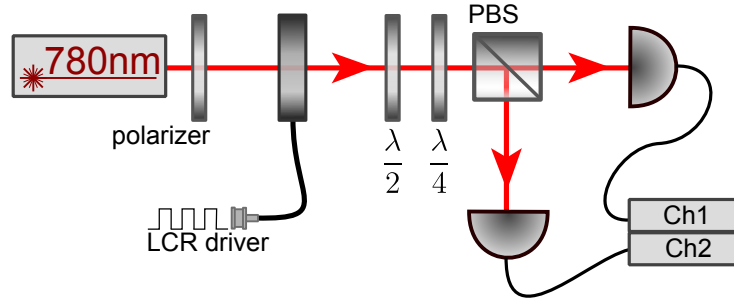


Figure 4.2: Setup to measure the Stokes parameter of an arbitrary polarisation. The half and quarter wave plate map plus minus 45 and left right circular on horizontal and vertical polarisations which are then recorded in the two output channels.

to find the four parameters:

$$S_0 = I(H) + I(V) = I(R) + I(L) = I(+) + I(-)$$

$$S_1 = I(L) - I(R)$$

$$S_2 = I(+) - I(-)$$

$$S_3 = I(H) - I(V)$$

The labels are H : horizontal, V : vertical, L : left circular, R : right circular, $+$: +45 degrees with respect to horizontal and $-$: -45 degree with respect to horizontal. The formalism is easily expanded to quantum objects and used to describe quantum states for two level systems[85, 140, 33]. Normalized with S_0 , the values of S_1 , S_2 and S_3 are associated with the vectors on the *Poincaré sphere* (see figure 4.3). Each pole of the sphere represents a pure polarisation in the three perpendicular bases defined by Stokes. S_0 , the intensity, is equivalent to the length of the vector. Pure polarisations and mixes of them should have a length of exactly one and point to the surface of the sphere. A shorter vector indicates un-polarised light or, if the range also extends to values larger one, measurement errors. Indeed, a projection setup as in figure 4.2 relies on the half- and quarter-wave plate to reliably produce the above mentioned mapping. Manual rotation, non-perpendicular beams to the surface of the wave plates, and differences in the detectors can easily produce uncertainties in the vector position.

Figure 4.3 a) illustrates the effects of quarter- (red) and half-wave plates (blue) rotated by $\beta = 45^\circ$ and $\alpha = 22.5^\circ$ on polarised light. In the drawn example, an originally right circular ($|R\rangle$) polarised beam is altered to $|+\rangle$ (plus 45 degrees with respect to $|H\rangle$) with a $\frac{\lambda}{2}$ plate (blue). The effect of the wave plates is changed by the rotation angle (α or β). The zero position is defined as the position where no change is made

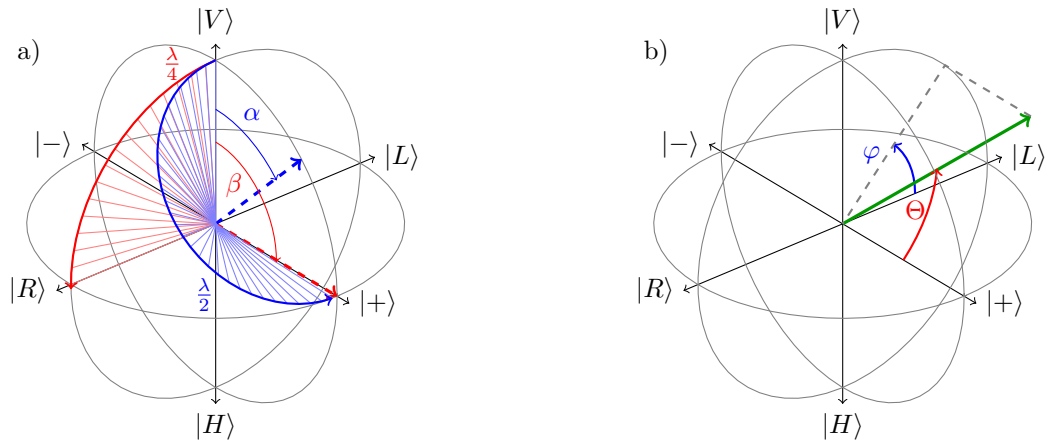


Figure 4.3: a) Effect of $\frac{\lambda}{2}$ and $\frac{\lambda}{4}$ on a state vector on the Bloch sphere. $\frac{\lambda}{2}$ plates rotate the state vector by π around an axis set by the physical rotation of the crystal (α and β); $\frac{\lambda}{4}$ do the same with $\frac{\pi}{2}$. b) Angles used in figure 4.5 to analyse switching speed. The use of spherical coordinates reduces the number of important parameters to 2.

to the incoming beam. The drawn angles α and β are double the physical rotation. A half wave plate will rotate the vector by 180 degrees around this axis, while a quarter-wave plate does the same by 90 degrees. Therefore, a combination of both can reach any point on the Poincaré sphere. In the analysis scheme of figure 4.2 the following angles are used:

	H/V	L/R	+/-
$\frac{\lambda}{2}$	0°	0°	22.5°
$\frac{\lambda}{4}$	0°	45°	0°

Figure 4.3 b) illustrates angles in spherical coordinates used for the further analysis (figure 4.5). The following sections show measurements with the above method which illustrate the change in polarisation a liquid crystal retarder can produce as well, as the temporal performance.

4.3 Accessible Polarisation

As mentioned earlier, the achievable retardance in LCRs depends on their thickness because it is proportional to the path travelled inside the birefringent medium. The LCR¹ has a default phase shift of $4\pi/3$ if no field is applied. Figure 4.4 shows the changing retardance for different applied peak to peak voltages. Subfigure a) plots phase shift versus voltage, where phase shift is defined as the angle between the incoming and shifted polarisation, projected onto the $|H\rangle$ - $|V\rangle$ and $|R\rangle$ - $|L\rangle$ plane. Subfigure b) shows the same data as full vectors

¹Thorlabs LCR-1111-B

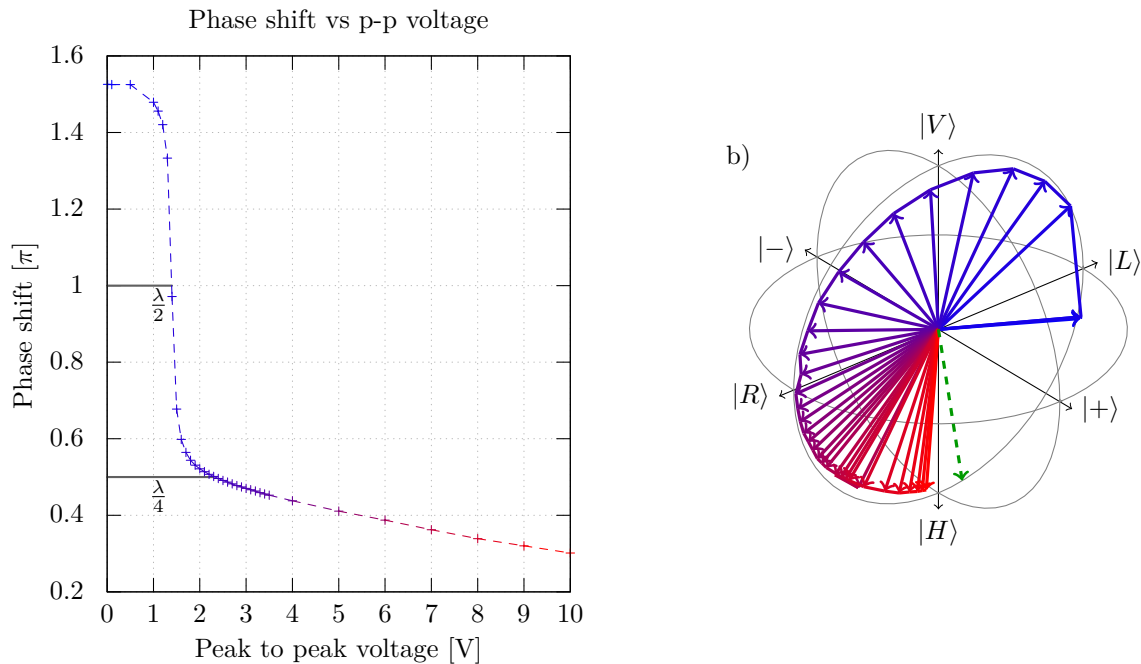


Figure 4.4: a) Change of the polarisation for different peak to peak voltages. b) The same measurement, visualized as the Poincaré Sphere. 0V blue to 10V red. The dashed green polarisation state arrow indicates the input polarisation with no liquid crystal retarder. The retardance in a) is defined as the angle between the green state vector and the vector at the voltage in question. One wave retardance corresponds to an angle of π in radians.

on the Poincaré Sphere, including the incoming polarisation shown in dashed green. Values in 4.4 a) were calculated as the angle between incoming (green) and final polarisation vector (blue to red) in the plane that the two vectors span.

Maximal dynamic range is achieved if the orthogonal axes (fast and slow) of the LCR are aligned at 45° with respect to an incoming, linear polarisation. In the test configuration, a polariser was used to create linear light, matching the horizontal output channel of the polarising beam cube analyser. The LCR was then introduced and rotated until the intensity in the vertical output channel reached a minimum. The measured response of the element to different peak-to-peak voltages is highly non-linear, especially in the desired regime where the polarisation is changed from linear to circular or vice versa. This means that a target phase shift of π requires finer amplitude control than a phase shift of $\pi/4$.

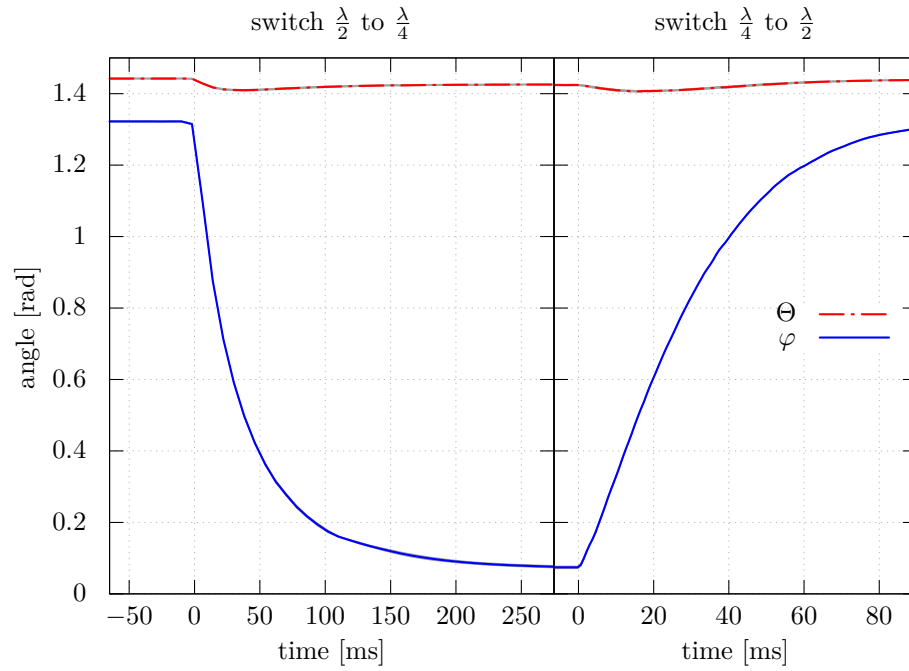


Figure 4.5: Polarisation change from $\frac{\lambda}{2}$ to $\frac{\lambda}{4}$ (left) and back (right). The spherical coordinate angles are defined in figure 4.3 b). Traces were averaged over 20 measurements, the standard deviation is narrow enough that it vanishes in the trace. The time scales for the two switching directions are almost a factor of ten apart.

4.4 Performance

The following section presents the temporal switching performance between the two target states $\frac{\lambda}{2}$ and $\frac{\lambda}{4}$. The same analysis setup as in figure 4.2 were used, traces of the two output channels were recorded in all projection configurations. Figure 4.5 shows the combined traces of 20 switching operations. The two angles φ and Θ are defined as indicated in figure 4.3. Ideally Θ should stay constant at $\frac{\pi}{2}$ and φ vary from 0 to $\frac{\pi}{2}$ (see figure 4.3 b). The most noticeable discrepancy is the reduced range of φ . Figure 4.4 a) shows that the two states of interest lie, with respect to voltage, on the steep slope. This puts high constraints on the alignment precision. Section 4.5 will comment further on other possible error sources while section 4.6 outlines possible solutions.

The underlying process to change retardance is the realignment of the molecules forming the crystal by the new field configuration. This however takes time, dependent on the new field is stronger than the previous and by how much. Relaxation to default state with random orientation is expected to be slow because there is no driving force to accelerate the process. Naturally the switching times between states depend on the time it takes the molecules to react or relax. Switching from $\frac{\lambda}{2}$ ($V_{p-p} = 1.58V$) into the $\frac{\lambda}{4}$ ($V_{p-p} = 2.20V$)

position takes $\approx 200\text{ms}$ whereas the opposite only takes $\approx 80\text{ms}$. The long time-scale switching times are due to the relative low amplitude changes between the two settings. Changing from $0V_{p-p}$ to $15V_{p-p}$ takes 8ms and 0.12ms for the reverse¹. However the cycles are highly reproducible and the variation over 20 cycles is lower than the line thickness in the plots.

4.5 Misalignment Effects

Two main components are important for optimal performance of a liquid crystal retarder: the input polarisation, and the axis of the liquid crystal itself. In the scope of this analysis the alignment of the wave plates in the analyser, the different ranges of the diodes for both channels and background noise are also considered. All measurements were conducted manually; a precision of ± 1 degree can be assumed to reproduce wave plate orientations. This leads to an uncertainty of the same angle on the Poincaré sphere. The different response curves of the diodes for the two channels were accounted for by using the sum of both channels per measurement point as the total intensity (S_0) in the *Stokes parameters* to normalize S_1 , S_2 and S_3 . Background intensities were recorded and subtracted for all traces. The overall error is estimated to be ± 2 degrees on both spherical coordinates.

Misalignment of the axis of the LCR is more severe. Such an effect is shown in figure 4.6 (note that for clarity, the sphere is rotated compared to previous plots). The measurement routine is the same as for figure 4.4. Instead of rotating around the $|+\rangle$ axis, the new pivot point lies somewhere between $|+\rangle$ and $|H\rangle$ (indicated by the dashed green axis). This causes the output polarisation to miss the pole ($|V\rangle$) and only mixed polarisations can be produced. A slight misalignment of this type is also visible in figure 4.4, the trace does miss the pole. Any impurity in the incident polarisation (any $|+\rangle$ and $|-\rangle$ components) has a similar effect and is mapped to the output state.

The highly non-linear relation between applied peak to peak voltage and retardance also causes misalignments in voltage to have significant effects on the output polarisation². Figure 4.7 a) shows the trace between the two states analysed in figure 4.5. Complete vertical polarisation was, despite careful alignment of the voltages, not reached.

¹according to datasheet

²this applies for the analysed configuration where the LCR is used to change between states mimicking a quarter and half wave plate. See section 4.6 for different approaches.

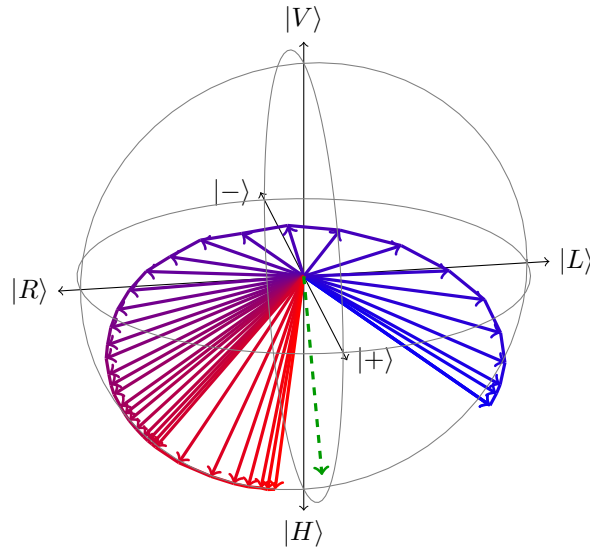


Figure 4.6: Voltage sweep from 0V (blue) to 10V (red) for a misaligned liquid crystal retarder. The misaligned axis with respect to the incoming polarisation causes the polarisation vector to rotate around an undesired axis in the $|P\rangle - |M\rangle$ & $|H\rangle - |V\rangle$ plane (green dashed axis). As indicated in figure 4.3, the position of this axis is determined by the orientation of the fast axis of the crystal. Note the rotated perspective with respect to figure 4.4

Non-perpendicular beams

Wave plates operate by changing the phase velocities of light field components along their fast and slow axes differently. The difference between a zero-order and multi-order wave plates is the thickness, which sets the retardance. The path length in the medium also changes if the light hits the wave plate under an angle. This is especially critical for thicker elements as it scales as $d \sin(\alpha)$, where d is the thickness and α the incident angle. Therefore we expect a change in phase shift for different incident beams. Figure 4.7 b) shows the output polarisation of the two settings ($\lambda/4$ and $\lambda/2$ retardance of the LCR) from above for 0° to 10° (blue to red) input beam angle with respect to the surface of the LCR. Higher angles add significant components in the $|+\rangle$ and $|-\rangle$ polarisations; collimated beams should be used to ensure controlled polarisation changes.

4.6 Possible Improvements

Two main issues need to be addressed: precise control of end polarisation (for example voltage control), and faster switching speed. Both these problems arise from the fact that the voltage difference between the two chosen states is only 0.7V. This is very low when compared to the complete range of 0V to 10V.

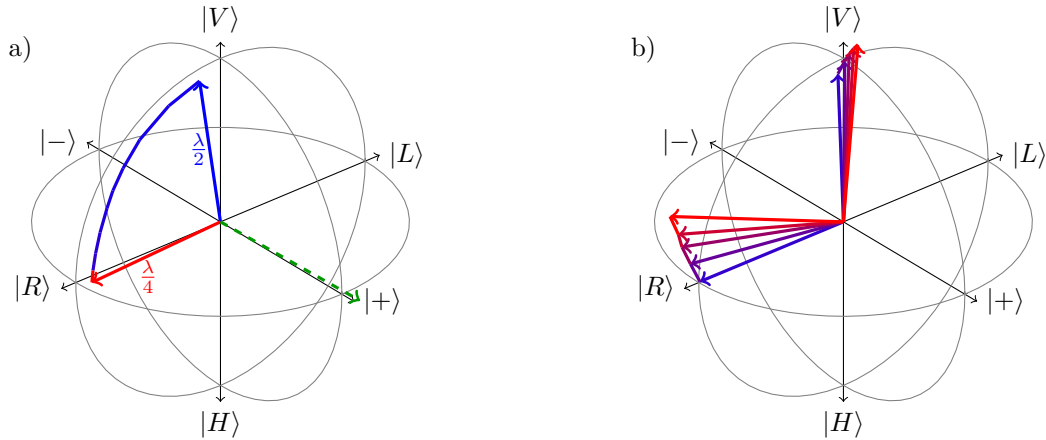


Figure 4.7: a) rotation reference axis extracted from the $\lambda/2$ and $\lambda/4$ position of the LCR. The dashed green axis is perpendicular to both polarisation states and proves that the orientation of the of the LCR element is well aligned. b) Deviation from the measurement in a) for different incident angles starting from 0 to 10 degrees (blue to red) in 2 degrees steps.

Switching speed is improved for larger voltage differences ($\approx 10ms$ and $\approx 0.3ms$ rise and fall time for 10 volts difference).

Taking figure 4.6 as a basis, an incoming polarisation and LCR orientation can be found that for a $\approx 10V$ voltage change the transition $|H\rangle \leftrightarrow |+\rangle$ can be driven. An additional quarter wave plate needs to be introduced in the output beam, to map $|H\rangle \rightarrow |H\rangle$ and $|+\rangle \rightarrow |R\rangle$. Although the retardance range is larger in this case, so is the difference in driving voltage, leading to faster switching. The downside of this is the addition of yet another optical element, the last quarter-wave plate which also needs to be precisely aligned to prevent errors.

As an alternative to this method, the retardance change can be increased. Instead of changing by $\pi/4$, a rotation by $3/4\pi$ could be used. Figure 4.4 shows that the polarisation states $|L\rangle, |V\rangle, |R\rangle$ and $|H\rangle$ are accessible. For the tested region a retardance of 0 is not reached, but could be approached closer by increasing the driving amplitude. The difference to the previously presented and analysed configuration is the additional shift of π which causes the initial polarisation to be reversed, before changing to the target polarisation. The overall speed will be faster, but it is unclear if the path taken on the Poincaré sphere has any influence on the molasses temperature. This testing configuration can be used without any extra optical elements.

Summary

This chapter described the circuit used to drive a liquid crystal retarder and the performance of the device in polarisation and time. Polarisation control seems satisfactory to change the configuration from $\sigma^+-\sigma^-$ to $\text{lin} \perp \text{lin}$ in a magneto optical trap, even when including possible error sources. Switching speed is very slow, 200ms rise and 20ms fall time. A different configuration could be used to improve the reaction time by an estimated order of magnitude. It is not clear if the switching speed does influence molasses temperature. So far the devices have not been tested on a magneto optical trap as other tests had priority on the system.

5 Experiment

The experiment discussed is part of GG^{top}(Gravity Gradient Technology and Opportunity Programme), created to explore underground mapping through gravity (gradient) signals. The apparatus presented in this work is the sensor head which will record gravity signals at first and gradients in the second stage. A map of such measurements allows us to infer the local density distribution and hence localise underground features. The resolution of the created map scales with the density of measurement points and their accuracy, both of which are costly in a field survey due to time constraints. A settling and moving period needs to be taken into account, when looking at the overall time budget. A sensor can be highly accurate and reach this accuracy very quickly, but if the time it takes to reposition the device is long, this advantage is nullified over the entire survey.

This movement time in particular, is the main hurdle for a cold atom based gravity sensor. While the measurement process takes around 200ms and there is no settling time, a considerable amount of support electronics and equipment is needed. This ranges from the vacuum system itself including the vacuum pumps to the lasers and their stabilisation equipment, to the light distribution network. All parts require power and, especially the optical components, thermal and mechanical isolation and protection. Both of these come at the cost of weight.

The task is therefore to design a system which is transportable but at the same time able to reach a prototype stage quickly. For this reason, available technology is chosen over the development of completely new approaches[39]. The vacuum system is therefore constructed with standard CF knife edge connectors and commercially available laser systems are used. The main compromise taken are the light distribution elements which, in order to shrink the optical table filling free space equivalent into a 19" rack compatible unit, consists entirely of spliced fibre based components. The advantage of having a compact system which does not lose coupling into fibres comes at the costs of inflexibility. It is hard to add or remove components once the system is in place or monitor the propagation of light throughout the path. Any error in the network is therefore harder to fix and propagates through the complete system.

5.1 Vacuum System

Magneto-optical trapping and atom interference are only possible if the atom cloud is separated from the surrounding and not destroyed by high background gas pressure. They are therefore placed inside a vacuum chamber at low pressure in the 10^{-10} mBar region. Titanium¹ is chosen for as the vacuum chamber material because it is non magnetic and has a high resistance. The first property reduces any disturbing magnetic fields, while the second suppresses eddy currents when the magnetic coils are switched on or off. Figure 5.1 shows a schematic of the complete system with its components. The centre is a three dimensional magneto optical trap (3D MOT) which prepares atoms for the interferometer. It is loaded from a rectangular two dimensional MOT, acting as a high flux atom source (flux of atoms is indicated by the red arrow towards the 3D MOT). Rubidium atoms are gathered from a reservoir at room temperature, separated by a valve, to close off the flow completely. The atom beam formed in the 2D MOT and exit the chamber through a hole, whose dimension is set by a $\text{\O}5\text{mm}$ carbon tube to absorb any excess rubidium. A small two litre ion pump, followed by a second carbon tube of $\text{\O}10\text{mm}$ in the connection tube to the 3D MOT chamber form a differential pumping stage. This allows high background pressure in the 2D MOT chamber while lower pressure can be maintained in the 3D MOT area for maximal lifetime and minimal loss rate of the trap. The main trapping chamber connects to the main valve on a T-piece which also houses the primary pump, a SAES NEX Torr 100-5, combined ion and non evaporative getter pump. The pump reads 10^{-10}mbar in this region or better, depending if the MOT is running or the pumps had time to clear residual gases completely. The pressure in the 2D MOT is unknown but readings from the pump in the differential pumping stage suggest 10^{-8}mbar order of magnitude.

At the bottom of the main trapping chamber, a 20mm thick window is mounted at an angle to allow access for the *Raman beams*. The thickness of the window ensures that it will undergo minimal deformation when the chamber is under vacuum, while the angle eliminates the risk of a standing wave forming with window at the opposite end of the system. A vertical tube, 0.5 metre in length, above the main trap provides space for long arm interferometers when atoms are launched vertically. Two cubes, one located directly above the main trap, the second at the top of the vertical tube, allow horizontal optical access. They are intended for the extended gradiometer operation where a second, identical, experiment would be placed next the first and Raman beams in the horizontal plane are used to measure the gravity gradient components perpendicular to the tube orientation.

¹this does not apply for the pumps and valves, as well as for the t-piece they are attached to

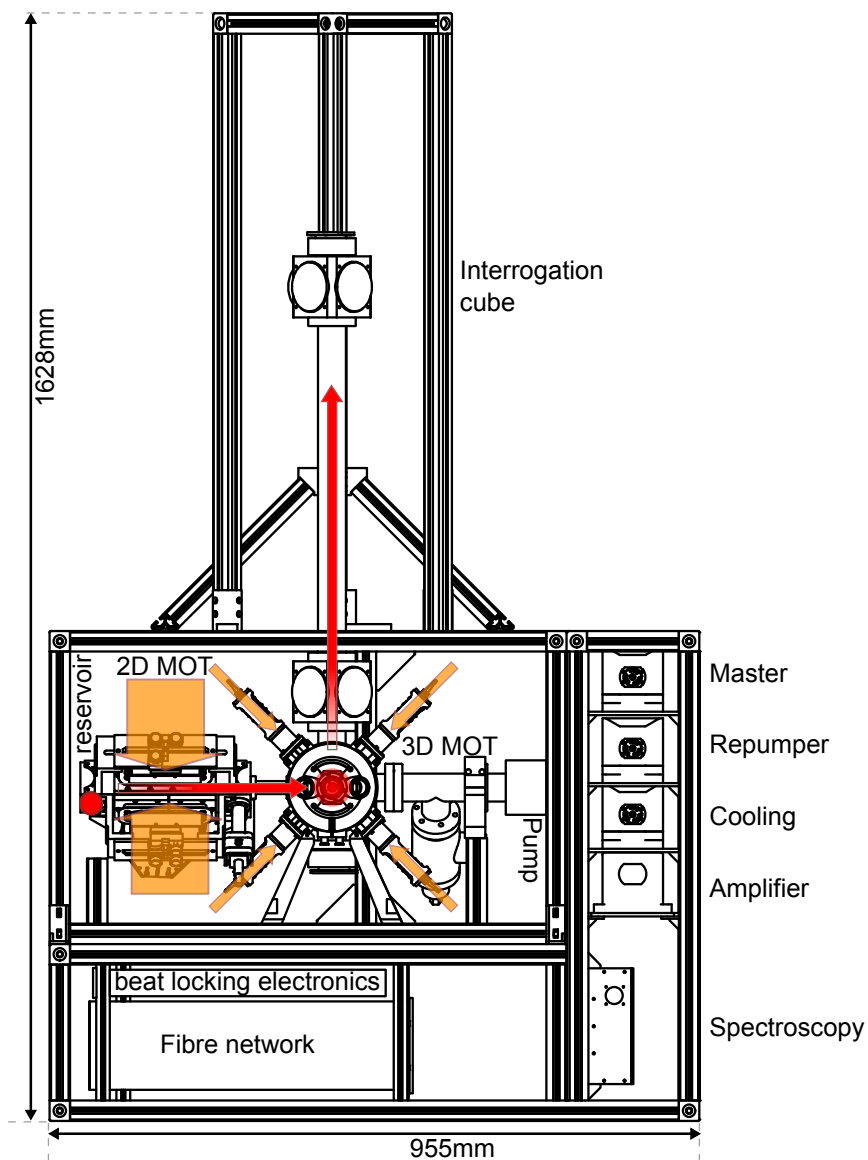


Figure 5.1: Schematic of the vacuum and laser system components. The path of the atoms is indicated by red arrows, laser beams are drawn in orange. Atoms from a Rubidium reservoir at the back of the rectangular 2D MOT chamber are pushed into the 3D MOT chamber, where they are cooled in all primary directions. A frequency shift of the upper and lower trapping beams pushes the atoms on a vertical trajectory into the interferometer tube.

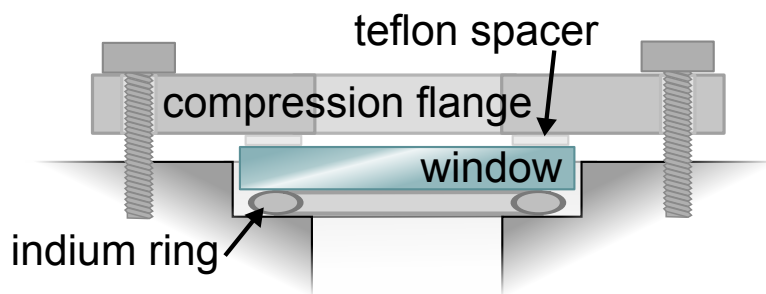


Figure 5.2: Indium sealing. The window is set on a ring of indium and pressed onto through a compression flange. To prevent damage to the window through the metallic body of the flange, a Teflon spacer is added. The torque on the screws pushing the compression flanges is around 1 to 1.5Nm. This compresses the indium to a thin layer.

5.1.1 Vacuum Techniques

Connections of the individual chamber parts (2D MOT, pumps, 3D MOT, tube,...) are fitted with CF type knife edges and copper gaskets. All windows are attached with *indium seals*. A ring of the soft metal is used as a seal between window and titanium chamber (see figure 5.2). The window is then pressed against the chamber with a *compression flange* with typical torques of 1Nm to 1.5Nm. To prevent damage to the window during this process, it is separated from the aluminium parts by a Teflon spacer.

Prior to assembly, all metal parts were cleaned by a three stage cleaning process in an ultrasonic bath with Acetone, Isopropanol and Helmanex. This removes any residuals of grease and oil left from the manufacturing process. The forming water layer and other contaminants were removed when the system was baked for five days at 120 °C with an attached to a turbo molecular pump. The temperature is limited by the melting point of the indium (156 °C) used in the window seals. Parts that can take higher temperatures, such as the all metal valves, t-pieces and the tube, were pre-baked at 250 °C to clear any potential contamination. The non-evaporative getter element and ion pumps were activated after the completion of the baking cycle. At this stage the pressure is low enough that the elements are not immediately saturated by residual gases.

5.1.2 System Mounting

The vacuum system is suspended in an aluminium frame (see figure 5.1) of the dimensions H: 162.8cm x W: 95.5cm x D: 45.9cm and a total weight of approx 60kg. This package also includes the laser systems, spectroscopy and offset electronics as well as the fibre network to distribute the light. The control and command electronics are located in the rack unit. This ensures that all optical connections are within the frame while electrical connections, which are typically more robust against external influences, join elements

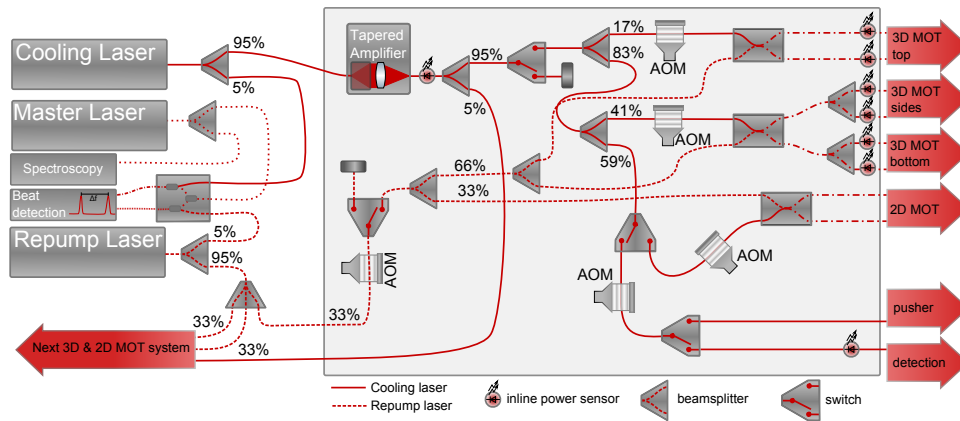


Figure 5.3: Fibre and laser network. Light from a master laser unit, stabilised to a Rubidium spectroscopy is mixed with light from the cooler and repumper laser. Both are stabilised to this reference. A fibre network distributes the light to 6 outputs for the 3D MOT where two ports can use an AOM to shift the output frequency and amplitude. AOMs and mechanical switches are used to mix light and control individual outputs.

with the control electronics in a rack unit next to the experiment. In a later state of the project, the frame is intended to be mounted on an autonomous vehicle to aid automated surveys.

5.2 Laser System

Light for the atom trap is provided by three New Focus TLB-6913 VortexTM II Tunable Lasers¹ mounted next to the vacuum chamber. The power output into the fibre network is 20mW per unit. One laser acts as a master laser and is referenced to a rubidium spectroscopy cell (see section 5.2.2) while the other two are stabilised to a defined offset to said master laser (see section 5.2.2). One unit acts as the repump laser and is directly fed into the fibre network, which distributes the light into the trap outputs. The second one is stabilised to the cooling transition and amplified with a New Focus TA-7613-P VAMPTM Tapered Semiconductor Amplifier to 500mW before being fed into the fibre system and consequently distributed to the output ports.

Figure 5.3 shows a schematic of the distribution system (a picture can be found in figure E.1 in E). All of the fibres are polarisation maintaining with a PANDA (**P**olarisation-maintaining **and** **A**bsorption reducing fibres) core, which should maintain linear polarisation on two axes better than 20dB over the length of the network. Fibre splitters are Evanescent Optics polarisation maintaining fibre splitters with various ratios and mechanical switches from LEONI. Acusto-optical modulators (AOMs) are Gooch & Housego Fibre-Q

¹Master, repump and cooling laser

modulators for 780nm with a frequency upshift of 80MHz¹. The combination of an AOM and fibre switch is used for fast and complete extinction of the light. Both of these components are necessary, because the extinction of the AOMs is not sufficient for reliable state preparation, where the smallest amounts of resonant light are enough to move population into unwanted states. The fibre network was connected by splicing the individual parts together and to eliminate the risk of misalignment. The efficiency of the individual components as well as the usable light power at the end of the network, depends on the quality and alignment of the polarisation at the first element. Despite the use of polarisation maintaining fibres, imperfections in the splices and initial light coupling cause errors to build up in the system (see 6.7).

To stabilise the light to the necessary laser frequencies, a portion of the master laser's power is fed into a spectroscopy and referenced to a rubidium 85 transition (see 5.2.2). Small fractions of the cooler and repumper light are mixed with the other part of the master light to create two beat signals which allow stabilisation to a defined offset (see 5.2.2). Cooling light is divided into six outputs for the three dimensional MOT and two for the two dimensional MOT. Each 3D MOT beam has an output power of $\approx 15\text{mW}$, while each 2D MOT beam reaches $\approx 60\text{mW}$. Light for the 2D MOT can be diverted into an extra output as a detection beam. Cooler light for the two output ports for the 3D MOT beam labelled as 'top' passes through a separate AOM than the light for the other four to allow small frequency detuning between the upper and lower trapping beam. A shift in frequency between these sets of beams creates a moving frame which launches the atoms vertically from the trap (see section 6.4) and prepares for atom interferometry.

The laser system but also the previously discussed vacuum system was designed for an extension to measure multiple components of the gravity gradient tensor. The vertical gradient is easily available along the vertical tube and the vertical directions were planned to be realised with a second, identical setup. The interrogation cubes are oriented in such a way that they could point to an identical apparatus and a horizontal Raman beam could probe two clouds simultaneously. The fibre system features an output 'next 3D & 2D MOT system' which has two repumper outputs and a cooling light output with enough power to seed an extra tapered amplifier of the same make as the one used in the presented network. Therefore a single locking scheme could stabilise up to three identical experiments with access to more than one gradient direction.

Telescopes

Telescopes are designed to create a collimated beam with the correct polarisation for the two and three-dimensional MOT (see figure 5.4). Sub-figures a) and b) show perpendicular cuts through the telescopes for

¹The transmission efficiency is 50%

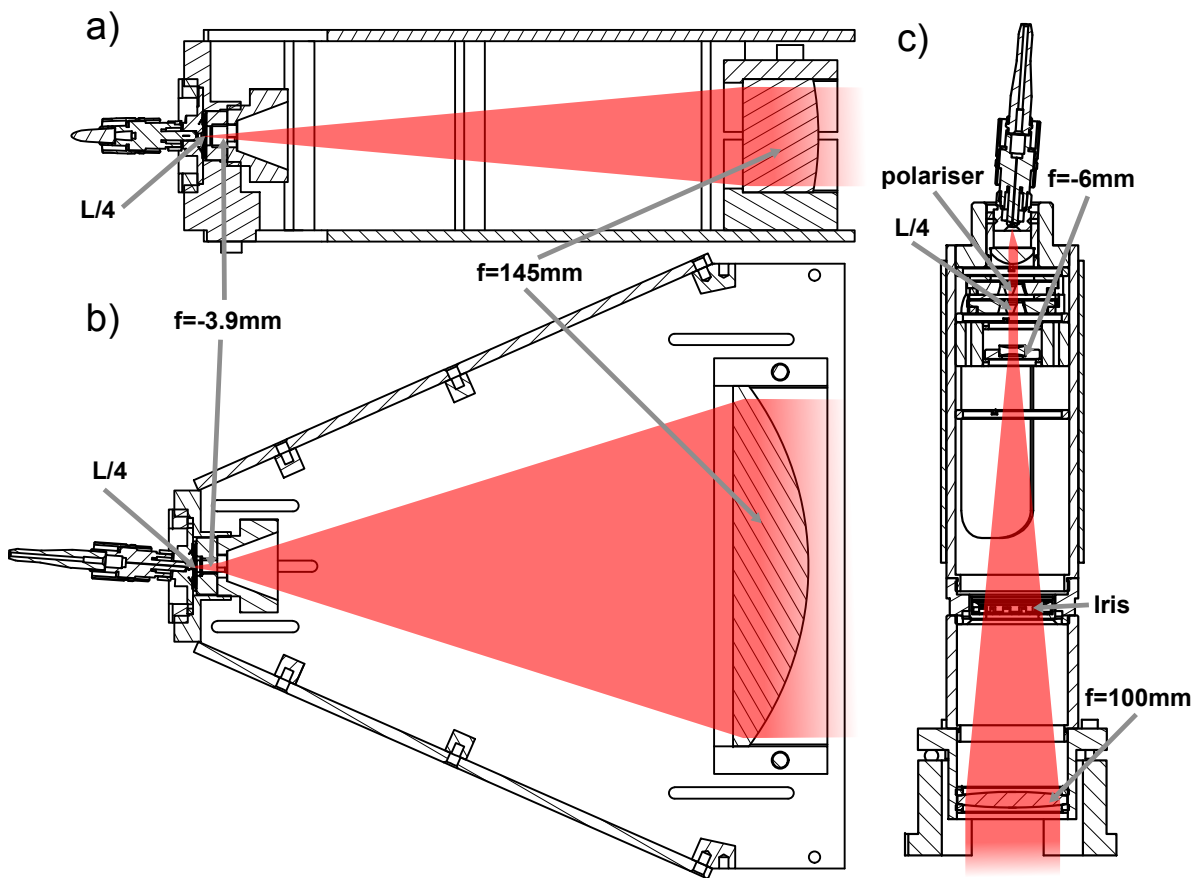


Figure 5.4: Telescopes used in the two (subfigure **a** and **b**) and three dimensional MOT (subfigure **c**). Both designs use as few optical components as possible and are directly attached to the vacuum chamber. a) and b) are perpendicular cuts. A cylindrical lens with a focal length of $f = -3.9\text{mm}$ expands the light coming from the bare end in a single direction and a common lens with $f = 145\text{mm}$ ensures collimation along both axes. c) uses a fibre collimator and expanding lens to ensure minimal polarisation errors by the wave plate. The telescope is mounted on rubber balls, allowing small tilt alignments.

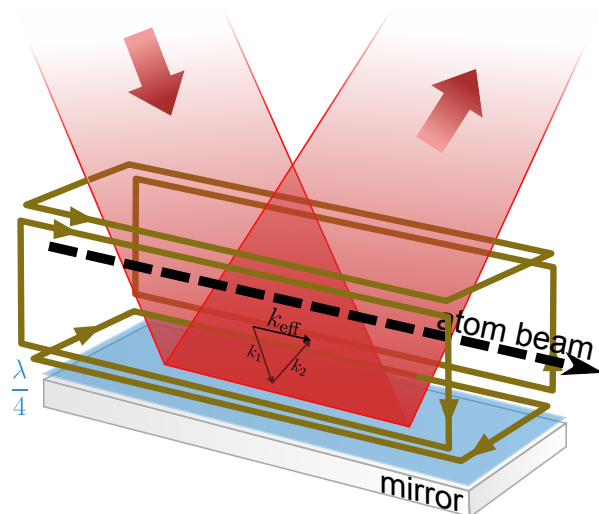


Figure 5.5: Magnetic coils and optical components of the two dimensional trap used as an atom source. Two pairs of rectangular coils create a field of zero amplitude along the primary axis and a linear gradient perpendicular to the same. Elliptical beams at an angle (only one pair shown, the second one is perpendicular) cool and create a pushing force along the symmetry axis (dashed arrow, see addition of k_1 and k_2).

the two dimensional MOT. Light from an angled fibre connector is passed through a half wave plate and expanded along one axis with a cylindrical lens (see b)). The perpendicular direction is not affected and the beam expands freely before being collimated in both directions. The collimating element is the central part of a spherical lens with a focal length of 145mm. The output light beam has an aspect ratio of 1:3 and is circularly polarised. The complete assembly attaches directly to the vacuum chamber and allows for a tilt of up to 10 degrees to create a pushing force (see section 5.2.1).

Figure 5.4 c) shows a cut of the geometry used in the telescopes of the 3D MOT. Light from a fibre collimator passes through a polariser and quarter-wave plate before being expanded by an $f=-6\text{mm}$ lens. The final $f=100\text{mm}$ lens collimates the beam at the maximal diameter of 2.54mm. An iris can be used to align opposing telescopes on the main chamber. The assembly is resting on six rubber balls and fixed by three socket and three set screws. Compression of the rubber balls allows steering while the set screws fix the telescopes in place. This approach ensures minimal misalignment if the complete setup is moved and subject to vibrations. The polariser, as the first element after the fibre collimator, ensures constant output polarisation but polarisation drifts due to birefringence changes in the fibres cause power fluctuations in the telescope.

5.2.1 2D MOT Geometry

The two dimensional MOT based atom source was designed to be compact and high flux using the same approach as in [76]. The vacuum body is an elongated rectangle with four windows and four rectangular coils. Figure 5.5 shows a sketch of the coil geometry and one pair of beams, $\frac{\lambda}{4}$ and mirror assembly. The four coils produce a field of zero amplitude in the centre (dashed line) and a linearly increasing gradient along all perpendicular directions. The magneto-optical trapping mechanisms are therefore active only along two perpendicular directions but not along the third. Commonly, an additional pushing beam is used to force atoms into the main chamber. To save this component, the main cooling beams are injected under an angle (around 5 degrees). Section 2.1 argued that counter propagating light beams create a damping force on the atoms. If this balance is broken by introducing an angle between the beams, the summed up forces will point in the direction of the sum of wave vectors. For the case of the geometry in figure 5.5 a pushing force is created along the centre line indicated by the dashed arrow that will create a flux of atoms out of the trap. Not using a pushing beam saves the effort of creating a third frequency, next to cooling and repumping light, which lies between cooling and detection and would require an additional acousto-optical modulator with the necessary driving electronics.

5.2.2 Laser Frequency Stabilisation

To capture rubidium 87, the cooling light needs to be stabilised to the main cooling transition (connecting the $F = 2$ and $F' = 3$ levels, see figure 2.7), while the repump laser connects the $F = 1$ and $F' = 2$ levels. Additionally cooling light is red detuned by $\approx 15\text{MHz}$ for best Doppler cooling performance. If, as in this setup, a single light source is used for cooling and detection, the emission frequency needs to be controllable during experimental sequences. Figure 5.7 shows a wider scan produced by the *modulation transfer spectroscopy* discussed later. The necessary repumper transition is located $\approx 1\text{GHz}$ on the right of the $Rb^{85}F = 1$ transition with roughly half the amplitude. Direct stabilisation to this transition is more difficult because the signal size is smaller than the one of other transitions. Stabilising the cooler laser to the required rubidium 87 $F = 2$ transition is straightforward, however moving the frequency freely around the point requires additional effort. For this reason, a double offset lock scheme is employed. The master laser is referenced to a transition of the rubidium 85 isotope located between the transitions of interest while the other two can have a variable offset to this transition.

The New Focus TLB-6913 VortexTM II Lasers used for the master, cooling and repump frequencies are extended cavity diode lasers (ECDLs). Light produced by a laser diode[145] is passed through a cavity that

is formed with the diode on one side and a grating controlled by a piezo actuator on the other side. The cavity narrows the emitted linewidth¹ and the grating allows fine control of the emitted frequency through its tilt. Frequency drifts originate from thermal fluctuations, which change the resonance conditions in the cavity, as well as processes in the diode such as changes in resistance when the element heats up or cools down. Each laser unit is controlled through a Newport LB1005 Servo Controller which contains a PID (proportional-integral-derivative) feedback loop. The piezo position is adjusted until the *error signal* reaches the desired reference level. This is done with a high repetition and effectively stabilises the laser frequency to the required value. For absolute frequency stabilisation, a modulation transfer spectroscopy references the master laser to a transition in a rubidium sample while cooling and repump lasers have a defined offset created by a side-of-filter locking scheme.

Modulation Transfer Spectroscopy

The most reliable method for creating an absolute frequency reference of an atomic transition is to probe the transition itself in a separate test sample. In case that samples with the desired frequency are not available, or hard to produce, a stable cavity offers a good alternative[64, 134]. To record an absorption spectrum, a laser beam is passed through a vapour cell and its intensity measured on a photo diode. While scanning the frequency of the laser, absorption of the light increases as the resonance is crossed and the transmission decreases. A thermal sample has a wide velocity distribution and hence a Doppler broadened decrease in transmission is observed. The fine structure² is completely covered by the broadened signal³. To remove this shadowing, Doppler free methods are used[144]. A counter propagating pump beam will promote atoms to the excited level; because they are already excited, the intensity of the probe beam is not reduced for atoms whose Doppler shift is cancelling relative to the frequency of the counter-propagating light. The hyperfine transitions appear within the Doppler broadened absorption dip. To completely eliminate Doppler based influence and maximize the slope of the error signal, *modulation transfer spectroscopy* is used[126, 84].

Figure 5.6 shows the optical components and basic electronic elements of a *modulation transfer spectroscopy*. Light is split on a polarising beam splitter (PBS) in equal intensities. The transmitted part passes through a glass cell containing rubidium vapour and is monitored on a diode. The reflected part is phase modulated with an *electro-optical modulator* (EOM) and injected into the cell in the opposite direction. The counter propagating beams ensure Doppler free hyperfine resolution. *Modulation transfer spectroscopy* uses

¹specified to $\leq 300\text{kHz}$ compared to several MHz on lasers without the cavity

²Transitions between the F states

³See e.g. the DAVL signal in figure 5.7, which in contrast to the spectroscopy signal is not Doppler free

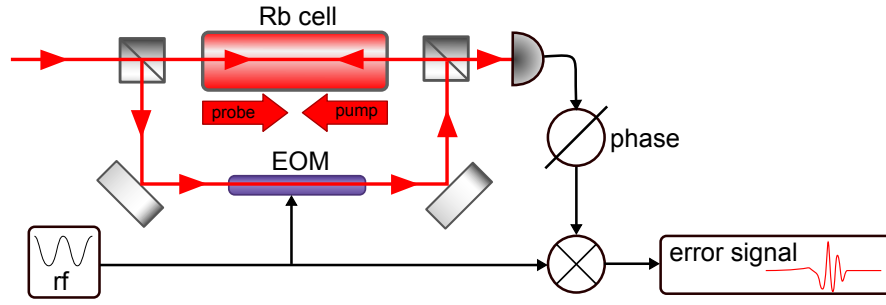


Figure 5.6: Modulation Transfer Spectroscopy. The phase modulated pump beam (lower beam through the EOM), overlaps in the Rubidium cell with the counter-propagating probe beam. If the Doppler free resonance condition is met, excitation is transferred from the pump to the probe beam, creating a beat signal which is detected on the photo diode. Demodulating with the EOM driving frequency extracts the error signal.

a four-wave mixing process in which the transmitted beam is referred to as the *probe beam* and the reflected, phase modulated, as the *pump beam*. The field of the phase modulated pump beam can be written as

$$E = E_0 \sin(\omega_c t + \delta \sin(\omega_m t)) \quad (5.1)$$

with the modulation index δ (typically $\delta < 1$, which means only a single sideband on each side is generated) and the modulation frequency ω_m . The overlapping beams in the vapour cell stimulate the four-wave mixing processes which causes light of the pump beam, travelling away from the diode, to be emitted into the field of the probe beam, which is monitored on the diode[15]. Both fields create a beat signal on the diode of the form[84]

$$S(\omega_m) = \frac{C}{\sqrt{\Gamma^2 + \omega_m^2}} J_0(\delta) J_1(\delta) \left[\left(L_{-1} - L_{-\frac{1}{2}} + L_{\frac{1}{2}} - L \right) \cos(\omega_m t + \phi) \right. \\ \left. + \left(D_1 - D_{\frac{1}{2}} - D_{-\frac{1}{2}} + D_{-1} \right) \sin(\omega_m t + \phi) \right] \quad (5.2)$$

with the *Bessel functions* $J_n(x)$ and

$$L_n = \frac{\Gamma^2}{\Gamma^2 + (\Delta - n\omega_m)^2} \quad D_n = \frac{\Gamma(\Delta - n\omega_m)}{\Gamma^2 + (\Delta - n\omega_m)^2}. \quad (5.3)$$

This process has a very narrow acceptance window for atoms that do not experience a Doppler shift in respect to the beams. The DC component on the diode is a normal Doppler free absorption type signal. However, the AC signal in equation (5.2) is the one of interest. The additional sin and cos terms require demodulation at the driving frequency of the EOM but once done so, the resulting signal is virtually Doppler free, narrow

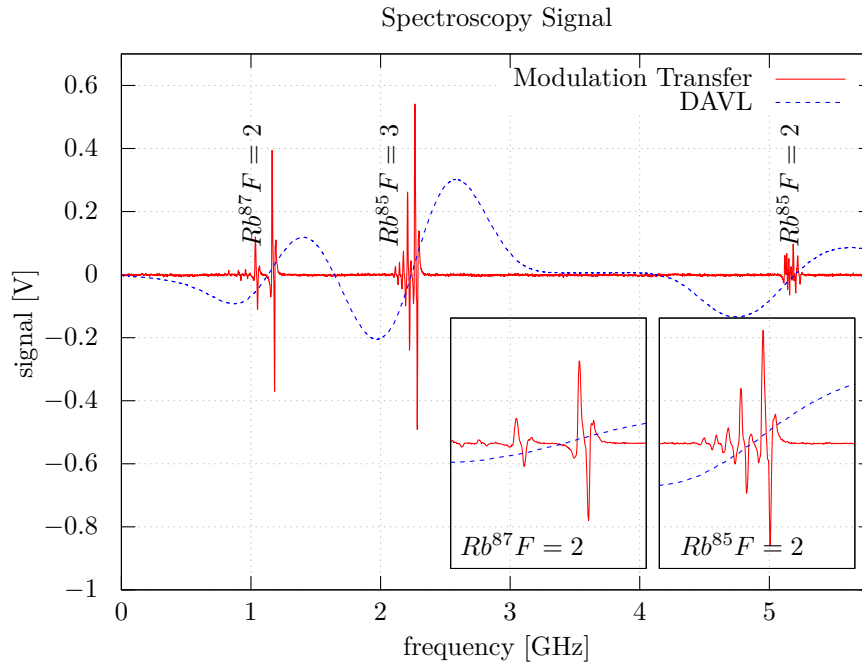


Figure 5.7: Spectroscopy signal of a Rubidium vapour cell. Visible are 1 transition of Rubidium 87 and two of Rubidium 85. The cut off *Repump transition* is located around 5.2 GHz to the right of the $Rb^{85}F = 2$ transition. The red plot is taken from the used *Modulation Transfer Spectroscopy* which produces a Doppler free signal that is able to resolve the hyperfine structure. For comparison the signal of a *Dichroic Atomic Vapour Lock (DAVL)*, in a non Doppler free version. The Doppler broadening shadows any hyperfine structure.

and steep (see figure 5.7). Additionally there is no background signal and only a single zero crossing if the resonance condition is met. This makes the technique ideal for precise stabilisation to a vapour reference. The only possible downside is the mentioned narrow acceptance range. If a significant external influence causes the lock to lose its reference, it is more likely to find a stable position at the neighbouring peak rather than the original one. *Dichroic atomic vapour lock (DAVL)* error signals in comparison are broad over hundreds of MHz, so the lock will easily recover to roughly the same position. However, in the DAVL setup the exact position is not only relaxed by the slope of the signal but can also be shifted by polarization changes and external magnetic fields. Both influences are very likely in a noisy environment such as the ones a mobile experiment will encounter.

Figure 5.7 shows the error signal created by a *Dichroic Atomic Vapour Lock (DAVL)*[90] in a non Doppler free configuration and a modulation transfer spectroscopy cell as discussed above(see figure 5.6). Both signals were created simultaneously with light from the same scanning laser. The dashed blue trace is the output of the DAVL setup. No hyperfine transitions are resolvable, and the D2 line of rubidium 87 and Rubidium 85 are Doppler broadened. The red trace is from the *modulation transfer spectroscopy* which stabilises the

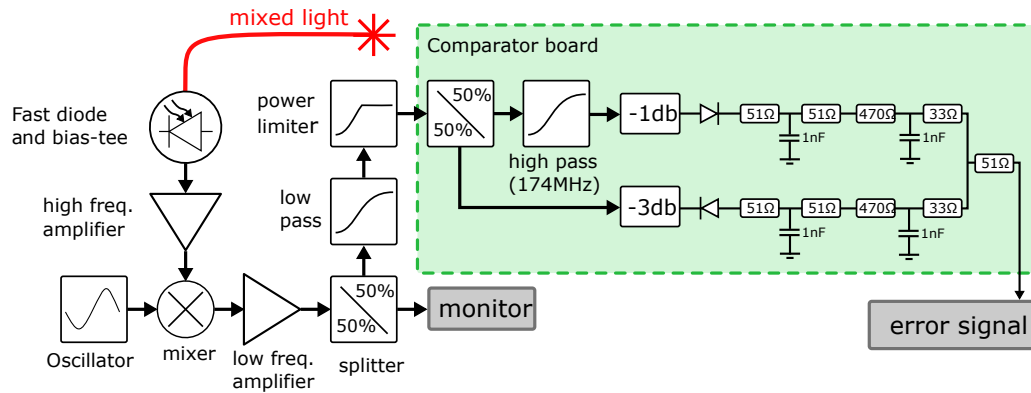


Figure 5.8: Schematic of the offset lock circuitry. The beat node is recorded on a reverse biased fast photo diode. After mixing with an almost equal frequency, the difference is amplified further and fed into a comparison circuit[115] which produces an DC error type signal if the input frequency is below or above the edge of the band-pass filter.

Master laser of the experiment. The scan does not include the $F = 1$ transition of rubidium 87 to which the repumper laser needs to be stabilised, it is located to the right of the plot, $\approx 6.7\text{GHz}$ away from the rubidium 87 $F = 2$ transition.

Offset Locks

With the master laser emitting on the rubidium 85 $F = 2$ transition, the cooling laser needs to be 5.5GHz away and the repump laser 1.2GHz respectively. The error signal generating circuit for the *side of filter technique*[115] is sketched in figure 5.8. Light from the fixed master laser and the laser to stabilise is mixed to create a beat signal on a reverse biased fast photo-diode. The frequency of a local oscillator is subtracted and the result passed to a comparison circuit (green background). The use of low frequency amplifiers after the mixing and a low pass filter ensures that only the difference $\omega = \omega_{\text{beat}} - \omega_{\text{osc}}$ of frequencies arrives at the electronic circuit which was taken from [115]. The incoming signal is split with a power splitter, one arm is passed through a high pass filter, both arms are then attenuated to account for the effect of the filter and subsequently injected into a comparison circuit. For the case of an input frequency that is above the cut-off of the filter, there is equal power on both paths after the attenuators. The comparison circuit therefore outputs around 0V as the difference of the two paths. As the incident frequency moves into a range which is attenuated by the band-pass filter, the power in the two arms is no longer equal, leading to a negative output voltage. Figure 5.9 shows the response for different input frequencies and powers. As expected, a slope connects an area of negative voltage (input lower than $\approx 174\text{MHz}$, the cut-off of the filter) and around 0V when both arms contain the same amount of power. The ideal *lock point*, the point the PID-control stabilises

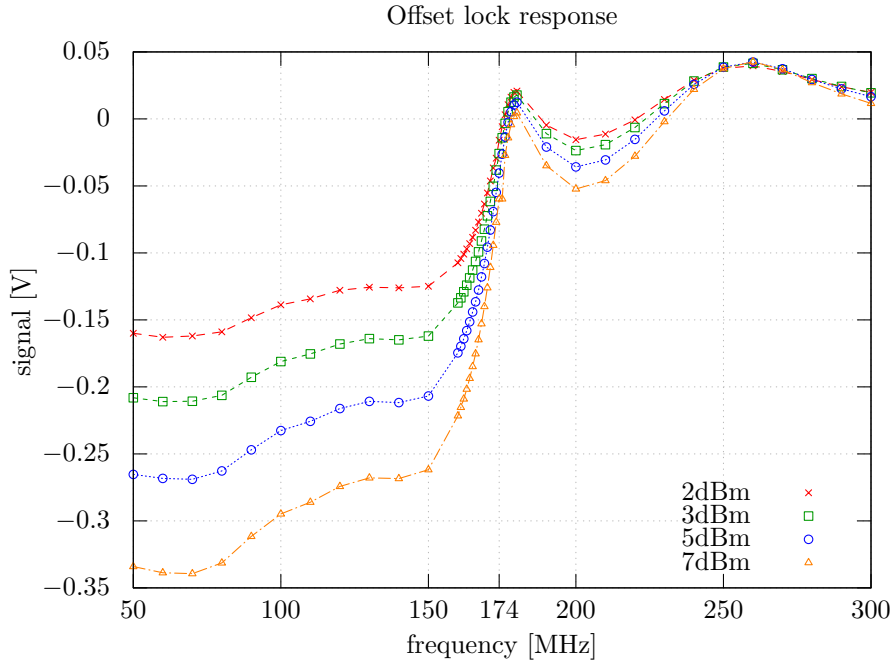


Figure 5.9: Response of the offset comparison board to different input frequencies and input powers

to, is at the steepest slope that is around 174MHz. Therefore with the matching mixed in frequency, a laser can be stabilised to a difference of

$$\omega_{\text{stabilised}} = \omega_{\text{mix}} \pm 174\text{MHz} + 80\text{MHz} \quad (5.4)$$

with respect to the master laser. The \pm enters because the error signal is symmetric around 0MHz and the additional 80MHz are created by the AOMs in the fibre system. Figure 5.10 shows traces of the spectroscopy signal in a) and the signals produced by the filter in b) and c). The signal in c), created by beating the repumper and master laser together, has the same shape as the response measured in figure 5.9. It is mirrored around 0MHz because only absolute frequencies are measured. The signal is inverted to allow locking to a negative slope. b) shows a trace of the cooler laser, mixed with two additional frequencies. The larger one at $\approx 1\text{GHz}$ stays fixed, while the second frequency, 80MHz in the shown trace, is created by a direct digital synthesizer (DDS)¹ which is capable of fast and programmable frequency changes. This allows controlled frequency shifts of the cooling light to, for example change the frequency from a typical MOT situation, where the light is $\approx 2.5\Gamma$ detuned to begin on resonance for detection.

Changing the mixed in frequency does not immediately affect the locking point. The error signal is

¹Novatec 409B

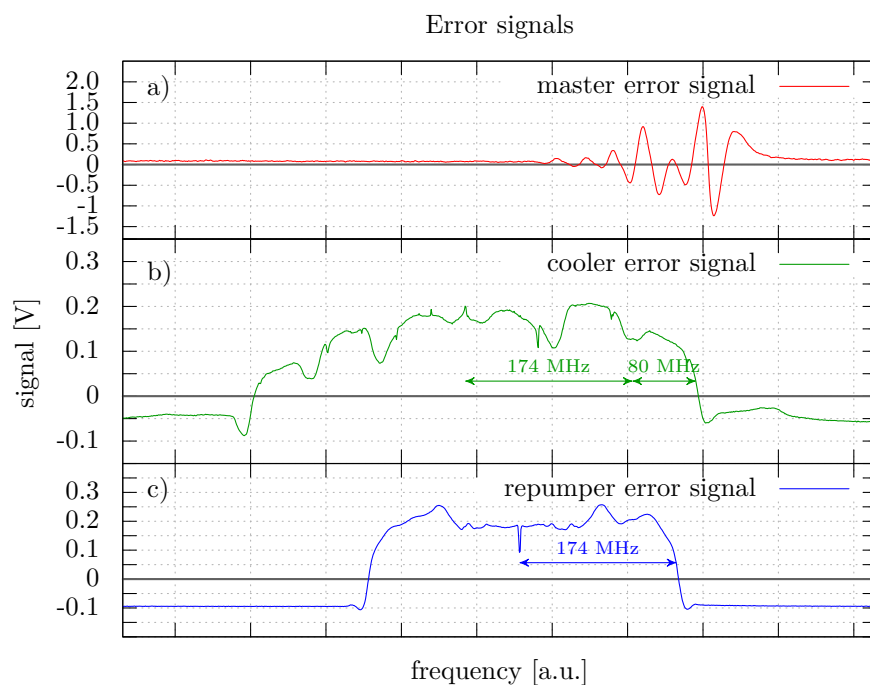


Figure 5.10: Error signals as seen by the PID controller. a) from the modulation transfer spectroscopy cell, zoomed to the $Rb^{85}F = 3$ transition. b) Cooler laser beating with the master laser and an additional, tunable 80MHz frequency mix in. c) Repump laser mixed with the master laser. Note that the y-axis is shared whereas the x scaling changes. Scanning is realized by applying a triangular voltage modulation to the master laser only. b) and c) are inverted with respect to figure 5.9

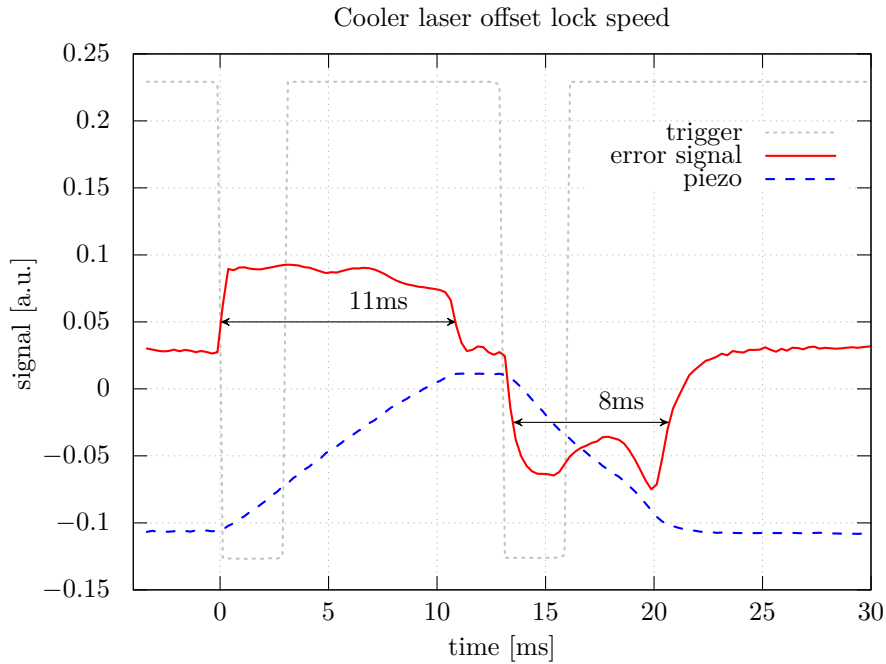


Figure 5.11: Error signal from the offset lock electronics and voltage of the PID box to the piezo controller when 80MHz are added and subtracted to the offset mix in circuit. Because the lock point is not central in the slope, the response is asymmetric if 80MHz are added or subtracted.

displaced immediately but the time it takes the locking circuit to move to the new position depends on the parameters of the PID control loop. Figure 5.11 shows a response to a frequency change of 80MHz. Shown as dashed grey lines are the trigger signals sent to the DDS which initiate the frequency change on a falling edge. Shown in red is the error signal generated by the circuitry, in this plot it is stabilised to a signal of $\approx 0.025\text{V}$, not zero, through an artificially added offset to fine tune the locking point. As expected, the error signal is moved to a positive or negative offset once the mixed in frequency is changed. The blue trace shows the voltage that is sent to the piezo to modify the emission frequency. While close to the ideal level, this voltage is stable. If the error signal is displaced the PID circuit starts to move the laser frequency to reach the designated lock point again. Due to the asymmetry of the flank (see figure 5.10) the response time for adding 80MHz (first step: 11ms) and subtracting 80MHz (second step: 8ms) is also asymmetric.

Lock Stability

Long term stability of the lasers was measured with a HighFinesse WS02 wavelength meter. The device measures the frequency of incident light through a high precision cavity. Drifts of the cavity are therefore mapped onto the measurements. Figure C.2 shows the recorded trace of the master laser over 3.5 hours. The

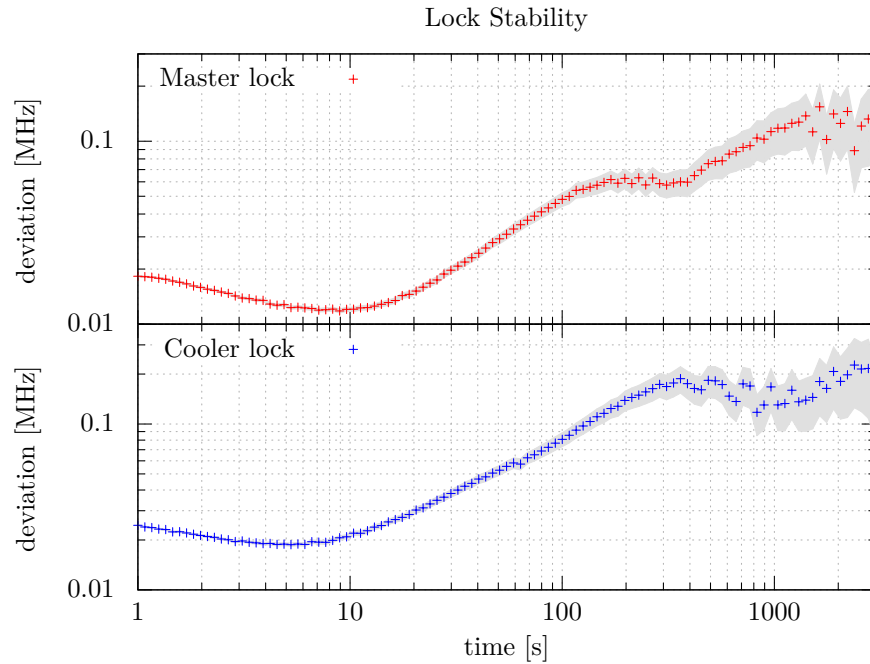


Figure 5.12: Allan deviation of locked master and cooler laser. The long term drift originates from reference cavity, rather than, lock instabilities.

signal features a linear drift, followed by a plateau. The linear component of the drift was corrected for as it is assumed to originate from the measurement cavity rather than the laser.

Figure 5.12 shows the Allan deviation of the stabilised master and offset stabilised cooler laser. The higher deviation values for longer time samples can be explained by the drifting cavity which can have a more complex behaviour than just a linear drift. For a typical operation time, stability of the master lock can be assumed to be 15kHz or better. The trace of the cooler follows the master, but the additional locking stage adds uncertainty and leaves the lock stable to 20kHz within 10s. The assumption that long term drifts in figure 5.12 originate from the cavity rather than the laser are supported by the daily performance of the experiment: the trap is optimized by adjusting the frequency setting of cooler and repumper. Specifically the cooler has an acceptance width of less than 1MHz. During the day, the locking points do not need to be readjusted so it can safely be assumed to be stable to at least this order of magnitude. Optimal positions do not drift over time which also supports the assumption of cavity dominated drift.

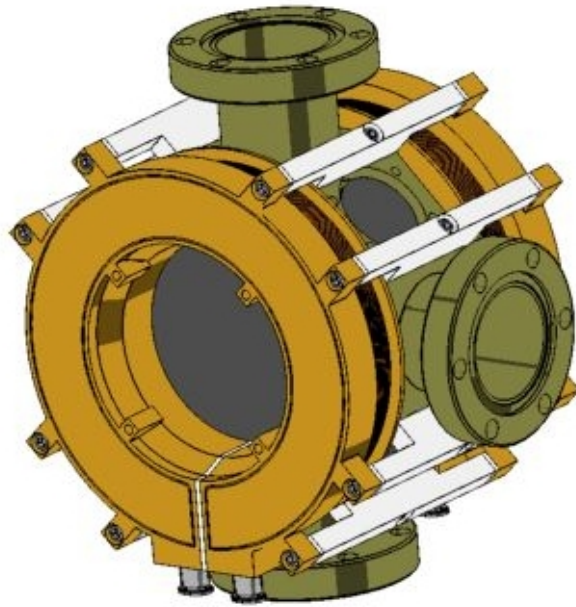


Figure 5.13: Rendered view of the main trapping chamber (green) and attached coils (brown in golden housing). The vacuum chamber is made from titanium and the coil holders are slotted to prevent eddy currents. The coils body features a trench for water cooling if the heat dissipation within the magnetic shielding becomes problematic.

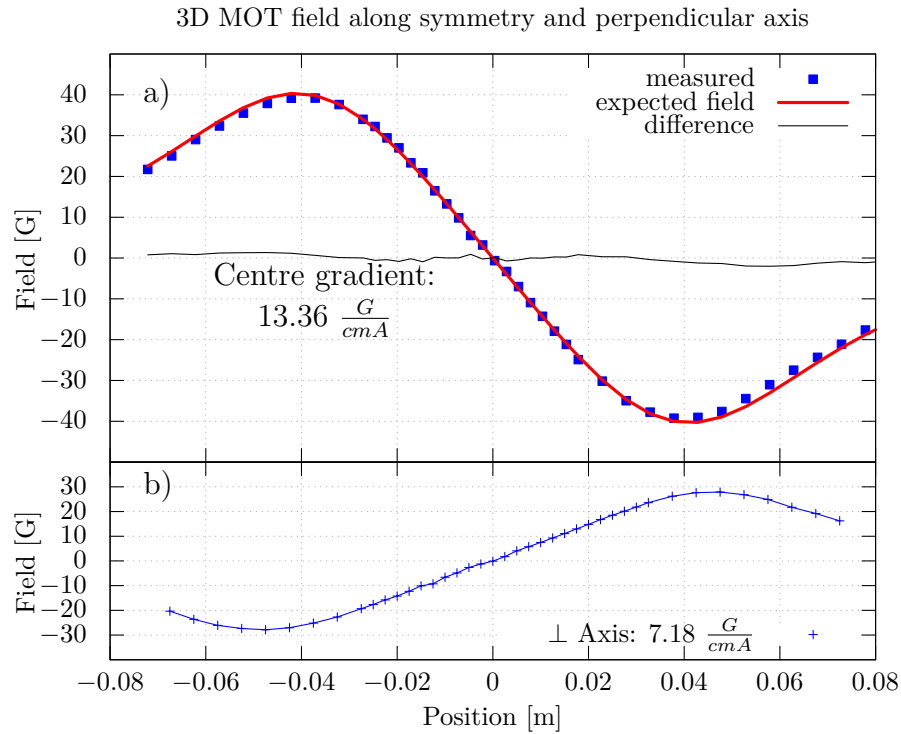


Figure 5.14: Magnetic fields created by the 3D MOT coils measured along the symmetry axis a) and perpendicular to this axis, centrally between the coils. Measured points are compared to the expected fields which respect the increasing distance of individual windings. The total number on each side is $N=357$. The difference between theory and measurement is plotted to highlight the minimal difference. b) shows a measurement in the plane perpendicular to the symmetry axis in the centre between the coils. As expected from expression(2.28), the gradient is half of that along the symmetry axis measured in a). To create a sufficiently high gradient for MOT operation, 2A are necessary to reach the anticipated 15G/cm.

5.3 Magnetic Fields

Apart from a stable and matching laser frequency, a magnetic field is key to building an atom trap (see 2.2). A linear magnetic field gradient is necessary over the trapping region (see 2.5) to shift the magnetic sub-levels and create a position dependent force. A pair of coils in *anti-Helmholtz configuration*¹ is commonly used to generate the gradient. Large atom numbers are achieved for gradients around $15 \frac{\text{gauss}}{\text{cm}}$.

Because the experiment is designed to be portable, specific care was taken to design coils which can run on a low current and dissipate minimal amounts of power. Figure 5.14 a) shows the field of the circular 3D MOT coils for a current of 1A along the symmetry axis. Blue points indicate measured values, the red line the expected field for the design parameters, 357 turns of a 1mm diameter copper wire, an inner coil radius of 39mm and 16mm width. The difference between theory and measurements was added to the plot to show

¹if the distance between the coils is $\sqrt{3}R$, where R is the radius, the 2nd and 3rd derivative at the centre point between them vanishes

that the design target is very well met. The gradient in the centre region is found to be $13.36 \frac{\text{G}}{\text{cm A}}$. Figure 5.14 b) shows a measurement along an arbitrary axis perpendicular to the symmetry axis of the coils. As expected from expression (2.28), the gradient in the centre region is half that of the symmetry axis.

During operation, a current of 2A is running through both coils. This value was found empirically and agrees with the expected value extracted from the central region in 5.14 b). Figure 5.13 shows a rendered image of the main chamber assembly with the field producing coils attached. They are wound onto a brass body which acts as a heat sink and also features in- and outputs for additional water cooling. Under operation, the assembly needs to dissipate 27Watts of power, which lead to a noticeable heating but no overheating. The water cooling is intended for later stages when the experiment is enclosed in a magnetic shield and dissipation through natural convection is limited. For the two dimensional MOT, two pairs of rectangular coils are used to produce linear field gradients perpendicular to the symmetry axis while the field on this axis stays zero.

Switching of Magnetic Fields

In the experimental sequence a fast and controlled switch off of the MOT coils is necessary to change into molasses phase. A simple cut of the current through the coils would lead to a long decay time that depends on the inductance and capacitance of the system formed by the coils and the power supply. This is typically in the order of hundreds of milliseconds, if the power supply is set into current limiting mode with the target value set to zero.

For an accelerated and controlled shut down, a semiconductor based and actively controlled switch is integrated. A insulated gate bipolar transistor (IGBT) acts as a switch, this is controlled by a MC33153 driver micro-controller. The circuit is protected with a varistor to account for high current peaks and completely isolated from the surrounding circuitry. The trigger signal is passed through an opto-coupler to the input of the controller element so that no cross connection between the grounds is possible. Figure 5.15 shows the voltage drop measured across a 0.5Ω shunt resistor for a switching cycle of the IGBT unit. The dashed red trace is the recorded trigger signal and the blue trace the voltage drop which is proportional to the current flowing through the measurement resistor.

Figure 5.15 a) shows the deactivation of the IGBT switch and the build up of the current, governed by the capabilities of the power supply¹. The relatively low target current (1.5A out of 10A possible with the power supply) is reached after $\approx 30\text{ms}$. If the IGBT circuit is engaged, the typical time to complete shut

¹ δ -Elektronika ES-300 Series 300W power supply for all coils

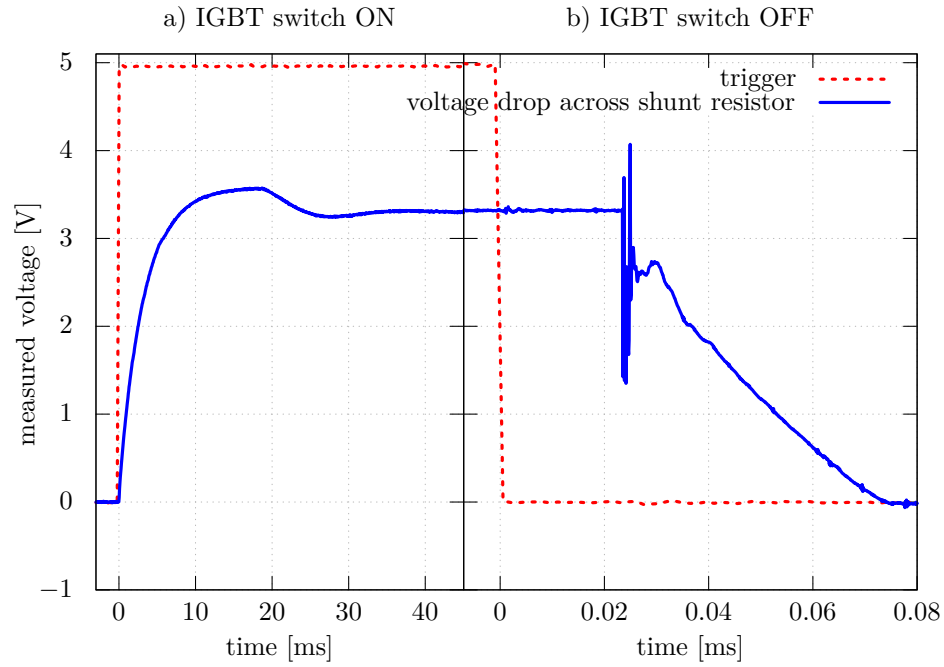


Figure 5.15: Switching speed of the IGBT (insulated gated bipolar transistor) elements used to switch coils of the main trap. Voltage is measured over a 0.5Ω shunt resistor (blue trace). The switch on characteristics are completely governed by the behaviour of the power supply.

off is approx $80\mu\text{s}$. Characteristics of the switching are the gap after receiving the trigger signal of $20\mu\text{s}$, the distortion, and the linear fall off. Time lengths of the individual steps, reaction time, and fall off time to zero are the same for repeated measurements, only the exact shape of the distortion changes. However this measurement only reflects the current through the coil wire, not the actual field and field produced by metal elements close to the coils. The main chamber is made from titanium, which has a high resistance and the coil holders, made from brass, are slotted to prevent the formation of eddy currents. Overall, the switch off time can safely be assumed to be in the order of $100\mu\text{s}$.

5.4 Compensation Fields

While an atom trap requires a magnetic field gradient to create the restoring force, any remaining field while imaging or driving Raman transitions adds noise. Imaging a MOT or molasses cloud with a high background field causes a movement of the cloud in the direction of the same. While the primary trapping field is ramped down, the atoms are influenced more and more by the overlying residual field which will create a uniform force in one direction, pushing the cloud out of the centre. Additionally, one can argue that sub-Doppler

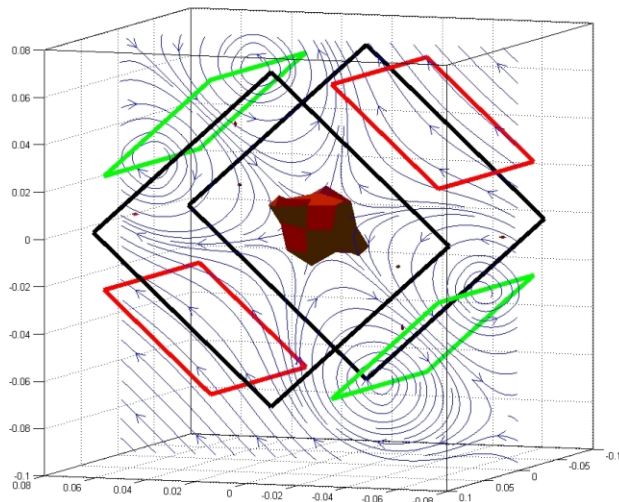


Figure 5.16: Background field (in the direction from the bottom front right to the upper left back corner) compensated by three coil pairs in the same geometry as mounted to the trapping chamber. The resulting field lines and the central area which attenuates the external field better than 10% are marked.

mechanisms work best in the absence of external fields as their mechanisms rely on the light shift of magnetic sub levels and optical pumping along them[128]. These influences are created by components that contain magnetic elements, such as optical isolators, or the earth magnetic field.

A well engineered compensation coil assembly should create a large uniform area in the centre to compensate for static magnetic fields. This is commonly done by placing rectangular coils around the experiment enclosure. Due to space restrictions, this first set of compensation elements is brought very close to the main chamber. Figure 5.16 shows a simulation of magnetic field lines created by 3 pairs of rectangular coils (red, green and black). The black compensation coils enclose the 3D MOT coils while the smaller ones are fitted around the 4 telescopes. In the shown arrangement, an earth magnetic field of 0.25G in the $[1,1,1]$ direction (from the centre to the point $[1,1,1]$ in the back top corner) is assumed. All coils are simulated with a single turn and the current for minimal field in the centre is calculated. The red centre area has a residual field of less than 10% of the earth magnetic field with a volume of approx. 4cm x 4cm x 2cm. The green pair is expected to have a current of 10.2A, the black pair of 6.1A while the red pair can stay idle. While this configuration is acceptable for preliminary tests, it is not able to create a large area of uniform compensation. The addition of a second, larger set of coils should provide better performance.

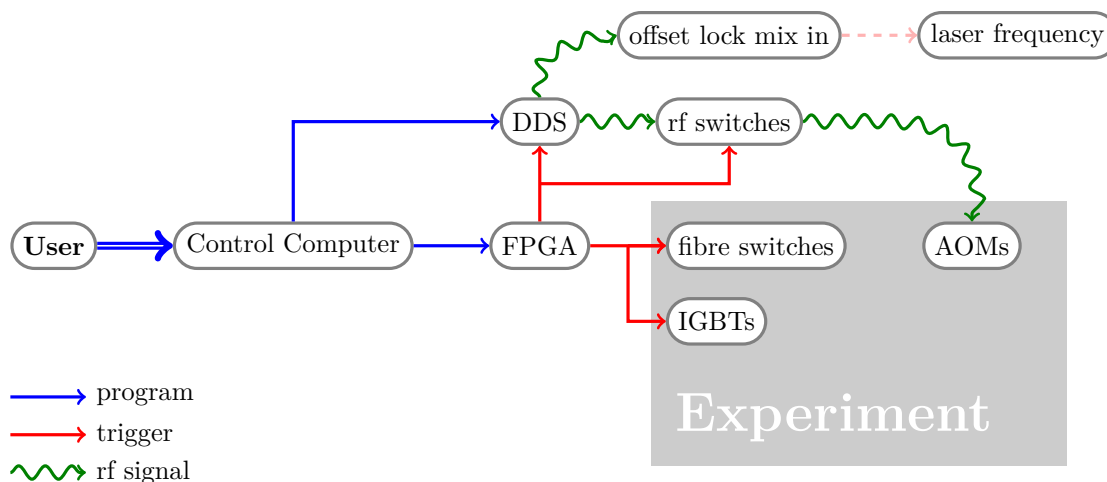


Figure 5.17: Diagram of the control lines in the experiment. A control computer loads frequency table information into the direct digital synthesizers to and an FPGA. The latter triggers execution of said tables and controls optical, radio frequency and current switches which in combination generate the light and frequency pulses necessary to drive the experiment.

5.5 Experimental Control

To run an atom interferometer sequence, precise control of the pulse timings is crucial. As shown in 3.1, a different length in laser pulse leads to a difference in population transfer. Any uncertainty in this timing will add to the errors in the interferometer signal. Fast digital signals are generated with a field programmable gate array (FPGA) on a National Instrument sbRIO-6932 board¹. Outputs are separated with buffer boards from the experiment to avoid any cross talk or back influence.

Figure 5.17 shows the general control scheme of the experiment. The operation parameters are set via a user interface and then processed by the main program located on a control computer. From here the sequence is loaded onto the FPGA as well as the two DDS units² which can store a table of instructions for two of their four channels. Once the sequence is started, the FPGA unit provides triggers for the table on the DDS which controls frequency, amplitude and phase of the rf signals. Fast disabling of the signal is ensured through additional rf switches which receive their control signal from the FPGA unit. One of the programmable DDS channels is used to provide an additional mix in frequency to modify the lockpoint of the cooler offset lock (see 5.2.2), and accordingly the laser wavelength. Capping or changing the frequency input to the acousto-optical modulators disables the selected light channel or changes the frequency of the passing light. Because the devices are fibre coupled, a change of frequency also introduces an attenuation of

¹Maximal resolution is 5ns

²Novatec 409B DDS with four output channels of which two are programmable

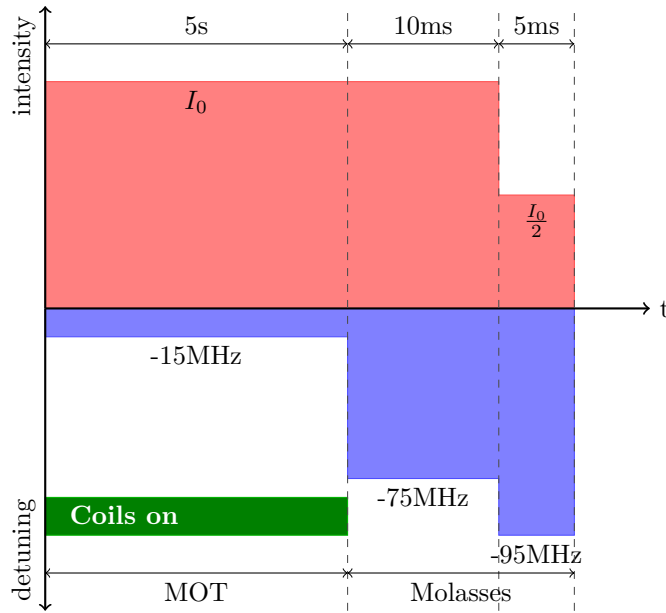


Figure 5.18: Molasses timing

the light's power (see figure D.1). Trigger signals to the fibre switches redistribute or disable light channels. Trigger signals to the IGBT are used to switch off the magnetic coils of the 3D and 2D traps.

5.5.1 Molasses Timing Sequence

A timing sequence for a simple molasses is shown in figure 5.18. The vertical axis is in units of intensity above the zero line and in units of detuning below, the horizontal axis is time (not to scale). For the first five seconds, the intensity in the beams, as well as the detuning, is kept constant while the coils are switched on. With this setting, the MOT is loading. The restoring force in a magneto optical trap and the high density prevents low temperatures, so typically the *Doppler limit* (equation (2.27)) is not breached. An additional phase without this source of heating, the *molasses phase* creates clouds which reach lower temperatures. As described in section 2.1, atoms in a light field with a certain detuning experience *Doppler cooling* and the light creates a viscous medium. To create this molasses phase, the magnetic coils are switched off and the detuning of the cooling laser is increased. Lower cloud temperatures are reached by increasing the detuning in a second step and decreasing the intensity of the beams. Atom cloud temperatures at the different steps are presented in sections 6.3.3 and 6.3.2.

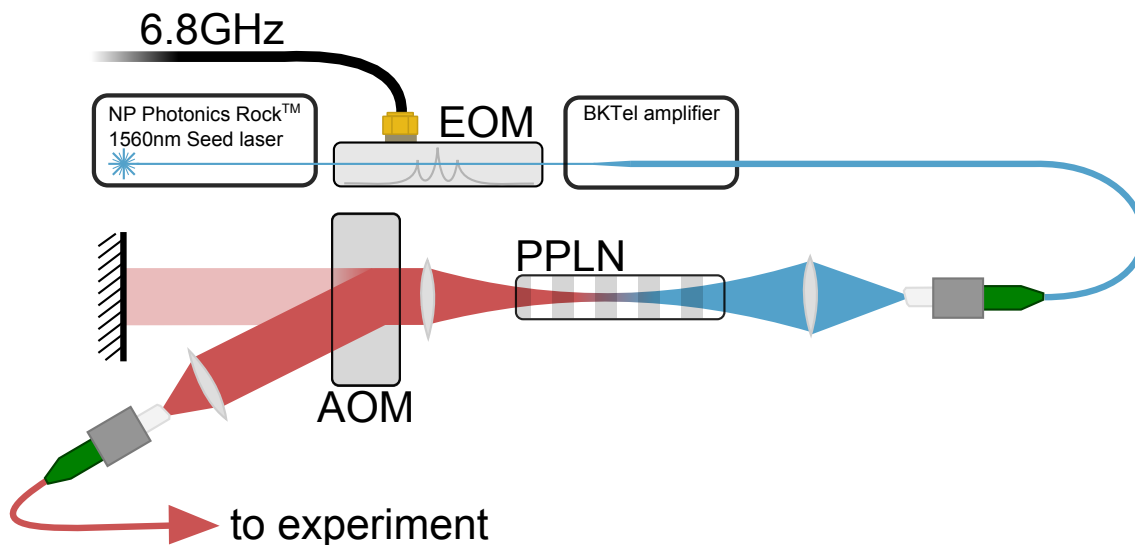


Figure 5.19: The Raman Laser System. A stable 1560nm seed laser is passed through an electro-optical modulator (EOM) which introduces a sideband at either side of the centre frequency (6.8 GHz, the separation of the $F=1$ and $F=2$ ground levels). After being amplified to a maximum of 18W, the light is passed through a periodically poled lithium niobate (PPLN) crystal which uses combines two 1560nm photons to a single 780nm photon. An acousto-optical modulator (AOM) is used for fast and precise timing control.

5.6 Raman Laser

Light for the *Raman pulses* has higher performance requirements than the light used for atom trapping. It should be of a narrow linewidth and stable intensity, frequency and phase over time. The narrow linewidth ensures good coherence of the selected atoms, a changing intensity leads to different Rabi oscillation frequencies. Most crucial is the relative phase between the two Raman frequencies (see section 3.2.3). It is possible to achieve this by phase locking two separate lasers emitting at the two Rabi frequencies but this added complexity was eliminated by using a 1560nm EOM to generate sidebands at 6.8GHz. The light is then converted to 780nm in a frequency doubling crystal. The seed is a NP Photonics laser with a linewidth $\leq 3\text{kHz}$, passing through a fibre coupled EOM from Photline and then amplified by a BKTel photonics fibre amplifier¹ to a maximum of $\approx 18\text{W}$ (see figure 5.19). The 1560nm light is free-space focused into a periodically poled lithium niobate (PPLN) crystal². The crystal is stabilised to a temperature of 185.2°C , which ensures that the frequency up-conversion criterion inside the crystal is met because a change in temperature would also change the crystal's lattice separation.

The 1560nm EOM is driven with a precision microwave source at 6.834GHz, the splitting of the $F=0$ and $F=1$ $5^2S_{\frac{1}{2}}$ level, plus the necessary detuning. This produces two side-bands separated by this frequency from

¹THPOA-SFP527

²Dectronic

the inserted. The power and signal shape going to the EOM are chosen that the sidebands carry equal power as the main feature. Therefore a third of the total power is in each of the three frequencies. The conversion crystal outputs three wavelengths: $780\text{nm} \pm$ the sidebands. One of this sidebands and the central frequency are used as the two *Raman frequencies*.

This approach benefits from a long history of technological development of devices for the telecommunication wavelength (1560nm) and the resulting availability of stable, high power and narrow linewidth system. By coincidence 1560nm is exactly double 780nm and frequency conversion can be used. At this stage a free space PPLN crystal is used but this will eventually be replaced with a fibre coupled equivalent in the final device. For the preliminary results shown below, the seed laser was not stabilised to an absolute reference. This is possible because the intrinsic stability is high enough to operate a magneto optical trap without additional stabilisation for ≈ 10 minutes in a noisy¹ environment. The most crucial requirement for Raman transitions is the *relative stability*, which is set by the microwave source. The absolute frequency has only minor influences on the Raman transition efficiency and frequency (see figure 6.11) and can fluctuate if the detuning is large enough.

Summary

A compact vacuum system was developed using standard knife edge and copper gasket based connections between metal parts, and indium seals between metal and glass. The vacuum chamber consist of a two dimensional MOT as an atom source connected through a differential pumping stage to a three dimensional trap which features the main pump and a vertical tube for the launched atoms. Coils for the system were designed to operate on minimal power dissipation to make the system easily portable. An FPGA unit provides fast and precise trigger control to switches for fibres, coils and frequency generators, which are programmed from the main control computer. A free space Raman laser system, based on a telecommunication wavelength laser, sidebands of the same with a frequency doubling module serves as the light source for *Raman pulses*.

¹The system was used at multiple public exhibitions where the settings were adjusted that instead of two Raman frequencies, cooling and repumping light are produced.

6 Results

The following sections present the first results of the GG^{top} apparatus. During the creation of this thesis, the experiment was planned, assembled and commissioned for basic operation, the creation of atom interference fringes as the first milestone towards gravity measurements. First, working parameters such as the loading and lifetime of the magneto optical trap will be presented, followed by cloud temperature measurement, and finally *Ramsey fringes* (section 6.6) the interference of matter, as a first milestone towards gravimetry. Operation of the system is currently limited by shortcomings, such as the fibre network stability and the presented results should be seen as proof of operation principle.

6.1 MOT Loading

The main three dimensional trap is loaded from a two dimensional MOT (see 5.2.1). In the used configuration, the pushing as well as the cooling and trapping power depends, on the intensity in the beams as described in 2.1. Figure 6.1 shows a measurement of the loading rate in the main trap for different powers in each of the two elliptical beams. As expected from equation (2.24) the loading rate increases linearly with power until a point of saturation is reached. The equation also implies that the scattering force cannot increase above a certain power level because all atoms will be in the excited state. This effect starts from around 100mW, when the loading rate plateaus.

6.1.1 Fluorescence Imaging

A typical loading curve of the 3D MOT is shown in figure 6.3. Light that is emitted from the fluorescing atom cloud into a solid angle is focused onto a reverse biased diode¹. Figure 6.2 shows the geometry of the atom trap, the collecting lens and the diode. The response of the photo diode is calibrated for different input powers of 780nm light. The power output of a single atom in the cloud emitted into this solid angle is given

¹Thorlabs DET100A

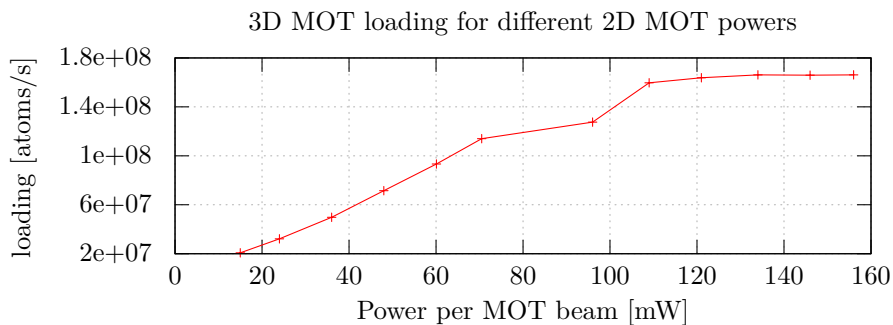


Figure 6.1: Loading rates in the 3D MOT for different powers per 2D MOT beam. The loading rates increase linearly with power but plateau for more than 100mW per beam. The same way three dimensional traps experience heating effects for high beam powers due to multi-photon effects, the source flux cannot increase if these effects become significant.

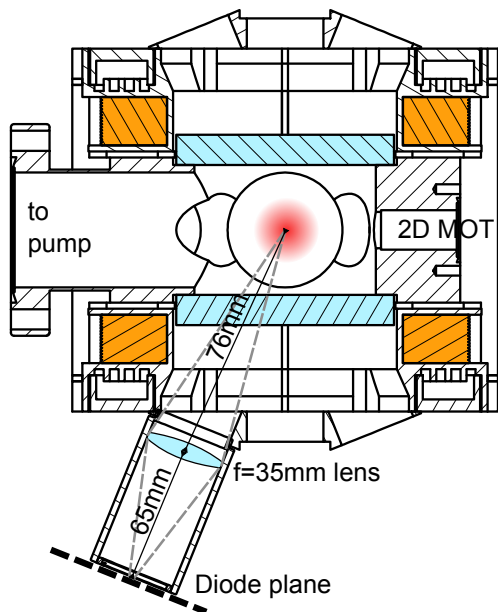


Figure 6.2: Geometry of the main chamber for how the fluorescence of the trapped atom cloud is captured. The detector is a reverse biased large area photo diode (Thorlabs DET100A) which detects light of a solid angle of $7.17 \cdot 10^{-7}$. The lens of focal length $f = 35\text{mm}$ is located 76mm from the centre of the trap, the diode is $\approx 65\text{mm}$ away from the lens, collecting all of the light collected by the lens.

by

$$P_{\Omega} = \Gamma \rho_e \Omega E_p \quad (6.1)$$

where Γ is the linewidth, Ω the solid angle and E_p the energy of one emitted photon. Emission can only happen from an excited state and the probability of the atom being in the state is given by

$$\rho_e = \frac{\frac{s_0}{2}}{1 + s_0 + \left(\frac{2\Delta}{\Gamma}\right)^2} \quad (6.2)$$

with the saturation parameter s_0 as in equation (2.21). This allows us to calculate a factor which relates volts to atoms on the y-axis for loading and lifetime plots.

6.1.2 Pressure Estimation

The loading behaviour of a MOT allows for the estimation of the background pressure at the location of the trap. Recalling equation (2.30), the filling of the trap is described by

$$N(t) = \frac{R_f}{\gamma} (1 - e^{-\gamma t}) \quad (6.3)$$

where R_f is the loading rate and γ the loss parameter[5]. This model only considers losses due to background gas collisions, but can be expanded via $\gamma \rightarrow \gamma + \bar{n}\beta$ to include two body losses (β) dependent on the average density in the trap. The fit in figure 6.3 uses the simplified model and the agreement is good enough to justify its use.

Fitting equation (6.3) to the measured data yields values for R_f and the loss rate γ . Although introduced as a single parameter, γ is composed of the combined effect of all background gas species, which enter with different strength. More generally γ can be decomposed into contributions of different species i via[5]

$$\gamma = \sum_i \gamma_i \quad (6.4)$$

Unless a mass spectrometer is used to measure the magnitude relations of the background gas, no definite statement about the individual γ_i can be made because the relative ratio is necessary. The γ_i for He, H₂O, N₂, Ar and CO₂ are in the order of $\mathcal{O}(2.5 \cdot 10^7 \text{ Torr}^{-1} \text{ s}^{-1})$. H₂ and Rb in the order of $\mathcal{O}(4.5 \cdot 10^7 \text{ Torr}^{-1} \text{ s}^{-1})$. The exact composition of background gases in the chamber is unknown but for a reasonable estimation, the average value of the quoted values in [5] was used, which leads to a pressure of $3.3 \cdot 10^{-9} \text{ mbar}$. For comparison,

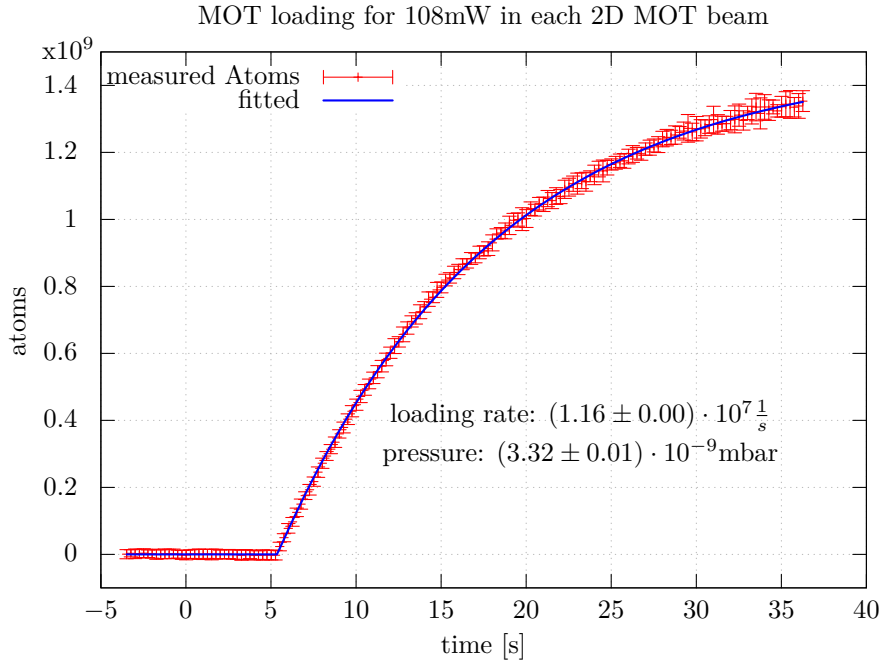


Figure 6.3: Measured loading curve (red points) and fitted exponential behaviour which allows extraction of the loading and loss rates. The latter can be used to estimate the pressure in the chamber.

the ion pump attached to the main chamber (physical separation about 20cm without any angles) quotes a pressure of $\approx 5 \cdot 10^{-10} \text{mbar}$. This order of magnitude difference can arise due to the combined assembly of non evaporative getter and ion pump. The electrodes of the ion pump are located directly behind the getter elements which acts as a shield, therefore giving lower values. Measuring pressure at the position of the experiment is more meaningful than at the pumping position where readings can be influenced by differential pumping effects.

6.2 Lifetime

Another direct measure for the quality of the trap is the lifetime. This is the time that the atoms stay trapped, and is measured by cutting the source and observing the depletion. Figure 6.4 shows a diode signal recorded from the three dimensional trap after disabling the magnetic fields of the 2D MOT. This immediately cuts the atom flow and the main trap should show an exponential decay of the shape

$$N(t) = N_0 \cdot e^{-\Gamma t} + C \quad (6.5)$$

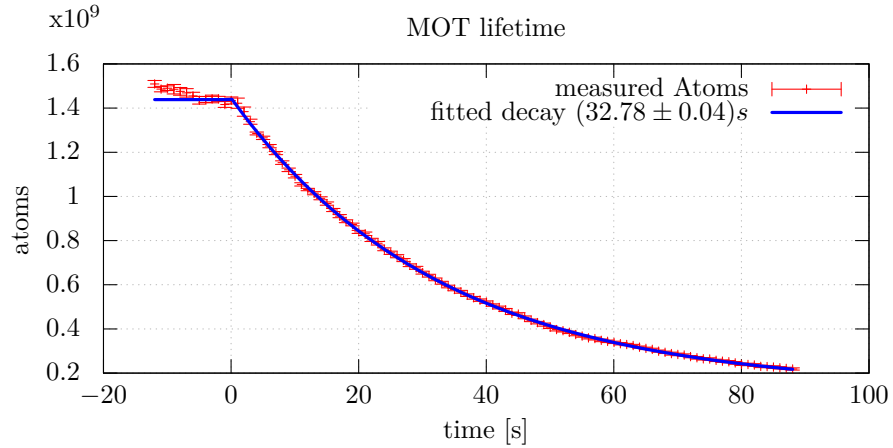


Figure 6.4: Lifetime of the three dimensional trap. The source (2D MOT) was switched off and the fluorescence of the atoms in the trap recorded on a photodiode over time. The decay time of an exponential is a relative measure for the trap performance.

which was fitted (blue line) to the data (red points). The calculated decay time of 32s shows that no major leaks are present in the chamber and indicates that the atoms stay long enough in the trap for further steps in the experimental sequence to be carried out. Keeping the underlying processes in mind, and comparing equation (6.3) and (6.5), one would expect the loss parameters γ and Γ to be equal because they reflect both the loss mechanisms present. However from figure 6.3 one gets $\gamma = 0.0786$ and from figure 6.4 $\Gamma = 0.0305$ which indicates a higher loss rate by almost a factor of three while loading the MOT compared to the lifetime measurement. This effect can originate from the hot atom beam generated by the 2D MOT hitting the main trap. The created additional disturbances give rise to additional loss channels. Additionally, the 2D MOT fields are switched off during lifetime measurement. Because of the proximity of the chambers the additional fields can influence the main trapping region by offsetting the point of zero magnetic field and altering the gradients. This changes the trap's geometry and therefore loss and loading rates.

6.3 Cloud Temperature

Even though the loading and lifetime of the atomic trap are important parameters, which set the repetition rate of the experiment and likely losses due to pressure, they are not good indicators for the temperature of the atom cloud. As discussed in section 2.2, temperature, or average velocity of the atom ensemble, is a measure of the trap's depth. Compared to a gas described by the kinetic gas theory, the amount of trapped atoms in a MOT is very low and not they are not in thermal equilibrium with the surroundings, hence the term 'temperature' is used differently. In cold atoms experiments *temperature* is merely used as an analogue

to mean energy, and therefore speed, of the atoms (see equation (2.23)). They relate to each other via

$$\frac{1}{2}m\bar{v}^2 = \frac{3}{2}k_B T \quad (6.6)$$

which assumes that energy and speed have a Gaussian distribution. Certainly, this can be assumed for a longer, free evolution of the atom cloud. The trapping potential sets the shape, while the atom gas is confined. A series of pictures at increasing time of expansion, the *time of flight* (TOF) method, is used for precise cloud temperature measurements.

6.3.1 Absorption Imaging

While being held in the magneto-optical-trap, the atoms constantly emit light, and a picture of the fluorescence is easily recorded with a camera. However, once the trap is switched off, any directed light pulse causes momentum transfer and therefore changes the shape of the cloud. This is especially true for fluorescence images, because a significant amount of photons need to be scattered for the camera to record an image. The preferred alternative is *absorption imaging*. In this technique, the shadow of the cloud during a short (typically $\approx 5\mu s$) resonant light pulse is imaged. Photons are absorbed from the light beam and randomly emitted by the cloud, creating a shadow on the camera. Exactly like in normal photography, the short exposure time guarantees that the picture has a minimal motion blur. To correct for patterns within the beam, such as those caused by diffraction, a picture of the flash only is stored as the *light field image*. Dividing this reference image, pixel by pixel value, by the image including the atoms and taking the logarithm yields the *optical density* (OD)

$$OD = \ln \left(\frac{I_{\text{ref}}}{I_{\text{shadow}}} \right) \quad (6.7)$$

The numerator is the light field image, and shows the Gaussian shape of the detection beam. The denominator has this shape minus the shadow of the cloud in outer regions of the beam profile. Care was taken that neither the light field alone nor the image with the cloud's shadow saturate or completely block the camera to prevent false readings. A reliable estimation of the cloud size is difficult because the image contains speckles, diffraction fringes and the shadow of the cloud is placed in an area of changing intensity of the detection beam. The optical density as in equation (6.7) removes all these features leaving only the Gaussian shaped cloud. Figure 6.5 shows such a process. To reduce pixel noise error, a smoothing filter over an area of 10x10 pixels is applied. This eliminates extreme singular values in the optical density caused by pixels, without affecting the inferred atom number.

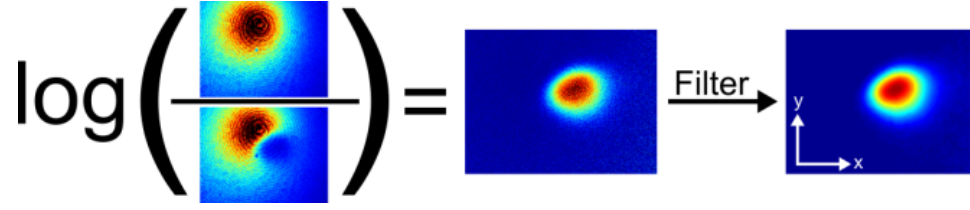


Figure 6.5: Exemplary optical density extraction from a molasses time of flight images (1024x768 pixels). The ‘numerator’ of the fraction in the logarithm is the *light field image*, an image of the detection beam without atoms. The ‘denominator’ is an image with an atom cloud, showing the shadow. Optical density is recovered via equation (6.7), dividing the intensity pixel values of each position and taking the logarithm. Artefacts due to clipping of the detection beam or dust particles are eliminated, a filter over a 10x10 pixel area smooths the shape and makes fitting of two dimensional Gaussians easier.

Once the optical density is obtained, it is related to the density $n(x, y, z)$ of the cloud via

$$\text{OD}(x, y) = \sigma \int_{-\infty}^{\infty} n(x, y, z) dz \quad (6.8)$$

for the two dimensional image taken. σ is the *absorption cross section* of rubidium:

$$\sigma = \frac{\sigma_0}{1 + 4 \left(\frac{\Delta}{\Gamma}\right)^2 + \frac{I}{I_{\text{sat}}}} \quad (6.9)$$

where the on resonance cross section is $\sigma_0 = \frac{3\lambda^2}{2\pi}$ ¹. With this assumption, the number of atoms is calculated via

$$N = \frac{1}{\sigma} \int_{-\infty}^{\infty} \int_{-\infty}^{\infty} \text{OD}(x, y) dx dy = \frac{\Delta x \Delta z}{\sigma} \sum_i \sum_j \text{OD}(x_i, x_j) \quad (6.10)$$

where the second form is the discrete version for pixels of the size $\Delta x \times \Delta y$ on a camera chip². The atom number is easily extracted from any image/light field pair, if the shadow does not block all of the light and the flash does not saturate the camera.

For a long enough expansion time, the shape of the cloud approaches a three dimensional Gaussian because no confining or otherwise shaped potential is present:

$$\begin{aligned} n(x, y, z) &= \frac{N}{(2\pi)^{\frac{3}{2}} \sigma_x \sigma_y \sigma_z} e^{-\left(\frac{x^2}{2\sigma_x^2} + \frac{y^2}{2\sigma_y^2} + \frac{z^2}{2\sigma_z^2}\right)} \\ \Rightarrow n(x, y) &= \int_{-\infty}^{\infty} n_0 e^{-\left(\frac{x^2}{2\sigma_x^2} + \frac{y^2}{2\sigma_y^2} + \frac{z^2}{2\sigma_z^2}\right)} dz \end{aligned}$$

¹for Rubidium: $\sigma_0 = 290.7 \cdot 10^{-15} \text{m}^2$ and $I_{\text{sat}} = \frac{\pi \hbar c}{3\lambda^2 \tau} = 1.64 \frac{\text{mW}}{\text{cm}^2}$

²The used camera is a ImagingSource DMK 31BU03 camera, using a Sony ICX204AL chip with a pixel size of $4.65 \mu\text{m} \times 4.65 \mu\text{m}$. A calibration image, taken of a ruler at the distance of the cloud is used to calibrate the magnification and relate pixel size to imaged length.

σ_i is the width of the Gaussian in direction i . Using equation (6.6), the width of the cloud at a later time t is then

$$\sigma_i^2(t) = \sigma_{i0}^2 + \frac{k_B T_i}{m} t^2 \quad (6.11)$$

and the temperature is calculated from

$$T_i = \frac{m}{k_B} \frac{\sigma_{i2}^2 - \sigma_{i1}^2}{t_2^2 - t_1^2} \quad (6.12)$$

Consequently, the time since release of a sequence of images squared, plotted against fitted widths σ_i^2 of the clouds squared, is proportional to the temperature by a factor of $\frac{m}{k_B}$. To relate the physical size to the number of pixels on the camera sensor, a picture of a ruler placed in front of the sensor at the distance of the cloud is used. The widths σ_i are found through the fit of a two dimensional Gaussian at an angle to the x and y-axis of the camera sensor. The following sections show temperatures of the MOT and molasses phases. All measurements share an asymmetry of up to a factor of two of the cloud, which hints to polarisation instabilities in the fibre system.

6.3.2 MOT Temperature

A better performance criterion for a magneto optical trap, beside the loading speed, is the temperature of the produced atom cloud. Figure 6.6 shows the time since the release from the the trap squared versus the found widths (x and y direction on the CCD chip) squared. According to equation (6.12), the slope of a linear fit through the measured points is proportional to the temperature by a factor of $\frac{k_B}{m_{Rb}}$.

Each point in figure 6.6 consists of twenty images. A two dimensional Gaussian was fitted to the extracted image the the found widths recorded. Two things are noteworthy: Firstly the expansion of the cloud is not uniform and secondly the error increases for longer time of flights. The increasing spread originates from the high temperature which causes the cloud to disperse quickly and also non uniformly. This adds to observed deviation from the ideal Gaussian shape. One possible reason are changing trapping efficiencies in different regions of the trap and/or power imbalances. Additionally, a not fully compensated magnetic field creates a force during the molasses phase due to the Zeeman shift. This creates an accelerated drift.

6.3.3 Molasses Temperature

Section 2.3 gave two elementary temperature limits for cooling rubidium atoms: the *Doppler limit* at $145\mu K$ and the *recoil limit* at $0.37\mu K$. The latter is the energy transferred by one photon, which can be assumed to be the smallest energy unit possible in a trap based on absorption and emission of photons. The measure-

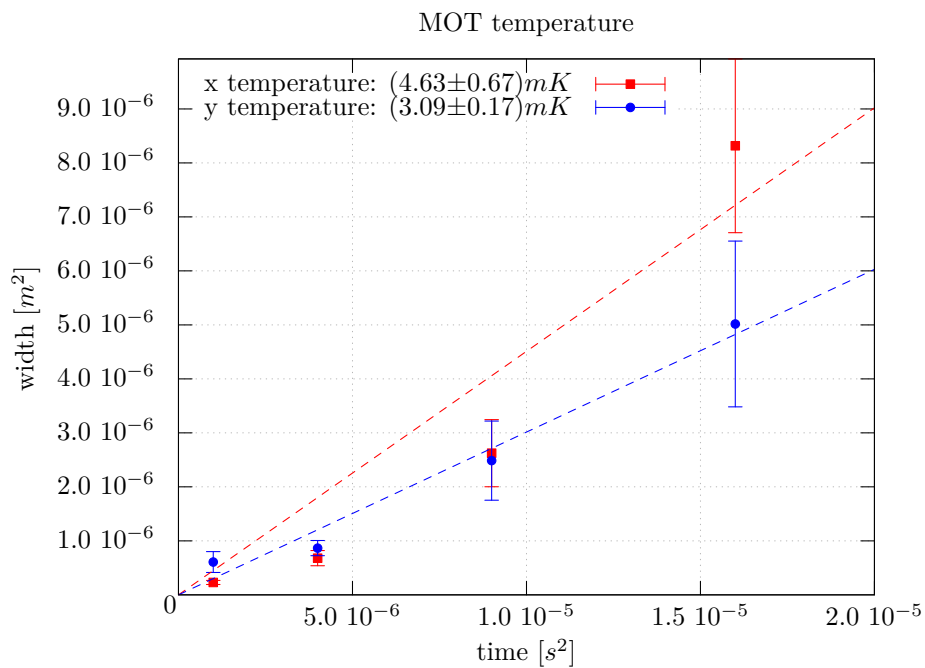


Figure 6.6: Temperature of an atom cloud released directly from the magneto optical trap with $\approx 10^8$ atoms. The detuning of the cooling laser was set 15MHz from resonance. The increasing size of the errorbars is caused by an increasing deviation from a Gaussian shape of the imaged cloud. This hints power imbalances and not compensated magnetic fields in the outer region of the MOT, causing non uniform expansion. Additionally the atom number fluctuates significantly with $8.01 \cdot 10^7$ for 1ms, $9.62 \cdot 10^7$ for 2ms and $6.79 \cdot 10^7$ for 3ms time of flight time.

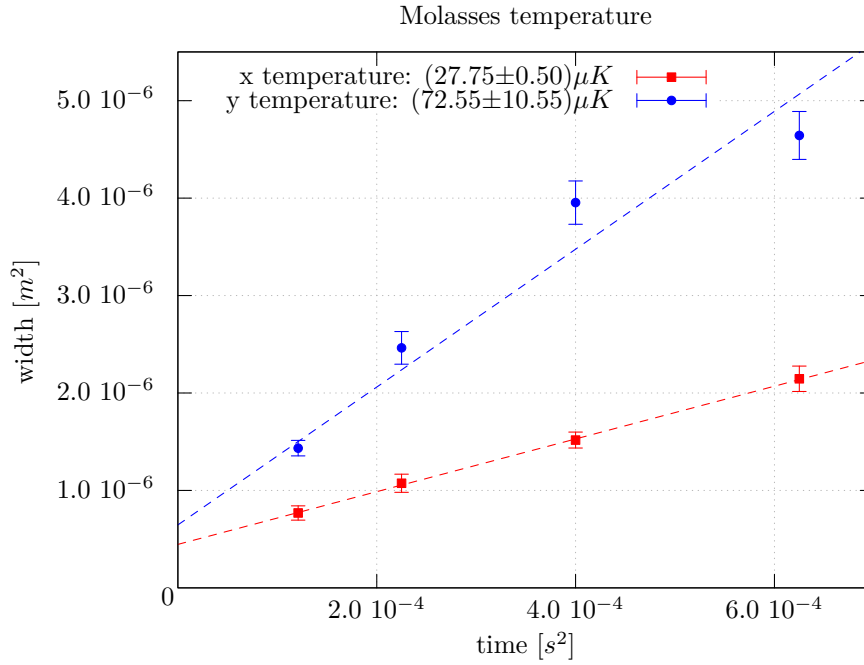


Figure 6.7: Temperature of an atom cloud with initially 9.6^7 rubidium atoms created in an optical molasses phase of 20ms length and a detuning of 80MHz from resonance. Spread of the cloud compared to direct release from the trap is reduced by a factor of 20. Again the loading behaviour is not the same for the same sequence parameters. After 11ms time of flight, the cloud has $0.58 \cdot 10^8 \pm 6.7 \cdot 10^6$, for 15ms $0.9 \cdot 10^8 \pm 9.6 \cdot 10^6$ for 20ms $1.1 \cdot 10^8 \pm 1.2 \cdot 10^7$ and for 25ms $0.96 \cdot 10^7 \pm 1.9 \cdot 10^7$ atoms. This instability is one of the reasons why the fitted lines do not meet at the origin.

ment in figure 6.6 shows a temperature well above these two limits and therefore too hot for interferometer experiments. An atom would travel in $\approx 4ms$ from the centre of the vertical tube to either side and collide with the wall. This time frame is simply not long enough for any experimental sequence. Assuming a time window of 200ms for the complete interferometry sequence, the atoms would need to have a temperature $T_c < 28.9mK$ to not collide with the walls of the tube.

Lower temperature are reached through an additional *molasses phase*. Any heating effects created by the restoring force are eliminated by turning off the magnetic field of the trap. The atoms are now in the previously discussed viscous medium and their behaviour is controlled by the Doppler cooling force. An increase in detuning of the cooling laser also increases the cooling effect. Figure 6.7 shows the expansion of a cloud released from the trap and held in a molasses phase of 20ms and an additional 80MHz detuning. Fits show temperatures of $27\mu K$ and $75\mu K$ for the x- and y-directions. Although still quite ‘hot’ for cold atom experiment standards, the temperature is already significantly below the *Doppler limit* and a factor of 20 colder than the trap.

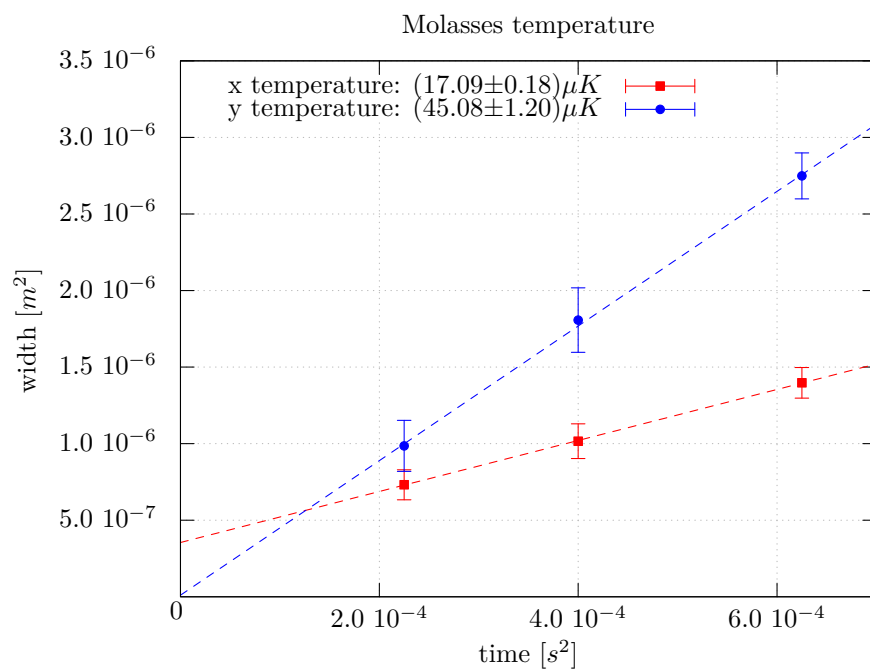


Figure 6.8: More efficient multi step molasses. The steps are +50MHz for 10ms and +70MHz for 5ms relative to the MOT frequency, where the intensity is decreased to 50% in the last step. Again the sequence struggles with large instabilities of the loading MOT giving $1.07 \cdot 10^8 \pm 2.2 \cdot 10^7$ for 15ms, $1.32 \cdot 10^8 \pm 1.8 \cdot 10^7$ for 20ms and $1.53 \cdot 10^8 \pm 1.6 \cdot 10^7$ atoms for 25ms time of flight. Expected is an opposite trend that the number of atoms is decreasing with increasing time of flight.

Varying the detuning and intensity of the cooling light allows further optimisation. Particularly the smooth ramping down of intensity at the end does remove potential imbalance effects created through the rapid switch off. Figure 6.14 shows the steps used in the left part. The temperature reached is lower by almost a factor of two compared to the previous measurement in figure 6.7.

To address the previously mentioned issue of fast expanding clouds, experiments which use long times for the freely expanding cloud, use Bose-Einstein-Condensates. If this option is not available, velocity selection via Raman pulses is possible [75], which has the downside of a large atom loss (see section 3.2.6 and figure 3.6). Another approach is the δ -kick cooling technique[4, 101] which uses a magnetic field pulse to modify the phase space to essentially stop the expansion of a thermal cloud. Although difficult to implement, this method can be very effective and yield high atom numbers at the desired temperature.

One clear limitation of the trap presented is power instability of the light, which leads to asymmetries along the x- and y-directions. The used camera is looking down along the symmetry axis of the magnetic field in the trap and should therefore see a uniform expansion of the cloud in the recorded plane. However all measurements show differences between the two directions of almost a factor of two. Section 6.7 will discuss which influences lead to changes in the fibre network and how they relate to the observed behaviour.

6.4 Atom Launch

Chapter 3 showed that the phase of a freely falling atom interferometer depends on the local gravity field. The requirement is a cold cloud as discussed in the previous sections for controlled cloud expansion during the interferometer time. The second limitation is the traveled distance of the cloud. If dropped from the trap, the atoms will quickly leave the area of optical access. This effect is already visible while recording time of flight sequences with molasses where the cloud reaches the border of the sensor for long expansion times. Chapter 3 showed that a larger interferometer area will increase the contrast of the signal and hence longer interferometer times are preferable. This is achieved by cooling atoms in a molasses phase followed by a vertical launch. The available interrogation time can be doubled, if the π -mirror pulse is applied at the apex of the free fall trajectory. A *moving molasses* configuration[55, 36, 72, 24] pushes atoms from the trap position upwards, creating an *atomic fountain*.

By using one acousto-optical modulator for the side and upwards pointing MOT beams and a second one for the downwards pointing beams, allows independent frequency tuning (see figure 5.3) of the two sets. They operate with a common frequency upshift of 80MHz during MOT and molasses phase. Forces in the trap are equal between facing trapping beams as in figure 6.9 (dashed lines). This balance is broken if one

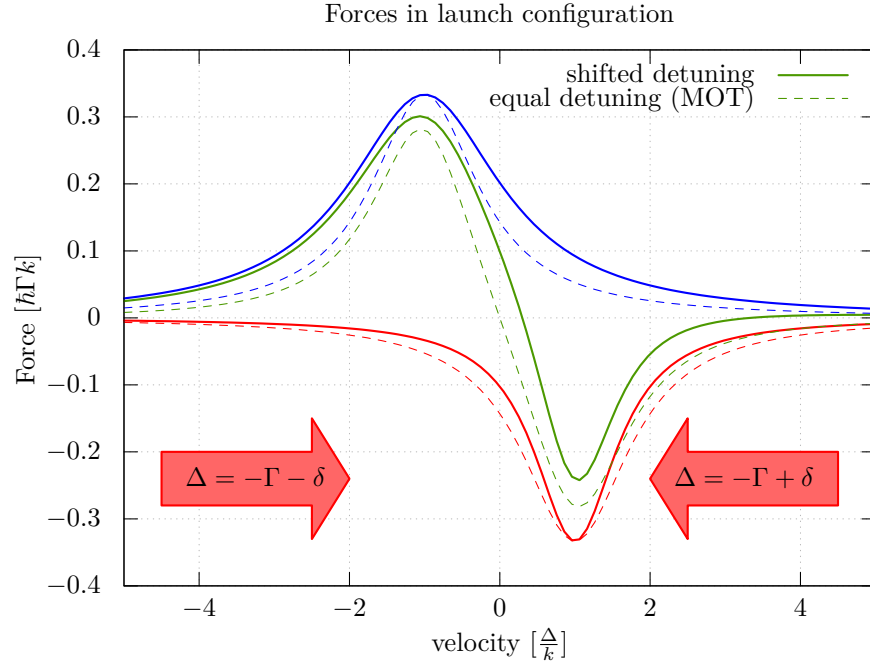


Figure 6.9: Scattering forces during launch configuration. The dashed are taken from figure 2.4. The solid differ in the detuning. Instead of assuming $\Delta = \Gamma$ for both beams, the blue beam has $\Delta = 1.3\Gamma = \Gamma + \delta$ and the red $\Delta = 0.7\Gamma = \Gamma - \delta$. In this configuration, the damping force is zero for a frame moving with the speed $\frac{\delta}{k}$. The atoms are therefore accelerated.

beam is detuned by $+\delta$ while the other is shifted by $-\delta$ (solid lines). The width of the underlying peaks changes asymmetrically and so the sum of both forces changes. The point of zero force on the atoms is now moved to a velocity $\neq 0$. Instead of accumulating atoms with $v = 0$, the new equilibrium speed is now offset to

$$\begin{aligned} v &= \frac{|\delta_1| + |\delta_2|}{2k_{\text{eff}}} \\ &= \frac{\delta}{k_{\text{eff}}} \end{aligned} \quad (6.13)$$

where k_{eff} is the projection of the wave vectors on the resulting launch direction. The second line is valid for a symmetric detuning of $\delta_1 = \delta_2 = \delta$. In the used configuration $k_{\text{eff}} = \sqrt{2}k$ because atoms are launched at 45 degrees with respect to the detuned MOT beams. The force on atoms with zero velocity yields

$$F_{\text{scatt}}|_{v=0} = \frac{\hbar k \Gamma s_0}{2} \left[\frac{1}{1 + \frac{4(\Delta + \delta_1)^2}{\Gamma^2} + s_0} - \frac{1}{1 + \frac{4(\Delta - \delta_2)^2}{\Gamma^2} + s_0} \right]. \quad (6.14)$$

Assuming the majority of atoms were slowed down close to zero speed, this is the average acceleration

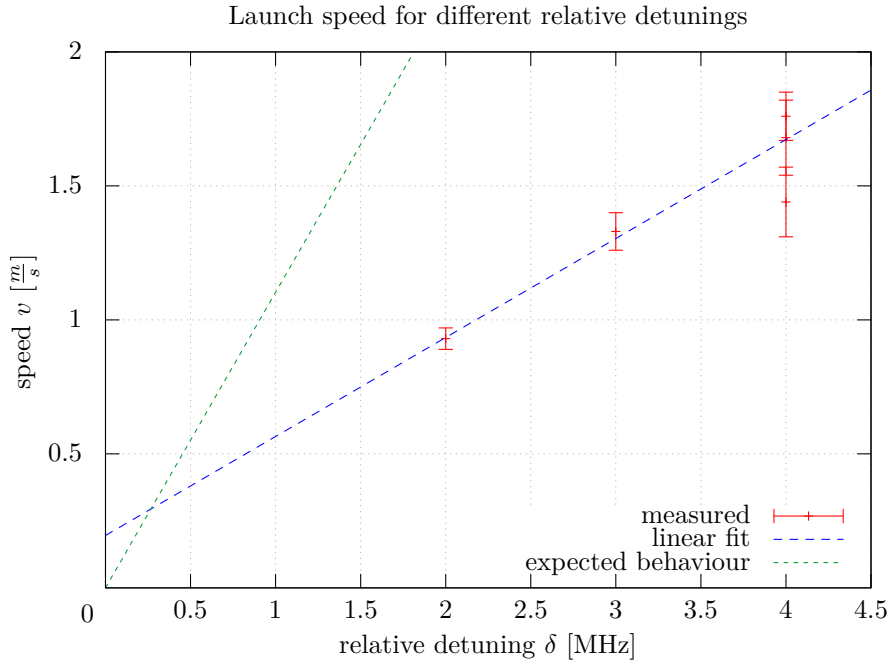


Figure 6.10: Centre of mass speed for an atom cloud launched from a magneto optical trap by introducing relative detuning between the upper and lower trapping beams. Relative detuning is defined as $|\delta_1| + |\delta_2|$. The expected speed for a two dimensional beam cross is shown as a dotted line[117, 13]

experienced.

Figure 6.10 shows measured cloud speeds for different relative detunings ($|\delta_1| + |\delta_2|$). The measurement point cluster at 4MHz result from symmetric ($\delta_1 = -\delta_2 = 2\text{MHz}$) and asymmetric ($\delta_1 = 1\text{MHz}$, $\delta_2 = 3\text{MHz}$) configurations. Values were extracted from a series of fluorescence pictures (see figure F.2) and the speeds extracted through linear fits (see figure F.1). The found horizontal and vertical centre position of the cloud is marked with a cross. Intensity of the beams is ramped down to zero 1ms after the sequence starts over 1.5ms. This reduces the clouds visibility in some of the images, because fluorescence was recorded. As expected, a symmetric detuning of $\pm 2\text{MHz}$ and $+1\text{MHz} - 3\text{MHz}$ produces the same speed in the cloud (see figure F.1 yellow and blue trace) but the shape of the launched cloud differs significantly. In the symmetric case, the cloud seems to stretch and then fade. In comparison the $+1-3\text{MHz}$ configuration does not produce an elongated but a quickly vanishing cloud. This indicates that less atoms are accelerated. The case of $\pm 3\text{MHz}$ gives a clearer insight. The fourth image in the series shows the found centre above the clearly visible ball of atoms. Hidden in the colour coding of the image is a vertical stream. Looking at figure 6.9 it becomes clear that, because of the high detuning, only fast atoms are accelerated, the remaining colder cloud is eventually blown away. Therefore a stepped sequence, matching the detuning of the launch beams with the velocity

distribution of the cloud should accelerate a higher number of rubidium atoms. It is noteworthy that the shown images are taken from a test which did not include a molasses phase before the launch. Therefore it can be assumed that the velocity spread remains high. Starting with a molasses phase for an even temperature distribution followed by a separate launch step should minimize partial acceleration as observed in figure F.2 d). Figures 6.10 and F.1 did only consider vertical velocity components. Images taken can be used to estimate the horizontal acceleration in the picture plane but any movement out of plane is hidden. Horizontal displacement of the cloud was found to be negligible.

Figure 6.10 also plots the expected speed of a moving frame produced by a two dimensional cross where the two upper beams are detuned by -2δ compared to the lower beams which are shifted by $+\delta$ to the MOT condition. The slope is larger by a factor of two and contrary to the measured values crosses the origin. The discrepancy is caused by the third beam pair which in the used configuration does the same frequency shift as the beams coming from the bottom (see figure 5.3). This leads to an incomplete launch, increasing the velocity spread in the launch direction but reducing the speed of the cloud's centre.

Atom Launch through Optical Lattice

The *moving molasses* technique is straightforward to implement but not the only possible. It is very efficient in launching the majority of the atoms but because the accelerating force is velocity dependent, stretches out the accelerated atom cloud. A very uniform velocity distribution is required to overcome this problem, which is hard to achieve. An alternative method, which selects atoms of a very narrow velocity class, is launching by means of an optical lattice[137, 77, 68]. Two counter propagating, far detuned laser beams form a standing wave. The dipole force traps the atoms in the forming one dimensional lattice structure. If one laser is detuned against the other, the lattice moves. Atoms within the lattice are accelerated and can be launched with a high degree of precision. The bottleneck is the loading into and releasing from the lattice. While a moving molasses has a broad acceptance range of velocities, only a small velocity class is loaded in the optical potential.

6.5 Rabi Oscillations

Chapter 3.1 laid out the basics of atom interferometry and the working of *Raman transitions*, used to create beam splitters and mirrors for the atoms. Two frequencies transfer population between the $F = 2$ and $F = 1$ state of the Rubidium atoms in a controlled way. Both are stable and no spontaneous decay into a lower

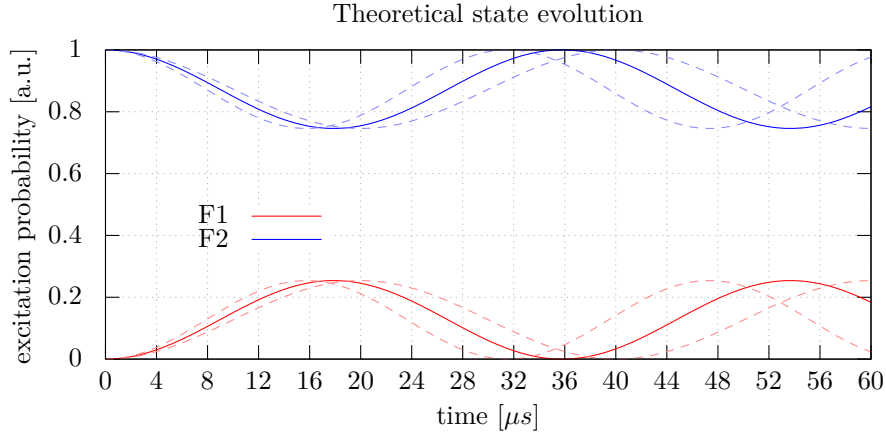


Figure 6.11: Theoretical population evolution of $F=2$ and $F=1$ rubidium system if all the atoms are initially in the $F=2$ state and σ^+ polarisation is used. The solid lines assume a seed laser frequency of 1560.475nm, the dashed of an error of ± 0.002 nm. Results are preliminary and intended to show that atom interferometry is possible, so the wavelength was not actively stabilised and was not cross checked against a stable reference. Errors within this range are possible.

energy level is possible. At the end of the molasses sequence, the atoms are mostly prepared in the $F = 2$ because the *repumping light* ensures that atoms in the $F = 1$ are pumped to the other state.

Raman light was produced with the laser system presented in section 5.6. The beam with a total output power of 1.5W is expanded to the total 38mm diameter of the vertical tube. A quarter-wave plate converts the light to σ^+ for a co-propagating configuration. The EOM sideband modulation creates three frequencies: a centre frequency and two ± 6.8 GHz satellites. One of these plus the carrier were used as the two Raman frequencies. To keep the initial configuration simple, no m_f sub-state preparation was used. Figure A.1 indicates possible transitions from the $F = 2$ to $F = 1$ state for linear (π) and circular (σ^+ and σ^-) cases. The co-propagating σ^+ configuration allows for five possible transitions through the absorption and emission of two photons of this polarisation. Deterministic population of certain levels and the use of a bias field would limit the possibilities to a single transition. This is used for a gravity measurement sequence when a better signal to noise ratio is required.

Figure 6.11 shows a plot of the expected behaviour for the above parameters and the use of equations (3.15) and (3.16). The centre line assumes a seeding frequency of 1560.475nm, the two dashed lines indicate changes of ± 0.002 nm. An error of this scale is possible as the laser was not stabilised to an external reference and the reading was taken from the provided controls. The model also assumes an equal distribution of atoms in $m_f \in [-1, 0, 1]$ as no pre-selection was done. However a change in this assumption to a single transition would alter the oscillation frequency. From this simple model, a $\frac{\pi}{2}$ time of $\approx 10\mu\text{s}$ is expected.

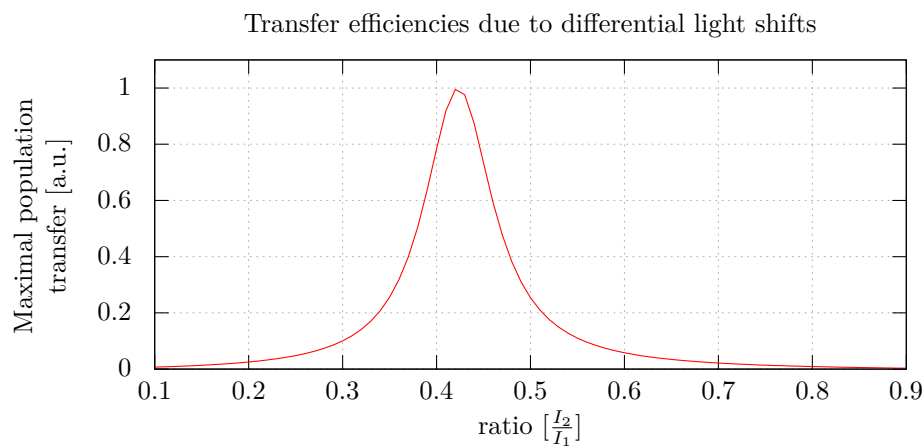


Figure 6.12: Differential light shifts calculated for different ratios of the two Raman lasers with the model from figure 6.11. An equal power ratio does lead to incomplete population transfer. This is because the involved levels shift differently with respect to the frequency and intensity of the beams. A carefully chosen power ratio allows elimination of the shift.

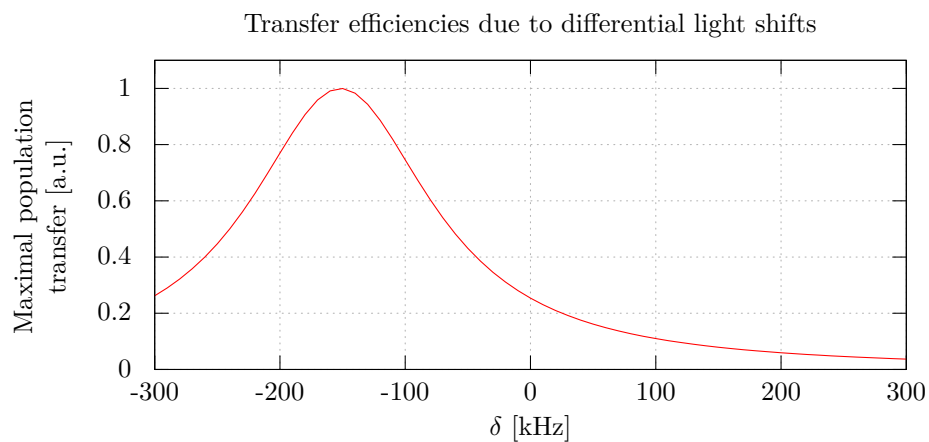


Figure 6.13: Maximal state transfer in *Raman pulses* for varying detuning δ (see figure 3.2). Instead of changing the intensity ratio of the two Raman lasers, the detuning δ can be changed to achieve full population transfer. This calculation assumes $I_1/I_2 = 1/1$

The model also predicts a low contrast of $\approx 22\%$ due to the incomplete population transfer. This is caused by the differential light shift, produced by the interaction of the energy levels with said light fields. The intensity dependent detuning in addition to δ and Δ shown in figure 3.2 is added but can be corrected for with the right choice of laser intensities. Figure 6.12 shows estimations from the same model as in figure 6.11 for varying power ratios. A change to $I_s = 0.42I_1$ should allow complete population transfer. Alternatively the detuning δ can be altered to have the same effect. Figure 6.13 assumes $I_1/I_2 = 1/1$ and records the maximal population transfer for varying δ . In a laser system such as the one used (see figure 5.19) this is achieved by changing the shape of the driving frequency in the EOM.

6.5.1 Experimental Sequence

To detect *Rabi oscillations*, a molasses sequence as discussed in 6.3, created a cold cloud of atoms. Figure 6.14 shows a timing graph (time axis not to scale) of this sequence. After a short expansion time, a *Raman pulse* of variable length is applied to probe the time axis of figure 6.11. Atoms are in the $F = 2$ state while in the molasses phase, the *Raman pulse* is therefore expected to transfer population into the $F = 1$ state. After expansion of $200\mu\text{s}$, populations in the $F = 1$ and $F = 2$ states are read out in fluorescence via resonant detection pulses of $100\mu\text{s}$ length. Atoms are then removed from the cloud by $100\mu\text{s}$ pulse from just the upper telescopes. Both pulses did not contain any repumping light to eliminate change of the $F = 1$ population. A $100\mu\text{s}$ pulse of just repumping light transfers atom from the $F = 1$ to $F = 2$ state. A final resonant detection pulse of $100\mu\text{s}$ maps the population on a diode signal.

An exemplary oscilloscope trace of the fluorescence signal throughout the sequence is displayed in figure 6.15. It covers the loading of the MOT (finishing at $t=0$) and molasse time (up to $t=15\text{ms}$) followed by the two detection peaks. The first one is proportional to the atomic population that remained in the $F = 2$ state and was not transferred by the *Raman pulse*. The second one is proportional to the population, that was initially moved to $F = 1$ and then back to $F = 2$ for detection. The height ration of the peaks responding to the two detection pulse, minus the background, gives the population ratio between the two states of the interferometer. The background level, visible at the right end of the plot, needs to be subtracted.

6.5.2 Extracted Oscillation

Ratios of these two peaks are shown in figure 6.16 for *Raman pulse times* between $1\mu\text{s}$ and $34\mu\text{s}$. The resulting trace behaves as a damped oscillation and was fitted with a decaying sine wave. Imperfections in the population transfer introduce losses proportional to the length of the sequence and lead to the decay of

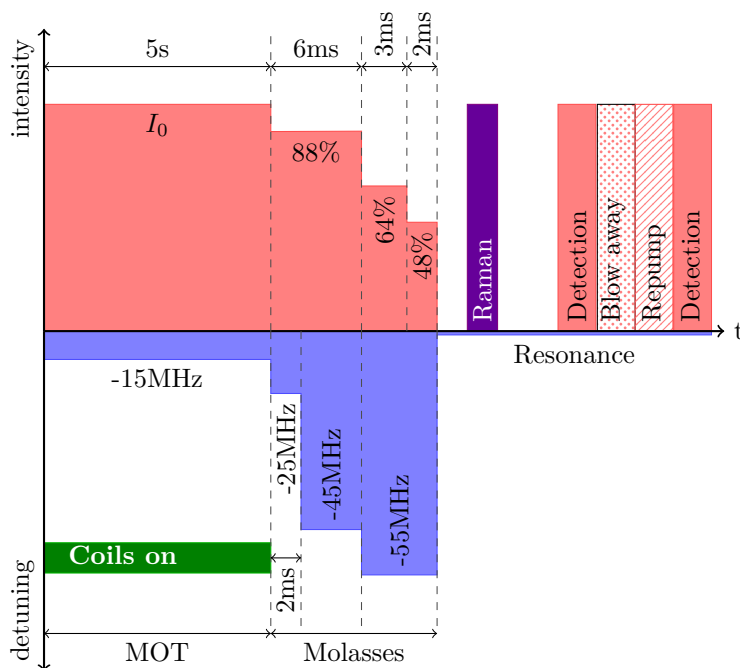


Figure 6.14: Experimental sequence in trapping intensities and detuning. The first part is a molasses phase as discussed in 6.3. After that a *Raman pulse* of variable length is applied. After some additional expansion time, atoms in the $F = 2$ state are recorded in fluorescence with a $100\mu\text{s}$ pulse from all MOT telescopes, followed by a *blow away* pulse from only the upper telescopes to remove the same atoms. A $100\mu\text{s}$ *repump pulse* of repumping light only is applied to transfer atoms moved to the $F=1$ state by the Raman pulse back into $F = 2$ and they are then made to fluoresce with another $100\mu\text{s}$ pulse of resonant light from all telescope beams. By comparing the response, the fraction of transferred atoms can be determined.

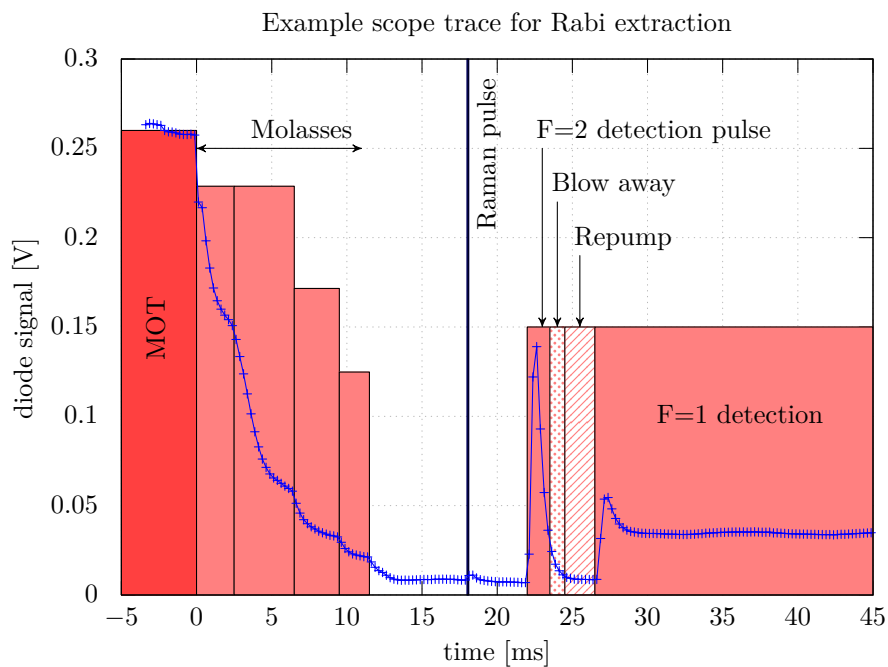


Figure 6.15: Example diode response from a sequence as in 6.14. The shown trace covers the end of the MOT phase ($t=0$ in the plot), the molasses phase and the various pulses to transfer population. To extract the amount of atoms transferred from $F = 2$ to $F = 1$, one needs to compare the height of the peak marked ‘not transferred’ with the one ‘transferred’ who correspond to the initially not transferred population (first peak) and the pumped $F = 1$ population (second peak). Pulses for the molasses are drawn in the background. The vertical separating lines indicate different frequencies, the height gives an indicator for their intensity (not to scale). Steps in the molasses phase include a linear shift in frequency while the lock adjusts to the new set point (see figure 5.9).

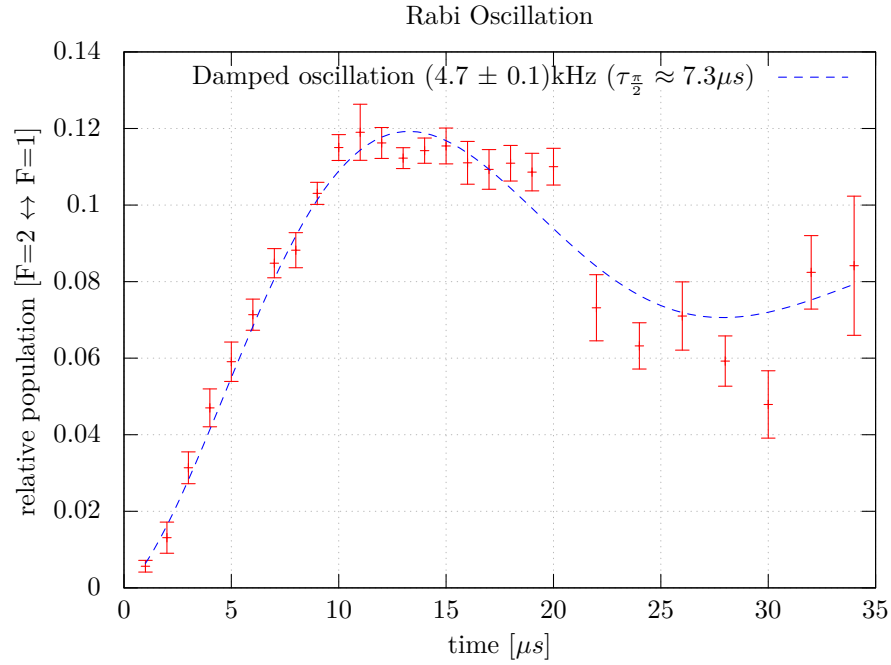


Figure 6.16: Population ratios for different *Raman pulse* lengths. As expected from a Raman induced population transfer, the ratio is oscillating over a period of $7.3\mu\text{s}$. The high damping of the oscillation is due to the wide velocity distribution in the initial cloud and imperfect population transfer and removal in the sequence.

signal. The high temperature of the cloud supports a fast decay due to the high velocity spread. The extracted $\frac{\pi}{2}$ time is $7.3\mu\text{s}$, which is in rough agreement with the model in figure 6.11 of $\approx 10\mu\text{s}$. Possible transitions between the two states and their relative strength are the main influences on the oscillation frequency. No preparation and the absence of a bias field lead to a high uncertainty in initial state and could therefore lead to this discrepancy.

6.6 Ramsey Fringes

Basic atom interference is, once Rabi oscillations have been observed, a single step away. A second, equal Rabi pulse, separated by a longer free evolution time from the first one closes a basic interferometer and produces *Ramsey fringes*. This method was originally developed for spectroscopy of molecules[113] and uses two oscillatory fields. As all interferometer schemes, it is able to map small changes to a bigger observable. This lead to the observation of a single photon in a cavity by a Rydberg atom travelling through two cavities[65, 66, 9]¹.

¹For these experiments the Nobel prize was awarded in 2012 to S. Haroche and J. Wineland

Ramsey fringes can be understood in the frequency picture[31], which is shortly presented in the following. A two level system of the states $|+\rangle$ and $|-\rangle$ in an external laser field of frequency ω_L and the *Rabi frequency* Ω , has the *Hamiltonian*

$$\begin{aligned}\mathcal{H} &= \mathcal{H}_0 + \mathcal{H}_I \\ &= \frac{\hbar\omega_0}{2} (|+\rangle\langle+| - |-\rangle\langle-|) + \frac{\hbar\Omega(t)}{2} (|+\rangle\langle-| e^{-i\omega_L t} + |-\rangle\langle+| e^{i\omega_L t})\end{aligned}\quad (6.15)$$

where the second part describes the interaction with the light field. The evolution of any quantum mechanical system is expressed through the evolution operator $|\Psi(t)\rangle = e^{-i\frac{\mathcal{H}}{\hbar}t} |\Psi(0)\rangle = U(t) |\Psi(0)\rangle$. Because we are interested in changes on short time scales, it is helpful to look at small perturbations of the operator by the interaction part of the Hamiltonian \mathcal{H}_I

$$U(t_f, t_i) = U_0(t_f, t_i) + \int_{t_i}^{t_f} U_0(t_f, t) \mathcal{H}_I U_0(t, t_i) dt \quad (6.16)$$

where $U_0(t)$ is the operator of the system Hamiltonian \mathcal{H}_0 . The evolution between the two states of the system reads

$$\langle+|U(t_f, t_i)|-\rangle = \int_{t_i}^{t_f} e^{-i\omega_0(t_f-t)/2} \frac{\Omega(t)}{2} e^{-i\omega_L t} e^{i\omega_0(t-t_i)/2} dt \quad (6.17)$$

$$= \frac{1}{2} e^{-i\omega_0(t_f+t_i)/2} \int_{t_i}^{t_f} \Omega(t) e^{i(\omega_0-\omega_L)t} dt \quad (6.18)$$

if the time variable is changed from $t \rightarrow t' = t - t_a$, the integral's borders become $t_i - t_a$ and $t_f - t_a$. The differences $t_a - t_i$ and $t_f - t_i$ are large compared to the pulse length τ , which means that the limits effectively extends to $\pm\infty$. The integral term now has the form as the *Fourier transformation* $g(\omega)$ of $\Omega(t_a + t')$ in units of $\omega_0 - \omega_L$. Therefore the evolution of the state is

$$\langle+|U(t_f, t_i)|-\rangle = \frac{1}{2} e^{-i\omega_0(t_f-t_i)/2} e^{i(\omega_0-\omega_L)t_a} g(\omega_0 - \omega_L). \quad (6.19)$$

The population transfer probability becomes

$$P_{|+\rangle}(\omega_0 - \omega_L) = |\langle+|U(t_f, t_i)|-\rangle|^2 = \frac{1}{4} |g(\omega_0 - \omega_L)|^2 \quad (6.20)$$

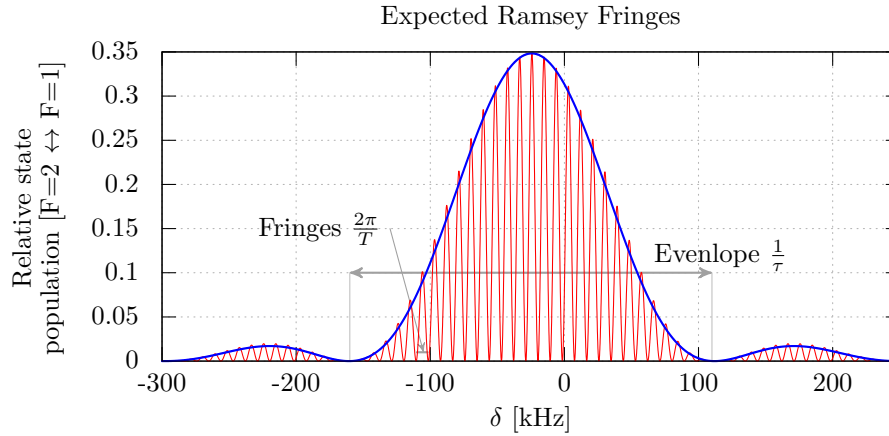


Figure 6.17: Expected Ramsey fringes for two pulses of $\tau = 7.3\mu s$ separated by $T = 100\mu s$. The curve was obtained with the same algorithm in figure 6.11 derived from equations (3.15) and (3.15). The red line shows the result of the complete sequence, the blue dashed line is the result of just a single pulse of time τ .

Because the state evolution is transformed from a state to a frequency picture, we expect a width of $\frac{1}{\tau}$ in frequency space of units $\omega_0 - \omega_L$ and after the first pulse was applied. Figure 6.17 shows an extension of the algorithm used in figure 6.11, implementing equations (3.15) and (3.16), by extending the sequence to two *Raman pulses* of $\tau = 7.3\mu s$ separated by the time $T = 100\mu s$. The blue dashed line shows the state of the system after a single pulse of time τ , the red solid line after the full sequence of $\tau - T - \tau$. The relatively low contrast is caused by the low state transfer probability already noticeable in figure 6.11. The model shows that a non centred envelope originates from non-compensated light shifts. Figure 6.12 shows that there is a power ratio of both *Raman beams* for which the additional detuning is completely compensated and the feature in figure 6.17 is centred around $\delta = 0$. For a full length *Ramsey sequence* consisting of two pulses of length τ and a gap of time T , the probability to find the system in the excited state reads

$$P_{|+\rangle}(\omega_0 - \omega_L) = \frac{1}{2} |g(\omega_0 - \omega_L)|^2 [1 + \cos((\omega_0 - \omega_L)T)] \quad (6.21)$$

which means that the envelope from equation (6.20) is modulated with a second oscillation with a spacing of $\frac{2\pi}{T}$. A scan of the frequency difference $\omega_0 - \omega_L$ is realised experimentally with a change in EOM frequency. This changes the detuning between the Rabi frequencies. Figure 6.18 shows the extracted population for a sequence of two $7.4\mu s$ pulses, separated by a $100\mu s$ gap. Population ratios were extracted the same way as explained in the previous section. Figure 6.18 shows two such measurements, for different sampling interval. The oscillation of the sub structure is clearly visible, however the envelope shape cannot be guessed due to drift and contrast issues.

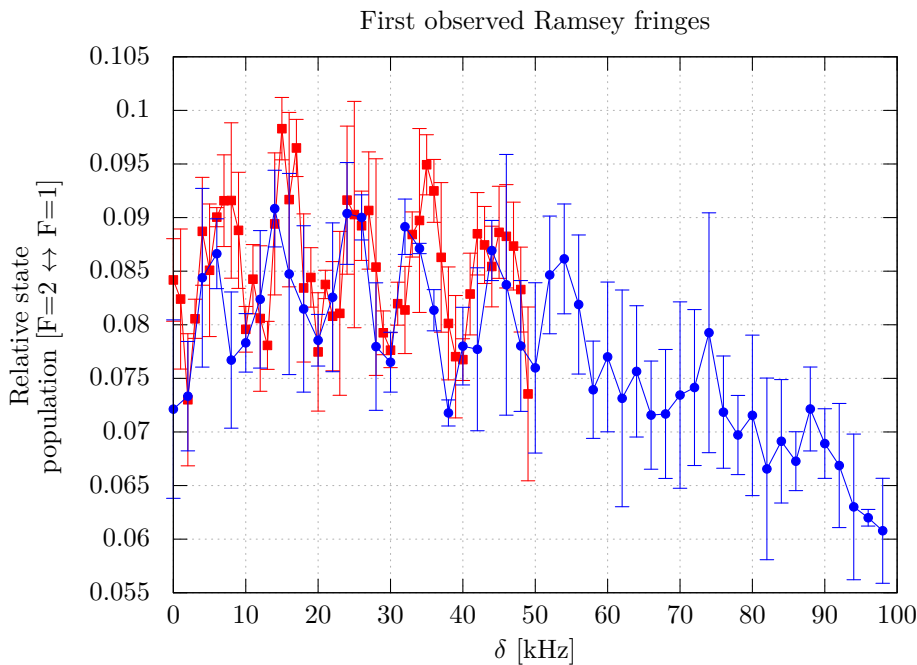


Figure 6.18: Ramsey fringes from two measurement sets with different frequency steps (red 1kHz, blue 2kHz). The rf frequency used to drive the EOM in the Raman laser system (figure 5.19) is scanned and the population ratio of the two states extracted as in figure 6.15. The two pulses are $7.4\mu\text{s}$ long with a separation of $100\mu\text{s}$.

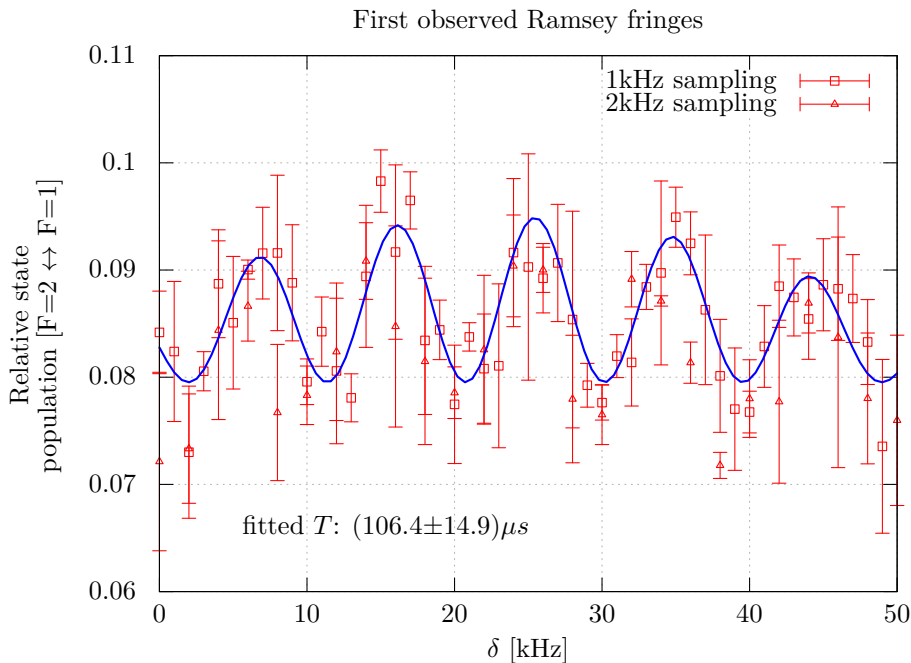


Figure 6.19: Zoom of the data from figure 6.18. A sine wave modulated by a \sin^2 envelope and an offset has been fitted. The spacing of the fringes recovers the pulse separation time of $100\mu\text{s}$. The τ pulse time cannot be extracted

Figure 6.19 shows the region of overlap between 0kHz and 50kHz. A \cos^2 function modulated with a second \cos^2 function and a global offset was fitted to the data (dashed line) to extract the spacing of the pulses T . The found result of $(109.4 \pm 14.9)\mu s$ is in agreement with the used spacing of $T = 100\mu s$.

Ramsey fringes in a co-propagating configuration are a first step towards a full interferometer sequence because the insensitivity to Doppler shifts makes it easier to find, as the constraints on the cloud temperature are relaxed. Another complication for interferometer paths of atoms using *Raman pulses* is that they separate further which brings the problem of aligning the interferometer in a way that their trajectories meet again. A miss of overlap can be caused by movement or rotation of the apparatus during the sequence time.

Gravity Value Extraction

To extract a value of local acceleration from the atom interferometer's output, the population in the $F = 2$ and $F = 1$ states is measured. Similar to equation (6.21), the probability of find an atom in the excited state ($F = 2$) is (see equation (3.33))

$$P_{|e\rangle} = \frac{1}{2} [1 - \cos(\Phi_{\text{total}})] \quad (6.22)$$

$$= \frac{1}{2} [1 - \cos(\mathbf{k}_{\text{eff}}\mathbf{g}T^2 + \phi_1 - 2\phi_2 + \phi_3)]. \quad (6.23)$$

For the discussed Raman laser system $\phi_1 - 2\phi_2 + \phi_3 = 0$ holds, because the second frequency is generated by an EOM and the pulses have therefore a common phase reference. If now the phase of the driving frequency is scanned in phase, a sinusoidal curve is expected. Fitting the recorded values to the above equation yields a value for $\mathbf{k}_{\text{eff}}\mathbf{g}T^2$ and therefore an estimate for \mathbf{g} .

However under normal conditions $\mathbf{k}_{\text{eff}}\mathbf{g}T^2 \gg 2\pi$ which leaves an uncertainty and requires an initial knowledge of \mathbf{g} for the above method. To eliminate this ambiguity, the separation between the two Raman frequencies is chirped, which adds an additional phase shift. Keeping the phase relation of the lasers constant and just varying the chirp rate allows to find a setting[123] where

$$\mathbf{k}_{\text{eff}}\mathbf{g}T^2 + \Delta_{\text{chirp}} = 0. \quad (6.24)$$

Alternatively the pulse separation T can be altered and a fringe depression identified whose position does not change[24]. Identification of this setting has two advantages: it eliminates the ambiguity and it allows faster gravity estimations. While fitting a sine function requires measurement of multiple data points, the system

operate at the steepest part of the slope on either side of the centre fringe. If a change in gravity alters the signal, it can easily be calculated under the assumption that it did not change the phase by more than 2π . This requires significantly less time and therefore increases the measurement speed.

6.7 Stability

Although interference fringes are clearly visible in figure 6.6, they are of low contrast and have a varying offset. Non optimal molasses temperatures are the most likely cause for the low contrast. The best temperatures reached are in the order of $20\mu K$, which is an order of magnitude above the desired goal. A high atom temperature and therefore a large velocity spread leads to a quick expansion of the cloud which causes reduced overlap, but also less contributing atoms to the signal at a given point within the cloud. Variations like this originate from intensity fluctuations in the magneto optical trap. Polarisation impurities that have built up while the light travels through the fibre network are compensated for with a polariser in every telescope which translates polarisation instabilities to intensity instabilities. Figure 6.20 shows an image of a PANDA¹ type core fibre as it is used in the network. The light mode is guided in the central, $\approx 5\mu m$ large, core with two adjacent stress structures. These additional bigger features maintain constant pressure on the central core and induce birefringence, which leads to the support of only a single linear polarisation. This polarisation is oriented along either the ‘slow’ or ‘fast’ axes of the fibre. The rotation is referenced with a key, marked with a dotted feature on one side, aligned to the slow axis here. The central and stress cores of two adjacent fibres need to be carefully aligned in splices and fibre coupled devices. Any deviation leads to light in the other channel. Light modes of both axes interfere at the fibre exit and create, depending on the current phase shift between the two, arbitrary polarisations from linear over elliptical to circular. Small temperature or mechanical disturbances change the local birefringence of the fibre and with it the refractive index. This is caused by local shadowing of the wanted stress on the core and creates the observed polarisation fluctuations.

The mere size and length of the network causes small errors to build up as the light travels through multiple splices and components. While a polarisation maintaining fibre patchcord is specified to extinction ratios² around 30dB, light at outputs of the network only reaches 5dB to 10dB. This value changes during the day depending on the heat emitted by individual components and external fluctuations. The resulting power imbalances are problematic, especially in the opposing ports of the MOT, because they are uncorrelated.

¹Polarisation maintaining **AND** Absorption reducing

²the ratio of polarisation in the two axes

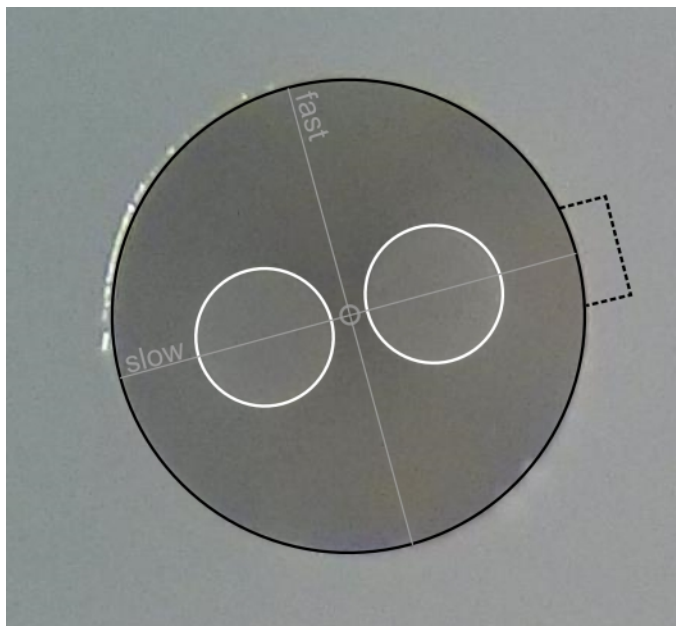


Figure 6.20: Image of a PANDA type polarisation maintaining fibre. The individual features are highlighted for better visibility. The gray central circle is the light carrying core of $\approx 5\mu\text{m}$. The white circles enclose the stress cores which create birefringence in the main core that only one polarisation mode is supported. The dotted feature marks the position of the key on the fibre connector if aligned to the slow axis. Polarised light is conducted along both axes, the used devices uses keys oriented to the slow one.

This leads to force imbalances in the trap and ultimately to a movement of the atom cloud.

Figure 6.21 features power fluctuations in a 3D MOT telescope recorded with a polarising beam cube for pick up and a photo diode. 6.21 a) shows a short time measurement where the fibre was manually moved after 0.4s. Fluctuations in the output power correlate with the movement as the changed position of the fibre causes birefringence in the core. If the injected polarisation is not clean, such small changes will cause larger polarisation changes. 6.21 b) shows a long term measurement without artificial influences. The observed changes caused by thermal fluctuations are enough to induce power fluctuations in the order of 15%.

6.7.1 Experimental Reproducibility

Section 2.2 hinted that intensity changes in the trapping beams do lead to power imbalances, which influence the traps centre. Figure 6.22 shows extracted cloud centres, taken from a series of temperature measurements. They were found by fitting a two dimensional gaussian profile to the absorption image. The initial position is marked in red and over the course of 40 minutes to the blue marked points. In this time, the trap centre shifts upwards, does a fast movement to the left side and slowly moves back towards the starting position. Additionally the atom number is reduced at position further away from the starting by up to an order of

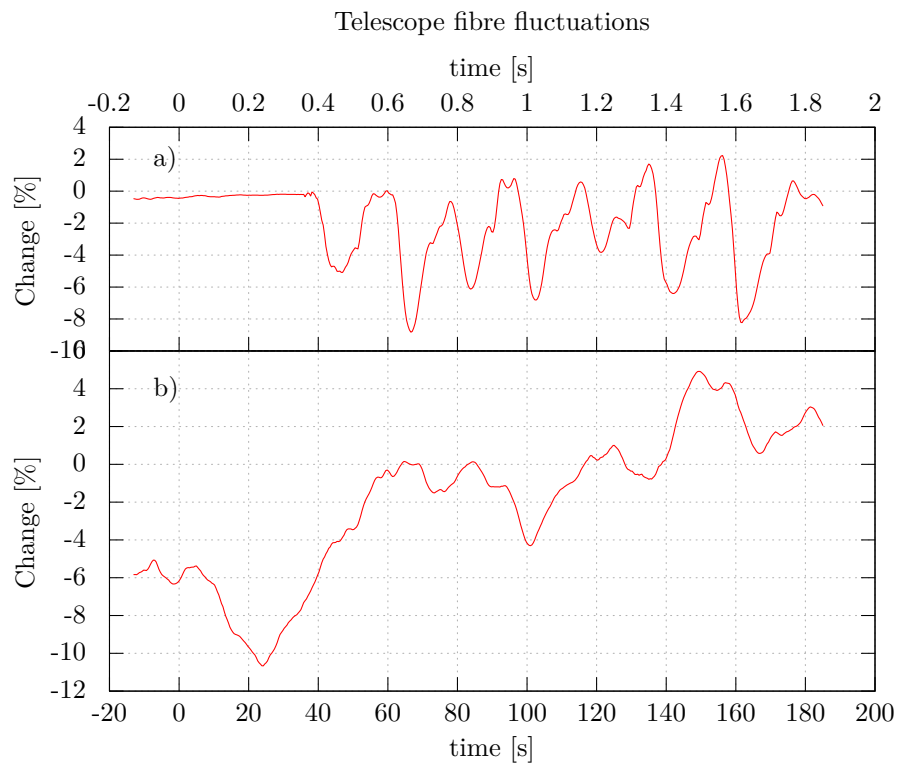


Figure 6.21: Power fluctuations measured by reflecting parts of the beam power onto a diode. a) starting from 0.4s, a manual disturbance was introduced by moving the fibre. b) Long term power drifts without artificial influence. 100% on the x-axis is defined as the average value of the measurement.

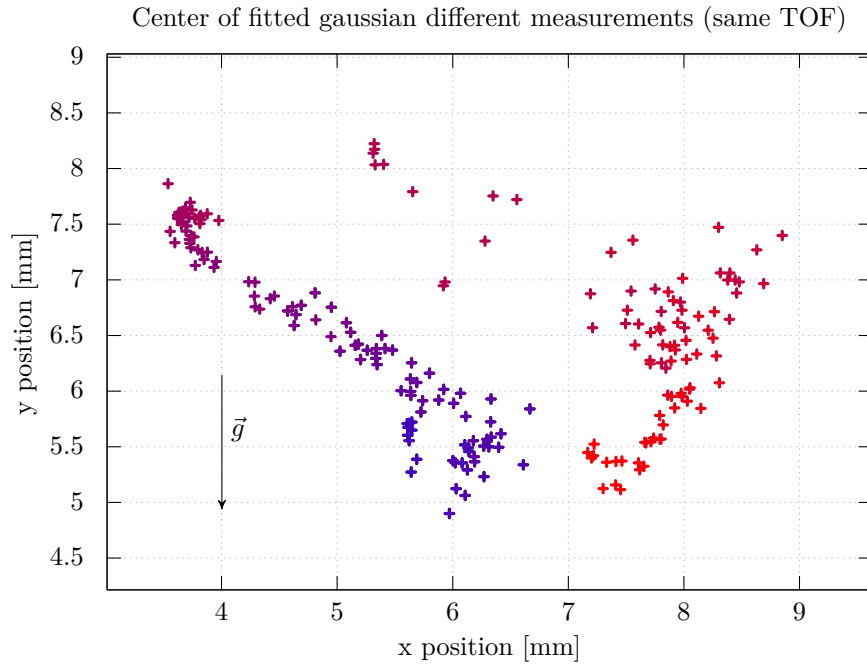


Figure 6.22: Centre of a fitted Gaussian to images taken with the same time of flight but consecutively over 40 minutes. The linear time axis is encoded in the colour of the positions, going from red to blue. Accompanied with the drift is a reduction in atom number by up to a factor of two for position away from (6.0mm,5.5mm), the optimal position.

magnitude. Power imbalances do not only lead to shifted centre of traps but can also produce complex trapping patterns[128]. In combination with slightly misaligned beams, geometries reaching from extended cigar shapes to ring formations[10] are possible.

The biggest experimental problem with drifts is the non-reproducibility of the atom cloud's temperature and position. For example a changed starting position significantly alters the trajectory from a moving molasses. Also molasses phases are sensitive to power changes. Figure 6.23 shows one consequence, if the power imbalance in the 3D MOT is shifted to a position where the trap becomes unstable. The jigsaw pattern is created while the trap loads, becomes unstable and reverts to a more stable position but with less atoms, moves slightly which enables loading of more atoms for a short time but oscillates back to lossy position. This type of error is the significant source of contrast loss and high cloud temperatures, which currently limits the experiment.

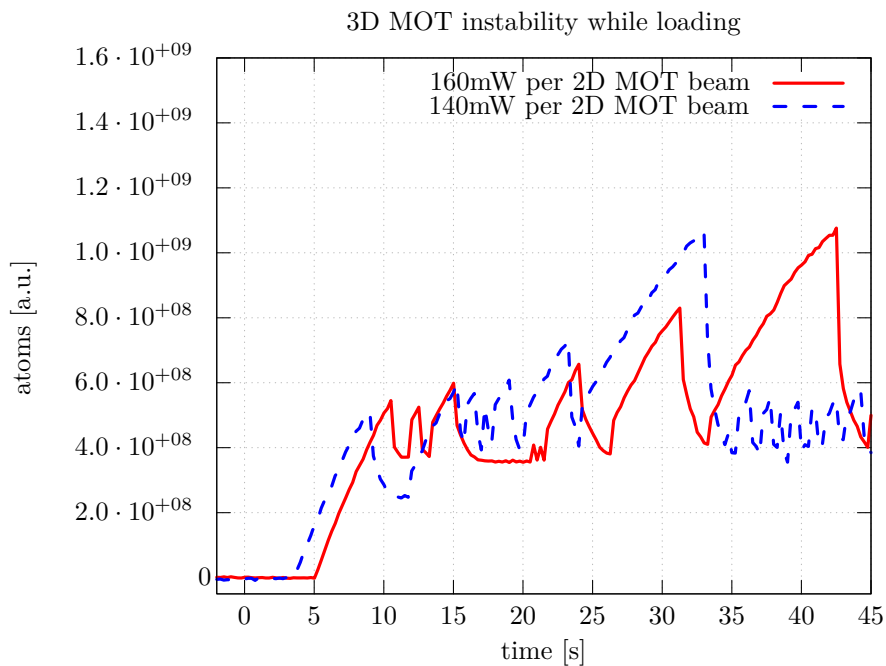


Figure 6.23: Fluorescence from the 3D MOT while loading with different powers in the 2D MOT. The traps seems to be stable at an intermediate position, load and then collapse back randomly.

Summary

This chapter described the basic performance of the experiment and presented measured temperatures of the atomic cloud. Although strong limitations due to the stability of the used fibre network are imposed, a vertical launch of the atomic cloud as well as basic interference fringes, using a Ramsey sequence, were demonstrated. This puts the apparatus in a position where it can be used as basis from which with further improvement. An atom interferometer to measure local gravity can be constructed. The current performance of the system is highly limited by the polarisation stability of the fibre network.

7 Conclusion

Although the last chapter finished with the current drawbacks of the experimental design, the complete project is well capable of measuring gravity within the next year. The main challenge does not lie within the physics behind atom interferometry but the engineering necessary to build a system that can function in changing conditions. For this purpose greater emphasis was put on the discussion of design choices which enable a portable system. While the integration of custom laser systems was left open for a next iteration of the system, the main difference to conventional, lab based experiments is the compact fibre network for light delivery. The presented work showed that the network bears more problems than anticipated, even in a controlled environment, such as a laboratory. More specialised tests investigating the performance, especially the polarisation stability, of fibre components and fibre splices will help to understand possible limitations and show solutions.

However within the capabilities of the system, sufficient performance of the atom trap, basic launch facility and atom interference was demonstrated as milestones towards gravity measurements. The currently limiting parameter was identified as the polarisation stability of the used fibre network which has twofold consequences: polarisation and intensity fluctuations lead equally to changing trap parameters which result in varying starting conditions for the atom interferometer sequence. The changing cloud temperature, position and size washes out contrast as the cloud moves inside the Raman beam and therefore adds uncontrollable phase additions to the signal.

Outlook

Changing birefringence along the fibre length is the major, misalignment in splices and in-fibre components minor, cause of drifting polarisation at the output of the fibre. Any thermal or mechanical change alters the conditions and creates different stress on the fibre's core and therefore changing polarisation. Isolation of the system can reduce the effect but is unlikely to completely eliminate it due to the sensitivity over the

full network's length. As passive measures are limited, active methods can provide help. One approach was presented in chapter 4 in a different context. Originally intended to serve as a device to quickly change between two distinct polarisation settings, it can be extended to an active correction system. The liquid crystal retarder's (LCR) driving signal can change between two static amplitude settings by switching between two gain settings in an amplification loop. If the gain defining resistors and the switch are replaced by a digital potentiometer, arbitrary settings and hence retardance are possible. In combination with a compact polarisation readout stage in, for example the telescope, a feedback loop could be build to stabilise the polarisation of the light. The correction is limited by the reaction speed of the LCR elements but if passive isolation provides a high enough damping, it is well within reach. One alternative is the direct manipulation of the phase relation between the fast and slow axis of the emitted light. The stress on the fibre core could be changed to produce the desired condition. An external piezo electric element exerting force on an area just before the coupler could be one solution. However constantly changing stress and potentially in a non safe region could degrade the optical guiding capabilities. To move the modification outside of the fibre, an electro optical modulator could be placed at the fibre. Although non invasive on the fibre, this approach does require significant electronic support.

Gravity Signals and Gravity Gradiometry

The targeted application is the localisation of underground structures with increased accuracy and speed over available sensors. Although both are intrinsic features of an atom interferometer, gravity signals suffer from rapid loss of contrast at larger distances because the signal falls of with $1/r^2$ (see equation 1). One way around this problem is to look at the gravity gradient. For a point source of mass M , the change of the vertical (z) gravity component is

$$\frac{\partial g_z}{\partial z} = \frac{GM(x^2 + y^2 - 2z^2)}{(x^2 + y^2 + z^2)^2} \quad (7.1)$$

where G is the gravitational constant. Figure 7.1 shows the simulated acceleration along z created by a cube of unit size and density located at the origin. Shown are traces for measurements at a height for $z = 3$ and $z = 4$. The fast decrease in signal strength and the absence of features of the source are noticeable. The gradient of the two, although smaller in amplitude, decays less quickly with increasing distance and still carries information about the source's shape. It also shows a zero crossing, respective decrease to almost zero, at a characteristic distance which makes it easier to locate objects. Specifically atom interferometers gain from high common noise rejection if operated in a gradiometer configuration. This is specifically helpful if the device is to operate in a noisy environment and active stabilisation methods alone are not enough.

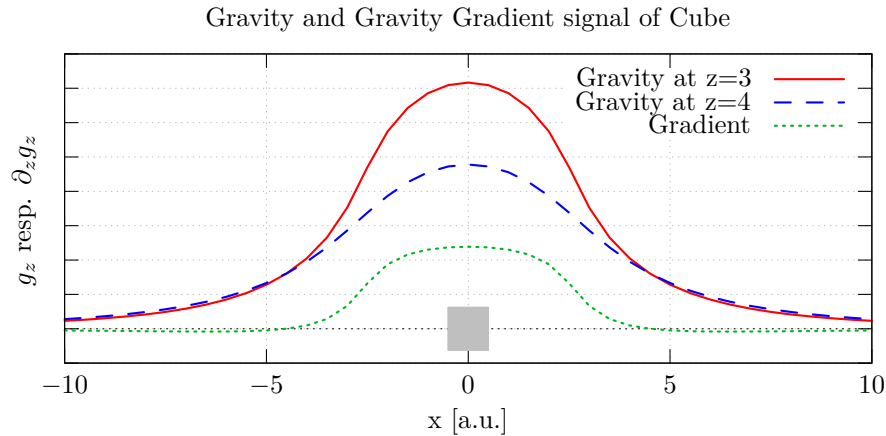


Figure 7.1: Vertical component of the gravitational acceleration created by a cube of unit size located at the origin of the coordinate system. The curves shown for measurements at heights $z = 3$ and $z = 4$ illustrate the rapid decay and fast approach of a Gaussian shape, hiding all of the source structure. The gradient, difference of the two signals, preserves contrast and shape of the source.

The gradient may also help to overcome the inversion problem: An object at a distance d produce the same gravitational potential as an object half the size at a distance $\sqrt{2}d$. By investigating more components of the gravity tensor, the ambiguity cannot be completely eliminated but at least reduced.

This project showed also that the technology atom interferometry is getting ready to leave the laboratory and become a compact system. This opens a wider range of applications as sensor arrays can be used when sensors become smaller. For example a gravitational wave sensor, with a different sensitivity spectrum than laser interferometer based systems, could be built [41, 40, 135]. The reachable commercial application includes the search for resources, for which already Eötöv's device was used but also long and short range monitoring. Precise gravity maps can, if created on a global scale, be used to monitor the thickness of ice shields or ground water levels, but also for navigation. A submarine needs to surface in regular intervals to confirm its position. However with a precise gravity sensor it could use the local signal and compare it to a pre-recorded map to do the same. Even active navigation by monitoring the changing signal and hence looking for sub sea mountain ridges or cliffs is possible. The specific use depends on the achievable performance of the sensor's reading but the discussion and experimental work show that atom interferometry has the potential to become the next generator of mobile sensors that can measure gravity to a previously unknown precision.

Appendix **A** Raman transitions in Rb87

Raman transitions connect the stable $F=1$ and $F=2$ states of rubidium (see figures 3.2 and 2.7). The expressions for the transition elements in equations (3.41) and (3.43) depend on the polarisation of the absorbed and emitted photon. Figure A.1 shows allowed transitions that connect $F=1$ and $F=2$ in colour, generally possible transitions in gray. The polarisation of the absorbed and emitted photon are the same, hence no paths with mixed polarisations are possible. The equation system describing the evolution the system in presence of two *Raman fields* (equations (3.15) and (3.16)) contains two *Rabi frequencies*, Ω_1 and Ω_2 connected with the two fields. Depending on the polarisation of the Raman light, the dipole element is a sum of all possible transitions and coupling combinations.

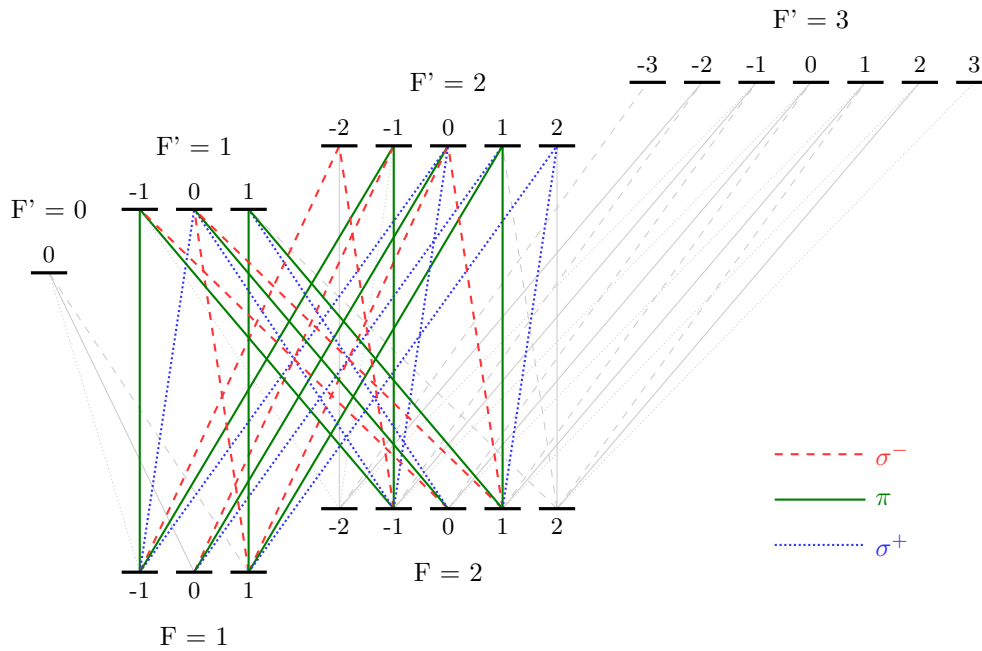


Figure A.1: Transitions driven in a *Raman pulse* to transfer population between the $F=1$ and $F=2$ states of Rubidium via different intermediate levels. Promotion to any of the F' levels is done by absorbing a photon of the appropriate polarisation, decay from F' to F via emission. Lines in bold and colour indicate transitions that will transfer between $F=1$ and $F=2$ while thin gray lines indicate in general possible transitions. Because a photon of the matching polarisation needs to be emitted in the Raman field, they are not contributing.

Appendix **B** Arduino firmware

Code used to generate a 2kHz square wave with the registers of the of an Atmega328. Registers were changed to create a down-sampled square wave with a stable 50% duty cycle from the 16MHz on-board clock. Once set in the `setup{}` code block, they take immediate effect and a 2kHz 0V to 5V square wave is output on pin 11. Additionally, to give a visual feedback on the trigger pins, the main program loop sets output pins connected to LEDs depending on the signal on an input pin for visual feedback.

```
// define the timer to count
#define CntValue 16000000 / 126000 / 1
// define the output and input pins
#define squarePin 11
#define sensorPin 3
#define state1Pin 4
#define state2Pin 5

void setup()
{
    // Enable timer 0 by disabling the power safe mode (ATMEGA328 manual page 94)
    PRR = 0;    // disables all power saving, default state

    // set the digital pinsn to output mode
    pinMode(sensorPin , INPUT);    // input to detect switch
    pinMode(state1Pin , OUTPUT);    // output indicator state 1
    pinMode(state2Pin , OUTPUT);    // output indicator state 2
    pinMode(squarePin , OUTPUT);    // 2 khz output pin
}
```

```
// set the timers for pin 11 and 3
TCCR2B = 0;          // stop timer2
TCNT2 = 0;          // clear timer2 counter
// adjust registers
TCCR2B = _BV(WGM22);
TCCR2A = _BV(WGM21) | _BV(WGM20);
TCCR2A |= _BV(COM2A0);
OCR2A = CntValue;
TCCR2B |= _BV(CS21) | _BV(CS20);
}
// give visual feedback on the trigger state
void loop()
{
  if (digitalRead(sensorPin)) {
    digitalWrite(state1Pin, HIGH);
    digitalWrite(state2Pin, LOW);
  } else {
    digitalWrite(state1Pin, LOW);
    digitalWrite(state2Pin, HIGH);
  }
}
```

Appendix **C** Laser Locking

C.1 Offset lock components

Microwave components used in the offset locks (see scheme in figure 5.8). An image of the circuit is shown in figure C.1 below. Tables C.1 and C.2 list the used components in order of usage starting with the beat signal on the diode and mix in frequencies respectively.

The beat nodes of the repump, respective cooling laser, with the locked master laser are recorded on a Thorlabs FDS02 photo diode. Both are reverse biased by MiniCircuits bias tees in the appropriate frequency range and the resulting signals amplified before being mixed with synthesized frequencies to create the difference of both in the region of 174MHz. This cut-off frequency is set by the low pass filter in the error signal board[115] and sets the zero crossing of the produced DC signal if the incoming frequency passes this limit (see figure 5.9). Before being fed into this board the signals are conditioned with low frequency amplifiers (up to 500MHz), low pass filters to eliminate unwanted sum or difference signals and a power limiter to ensure optimal performance of the board.

5.5GHz arm (repumper)			
Light input		Oscillator input	
Fast photo diode	Thorlabs FDS02	Oscillator	AME LO-45C-2200
Bias tee	MiniCircuits ZX85-12G+	Doubler	MiniCircuits ZX90-2-36-S+
High frequency amplifier	MiniCircuits ZX60-8008E+	Mixer	MiniCircuit ZXM-10G+
	Low frequency amplifier		MiniCircuit ZFL-500LN+
	Splitter		MiniCircuit ZFM-2-5+
	Low pass filter		MiniCircuit ZX75LP-158-S+
	Power Limiter		MiniCircuit VLM-33-5+
Error signal board			

Table C.1: Repumper beat microwave circuit

1.2GHz arm (cooler)

Light input		Oscillator input	
Fast photo diode	Thorlabs FDS02	Oscillator	AME LO-45C-0830
Bias tee	MiniCircuits ZFBT-4R2GW-FT+	Mixer	MiniCircuits ZX05-20H
High frequency amplifier	MiniCircuits ZJL-9G+	Amplifier	MiniCircuits ZX60-43-S+
	Mixer	MiniCircuit	MSC-2-5+
	Low frequency amplifier	MiniCircuit	ZFL-500LN+
	Splitter	MiniCircuit	ZFM-2-5+
	Low pass filter	MiniCircuit	ZX75LP-158-S+
	Power Limiter	MiniCircuit	VLM-33-5+
Error signal board			

Table C.2: Cooler beat microwave circuit

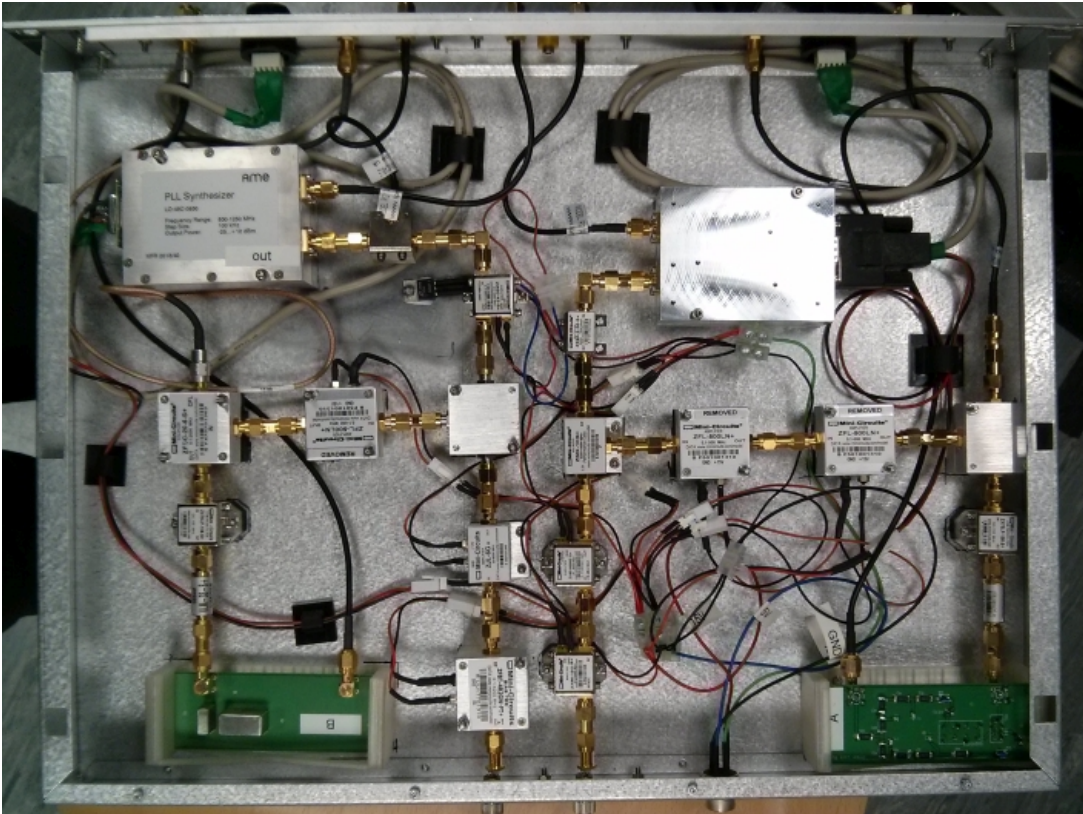


Figure C.1: Picture of the opened offset circuitry box. Mixed light is injected at the bottom centre in the respective arms (repumper on the right, cooler on the left).

C.2 Laser stability

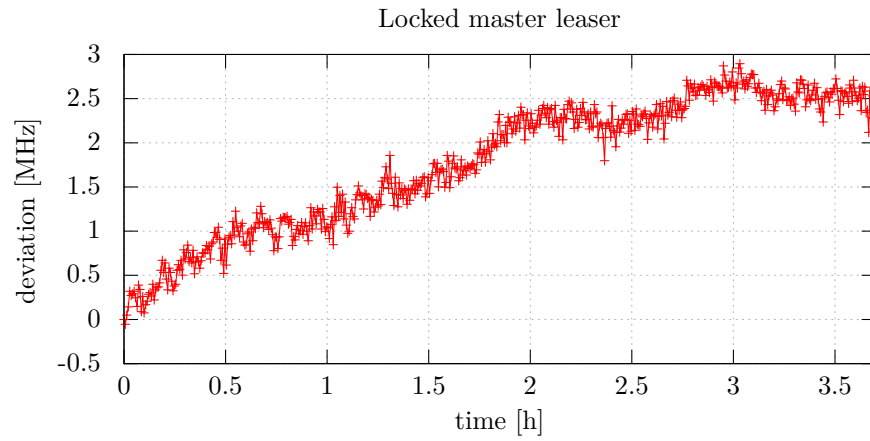


Figure C.2: Recorded trace of the stabilised frequency of the master laser. The measurement was performed using a High Finesse WSU2 wavelength meter, which uses a internal cavity. The drift is believed to originate from thermal expansion of said cavity as under operation of the atom trap, no readjustment of the lock is necessary and frequency dependent trapping performance is stable over a day of operation.

Appendix **D** AOM characteristics

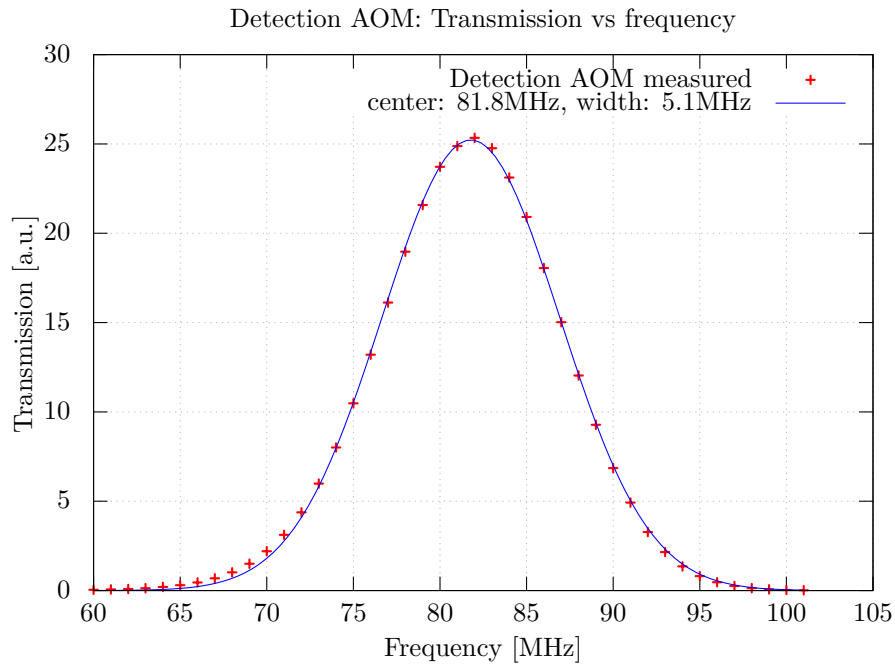


Figure D.1: AOM transmission for different input frequencies. Measured at the detection AOM.

Appendix **E** Apparatus images

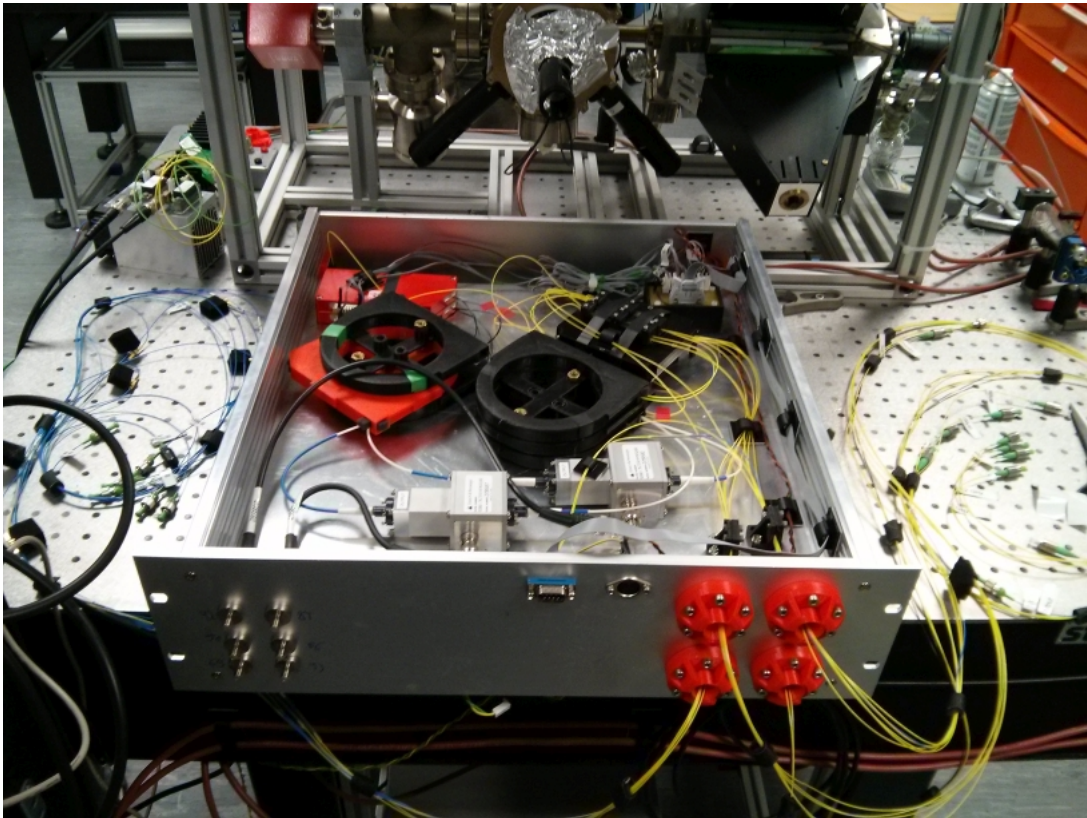


Figure E.1: Open fibre network box showing the upper layer with fibre splitters mounted in blue and black plastic protectors, fibre coupled AOMs (silver boxes with blue in- and output fibres) and fibre switches (red boxes in the far left corner).

Appendix F Atom Launch

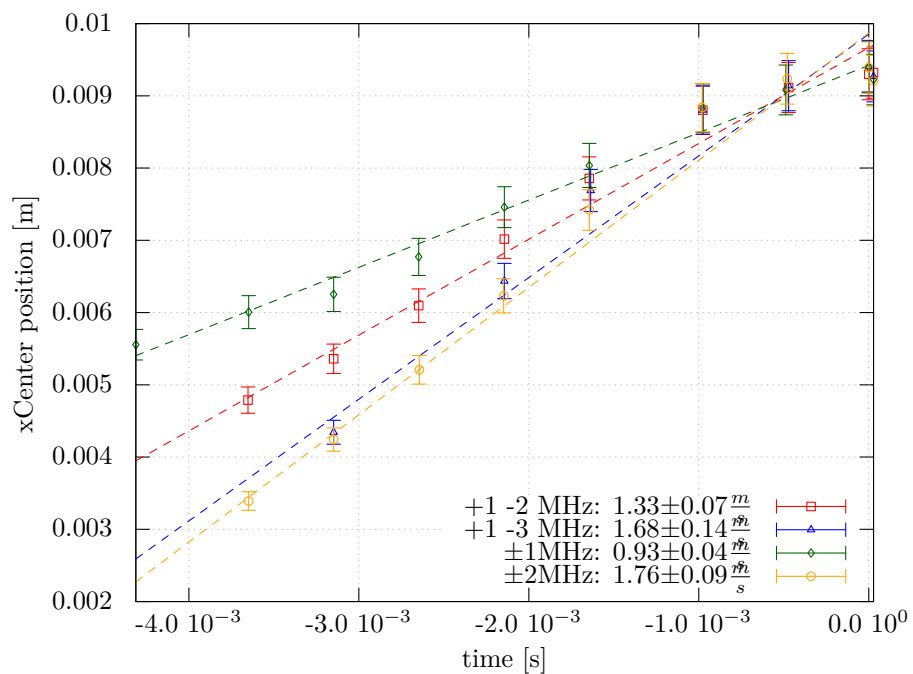


Figure F.1: Shown are the position of launched atom cloud in time for different detunings. Image were taken in fluorescence. The origin in the analysis program is in the top left corner of the image, hence the position decreases while the cloud moves upwards. The time reference was adjusted accordingly.

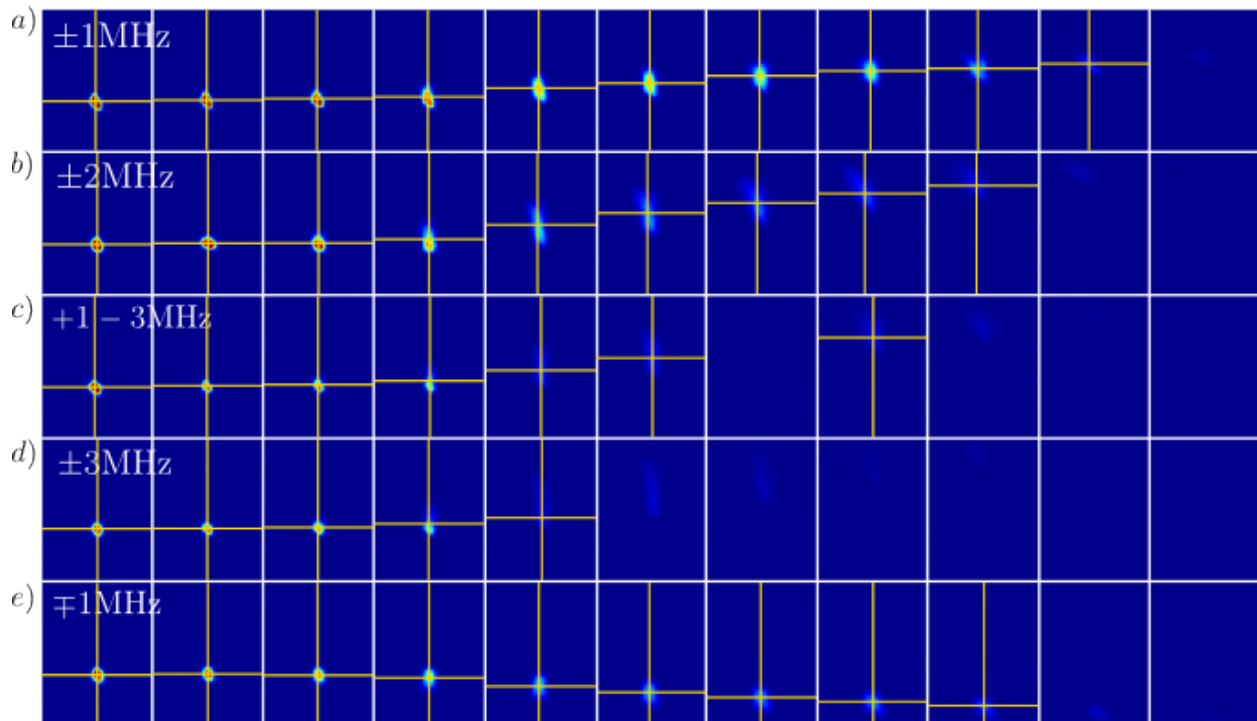


Figure F.2: Images of launched clouds for different detunings. a) to d) show positive detuning in the down facing beams, negative in the up facing beam, leading to upwards vertical launch. According to equation (6.13), only the sum of the absolute detunings should influence the speed. Although b) and c) should lead to the same frame velocity, the number of accelerated atoms differ. b) seems more effective, allowing for a longer tracing of the atoms. e) shows opposite detuning to a), leading to a downward acceleration. Atoms in a) wove with $0.94 \frac{m}{s}$, atoms in e) with $-0.93 \frac{m}{s}$, as expected with the same speed but in opposite directions. Yellow lines indicate the centre of clouds found by the algorithm and used in figure F.1 to determine the speed

List of References

- [1] ADAMS, C., AND RIIS, E. Laser cooling and trapping of neutral atoms. *Progress in Quantum Electronics* 21, 1 (January 1997), 1–79.
- [2] AGUILERA, D. N., AHLERS, H., BATTELIER, B., BAWAMIA, A., BERTOLDI, A., BONDARESCU, R., BONGS, K., BOUYER, P., BRAXMAIER, C., CACCIAPUOTI, L., CHALONER, C., CHWALLA, M., ERTMER, W., FRANZ, M., GAALLOUL, N., GEHLER, M., GERARDI, D., GESA, L., GÜRLEBECK, N., HARTWIG, J., HAUTH, M., HELLMIG, O., HERR, W., HERRMANN, S., HESKE, A., HINTON, A., IRELAND, P., JETZER, P., JOHANN, U., KRUTZIK, M., KUBELKA, A., LÄMMERZAHN, C., LANDRAGIN, A., LORO, I., MASSONNET, D., MATEOS, I., MILKE, A., NOFRARIAS, M., OSWALD, M., PETERS, A., POSSO-TRUJILLO, K., RASEL, E. M., ROCCO, E., ROURA, A., RUDOLPH, J., SCHLEICH, W. P., SCHUBERT, C., SCHULDT, T., SEIDEL, S., SENGSTOCK, K., SOPUERTA, C. F., SORRENTINO, F., SUMMERS, D., TINO, G. M., TRENKEL, C., UZUNOGLU, N., VON KLITZING, W., WALSER, R., WENDRICH, T., WENZLAWSKI, A., WESSELS, P., WICHT, A., WILLE, E., WILLIAMS, M., WINDPASSINGER, P., AND ZAHZAM, N. STE-QUEST test of the universality of free fall using cold atom interferometry. *Classical and Quantum Gravity* 31, 11 (2014), 115010.
- [3] ALTIN, P. A., JOHNSON, M. T., NEGNEVITSKY, V., DENNIS, G. R., ANDERSON, R. P., DEBS, J. E., SZIGETI, S. S., HARDMAN, K. S., BENNETTS, S., McDONALD, G. D., TURNER, L. D., CLOSE, J. D., AND ROBINS, N. P. Precision atomic gravimeter based on Bragg diffraction. *New Journal of Physics* 15, 2 (February 2013), 023009.
- [4] AMMANN, H., AND CHRISTENSEN, N. Delta Kick Cooling: A New Method for Cooling Atoms. *Physical Review Letters* 78, 11 (mar 1997), 2088–2091.
- [5] ARPORNTHIP, T., SACKETT, C. A., AND HUGHES, K. J. Vacuum-pressure measurement using a magneto-optical trap. *Physical Review A* 85, 3 (March 2012), 033420.
- [6] ASHKIN, A. Trapping of Atoms by Resonance Radiation Pressure. *Physical Review Letters* 40, 12 (March 1978), 729–732.
- [7] ASHKIN, A. Applications of Laser Radiation Pressure. *Science* 210, 4474 (December 1980), 1081–1088.
- [8] ASHKIN, A., AND GORDON, J. P. Stability of radiation-pressure particle traps: an optical Earnshaw theorem. *Optics Letters* 8, 10 (October 1983), 511.

- [9] AUFFEVE, A., MAIOLI, P., MEUNIER, T., GLEYZES, S., NOGUES, G., BRUNE, M., RAIMOND, J. M., AND HAROCHE, S. Entanglement of a Mesoscopic Field with an Atom Induced by Photon Graininess in a Cavity. *Physical Review Letters* *91*, 23 (December 2003), 230405.
- [10] BAGNATO, V. S., MARCASSA, L. G., ORIA, M., SURDUTOVICH, G. I., VITLINA, R., AND ZILIO, S. C. Spatial distribution of atoms in a magneto-optical trap. *Physical Review A* *48*, 5 (November 1993), 3771–3775.
- [11] BARRETT, B., GOMINET, P. A., CANTIN, E., ANTONI-MICOLLIER, L., BERTOLDI, A., BATTELIER, B., AND BOYER, P. Mobile and remote inertial sensing with atom interferometry. In *Proceedings of the International School of Physics "Enrico Fermi" Course 188 "Atom Interferometry"* (Bologna, 2014), G. M. Tino and M. A. Kasevich, Eds., IOS, Amsterdam; SIF, Bologna.
- [12] BERG, P., ABEND, S., TACKMANN, G., SCHUBERT, C., GIESE, E., SCHLEICH, W. P., NARDUCCI, F. A., ERTMER, W., AND RASEL, E. M. Composite-Light-Pulse Technique for High-Precision Atom Interferometry. *Physical Review Letters* *114*, 6 (February 2015), 063002.
- [13] BERTHOUD, P., FRETTEL, E., AND THOMANN, P. Bright, slow, and continuous beam of laser-cooled cesium atoms. *Physical Review A* *60*, 6 (December 1999), R4241–R4244.
- [14] BLATT, R., ERTMER, W., AND HALL, J. L. Cooling of an atomic beam with frequency-sweep techniques. *Progress in Quantum Electronics* *8*, 3-4 (January 1984), 237–248.
- [15] BLOCH, D., RAJ, R. K., PENG, K. S., AND DUCLOY, M. Dispersive Character and Directional Anisotropy of Saturated Susceptibilities in Resonant Backward Four-Wave Mixing. *Physical Review Letters* *49*, 10 (September 1982), 719–722.
- [16] BODART, Q. *Gravimétrie atomique: amélioration de l'exactitude et nouvelles géométries*. PhD thesis, Université de Paris, 2010.
- [17] BONGS, K., LAUNAY, R., AND KASEVICH, M. A. High-order inertial phase shifts for time-domain atom interferometers. *Applied Physics B* *84*, 4 (September 2006), 599–602.
- [18] BONSE, U., GRAEFF, W., AND RAUCH, H. Measuring angular deviations of neutrons of the order of 10^{-3} sec of arc. *Physics Letters A* *69*, 6 (January 1979), 420–422.
- [19] BORDÉ, C. J. Atomic interferometry with internal state labelling. *Physics Letters A* *140*, 1-2 (September 1989), 10–12.
- [20] BORDÉ, C. J., SALOMON, C., AVRILLIER, S., VAN LERBERGHE, A., BRÉANT, C., BASSI, D., AND SCOLES, G. Optical Ramsey fringes with traveling waves. *Physical Review A* *30*, 4 (October 1984), 1836–1848.
- [21] CASTIN, Y., AND DALIBARD, J. Quantization of Atomic Motion in Optical Molasses. *Europhysics Letters (EPL)* *14*, 8 (April 1991), 761–766.

- [22] CATALIOTTI, F. S., CORNELL, E. A., FORT, C., INGUSCIO, M., MARIN, F., PREVEDELLI, M., RICCI, L., AND TINO, G. M. Magneto-optical trapping of Fermionic potassium atoms. *Physical Review A* 57, 2 (February 1998), 1136–1138.
- [23] CHARRIERE, M. R. *Optimisation d ’ un capteur inertielle à atomes froids par une nouvelle technique de mesure accélérométrique combinant interférométrie atomique et oscillations de Bloch*. PhD thesis, 2011.
- [24] CHEINET, P., DOSSANTOS, F. P., PETELSKI, T., LE GOUËT, J., KIM, J., THERKILDSEN, K., CLAIRON, A., AND LANDRAGIN, A. Compact laser system for atom interferometry. *Applied Physics B* 84, 4 (September 2006), 643–646.
- [25] CHIOW, S., KOVACHY, T., CHIEN, H., AND KASEVICH, M. A. $102 \hbar k$ Large Area Atom Interferometers. *Physical Review Letters* 107, 13 (September 2011), 130403.
- [26] CHU, S., BJORKHOLM, J. E., ASHKIN, A., AND CABLE, A. Experimental Observation of Optically Trapped Atoms. *Physical Review Letters* 57, 3 (July 1986), 314–317.
- [27] CHU, S., HOLLBERG, L., BJORKHOLM, J. E., CABLE, A., AND ASHKIN, A. Three-dimensional viscous confinement and cooling of atoms by resonance radiation pressure. *Physical Review Letters* 55, 1 (July 1985), 48–51.
- [28] CIRAC, J. I., AND ZOLLER, P. Quantum Computations with Cold Trapped Ions. *Physical Review Letters* 74, 20 (May 1995), 4091–4094.
- [29] CLADÉ, P. Bloch oscillations in atom interferometry. In *International School of Physics "Enrico Fermi" Course 188 Atom Interferometry* (May 2014).
- [30] CLADÉ, P., GUELLATI-KHÉLIFA, S., NEZ, F., AND BIRABEN, F. Large Momentum Beam Splitter Using Bloch Oscillations. *Physical Review Letters* 102, 24 (June 2009), 240402.
- [31] COHEN-TANNOUJJI, C., AND GUERY-ODELIN, D. *Advances In Atomic Physics - An Overview*. World Scientific Publishing Co. Pte. Ltd., 2011.
- [32] COLELLA, R., OVERHAUSER, A. W., AND WERNER, S. A. Observation of Gravitationally Induced Quantum Interference. *Physical Review Letters* 34, 23 (June 1975), 1472–1474.
- [33] COLLETT, E. Stokes Parameters for Quantum Systems. *American Journal of Physics* 38, 5 (1970), 563.
- [34] COURTILOT, I., QUESSADA, A., KOVACICH, R. P., ZONDY, J. J., LANDRAGIN, A., CLAIRON, A., AND LEMONDE, P. Efficient cooling and trapping of strontium atoms. *Optics letters* 28, 6 (March 2003), 468–70.

- [35] DALIBARD, J., AND COHEN-TANNOUJJI, C. Dressed-atom approach to atomic motion in laser light: the dipole force revisited. *Journal of the Optical Society of America B* 2, 11 (November 1985), 1707.
- [36] DALIBARD, J., AND COHEN-TANNOUJJI, C. Laser cooling below the Doppler limit by polarization gradients: simple theoretical models. *Journal of the Optical Society of America B* 6, 11 (November 1989), 2023.
- [37] DAVIS, K. B., MEWES, M. O., ANDREWS, M. R., VAN DRUTEN, N. J., DURFEE, D. S., KURN, D. M., AND KETTERLE, W. Bose-Einstein Condensation in a Gas of Sodium Atoms. *Physical Review Letters* 75, 22 (November 1995), 3969–3973.
- [38] DAVISSON, C., AND GERMER, L. H. Diffraction of Electrons by a Crystal of Nickel. *Physical Review* 30, 6 (December 1927), 705–740.
- [39] DE ANGELIS, M., ANGININ, M. C., BEAUFILS, Q., BECKER, C., BERTOLDI, A., BONGS, K., BOURDEL, T., BOUYER, P., BOYER, V., DÖRSCHER, S., DUNCKER, H., ERTMER, W., FERNHOLZ, T., FROMHOLD, T. M., HERR, W., KRÜGER, P., KÜRBIS, C., MELLOR, C., DOSANTOS, F. P., PETERS, A., POLI, N., POPP, M., PREVEDELLI, M., RASEL, E. M., RUDOLPH, J., SCHRECK, F., SENGSTOCK, K., SORRENTINO, F., STELLMER, S., TINO, G. M., VALENZUELA, T., WENDRICH, T. J., WICHT, A., WINDPASSINGER, P., AND WOLF, P. iSense: A Portable Ultracold-Atom-Based Gravimeter. *Procedia Computer Science* 7 (2011), 334–336.
- [40] DELVA, P., ANGININ, M.-C., AND TOURRENC, P. A comparison between matter wave and light wave interferometers for the detection of gravitational waves. *Physics Letters A* 357, 4-5 (September 2006), 249–254.
- [41] DIMOPOULOS, S., GRAHAM, P. W., HOGAN, J. M., KASEVICH, M. A., AND RAJENDRAN, S. Atomic gravitational wave interferometric sensor. *Physical Review D* 78, 12 (December 2008), 122002.
- [42] DUNNING, A., GREGORY, R., BATEMAN, J., COOPER, N., HIMSWORTH, M., JONES, J. A., AND FREEGARDE, T. Composite pulses for interferometry in a thermal cold atom cloud. *Physical Review A* 90, 3 (September 2014), 033608.
- [43] DÜRR, S., NONN, T., AND REMPE, G. Fringe Visibility and Which-Way Information in an Atom Interferometer. *Physical Review Letters* 81, 26 (December 1998), 5705–5709.
- [44] EINSTEIN, A. Zur Theorie der Brownschen Bewegung. *Annalen der Physik* 324, 2 (1906), 371–381.
- [45] EINSTEIN, A. Strahlungs-Emission und -Absorption nach der Quantentheorie. *Deutsche Physikalische Gesellschaft. Verhandlungen* 18 (1916), 318–323.
- [46] EMILE, O., BARDOU, F., SALOMON, C., LAURENT, P., NADIR, A., AND CLAIRON, A. Observation of a New Magneto-optical Trap. *Europhysics Letters (EPL)* 20, 8 (December 1992), 687–691.

- [47] ENGLERT, B. G. U. Fringe Visibility and Which-Way Information: An Inequality. *Physical Review Letters* 77, 11 (September 1996), 2154–2157.
- [48] ERTMER, W., BLATT, R., HALL, J. L., AND ZHU, M. Laser Manipulation of Atomic Beam Velocities: Demonstration of Stopped Atoms and Velocity Reversal. *Physical Review Letters* 54, 10 (March 1985), 996–999.
- [49] ESTERMANN, I., AND STERN, O. Beugung von Molekularstrahlen. *Zeitschrift für Physik* 61 (1930), 95–125.
- [50] ESTÈVE, J., GROSS, C., WELLER, A., GIOVANAZZI, S., AND OBERTHALER, M. K. Squeezing and entanglement in a Bose–Einstein condensate. *Nature* 455, 7217 (October 2008), 1216–1219.
- [51] FARAH, T., GUERLIN, C., LANDRAGIN, A., BOUYER, P., GAFFET, S., DOSSANTOS, F. P., AND MERLET, S. Underground operation at best sensitivity of the mobile LNE-SYRTE cold atom gravimeter. *Gyroscopy and Navigation* 5, 4 (October 2014), 266–274.
- [52] FEYNMAN, R. P. Space-Time Approach to Non-Relativistic Quantum Mechanics. *Reviews of Modern Physics* 20, 2 (April 1948), 367–387.
- [53] FEYNMAN, R. P., VERNON, F. L., AND HELLWARTH, R. W. Geometrical Representation of the Schrödinger Equation for Solving Maser Problems. *Journal of Applied Physics* 28, 1 (1957), 49.
- [54] FISCHBACH, E., AND TALMADGE, C. Six years of the fifth force. *Nature* 356, 6366 (March 1992), 207–215.
- [55] FOOT, C. J. *Atomic Physics*. Oxford University Press, Oxford, 2005.
- [56] FRISCH, R. Experimenteller Nachweis des Einsteinschen Strahlungsrückstoßes. *Zeitschrift für Physik* 86, 1-2 (January 1933), 42–48.
- [57] FUJI, S. Geophysical prospecting. *Radioisotopes* 34, 2 (1985), 112–115.
- [58] GIESE, E., ROURA, A., TACKMANN, G., RASEL, E. M., AND SCHLEICH, W. P. Double Bragg diffraction: A tool for atom optics. *Physical Review A* 88, 5 (November 2013), 053608.
- [59] GORDON, J. P., AND ASHKIN, A. Motion of atoms in a radiation trap. *Physical Review A* 21, 5 (May 1980), 1606–1617.
- [60] GREINER, M., BLOCH, I., HÄNSCH, T. W., AND ESSLINGER, T. Magnetic transport of trapped cold atoms over a large distance. *Physical Review A* 63, 3 (February 2001), 031401.
- [61] GRIMM, R., WEIDEMÜLLER, M., AND OVCHINNIKOV, Y. B. Optical Dipole Traps for Neutral Atoms. In *Advances In Atomic Molecular and Optical Physics*, vol. 42. February 2000, pp. 95–170.

- [62] HAHN, E. L. Spin Echoes. *Physical Review* 80, 4 (November 1950), 580–594.
- [63] HÄNSCH, T., AND SCHAWLOW, A. Cooling of gases by laser radiation. *Optics Communications* 13, 1 (January 1975), 68–69.
- [64] HÄNSCH, T. W., AND COUILLAUD, B. Laser frequency stabilization by polarization spectroscopy of a reflecting reference cavity. *Optics Communications* 35, 3 (December 1980), 441–444.
- [65] HAROCHE, S. Controlling Photons in a Box and Exploring the Quantum to Classical Boundary (Nobel Lecture). *Angewandte Chemie International Edition* 52, 39 (September 2013), 10158–10178.
- [66] HAROCHE, S., AUFFEVES, A., MAIOLI, P., MEUNIER, T., GLEYZES, S., NOGUES, G., BRUNE, M., AND RAIMOND, J. M. Manipulating mesoscopic fields with a single atom in a cavity. In *Laser Spectroscopy* (February 2004), World Scientific Publishing Co. Pte. Ltd., pp. 265–272.
- [67] HILL, I. R., OVCHINNIKOV, Y. B., BRIDGE, E. M., CURTIS, E. A., AND GILL, P. Zeeman slowers for strontium based on permanent magnets. *Journal of Physics B: Atomic, Molecular and Optical Physics* 47, 7 (April 2014), 075006.
- [68] HOGAN, J. M., JOHNSON, D. M. S., AND KASEVICH, M. A. Light-pulse atom interferometry. In *Proceedings of the International Summer School of Physics "Enrico Fermi" on Atom Optics and Space Physics* (June 2007), p. 38.
- [69] HÖPE, A., HAUBRICH, D., SCHADWINKEL, H., STRAUCH, F., AND MESCHÉDE, D. Optical Trapping in a Cesium Cell with Linearly Polarized Light and at Zero Magnetic Field. *Europhysics Letters (EPL)* 28, 1 (October 1994), 7–12.
- [70] HOPKINS, S. A. *Laser cooling of rubidium atoms in a magneto-optical trap*. Phd, The Open University, 1996.
- [71] HOPKINS, S. A., AND DURRANT, A. V. Parameters for polarization gradients in three-dimensional electromagnetic standing waves. *Physical Review A* 56, 5 (November 1997), 4012–4022.
- [72] KASEVICH, M. A., AND CHU, S. Atomic interferometry using stimulated Raman transitions. *Physical Review Letters* 67, 2 (July 1991), 181–184.
- [73] KASEVICH, M. A., AND CHU, S. Measurement of the gravitational acceleration of an atom with a light-pulse atom interferometer. *Applied Physics B Photophysics and Laser Chemistry* 54, 5 (May 1992), 321–332.
- [74] KASEVICH, M. A., RIIIS, E., CHU, S., AND DEVÖE, R. G. rf spectroscopy in an atomic fountain. *Physical Review Letters* 63, 6 (August 1989), 612–615.

- [75] KASEVICH, M. A., WEISS, D. S., RIIS, E., MOLER, K., KASAPI, S., AND CHU, S. Atomic velocity selection using stimulated Raman transitions. *Physical Review Letters* 66, 18 (May 1991), 2297–2300.
- [76] KELLOGG, J. R., SCHLIPPERT, D., KOHEL, J. M., THOMPSON, R. J., AVELINE, D. C., AND YU, N. A compact high-efficiency cold atom beam source. *Applied Physics B* 109, 1 (October 2012), 61–64.
- [77] KOVACHY, T., HOGAN, J. M., SUGARBAKER, A., DICKERSON, S. M., DONNELLY, C. A., OVERSTREET, C., AND KASEVICH, M. A. Matter Wave Lensing to Picokelvin Temperatures. *Physical Review Letters* 114, 14 (April 2015), 143004.
- [78] LEE, J., GROVER, J. A., OROZCO, L. A., AND ROLSTON, S. L. Sub-Doppler cooling of neutral atoms in a grating magneto-optical trap. *Journal of the Optical Society of America B* 30, 11 (November 2013), 2869.
- [79] LETT, P. D., PHILLIPS, W. D., ROLSTON, S. L., TANNER, C. E., WATTS, R. N., AND WESTBROOK, C. I. Optical molasses. *Journal of the Optical Society of America B* 6, 11 (November 1989), 2084.
- [80] LETT, P. D., WATTS, R. N., WESTBROOK, C. I., PHILLIPS, W. D., GOULD, P. L., AND METCALF, H. J. Observation of Atoms Laser Cooled below the Doppler Limit. *Physical Review Letters* 61, 2 (July 1988), 169–172.
- [81] LÉVÈQUE, T., GAUGUET, A., MICHAUD, F., DOS SANTOS, F. P., AND LANDRAGIN, A. Enhancing the Area of a Raman Atom Interferometer Using a Versatile Double-Diffraction Technique. *Physical Review Letters* 103, 8 (August 2009), 080405.
- [82] LIN, Z., SHIMIZU, K., ZHAN, M., SHIMIZU, F., AND TAKUMA, H. Laser cooling and trapping of Li. *Japanese Journal of Applied Physics* 30, 7B (1991), L1324–L1326.
- [83] MALOSSI, N., BODART, Q., MERLET, S., LÉVÈQUE, T., LANDRAGIN, A., AND DOS SANTOS, F. P. Double diffraction in an atomic gravimeter. *Physical Review A* 81, 1 (January 2010), 013617.
- [84] MCCARRON, D. J., KING, S. A., AND CORNISH, S. L. Modulation transfer spectroscopy in atomic rubidium. *Measurement Science and Technology* 19, 10 (October 2008), 105601.
- [85] MCMASTER, W. H. Polarization and the Stokes Parameters. *American Journal of Physics* 22, 6 (1954), 351.
- [86] METCALF, H. J. Magnetic trapping of decelerated neutral atoms. *Progress in Quantum Electronics* 8, 3-4 (January 1984), 169–175.
- [87] METCALF, H. J., AND VAN DER STRATEN, P. Force on Two-Level Atoms. In *Laser Cooling and Trapping*, R. S. Berry, J. L. Birman, J. W. Lynn, M. P. Silverman, H. E. Stanley, and M. Voloshin, Eds. Springer US, New York, 1999, ch. 3, pp. 29–37.

- [88] METCALF, H. J., AND VAN DER STRATEN, P. Optical Molasses. In *Laser Cooling and Trapping*, R. S. Berry, J. L. Birman, J. W. Lynn, M. P. Silverman, H. E. Stanley, and M. Voloshin, Eds. Springer US, New York, 1999, pp. 87–97.
- [89] MICHALIK, L., AND DOMAŃSKI, A. Effective state of polarization of photon-beam. *Photonics Letters of Poland* 3, 1 (March 2011), 41–43.
- [90] MILLETT-SIKKING, A., HUGHES, I. G., TIERNEY, P., AND CORNISH, S. L. DAVLL lineshapes in atomic rubidium. *Journal of Physics B: Atomic, Molecular and Optical Physics* 40, 1 (January 2007), 187–198.
- [91] MINOGIN, V., AND SERIMAA, O. Resonant light pressure forces in a strong standing laser wave. *Optics Communications* 30, 3 (September 1979), 373–379.
- [92] MOLER, K., WEISS, D. S., KASEVICH, M. A., AND CHU, S. Theoretical analysis of velocity-selective Raman transitions. *Physical Review A* 45, 1 (January 1992), 342–348.
- [93] MÖLMEER, K. Friction and diffusion coefficients for cooling of atoms in laser fields with multidimensional periodicity. *Physical Review A* 44, 9 (November 1991), 5820–5832.
- [94] MONROE, C., ROBINSON, H., AND WIEMAN, C. Observation of the cesium clock transition using laser-cooled atoms in a vapor cell. *Optics Letters* 16, 1 (January 1991), 50.
- [95] MONROE, C., SWANN, W., ROBINSON, H., AND WIEMAN, C. Very cold trapped atoms in a vapor cell. *Physical Review Letters* 65, 13 (September 1990), 1571–1574.
- [96] MOSKOWITZ, P. E., GOULD, P. L., ATLAS, S. R., AND PRITCHARD, D. E. Diffraction of an Atomic Beam by Standing-Wave Radiation. *Physical Review Letters* 51, 5 (August 1983), 370–373.
- [97] MÜLLER, H., CHIOU, S., AND CHU, S. Atom-wave diffraction between the Raman-Nath and the Bragg regime: Effective Rabi frequency, losses, and phase shifts. *Physical Review A* 77, 2 (February 2008), 023609.
- [98] MÜLLER, H., CHIOU, S., HERRMANN, S., AND CHU, S. Atom Interferometers with Scalable Enclosed Area. *Physical Review Letters* 102, 24 (June 2009), 240403.
- [99] MÜLLER, H., CHIOU, S., LONG, Q., HERRMANN, S., AND CHU, S. Atom Interferometry with up to 24-Photon-Momentum-Transfer Beam Splitters. *Physical Review Letters* 100, 18 (May 2008), 180405.
- [100] MÜNTINGA, H., AHLERS, H., KRUTZIK, M., WENZLAWSKI, A., ARNOLD, S., BECKER, D., BONGS, K., DITTUS, H., DUNCKER, H., GAALLOUL, N., GHERASIM, C., GIESE, E., GRZESCHIK, C., HÄNSCH, T. W., HELLMIG, O., HERR, W., HERRMANN, S., KAJARI, E., KLEINERT, S., LÄMMERZAHN, C., LEWOCZKO-ADAMCZYK, W., MALCOLM, J., MEYER, N., NOLTE, R., PETERS, A., POPP, M.,

- REICHEL, J., ROURA, A., RUDOLPH, J., SCHIEMANGK, M., SCHNEIDER, M., SEIDEL, S. T., SENGSTOCK, K., TAMMA, V., VALENZUELA, T., VOGEL, A., WALSER, R., WENDRICH, T., WINDPASSINGER, P., ZELLER, W., VAN ZOEST, T., ERTMER, W., SCHLEICH, W. P., AND RASEL, E. M. Interferometry with Bose-Einstein Condensates in Microgravity. *Physical Review Letters* *110*, 9 (February 2013), 093602.
- [101] MYRSKOG, S., FOX, J., MOON, H., KIM, J., AND STEINBERG, A. Modified δ -kick cooling using magnetic field gradients. *Physical Review A* *61*, 5 (apr 2000), 1–6.
- [102] NAIRZ, O., ARNDT, M., AND ZEILINGER, A. Quantum interference experiments with large molecules. *American Journal of Physics* *71*, 4 (2003), 319.
- [103] PARK, C. Y., JUN, M. S., AND CHO, D. Magneto-optical trap loaded from a low-velocity intense source. *Journal of the Optical Society of America B* *16*, 6 (June 1999), 994.
- [104] PETELSKI, T. *Atom Interferometers for Precision Gravity Measurements*. PhD thesis, Universita di Firenze, 2005.
- [105] PETERS, A. *High Precision Gravity Measurements Using Atom Interferometry*. PhD thesis, Stanford University, 1998.
- [106] PETERS, A., CHUNG, K. Y., AND CHU, S. High-precision gravity measurements using atom interferometry. *Metrologia* *38*, 1 (February 2001), 25–61.
- [107] PHILLIPS, W. D., AND METCALF, H. J. Laser Deceleration of an Atomic Beam. *Physical Review Letters* *48*, 9 (March 1982), 596–599.
- [108] PHILLIPS, W. D., PRODAN, J. V., AND METCALF, H. J. Neutral atomic beam cooling experiments at NBS. *Progress in Quantum Electronics* *8*, 3-4 (January 1984), 119–127.
- [109] POLLOCK, S., COTTER, J. P., LALLOTIS, A., AND HINDS, E. A. Integrated magneto-optical traps on a chip using silicon pyramid structures. *Optics Express* *17*, 16 (August 2009), 14109.
- [110] RAAB, E. L., PRENTISS, M., CABLE, A., CHU, S., AND PRITCHARD, D. E. Trapping of Neutral Sodium Atoms with Radiation Pressure. *Physical Review Letters* *59*, 23 (December 1987), 2631–2634.
- [111] RABI, I. I., ZACHARIAS, J. R., MILLMAN, S., AND KUSCH, P. A New Method of Measuring Nuclear Magnetic Moment. *Physical Review* *53*, 4 (February 1938), 318–318.
- [112] RAMIREZ-SERRANO, J., YU, N., KOHEL, J. M., KELLOGG, J. R., AND MALEKI, L. Multistage two-dimensional magneto-optical trap as a compact cold atom beam source. *Optics Letters* *31*, 6 (March 2006), 682.

- [113] RAMSEY, N. F. A New Molecular Beam Resonance Method. *Physical Review* 76, 7 (October 1949), 996–996.
- [114] RAMSEY, N. F. A Molecular Beam Resonance Method with Separated Oscillating Fields. *Physical Review* 78, 6 (June 1950), 695–699.
- [115] RITT, G., CENNINI, G., GECKELER, C., AND WEITZ, M. Laser frequency offset locking using a side of filter technique. *Applied Physics B* 79, 3 (August 2004), 363–365.
- [116] ROURA, A., ZELLER, W., AND SCHLEICH, W. P. Overcoming loss of contrast in atom interferometry due to gravity gradients. *New Journal of Physics* 16, 12 (dec 2014), 123012.
- [117] ROY, B., AND SCHOLTEN, M. High-flux cold rubidium atomic beam for strongly-coupled cavity QED. *Journal of the Korean Physical Society* 61, 3 (August 2012), 359–364.
- [118] RUDOLPH, J., HERR, W., GRZESCHIK, C., STERNKE, T., GROTE, A., POPP, M., BECKER, D., MÜNTINGA, H., AHLERS, H., PETERS, A., LÄMMERZAHL, C., SENGSTOCK, K., GAALOUL, N., ERTMER, W., AND RASEL, E. M. A high-flux BEC source for mobile atom interferometers. *New Journal of Physics* 17, 6 (2015), 065001.
- [119] RUMMEL, R., YI, W., AND STUMMER, C. GOCE gravitational gradiometry. *Journal of Geodesy* 85, 11 (November 2011), 777–790.
- [120] SALOMON, C., DALIBARD, J., PHILLIPS, W. D., CLAIRON, A., AND GUELLATI, S. Laser Cooling of Cesium Atoms Below 3 μK . *Europhysics Letters (EPL)* 12, 8 (August 1990), 683–688.
- [121] SCHIEMANGK, M., LAMPMANN, K., DINKELAKER, A., KOHFELDT, A., KRUTZIK, M., KÜRBIS, C., SAHM, A., SPIESSBERGER, S., WICHT, A., ERBERT, G., TRÄNKLE, G., AND PETERS, A. High-power, micro-integrated diode laser modules at 767 and 780 nm for portable quantum gas experiments. *Applied optics* 54, 17 (2015), 5332–8.
- [122] SCHMID, S., THALHAMMER, G., WINKLER, K., LANG, F., AND DENSCHLAG, J. H. Long distance transport of ultracold atoms using a 1D optical lattice. *New Journal of Physics* 8, 8 (August 2006), 159–159.
- [123] SCHMIDT, M. *A mobile high-precision gravimeter based on atom interferometry*. PhD thesis, Humboldt University Berlin, 2011.
- [124] SCHULD, T., SCHUBERT, C., KRUTZIK, M., BOTE, L. G., GAALOUL, N., HARTWIG, J., AHLERS, H., HERR, W., POSSO-TRUJILLO, K., RUDOLPH, J., SEIDEL, S., WENDRICH, T., ERTMER, W., HERRMANN, S., KUBELKA-LANGE, A., MILKE, A., RIEVERS, B., ROCCO, E., HINTON, A., BONGS, K., OSWALD, M., FRANZ, M., HAUTH, M., PETERS, A., BAWAMIA, A., WICHT, A., BATTELIER, B., BERTOLDI, A., BOUYER, P., LANDRAGIN, A., MASSONNET, D., LÉVÈQUE, T., WENZLAWSKI, A., HELLMIG, O., WINDPASSINGER, P., SENGSTOCK, K., VON KLITZING, W., CHALONER, C., SUMMERS, D., IRELAND, P., MATEOS, I., SÓPUERTA, C. F., SORRENTINO, F., TINO, G. M.,

- WILLIAMS, M., TRENKEL, C., GERARDI, D., CHWALLA, M., BURKHARDT, J., JOHANN, U., HESKE, A., WILLE, E., GEHLER, M., CACCIAPUOTI, L., GÜRLEBECK, N., BRAXMAIER, C., AND RASEL, E. M. Design of a dual species atom interferometer for space. *Experimental Astronomy* 39, 2 (2015), 167–206.
- [125] SENGER, A. *A Mobile Atom Interferometer for High-Precision Measurements of Local Gravity*. PhD thesis, Humboldt-University Berlin, 2011.
- [126] SHIRLEY, J. H. Modulation transfer processes in optical heterodyne saturation spectroscopy. *Optics letters* 7, 11 (November 1982), 537–9.
- [127] SPEAKE, C. C., HAMMOND, G. D., AND TRENKEL, C. The torsion balance as a tool for geophysical prospecting. *Geophysics* 66, 2 (March 2001), 527–534.
- [128] STEANE, A. M., CHOWDHURY, M., AND FOOT, C. J. Radiation force in the magneto-optical trap. *Journal of the Optical Society of America B* 9, 12 (December 1992), 2142.
- [129] STEANE, A. M., HILLENBRAND, G., AND FOOT, C. J. Polarization gradient cooling in a one-dimensional sigma + - sigma - configuration for any atomic transition. *Journal of Physics B: Atomic, Molecular and Optical Physics* 25, 22 (November 1992), 4721–4743.
- [130] STECK, D. A. "Rubidium 87 D Line Data", available online at <http://steck.us/alkalidata>. Tech. rep., 2010.
- [131] STENHOLM, S. The semiclassical theory of laser cooling. *Reviews of Modern Physics* 58, 3 (July 1986), 699–739.
- [132] STOKES, G. G. On the Change of Refrangibility of Light. No. II. *Philosophical Transactions of the Royal Society of London* 143 (January 1853), 385–396.
- [133] STOREY, P., AND COHEN-TANNOUJJI, C. The Feynman path integral approach to atomic interferometry. A tutorial. *Journal de Physique II* 4, 11 (November 1994), 1999–2027.
- [134] THORPE, J. I., NUMATA, K., AND LIVAS, J. Laser frequency stabilization and control through offset sideband locking to optical cavities. *Optics Express* 16, 20 (September 2008), 15980.
- [135] TINO, G. M., AND VETRANO, F. Is it possible to detect gravitational waves with atom interferometers? *Classical and Quantum Gravity* 24, 9 (May 2007), 2167–2178.
- [136] TOLLETT, J. J., CHEN, J., STORY, J. G., RITCHIE, N. W. M., BRADLEY, C. C., AND HULET, R. G. Observation of velocity-tuned multiphoton "Doppleron" resonances in laser-cooled atoms. *Physical Review Letters* 65, 5 (July 1990), 559–562.

- [137] TREUTLEIN, P., CHUNG, K. Y., AND CHU, S. High-brightness atom source for atomic fountains. *Physical Review A* 63, 5 (April 2001), 051401.
- [138] TRUPKE, M., RAMIREZ-MARTINEZ, F., CURTIS, E. A., ASHMORE, J. P., ERIKSSON, S., HINDS, E. A., MOKTADIR, Z., GOLLASCH, C., KRAFT, M., VIJAYA PRAKASH, G., AND BAUMBERG, J. J. Pyramidal micromirrors for microsystems and atom chips. *Applied Physics Letters* 88, 7 (2006), 071116.
- [139] VON EÖTVÖS, R. Untersuchungen über Gravitation und Erdmagnetismus. *Annalen der Physik und Chemie* 295, 10 (1896), 354–400.
- [140] WALKER, M. J. Matrix Calculus and the Stokes Parameters of Polarized Radiation. *American Journal of Physics* 22, 4 (1954), 170.
- [141] WALLACE, C. D., DINNEEN, T. P., TAN, K. N., GROVE, T. T., AND GOULD, P. L. Isotopic difference in trap loss collisions of laser cooled rubidium atoms. *Physical Review Letters* 69, 6 (August 1992), 897–900.
- [142] WATTS, R. N., AND WIEMAN, C. E. Manipulating atomic velocities using diode lasers. *Optics Letters* 11, 5 (May 1986), 291.
- [143] WEISS, D. S., YOUNG, B. C., AND CHU, S. Precision measurement of \hbar/m Cs based on photon recoil using laser-cooled atoms and atomic interferometry. *Applied Physics B Lasers and Optics* 59, 3 (September 1994), 217–256.
- [144] WIEMAN, C., AND HÄNSCH, T. W. Doppler-Free Laser Polarization Spectroscopy. *Physical Review Letters* 36, 20 (May 1976), 1170–1173.
- [145] WIEMAN, C. E., AND HOLLBERG, L. Using diode lasers for atomic physics. *Review of Scientific Instruments* 62, 1 (1991), 1.
- [146] WINELAND, D. J., AND ITANO, W. M. Laser cooling of atoms. *Physical Review A* 20, 4 (October 1979), 1521–1540.
- [147] ZEPPENFELD, M., ENGLERT, B. G. U., GLÖCKNER, R., PREHN, A., MIELENZ, M., SOMMER, C., VAN BUUREN, L. D., MOTSCH, M., AND REMPE, G. Sisyphus cooling of electrically trapped polyatomic molecules. *Nature* 491, 7425 (November 2012), 570–573.

Acknowledgements

My gratitude is with Prof. Dr. Kai Bongs, head of the Quantum Matter Group, for his inspiration which kept the project going during its ups and downs.

Thank is also with my first supervisor Dr. Tristan Valenzuela and later Dr. Michael Holynski who helped with words and deeds. The experiment was made possible by my fellow PhD students Andrew Hinton and Georgios Voulazeris who spend the hours in the lab with me.

A lot of inspiration and ides were drawn from and developed with the team of the iSense project, Jonathan Malcolm, Clemens Rammeloo and Lingxiao Zhu, who had similar struggles and were never short of a good idea. A special thank you to Jon, who was so kind to check the script for spelling and grammar mistakes and corrected an infinite amount of commata.

Nomenclature

AOM **A**custo-**O**ptical-**M**odulator

DAVL **D**ichroic **A**tomic **V**apour **L**ock

ECDLs **E**xtended **C**avity **D**iode **L**asers

EOM **E**lectro-**O**ptical **M**odulator

IGBT **I**nsulated **G**ate **B**ipolar **T**ransistor

LCR **L**iquid **C**rystal **R**etarder

MOT **M**agneto-**O**ptical **T**rap

OD **O**ptical **D**ensity

PBS **P**olarising **B**eam **S**plitter

TOF **T**ime **O**f **F**light